# Fragility and Resilience of Bridges Subjected to Extreme Wave-Induced Forces

A thesis submitted in fulfilment of the requirements for the degree of Doctor of Philosophy

by


## Ismail M. I. Qeshta

BEng (Civil Engineering) (Honours), University of Malaya

MEngSc (Structural Engineering and Materials), University of Malaya

School of Engineering

College of Science, Engineering and Health

RMIT University

Melbourne, Australia


August 2019

## DECLARATION

I certify that except where due acknowledgement has been made, the work is that of the author alone; the work has not been submitted previously, in whole or in part, to qualify for any other academic award; the content of the thesis is the result of work which has been carried out since the official commencement date of the approved research program; any editorial work, paid or unpaid, carried out by a third party is acknowledged; and, ethics procedures and guidelines have been followed.

Ismail M. I. Qeshta

1 August 2019

## ACKNOWLEDGEMENTS

I would like to express my sincerest gratitude to my senior supervisor Professor Sujeeva Setunge for her guidance and support. Her wisdom and professionalism were crucial at every step of my study, and I owe her a great debt for advancing my academic and personal development. I would also like to express my deepest gratitude to my joint senior supervisor Dr M. Javad Hashemi, from Swinburne University of Technology, for his tremendous guidance, support and effort. I will be forever grateful for his time, dedication and friendship throughout my candidature. I would like to thank my associate supervisor Associate Professor Rebecca Gravina for her time, encouragement and support.

I would like to acknowledge the support from RMIT University, Australia in the form of RMIT PhD International Scholarship (RPIS) for my doctoral study.

My doctoral study experience at RMIT University has been great because of the help and support of many people. I would like to thank my colleague Ali Al-Attraqchi (Swinburne University of Technology) for his help with *OpenSees* simulations. I am grateful to Professor Riadh Al-Mahaidi (Swinburne University of Technology) for his great support during these years. Many thanks go to Dr Hassan Baji (Central Queensland University) for his help with the structural reliability analyses. I would like to thank Dr Hessam Mohseni (Department of Transport, Victoria) for his support at the initial stages of my doctoral study. I would also like to thank Dr Mohamed Elchalakani (The University of Western Australia) and Dr Yew-Chin Koay (Department of Transport, Victoria) for their feedback on my numerical models and research method.

I would like to acknowledge the Bushfire and Natural Hazards Cooperative Research Centre (BNH-CRC) group members at RMIT University: Professor Kevin Zhang, Dr Dilan Robert,

Dr Srikanth Venkatesan, Dr Long Shi and Dr Huu Tran for their remarks and feedback in our regular meetings. Many thanks go to all the staff at the School of Engineering, RMIT University for their kindness and support throughout my doctoral study journey.

I would like to extend my gratitude to my friend Kamil Braima (Murdoch University) for his advice and encouragement. I would like to thank my colleagues at the School of Engineering, RMIT University: Nizamuddin (Andy), Sakinul Islam, Maryam Nasim, Amila Dissanayake, Farook Kalendher, Akvan Gavanayake, Vahid Aryai, Rajeev Roychand, Zeinab Yazdanfar, Jagan Kummari, Tahir Siddiqui and Humair Baloch for their help and support.

Finally, I am truly grateful to my parents, brothers and sisters for their unconditional love and endless support, without which the completion of my studies would not have been possible.

## DEDICATION

*I would like to dedicate this work to:*

*my dear mother: Wafaa (Kamla) Khalil Qeshta*

*my dear father: Mohamed Ismail Qeshta*

*my brothers: Basel and Hamdan*

*my sisters: Walaa, Anfal, Omnia, Hadeel, Shatha and Ayat.*

## LIST OF PUBLICATIONS

- **Journal papers:**

1. Qeshta, I. M. I., Hashemi, M. J., Gravina, R., and Setunge, S. (2019). Review of resilience assessment of coastal bridges to extreme wave-induced loads. *Engineering Structures*, 185, 332-352. URL: https://www.sciencedirect.com/science/article/pii/S0141029618318194

2. Qeshta, I. M. I., Hashemi, M. J., Gravina, R., and Setunge, S. A methodology for development of fragility functions for bridges subjected to extreme hydrodynamic forces (journal paper draft under preparation for submission to *Journal of Structural Engineering*).

- **Conference papers:**

1. Qeshta, I. M. I., Hashemi, M. J., Gravina, R., and Setunge, S. (2018). Fragility analysis of non-ductile RC bridges subjected to extreme hydrodynamic forces. *Proceedings of the Ninth International Conference on Bridge Maintenance, Safety and Management (IABMAS 2018)* (pp. 1279-1285). Taylor & Francis Group. URL: https://www.taylorfrancis.com/books/e/9781315189390

2. Qeshta, I. M. I., Hashemi, M. J., Gravina, R., and Setunge, S. Fragility analysis of bridges retrofitted with FRP wraps and subjected to extreme wave-induced forces (conference paper draft under preparation for submission to *IABMAS2020*).

## TABLE OF CONTENTS

## LIST OF FIGURES

triangle of time; (c) resilience triangle of resources; and (d) resilience triangle of environmental impact.

## LIST OF TABLES

## LIST OF SYMBOLS, ABBREVIATIONS AND NOMENCLATURE

| Notation/Symbol | Definition |
|---|---|
| $d$ | sea water level |
| $\lambda$ | wave length |
| $T_p$ | wave period |
| $z$ | clearance |
| $H$ | wave height |
| $H_s$ | significant wave height |
| $H_{max}$ | maximum wave height |
| $\eta_{max}$ | crest elevation |
| $W$ | bridge width |
| $L$ | bridge length |
| $\theta$ | inclination angle along the longitudinal axis of bridge |
| $S$ | girder spacing |
| $d_g$ | girder height |
| $d^*$ | inundation ratio of surging free surface |
| $u$ | flow velocity |
| $C$ | force coefficient |
| $\rho_s$ | density of sea water |
| $b$ | width of the projected area of the structure |
| $h$ | depth of inundation |
| $g$ | gravitational acceleration |
| $V$ | displaced volume of water |
| $F_v^*$ | uplift reference force in Douglass et al. (2006) |
| $F_h^*$ | drag reference force in Douglass et al. (2006) |
| $A_v$ | horizontal projected area of the deck in Douglass et al. (2006) |
| $A_h$ | vertical projected area of the deck in Douglass et al. (2006) |
| $c_{v\text{-}va}$ | empirical coefficient for uplift force in Douglass et al. (2006) |

| | |
|---|---|
| $c_{h\text{-}va}$ | empirical coefficient for drag force in Douglass et al. (2006) |
| $N$ | number of girders in Douglass et al. (2006) |
| $c_r$ | additional reduction coefficient for the drag force in Douglass et al. (2006) |
| $F_w$ | downward force in McPherson (2008) |
| $Vol_{Bridge}$ | volume of displaced water in McPherson (2008) |
| $A$ | horizontal projected area in McPherson (2008) |
| $\delta_z$ | height between the deck surface and wave crest in McPherson (2008) |
| $F_{Hydrostatic\_Back}$ | water force at the backside girder in McPherson (2008) |
| $F_{Hydrostatic\_Front}$ | drag force in McPherson (2008) |
| $A_G$ | cross-sectional area of the spacing between girders in McPherson (2008) |
| $\gamma$ | density of water in McPherson (2008) |
| $\delta_G$ | girder height in McPherson (2008) |
| $n$ | number of girders in McPherson (2008) |
| $C_w$ | overtopping water factor in Xu et al. (2017) |
| $h_{back}$ | water height at the deck landward side in Xu et al. (2017) |
| $C_L$ | hydrodynamic force uplift coefficient in Xu et al. (2017) |
| $C_D$ | hydrodynamic force drag coefficient in Xu et al. (2017) |
| $b_1$, $a_1$, $a_2$, $a_3$ | abbreviated equations of coefficients defined based on the wave and deck parameters for Case I in AASHTO (2008) |
| $r$ | height of railing in AASHTO (2008) |
| $d_b$ | total height of girder and deck thickness in AASHTO (2008) |
| $\overline{W}$, $W^*$, $\beta$, $B$, $A$ | parameters defined based on wave and deck parameters for Case I in AASHTO (2008) |
| $\gamma_w$ | unit weight of water in AASHTO (2008) |
| $TAF$ | air entrapment factor in AASHTO (2008) |
| $d_s$ | level of storm water in AASHTO (2008) |
| $Z_c$ | clearance in AASHTO (2008) |
| $\omega$, $\alpha$ | parameters defined based on clearance, wave height, wave length and superstructure width for Case II in AASHTO (2008) |

| | |
|---|---|
| $L_x$ | deck length in Jin and Meng (2011) |
| $L_y$ | deck width in Jin and Meng (2011) |
| $L_z$ | deck depth in Jin and Meng (2011) |
| $C_h(T)$ | coefficients to account for the effect of period in drag force in Jin and Meng (2011) |
| $C_v(T)$ | coefficients to account for the effect of period in uplift force in Jin and Meng (2011) |
| $F_b$ | buoyant force in Jin and Meng (2011) |
| $C_{UP}$ | empirical uplift coefficient in Azadbakht and Yim (2014) |
| $C_{DV}$ | empirical drag coefficient in Azadbakht and Yim (2014) |
| $F_l$ | hydrodynamic uplift force in Azadbakht and Yim (2014) |
| $F_{v\_hs}$ | downward vertical (hydrostatic) force in Azadbakht and Yim (2014) |
| $F_{v\_s}$ | slamming vertical force in Azadbakht and Yim (2014) |
| $F_{h\_hs}$ | hydrostatic force in Azadbakht and Yim (2014) |
| $F_d$ | hydrodynamic drag force in Azadbakht and Yim (2014) |
| $F_b$ | buoyant force in Azadbakht and Yim (2014) |
| $\Phi(\cdot)$ | standard normal cumulative distribution function |
| $\mu$ | mean |
| $\sigma$ | standard deviation |
| $t$ | time vector, or restoration time |
| $X$ | structural parameters vector/ random variable |
| IM | intensity measure |
| $DM$ | damage measure |
| EDP | engineering demand parameter |
| $DV$ | damage variable |
| $Q$ | performance, as a function of time $Q(t)$, resources $Q(c)$ and environmental impact $Q(e)$ |
| $R$ | normalized resilience factor |
| $R_t$ | normalized resilience factor calculated from the performance-time relationship |

| | |
|---|---|
| $R_c$ | normalized resilience factor calculated from the performance-resources relationship |
| $R_e$ | normalized resilience factor calculated from the performance-environmental impact relationship |
| $I_t$ | importance factor for time |
| $I_c$ | importance factor for resources |
| $I_e$ | importance factor for environmental impact |
| $t_o$ | time at instant of occurrence of extreme hazard |
| $t_r$ | time required to restore the targeted functionality |
| $t_h$ | specific time horizon |
| $c$ | resource capacity |
| $c_o$ | initial resources at the instant of extreme event |
| $c_r$ | resources at the full performance |
| $c_h$ | fixed resource capping |
| $t_c$ | crash time |
| $t_n$ | normal time |
| $c_c$ | crash resources (cost) |
| $c_n$ | normal resources (cost) |
| $\Gamma$ | network performance index |
| $TTT$ | total travel time |
| $TTD$ | total travel distance |
| $\gamma_T$ | balancing factor for the total travel time |
| $\gamma_D$ | balancing factor for the total travel distance |
| $e$ | environmental impact |
| $e_o$ | initial environmental impact |
| $e_r$ | environmental impact at full performance |
| $e_h$ | fixed environmental impact value |
| $p_w$ | pressure of hydrodynamic force |
| $F$ | hydrodynamic force |
| $u_i$ | flow velocity increment |

| | |
|---|---|
| $h_j$ | inundation depth increment |
| $x$ | random variable realization (specific value)/intensity measure example |
| $f_X(x)$ | probability density function |
| $\mu_X$ | mean of random variable |
| [a,b] | uniform distribution range |
| MCS | Monte Carlo Simulation |
| $u_{max}$ | maximum flow velocity |
| $h_{max}$ | maximum inundation depth |
| $DS$ | damage state |
| $DS_j$ | damage state for one inundation depth |
| $\delta$ | pier drift |
| $\delta_{max}$ | maximum pier drift |
| $Fr$ | Froude number |
| $Fr_{limit}$ | Froude number limit |
| $P$ | base shear |
| LHS | Latin Hypercube Sampling |
| AV | Antithetic Variates |
| $V$ | random variable |
| $P_{f_i}^{(1)}$ | failure probability of first simulation run (Ayyub and Lai, 1991) |
| $P_{f_i}^{(2)}$ | failure probability of second simulation run (Ayyub and Lai, 1991) |
| $Var$ | variance (Ayyub and Lai, 1991) |
| $N$ | number of simulation cycles (Ayyub and Lai, 1991) |
| $P_{f_i}$ | failure probability at a certain cycle (Ayyub and Lai, 1991) |
| $Cov$ | covariance (Ayyub and Lai, 1991) |
| $\overline{P}_f$ | mean value of failure probability (Ayyub and Lai, 1991) |
| $hu^2$ | momentum flux |
| $h^2u^2/2$ | moment of momentum flux |
| c/c | centre-to-centre |

| | |
|---|---|
| dia. | diameter |
| *OpenSees* | Open System for Earthquake Engineering Simulation |
| $I_z$ | second moment of area about local *z*-axes |
| $I_y$ | second moment of area about local *y*-axes |
| $R_o$, $cR_1$ and $cR_2$ | parameters that control the transition from elastic to strain hardening stage in Giuffré-Menegotto-Pinto (GMP) (Menegotto and Pinto, 1973) model |
| $b_{sh}$ | strain hardening ratio of steel |
| FRP | fibre reinforced polymer |
| $P_{cr}$ | cracking load |
| $\Delta_{cr}$ | lateral displacement at first crack |
| $P_y$ | yielding load |
| $\Delta_y$ | lateral displacement at yielding |
| UDL | uniformly distributed load |
| $P_g$ | gravity load |
| $L$ | pier height |
| $A_g$ | total gross-sectional area of pier |
| $c$ | concrete cover thickness |
| $A_{sl}$ | cross-sectional area of longitudinal steel reinforcement |
| $n$ | number of longitudinal steel reinforcement |
| $A_{st}$ | cross-sectional area of transverse reinforcement |
| $s$ | spacing of transverse reinforcement |
| $n_p$ | number of FRP layers |
| $w_p$ | width of FRP jackets |
| $t_p$ | thickness of one FRP layer |
| $f_c'$ | concrete compressive strength |
| $f_y$ | steel yield strength |
| $C_d$ | drag coefficient of hydrodynamic force |
| COV | coefficient of variation |

| | |
|---|---|
| $IM_m$ | intensity measure that corresponds to a damage probability of 50% |
| $P_\sigma$ | standard deviations of the damage probability data points at $IM_m$ |
| $P_\mu$ | mean deviations of the damage probability data points at $IM_m$ |
| $P_\sigma^{initial}$ | standard deviations of the damage probability data points at $IM_m$ for initial bridge |
| $P_\sigma^{strengthened}$ | standard deviations of the damage probability data points at $IM_m$ for strengthened bridge |
| $P_\mu^{initial}$ | mean deviations of the damage probability data points at $IM_m$ for initial bridge |
| $P_\mu^{strengthened}$ | mean deviations of the damage probability data points at $IM_m$ for strengthened bridge |

## ABSTRACT

Bridges are susceptible to severe damage due to wave-induced forces during extreme events such as floods, hurricanes, storm surges and tsunamis. As a direct impact of climate change, the frequency and intensity of these events are also expected to increase in the future. The damages to bridges lead to substantial community impact during emergency and post-disaster recovery activities. Hence, viable restoration strategies are needed to enhance the resilience of bridges under extreme wave hazards. The research on the quantification of vulnerability and resilience of bridges under extreme wave forces is limited. In particular, vulnerability and resilience assessment tools for bridges under different hazard intensity levels are required to quantify the resilience. This research addresses these research needs by providing a comprehensive vulnerability assessment framework for bridges subjected to extreme hydrodynamic forces.

A comprehensive literature review is first conducted on the four resilience assessment elements, namely external wave force characterization, structural response, vulnerability assessment and resilience quantification to identify the existing gaps in knowledge, particularly in vulnerability and assessment methods.

Unified resilience indices, based on the "resilience triangle" concept, are proposed to take into account the effect of the consideration of resources (cost) and environmental impact and their relative importance to the decision makers in the resilience quantification. Such indices are important for stakeholders as they provide a linkage between the social (time), economic and environmental impacts in the assessment of restoration strategies.

An integrated vulnerability assessment framework for bridges with strong connectivity between super- and sub-structure is proposed. The framework includes both static and time-

history analyses to examine the performance of bridges subjected to significant hydrodynamic forces. The uncertainties in force and structural parameters are taken into account and the probability of damage is estimated using six damage states that define the pre- and post-peak response of bridge. The pier drift is taken as the engineering demand parameter. The use of two-parameter intensity measures that can provide an accurate estimation of the response of bridge such as momentum flux ($hu^2$) and moment of momentum flux ($h^2u^2/2$) is investigated.

To demonstrate the proposed framework, a numerical model is developed for a case study bridge located in a flood-prone region in Queensland, Australia. The accuracy of the piers model is validated using published works on small-scale pier specimens that have limited ductility. The effect of strengthening of bridge piers using fibre reinforced polymer (FRP) jackets is examined.

The overall fragility functions for all intensity measures (velocity, inundation depth, momentum flux and moment of momentum flux) are obtained for both initial and strengthened bridge. The reduction in scatter of fragility data is examined for the two-parameter intensity measures for all damage states. The viability of the use of FRP jackets for enhancing the resilience of bridges under extreme wave forces is also evaluated. The application of unified resilience indices based on the damage probability data obtained from fragility analysis is discussed for different intensities of the hazard.

The main contribution provided by this research is the comprehensive vulnerability and resilience assessment methods for bridges under extreme wave hazards. Such methodologies can assist in the evaluation of the different pre-disaster strengthening and recovery schemes for bridges. Decision makers (e.g., road authorities) can use the outcome of this research to

assess the different retrofitting options for bridges taking into consideration the time, cost and energy consumption associated with each option.

# CHAPTER 1

# INTRODUCTION

## 1.1 Background

Bridges are critical transportation infrastructure elements due to their important role in supporting the country's economic growth, facilitating timely access between the regions across the country and assisting the emergency response and recovery operations in the aftermath of natural disasters. In Australia, there are about 53000 road bridges that contribute to a total road length of more than 877000 kilometers (BITRE, 2018; Caprani, 2018; Wiggins, 2018). The past notable flood events in Australia have shown that bridges are susceptible to substantial damage due to the significant wave-induced forces (Pritchard, 2013). Queensland flood events resulted in 89 and 43 damaged bridges in 2010/2011 (central and southern areas) and 2013 (Lockyer Valley area), respectively (Setunge et al., 2014). The total damage cost of road infrastructure as a result of flood events in 2010 to 2012 and 2013 was about $7 billion and $900 million, respectively (Pritchard, 2013; Queensland Government, 2013). In addition, the post-disaster reconnaissance reports from other weather hazards around the world such as hurricanes, typhoons and tsunamis have shown that bridges are among the most vulnerable components in the transportation network (Ataei, 2013). For instance, hurricanes Ivan (of 2004), Katrina (of 2005), Ike (of 2008), Sandy (of 2012), Harvey, Irma and Maria (of 2017), Florence (of 2018), Indian Ocean and Tohoku tsunamis of 2004 and 2011, respectively, and typhoon Haiyan of 2013 all have caused severe damage to bridges (Akiyama et al., 2013; Bueno, 2017; Douglass et al., 2004; Ghobarah et al., 2006; Godart, 2017; Iemura et al., 2005; Kaufman et al., 2012; Kawashima and Buckle, 2013; Kosa, 2011; Mas et al., 2014; McAllister, 2014; McDonald, 2017; Moon, 2018; Mosqueda

et al., 2007; Pritchard, 2013; Robertson et al., 2007; Robertson et al., 2007; Stearns and Padgett, 2011; Unjoh, 2006). The effect of climate change and global warming on the rainfall rates and sea level rise would likely lead to an increase in the severity and intensity of these disasters, and hence bridges are expected to be subjected to more significant forces in the future events (Dale et al., 2001; ICF International, 2007; Knutson et al., 2010).

In the design of bridges, detailed quantification of the magnitude and action of forces is initially required. The variability of forces is a function of the inundation depth, wave parameters and bridge topologies. The main wave parameters include wave height, clearance and wave period, whereas bridge geometrical characteristics include the presence of air vents, deck support, deck inclination, girder type, girder spacing, railing or parapet type and the presence of nearby structures. In addition, different failure mechanisms may exist in bridges, depending on their design details and class (Figure 1-1). Bridge decks are generally uplifted and laterally displaced during the passage of waves. The connection between the deck and piers is among the major considerations taken in the analysis of bridges. More information on the failure of deck to substructure connections can be found in Refs. Hayes (2008); Lehrman et al. (2011); Livermore (2014); Robertson et al. (2007).

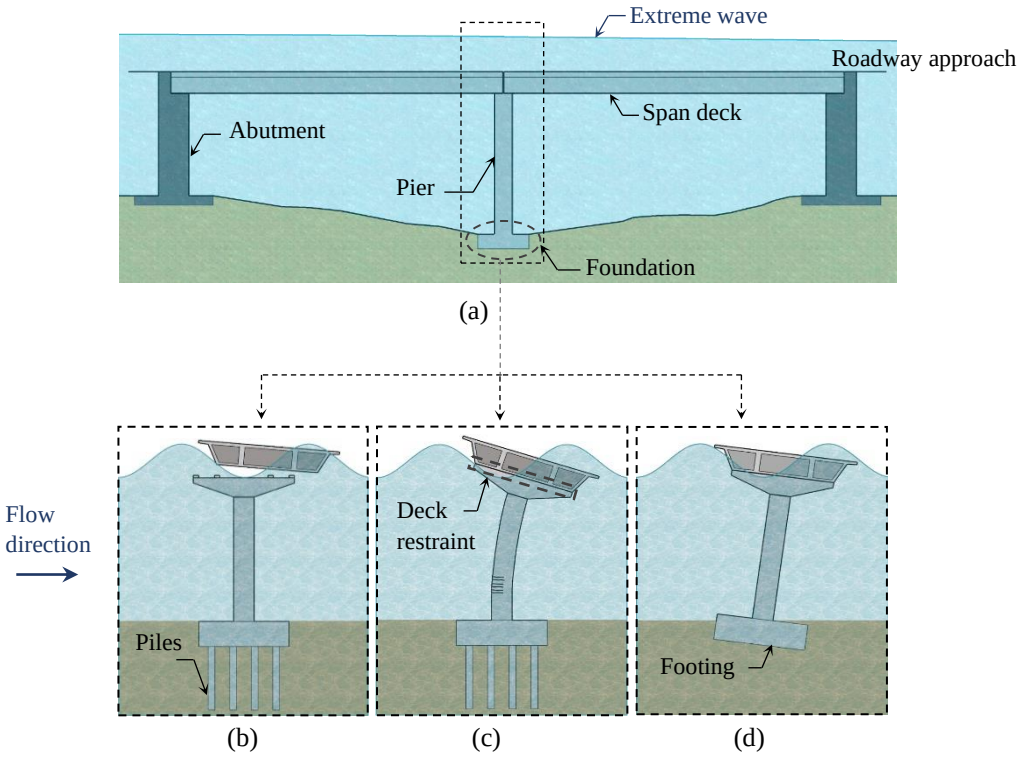


**Figure 1-1.** Illustrative diagram of potential damage in bridges subjected to extreme wave-induced forces: (a) bridge main components; (b) unseating of simply supported decks; (c) significant lateral displacements of piers in bridges with a strong deck-substructure connection; and (d) uplifting and lateral displacement of foundation.

The increase in post-hazard data has initiated research studies that address the sources of risk and resilience of bridges under extreme wave hazards. Resilience can be defined as the metric used to measure the performance of an infrastructure facility after an extreme event and during the recovery stage, while risk refers to the combination of extreme events probabilities and their consequences (Broccardo et al., 2015; Decò and Frangopol, 2011; Gidaris et al., 2017). In a more comprehensive definition, resilience refers to the ability of a system to reduce the probability of a shock, contain the shock when it occurs, and restore its performance rapidly after the shock (Bruneau et al., 2003). In this context, resilience loss is

defined by the size of the performance (quality) degradation from the instant of extreme event ($t_o$) to the time at full restoration of performance ($t_1$), as graphically shown in Figure 1-2. The development of a resilience evaluation framework can support the post-hazard rehabilitation and risk mitigation schemes, which requires vulnerability models of bridges to quantify the possible damage levels at the different hazards' conditions. Therefore, fragility functions that take into account different bridge classes and retrofitting schemes are essential to achieve this task.

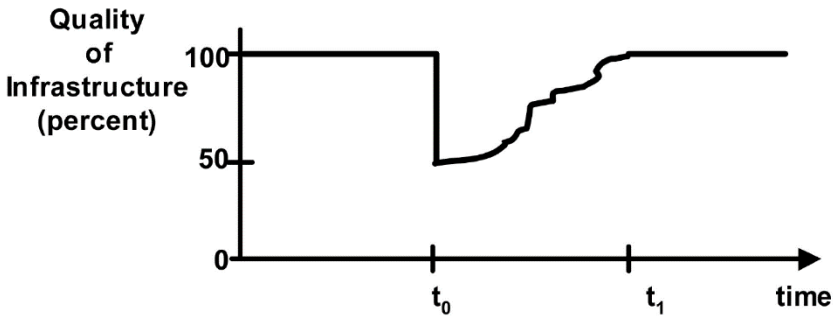


**Figure 1-2.** Conceptual definition of resilience (Bruneau et al., 2003).

## 1.2 Research Significance

Despite the increase in number of research studies on the performance of bridges subjected to extreme wave hazards over the past decade, there is currently no established framework with explicit procedures for the quantification of resilience. The multi-phase state of the art review presented in this research identifies this need by providing a detailed classification and identification of the existing methodologies related to force estimation, bridge element response and fragility and restoration models based on different hazard characteristics and

bridge classes. In addition, broader expressions for resilience that take into account resources and environmental effects are not covered in detail in the previous studies.

Most of the existing analytical fragility models for bridges subjected to extreme wave hazards have focused on simply supported decks. In addition, even though the use of retrofitting schemes such as shear keys and restrainer cables can prevent the large displacements of simply supported decks, extensive damage can occur in the substructure as a result of force transfer. Hence, the investigation of the effectiveness of a strengthening method (carbon fibre jacket) can assist in prioritizing the retrofit schemes for bridge piers.

The comprehensive framework adopted in this research provides a methodology for developing fragility functions based on nonlinear static pushover analysis. A better prediction of the bridge response is obtained in this study by using intensity measures that combine the two main elements of hydrodynamic forces, namely, inundation depth and velocity. The comparison of the fragility functions of the initial and retrofitted bridges can support informed decisions for a range of bridge classes in the network. Moreover, a framework for inclusion of the resources and environmental impact in resilience quantification is presented and its application is demonstrated.

### 1.3 Research Questions

Based on the comprehensive literature review conducted, the following main research questions have been identified:

1) What are the gaps in knowledge on resilience assessment for bridges under extreme wave loading?

2) How can the effect of resources and environmental impacts be included in a unified resilience index?
3) What is the analysis methodology to estimate the fragility of bridges?
4) How can the bridge be modelled to estimate the vulnerability under extreme wave loading?
5) How can the resilience of bridges be impacted by strengthening?

### 1.4 Research Aims

The overall aim of this research is to provide a comprehensive framework to quantify the resilience of bridges subjected to extreme wave-induced forces. To achieve this aim, the following specific objectives can be identified:

1. Review of methods for quantifying resilience of bridges subjected to extreme wave hazards.
2. Develop new expressions for resilience restoration that simultaneously account for the time, resources (cost) and environmental impacts of different recovery options with variable importance levels to different stakeholders.
3. Develop a framework for evaluating the vulnerability of bridges under wave-induced forces from flood and other wave hazards.
4. Develop a numerical method for modelling the fragility of bridges and validate the accuracy of the model using published works of small-scale bridge piers.
5. Examine the viability of the use of carbon fibre wraps as possible retrofitting schemes for bridge piers subjected to extreme wave hazards.

## 1.5 Research Scope

This research is subdivided into two main parts that are designed to achieve the overall aim of the study. The first part presents a comprehensive review of the resilience assessment of bridges that consists of four main phases: external wave-induced forces, structural response of bridges, vulnerability assessment, and post-disaster recovery. The first phase discusses the different types of forces initiated on the bridges and their influential parameters. It provides an overview of the relationship between these parameters and critical conditions. The empirical methods for estimating wave forces are also discussed and their practical uses and limitations are highlighted. The second phase addresses the different methods reported to examine the bridge response under wave hazards. The effect of deck connection details on the response of bridges is specifically discussed. The third phase discusses the existing methodologies adopted for developing fragility models for bridges, particularly under hurricane- and tsunami-generated waves. The last phase describes the different restoration models for bridges and explains the concept of resilience. In addition, the quantification of resilience using the resilience triangle concept is expanded in this part of the research to include the effect of resources and environmental impacts of different recovery options. The real application of unified resilience indices has been explained using a demonstration example within the engineering area.

The second part of research involves establishing a comprehensive framework for developing fragility models for bridges subjected to significant hydrodynamic forces. A three-dimensional finite element model of a 1/5 scale circular bridge pier was first developed and validated using published work. The pier model was then converted to a full-scale model and added to a typical four-span concrete girder bridge model. The deck is assumed to have

a strong connection with the substructure. The nonlinear static pushover analysis was used to obtain the capacity-demand relationship. Six main damage states were defined for the bridge using the capacity curve of the mean concrete and steel strengths, namely, (a) slight, which corresponds to first crack stage, (b) moderate, which corresponds to the yielding stage, (c) extensive, which corresponds to the peak (ultimate capacity) stage, (d) 10% drop in capacity, (e) 20% drop in capacity, and (f) 50% drop in capacity. The last three damage states that define the post-peak reserve strength are important for evaluating the ductility of bridge subjected extreme wave forces. The drift ratios are used as the engineering demand parameters (EDPs) for damage assessment, since the structure is subjected to lateral loads. The intensity measures adopted in the fragility analysis are the inundation depth, velocity, momentum flux and moment of momentum flux. The developed fragility framework is also examined on strengthened piers with carbon fibre jackets using non-linear time-history analysis.

## 1.6 Thesis Content

This thesis consists of seven chapters. The significance of developing the resilience framework along with aim and scope of this research are explained in this chapter. Based on the two main parts of this research discussed in the previous section, the additional chapters are outlined as follows:

*Chapter 2.* A detailed discussion of the past research and background information aligning within the four main relevant areas of research for bridges under extreme wave hazards is provided in this chapter.

*Chapter 3*. The use of unified resilience indices that consider resources and environmental impact is explained in this chapter.

*Chapter 4*. The proposed framework for fragility analysis of bridges subjected to extreme wave forces is discussed in this chapter.

*Chapter 5*. The development and validation of numerical model of case study bridge is presented in this chapter. The structural analysis of initial and strengthened bridge is discussed.

*Chapter 6*. The fragility functions for initial and strengthened bridge are compared and analysed in this chapter. The fragility analysis results are used to quantify the resilience restoration strategies considering the effect of recovery time, resources and environmental impact.

*Chapter 7*. The main conclusions and recommendations for future research are presented in this chapter.

# CHAPTER 2

# LITERATURE REVIEW

## 2.1 Introduction

The primary aim of this chapter is to present a detailed literature review on the resilience of bridges to extreme wave-induced forces. The interaction of the considerations related to design force and bridge details assists in the development of a comprehensive framework for the assessment of the vulnerability of bridges. However, the independence of each research area poses a challenge to current design and risk assessment studies. For example, most investigations on the estimation of forces assume absolute rigidity in the characterisation of the bridge deck. However, recent studies have shown that the deck's lateral stiffness can influence the magnitude of forces (Cai et al., 2017; Xu and Cai, 2015, 2017). Hence, detailed analyses of the structural behaviour of decks, girders and piers under different forces are required. Although provisions for estimating the forces for the design and retrofit of bridges have been published, these design procedures have some limitations related to their accuracy and applicability to extensive bridge and wave types (AASHTO, 2008; ASCE, 2016). In order to quantify resilience, four comprehensive modules, namely, (i) characterisation of external wave-induced forces, (ii) global and local structural responses of bridges, (iii) vulnerability assessment of damaged components, and (iv) post-disaster recovery, are discussed. These modules constitute the integrated knowledge needed for the prediction of the resilience of infrastructure under extreme wave-induced loads and are adopted from the classic framework of Performance-Based Earthquake Engineering (PBEE) methodology by the Pacific Earthquake Engineering Research (PEER) Center (Günay and Mosalam, 2013) (see Figure 2-1). The practical knowledge summarised here will assist in

outlining current advances and future needs in research on the resilience of bridges to extreme natural hazards.

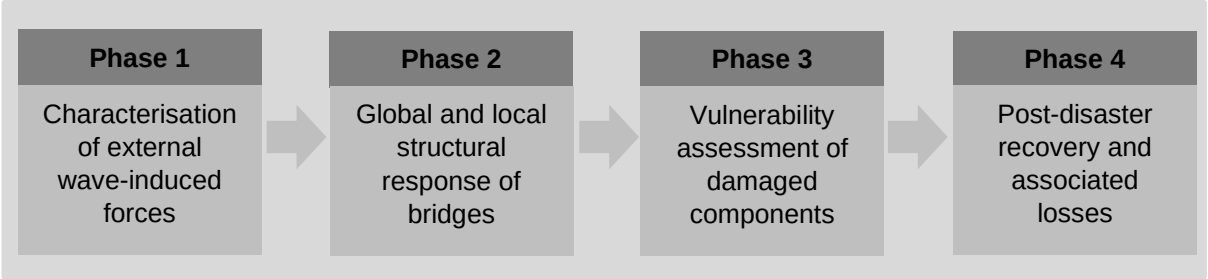


**Figure 2-1.** The four-phase resilience assessment of bridges.

## 2.2 Characterisation of Wave-Induced Forces

The first phase of resilience describes the broad classification of extreme wave-induced forces on bridges, which include hydrostatic, hydrodynamic and impact forces. However, they vary widely depending on the type of wave, which in turn, is affected by the location of the bridge. Figure 2-2 presents the two main types of bridges, based on their location and the types of forces. As the figure shows, the presence of waves on bridges adds additional force parameters that need to be identified. In addition to the seawater level ($d$), other parameters control the magnitude of forces, including the wave length ($\lambda$), wave period ($T_p$), clearance ($z$), wave height ($H$) and crest elevation ($\eta_{max}$). The wave length ($\lambda$) is the distance between two consecutive wave crests or troughs. The wave period ($T_p$) is the time taken for a wave to travel one wave length ($\lambda$). The clearance ($z$) is defined as the distance between the storm water level and deck bottom, and it has negative values when the storm level is above the bottom of the girders. The wave height ($H$) is defined as the distance between the

wave crest and its neighbouring trough. In extreme wave hazard records, significant wave height ($H_s$) is typically reported, which is the mean of the highest one-third of waves (AASHTO, 2008; Huang and Xiao, 2009). The maximum wave height ($H_{max}$) can be taken as $1.8H_s$ (AASHTO, 2008; Ataei and Padgett, 2012). The crest elevation ($\eta_{max}$) is the distance between the level of stormwater and the maximum elevation of wave crests (AASHTO, 2008; Douglass et al., 2006). Other parameters related to bridge geometry include deck width ($W$), length ($L$), inclination angle along the longitudinal axis ($\theta$), girder spacing ($S$), girder height ($d_g$), and the presence of air vents, parapet properties and lateral restraints (see Figure 2-3).

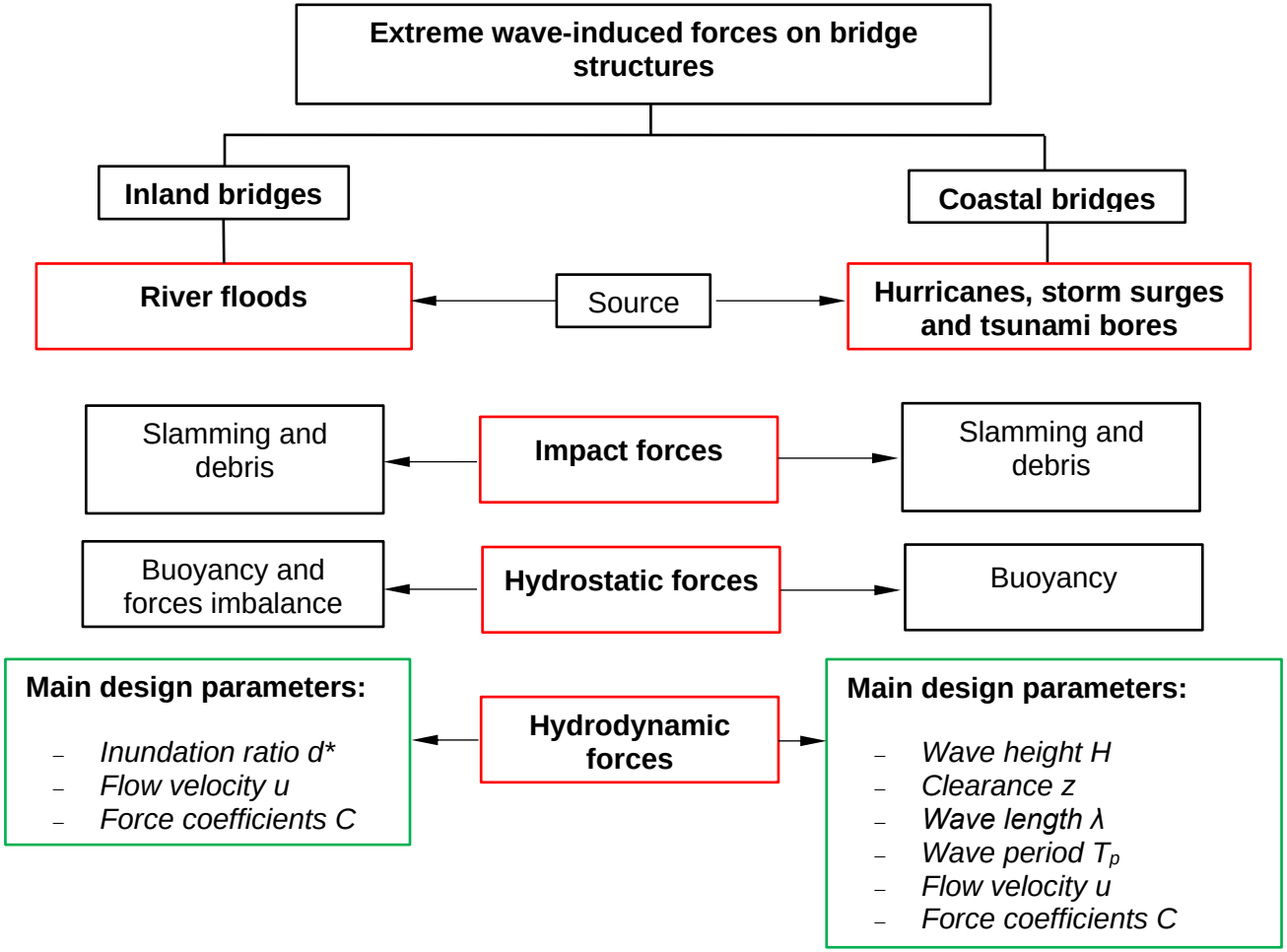


**Figure 2-2.** Classification of main forces on bridges.

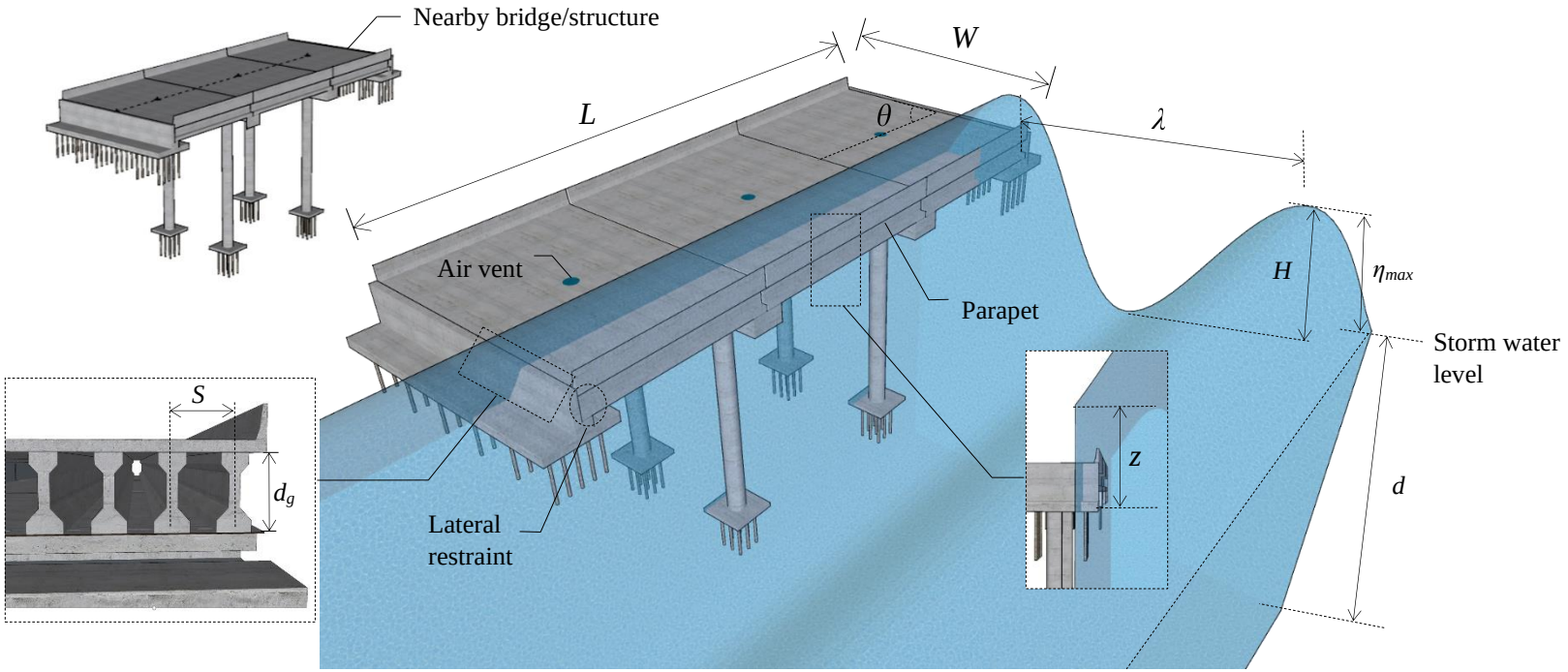


**Figure 2-3.** Exemplificative diagram for main wave force parameters.

(Note: $H$: wave height; $\eta_{max}$: maximum crest elevation; $\theta$: deck inclination angle; $S$: spacing between girders; $d_g$: girder height; $L$: length of bridge; $W$: width of bridge; $d$: storm water depth; $z$: clearance; $\lambda$: wavelength).

However, in inland bridges, surging free surface with minimal wave effects is usually predominant. Hence, the inundation ratio ($d^*$), flow velocity ($u$) and force coefficients ($C$) are usually sufficient for the prediction of the forces. The inundation ratio of surging free surface ($d^*$) is defined as the ratio of the relative distance between the elevation of the bottom of girders and the elevation of free water surface to the overall deck depth. The following sections discuss cases corresponding to severe forces and their inter-relationship with the flow and bridge characteristics. Note that the work presented in this research focuses on extreme wave-induced forces only; therefore, other types of damage caused by long-term flooding effects, such as scouring, are beyond the scope of this research. Information on the effect of scouring on bridge performance can be found in Refs. Deng and Cai (2009); Devi and Barbhuiya (2017); Ettema et al. (2004), among others.

### 2.2.1 Hydrodynamic Forces

In the theory of fluid mechanics, wave-induced hydrodynamic forces are defined as the vertical and horizontal force components that result from the shear and normal stresses initiated by the resistance of a structure to movement at moderate and high velocity steady flows (Azadbakht and Yim, 2014; Kerenyi et al., 2009). In the context of this research, the vertical and horizontal components of hydrodynamic forces are referred to as the uplift and drag forces. As these forces act on the deck, an overturning moment can also be initiated. The hydrodynamic force is a function of the velocity of flow, the projection area of the structure and the drag or lift coefficients, which are mainly dependent on the shape of the structure. The hydrodynamic force is expressed using the following equation (FEMA, 2008; Kerenyi et al., 2009):

$$F = 0.5\,\rho_s\,C\,b\,h\,u^2 \tag{2-1}$$

In Equation 2-1, $\rho_s$ is the density of sea water (usually taken as 1027 kg/m$^3$); $C$ is the force coefficient; $b$ is the width of the projected area of the structure; $h$ is the depth of inundation; and $u$ is the flow velocity. Investigation of the drag forces on bridges started as early as 1965 with the study documented by Tainsh (1965) on submerged inland bridges. It was reported that the presence of a deck increases the drag force by approximately 15%, while there is no significant effect of the spacing of girders. The study by Denson (1982) identified the effect of uplift forces and bending moments on inland bridges. Research on the forces on inland bridges continued with a series of investigations by Apelt (1986a, 1986b), Jempson et al. (1997) and Jempson (2000), who proposed reliable coefficient design charts for hydrodynamic loads. In addition, investigations by Kerenyi et al. (2009) showed that inland bridges with round edges have drag forces approximately 50% smaller than AASHTO-type girder bridges. Although early research by Denson (1978, 1980) related the failure of coastal bridges to the bending moments created by waves, it did not discuss the effects of other main parameters such as wave period and wavelength. The methodologies for the prediction of wave forces on flat plates and offshore platform structures using Morison's (Morison et al., 1950) approach were initially adopted for coastal bridges. However, the efficiency of such methods was questioned for the following reasons: a) the kinematics of waves are affected by the bridge decks, b) coastal bridges are located at small distances to still water level compared to offshore platforms, c) the width of bridges is significantly larger than the wavelength (up to four times the wavelength), and d) significant uplift forces are usually applied on coastal bridge decks due to the absence of air-relief openings (Bradner et al., 2010; Bradner et al., 2011; Douglass et al., 2006).

The main observations of the relationship between the wave forces and wave parameters are highlighted in Table 2-1. Each parameter is presented with its effect on uplift, drag, buoyant and slamming forces. Based on this information, the wave uplift force generally shows an increase with the wave height with either a polynomial or a linear trend (Bradner, 2008; Bradner et al., 2010; Bradner et al., 2011; Guo et al., 2015; Meng and Jin, 2007; Schumacher et al., 2008). Downward forces usually occur due to the suction of air pockets and the weight of overtopping water (Ataei, 2013; McPherson, 2008). Cuomo et al. (2009) reported that the increase in uplift forces depends on the difference between the crest elevation and the clearance. In addition, the drag force shows large magnitudes at small wave periods, whereas the uplift force increases with the increase in wave periods (Guo et al., 2015; Jin and Meng, 2011; McPherson, 2008; Xiang et al., 2018). However, Jin and Meng (2011) reported that the increase in drag force reduces at high wavelength/deck width ratios.

The research focus on the critical conditions of wave forces has recently included other factors related to bridge geometry, the existence of air entrapment and the location of the bridge. As reported by Mazinani et al. (2015), current studies concern mainly bridge superstructure parameters, and little attention has been given to the effect of pier geometries. A summary of the observations of these factors is presented in Table 2-2. The total uplift force is used in the table, as most research studies on this topic do not differentiate between hydrodynamic and hydrostatic (buoyant) uplift forces. The study by Marin and Sheppard (2009) showed that the increase in AASHTO girder depth results in an increase in uplift forces. In addition, the investigation of the effect of air entrapment involves two main approaches. In the first approach, the girder spacing area is filled with panels that had air openings, while in the second approach, air vents are created on the deck surface to allow

the air to be released during the wave passage (Azadbakht and Yim, 2016; Seiffert et al., 2015; Xu et al., 2016).

**Table 2-1.** Summary of state-of-the-art on inter-relationship between wave parameters and wave forces and critical conditions.

| Parameter | Variation in wave forces | | | | Main conclusions/remarks |
|---|---|---|---|---|---|
| | Uplift | Drag | Buoyancy | Slamming/impulsive | |
| Wave height | - Uplift forces show a linear increase with the increase of significant wave height (Guo et al., 2015; Meng and Jin, 2007).<br>- The forces have polynomial trend with the wave height (Bradner et al., 2010).<br>- The uplift forces are overcome by downward forces at larger wave amplitudes at low submergence (Seiffert et al., 2014).<br>- The forces are reported to show an increase with the increase in wave height/water depth ratio (Seiffert et al., 2015).<br>- An increase in forces with increase in wave height (Azadbakht and Yim, 2016).<br>- Peak values exceeded the bridge self-weight at H/*d*= 0.306, 0.361 and 0.417 (Xu et al., 2017). | - Polynomial increase in drag forces with increase in wave height was reported (Bradner et al., 2010).<br>- Drag forces show large values at high wave amplitudes at high elevations, and small values at small amplitudes at low elevations (Hayatdavoodi et al., 2014; Seiffert et al., 2014).<br>- Increase with wave height/water depth ratio (Azadbakht and Yim, 2016; Seiffert et al., 2015). | - Buoyant forces contribute significantly to magnitude of uplift forces when wave crest passes below deck (Azadbakht and Yim, 2016). | - No significant effect reported. | - Wave height is a major parameter in the magnitude of wave forces.<br>- Wave height effect is a function of level of submergence. |
| Submergence | - The uplift forces showed an increase with the increase in clearance up to deck self-weight (Huang and Xiao, 2009).<br>- Peak forces occur at inundation coefficients of -0.8, -0.76 and -0.74 for AASHTO II, IV and VI girders, respectively (Marin and Sheppard, 2009).<br>- At zero clearance, similar uplift force magnitudes are reported for both flat plate and bridge models (McPherson, 2008).<br>- Uplift forces show a decrease in magnitude at high submergence (Bradner et al., 2010).<br>- At large deck elevation, small uplift forces at small depths and large values at larger depths are reported (Hayatdavoodi et al., 2014). | - Drag forces are mainly caused by pressure of water at high submergence (Azadbakht and Yim, 2014).<br>- Decrease in drag forces at high submergence observed (Bradner et al., 2010).<br>- Large drag forces reported at relatively low submergence (Xu et al., 2015).<br>- Drag forces show an increase at a clearance equal to zero at high submergence, while they decrease at low submergence (described for elevated plates). This effect is less at low | - Buoyant forces show large magnitudes at large submergence levels (Azadbakht and Yim, 2014).<br>- The forces become significant when the water level increases to H/*d* = 2.95 (Douglass et al., 2006). | - Slamming force and weight of water create downward force on deck at high submergence levels (Azadbakht and Yim, 2014).<br>- Peak slamming forces occur at zero and small-range clearances. They reduce in large submergence cases (Guo et al., 2015).<br>- Rapid increase in uplift slamming forces with submergence in presence of air vents (Qu et al., 2017). | - Clearance is the main parameter of all wave forces.<br>- Overall, peak forces occur at sub-aerial conditions (low clearance), particularly uplift and slamming forces.<br>- Increase in forces has threshold inundation level, at which no significant increase is reported. |

| | | | | | |
|---|---|---|---|---|---|
| | - The uplift forces show large magnitudes at large submergence (Xu et al., 2015).<br>- At relatively low clearance ranges, forces increase with reduction in clearance (Guo et al., 2015).<br>- An initial increase in uplift force up to peak was reported, followed by a decrease (McPherson, 2008).<br>- Uplift forces change to downward forces as the free surface reaches the top of the deck (Azadbakht and Yim, 2014).<br>- Uplift forces show an increase at a clearance equal to zero at high wave amplitudes (Seiffert et al., 2014).<br>- Peak uplift forces occur at clearance equal to zero (Xu et al., 2017).<br>- Uplift forces show a decrease with increase in water depth, but not significant (Jin and Meng, 2011).<br>- Increase in uplift forces with increase in hydrostatic head (defined as crest elevation – clearance) (Cuomo et al., 2009). | submergence (Seiffert et al., 2014).<br>- Peak values occur at an inundation ratio equal to -1.22 (Xu et al., 2017). | | | |
| Wave period and wavelength | - Increase in uplift forces with increase in wave period (Jin and Meng, 2011; McPherson, 2008).<br>- Effect of water depth on uplift forces for high wave period becomes smaller (Jin and Meng, 2011). | - Largest drag forces occur at relatively small wave periods (Guo et al., 2015).<br>- Initial increase in drag forces, followed by decrease when wavelength becomes significantly larger than superstructure width (Jin and Meng, 2011). | - No significant effect reported. | - No significant effect reported. | - Wave forces generally show increase at relatively small wave periods. |

**Table 2-2.** Details of effects of bridge geometrical characteristics on magnitude of wave forces.

| Characteristic | Effect on forces | | | Main conclusions/remarks |
|---|---|---|---|---|
| | Total uplift | Drag | Slamming | |
| Deck/girder type | - Uplift forces show an increase with increase in depth of AASHTO girders (Marin and Sheppard, 2009).<br>- Flat plate and bridge models show similar uplift forces only at clearance close to zero (when water level is at bottom of girders) (McPherson, 2008).<br>- Failure of seaward girder reduces uplift force by about 25% (Azadbakht and Yim, 2014). | - Failure of seaward girder reduces drag force by about 15% (Azadbakht and Yim, 2014). | - No significant effect reported. | - The number of girders does not affect the magnitude of forces (Hayatdavoodi et al., 2014).<br>- Streamlined decks show smaller force magnitudes compared to girder decks (Kerenyi et al., 2009). |
| Girder spacing/number | - Decks with large girder spacing show less trapped air (Sheppard and Marin, 2009). | - No significant effect reported. | - Slamming forces decrease with reduction in number of girders (Sheppard and Marin, 2009). | - Overall force magnitude reduces in decks with fewer girders. |
| Contribution of air entrapment/effect of air vents | - Uplift forces in case of no air relief openings in panels between girders found to be six times larger than girders without panels (Seiffert et al., 2015). Apparent in the case of deck with large elevation above storm water level.<br>- Significant reduction in uplift forces with air vents of 0.5% (relative to area of deck), without much reduction at higher opening percentages (Xu et al., 2016).<br>- Effect of air vents more effective at shorter wave periods. However, reduction can be more significant at larger wave periods and wave heights (Azadbakht and Yim, 2016).<br>- Air relief opening of trapped air parameter (defined as percentage of difference of single and two-phase effects divided by two-phase effect) of 3% reduces uplift forces by up to 56% (Azadbakht and Yim, 2016). | - Effect of air-drilled holes between girders on drag forces less than effect on uplift forces (Seiffert et al., 2015).<br>- Drag forces show an increase at air vent openings of 0.5% and remain almost constant at higher percentages (defined as width of opening to area of deck ratio). Increase attributed to redistribution of water pressure between girders as air is released through openings (Xu et al., 2016).<br>- Drag forces show reduction in magnitude as a result of air entrapment (Seiffert et al., 2014).<br>- Drag forces show decrease of up to 39% with air opening ratio of 0.06 (Qu et al., 2017). | - Overall results show that use of air vents reduces impulsive forces for whole series of loading events. However, analysis using conservation of momentum and air/water compressibility shows that cushion effect under slabs without air vents reduces impact pressure on single element of superstructure and limits its rise time (Cuomo et al., 2009).<br>- Uplift and drag slamming forces show a decrease of up to 80% and 16% with opening ratio of 0.06, respectively (Qu et al., 2017). | - Effect of air entrapment is more pronounced on uplift forces than drag forces.<br>- Air vents or relief opening have a certain optimum percentage, after which no significant reduction in uplift forces is obtained. |

| | | | | |
|---|---|---|---|---|
| | - Uplift forces show decrease of up to 68% with opening ratio of 0.06 (Qu et al., 2017). | | | |
| Railing/parapet | - Increase in railing height increases uplift forces (Xu et al., 2017). | - Increase in railing height has more significant effect on drag forces than uplift forces (Xu et al., 2017).<br>- Use of perforation in parapet (21% of vertical deck projection) reduces drag forces by 17% (Lau et al., 2010). | - No significant effect reported. | - Further research is needed on different railing and parapet characteristics to draw clear conclusions on their effect on forces. |
| Lateral stiffness | - Less significant effect on uplift forces compared to drag forces (Bradner, 2008; Bradner et al., 2010; Bradner et al., 2011; Xu and Cai, 2015). | - Low stiffness of superstructure leads to significant increase in drag forces.<br>- Effect of inertia forces on total drag force becomes significant with increase in flexibility of deck/substructure interface (Xu and Cai, 2015).<br>- Higher rotations cause larger amplification (defined as drag in flexible bearing/drag in fixed bearing) of drag forces (Cai et al., 2017). | - Different trends in slamming forces between rigid and flexible support decks due to change in deck vibration characteristics (Xu et al., 2016). | - Structural vibration for design of retrofitting systems recommended to be limited to 1.0 s (Xu and Cai, 2015, 2017). |
| Deck inclination [a] | - Uplift forces are larger in inclined decks by up to 84% and 112% over flat deck with positive and negative angles towards seaward side, respectively (Bricker and Nakayama, 2014; Xu and Cai, 2014). | - Drag forces show large magnitudes in cases where total crest elevation is higher than seaward girder surface level.<br>- Forces increase up to 120% when deck inclination changes from -6° to +6° (Xu and Cai, 2014). | - No significant effect reported. | - Variation of moments is a function of both wave heights and deck inclination, as they depend on both magnitude of drag and uplift forces (Xu and Cai, 2014). |
| Nearby bridge/structure | - A factor of 0.9 is suggested for landward uplift over seaward force ratios (Xu et al., 2015). | - Factor of 0.8 is suggested for landward drag over seaward force ratios (Xu et al., 2015). | - No significant effect reported. | - Significant variation in forces occurs at relatively smaller gap between two decks (1 to 5 m in full-scale model).<br>- Disturbance in flow more significant in cases where gap between decks is 5 m (Xu et al., 2015). |

[a] The inclination angle is defined as the angle that the deck makes with the inlet or seaward side. Positive if it is upward and negative if it is downward.

Furthermore, Bradner et al. (2010) were the earliest researchers to report that the reduction in the deck lateral restraint stiffness has a more significant effect on the drag than the uplift forces. Xu et al. (Xu and Cai, 2015, 2017) conducted a further examination of this effect using lateral stiffness of between 15 kN/m and 1534 kN/m. The decks with the largest stiffness (1534 kN/m) showed the lowest magnitude of drag forces. In addition, the effect of inertia in the measurement of forces was found to be significant at low lateral stiffness. Hence, a stiffness limit of 383 kN/m (vibration period of 1 sec) was suggested for the design and retrofit of bridges (Xu and Cai, 2015, 2017). Other investigations of the effect of deck parapet, deck inclination and nearby bridges for different inundation ratios and clearances can be found in Refs. Bricker and Nakayama (2014); Chen et al. (2017); Lau et al. (2010); Xu and Cai (2014); Xu et al. (2015).

### 2.2.2 Hydrostatic Forces

As a wave approaches a bridge and the water level rises, two main static forces can be initiated, namely, buoyant and imbalance of water pressure. The buoyant forces are the uplift hydrostatic forces caused by the displaced water (Finnemore and Franzini, 2002):

$$F = \rho_s \, g \, V \tag{2-2}$$

In Equation 2-2, $g$ is the gravitational acceleration; and $V$ is the displaced volume of water. As presented in Table 2-1, the buoyant forces make a significant contribution to the uplift forces in the following cases: a) when the wave crest is below the deck, b) at large submergence levels, and c) when the wave height/water depth ratio is around 2.95 (Azadbakht and Yim, 2014, 2016; Douglass et al., 2006). The air entrapment significantly

increases the buoyant uplift forces, as discussed in the previous section. The accumulation of debris at the upstream side of inland bridges causes different water levels at the sides of the bridges, which cancels the equilibrium of hydrostatic pressure at both sides (Zevenbergen et al., 2012). The resulting differential magnitudes of hydrostatic forces lead to an overturning effect on the bridge. The hydrostatic force at one side of a vertical structure depends on the inundation depth, and it can be expressed as (FEMA, 2008):

$$F = 0.5\ \rho_s\ g\ b\ h^2 \qquad (2\text{-}3)$$

In Equation 2-3, $b$ is the width of the structure. Hence, an accurate estimation of the effect of hydrostatic forces requires the consideration of the effect of debris damming from the surrounding environment.

### 2.2.3 Impact Forces

Most of the available studies reported that the main causes of impact forces are the interaction of the bridge with the water surge and its collision with moving debris. The first type has been described in the literature as the “impulsive” or “slamming” force that results from the compression of entrapped air pockets and the transfer of momentum when the water impacts the deck surface (Azadbakht and Yim, 2016; Cuomo et al., 2009; Guo et al., 2015). Table 2-1 shows that slamming forces are mainly affected by the level of submergence. The amount of entrapped air and momentum transfer are functions of the clearance and wave height (Guo et al., 2015), and hence, a change in these parameters has an effect on the slamming forces. At high submergence levels, the forces show a decrease as the effects of air pockets diminish. In addition, air vents have been found to facilitate the impact of water

on the deck soffit, which results in larger slamming forces as the water increases above the bottom of the girders (Qu et al., 2017). Cuomo et al. (2009) noted that the pressure that the entrapped air creates below the deck causes a cushioning effect that reduces the impact of water on the deck soffit. The release of air through the relief openings removes the cushioning effect and leads to an increase in the slamming forces. However, the researchers limited their conclusion to the individual elements and highlighted that different cases of force magnitudes exist, when the whole deck is considered. For instance, Marin and Sheppard's (2009) analysis of an AASHTO girder bridge revealed that an increase in girder spacing decreased the magnitude of slamming forces. Debris types vary widely from a single wooden log to a large barge. Other factors play important roles in the impact force magnitudes, such as debris mass and velocity, added water mass, impact eccentricity and impact obliqueness. However, there is still insufficient discussion on the relationship between these factors and the resulting impact forces. For instance, a study by Nouri et al. (2010) of wooden debris showed that the contact duration is not affected by the velocity and mass of debris, whereas the data collected by Shafiei et al. (2016) using accelerometers indicated an increase in the contact duration for large acrylic debris masses. In addition, the investigations by Riggs et al. (2014) concluded that the added water mass does not depend on the velocity of debris, and the researchers did not recommend it to be considered in the estimation of impact force. However, Shafiei et al. (2016) and Ko et al. (2014) reported that the added water mass increased the impact force by up to 50% and 17%, respectively. An investigation by Haehnel and Daly (2004) of a rigid single-degree-of-freedom (SDOF) model revealed that the maximum impact force occurs when the collision of woody debris occurs at its centre and ends (minimum eccentricity and obliqueness). In addition, the relationship between obliqueness and impact force was found to take a sine function of the

angle that the impact direction makes with the debris longitudinal axis. More information on studies that have focused on the effect of velocity and shape of debris on the impact force and impulse can be found in Refs. Aghl et al. (2015); Aghl et al. (2014).

### 2.2.4 Empirical Methods for Estimation of Wave Forces

Recently, a number of studies have conducted parametric theoretical and experimental investigations to develop design-type equations for wave-generated forces on coastal bridges. The summary of the existing methods provided in Table 2-3 identifies the potential of each method and outlines its limitations which need to be addressed in future research. The earliest available empirical method for estimating the wave forces on bridge decks is the preliminary approach proposed by Douglass et al. (2006), following the devastating damage caused by hurricanes Ivan (of 2004) and Katrina (of 2005), and its main equations for the uplift ($F_v$) and drag ($F_h$) forces are expressed as follows:

$$F_v = c_{v-va} F_v^* \tag{2-4}$$

$$F_h = [1 + c_r (N-1)] c_{h-va} F_h^* \tag{2-5}$$

The main force components, $F_v^*$ and $F_h^*$, (denoted as reference forces) are initiated by the uplift and drag pressure applied on the horizontal ($A_v$) and vertical ($A_h$) projected areas of the deck, respectively. Hence, $F_v^*$ and $F_h^*$ are defined based on the projected areas, unit weight of water and the distance between the maximum crest elevation and the deck soffit ($\Delta z_v$) and centre of gravity of vertical projected area ($\Delta z_h$). Figure 2-4 shows a schematic of the main force parameters. The pressure is a function of the crest elevation from the centroid

of the front side for drag forces and the bottom of the deck for uplift forces. The reference force magnitude is modified using the coefficients $c_{v\text{-}va}$ and $c_{h\text{-}va}$ (defined as empirical coefficients) to consider the variation in forces. In Equation 2-5, $c_r$ is an additional reduction coefficient for the drag force, while $N$ refers to the number of girders. The method considers the static element of forces, and it assumes that there is a linear relationship between the forces and the hydrostatic pressure at the front of the deck. It is considered as a basic approach, and it can be further developed when more data are available.

**Table 2-3.** Comparison of empirical methods for estimating wave forces on bridge decks.

| Method | Main assumptions | Practicality | Limitation | Applicability based on direct measurements/other methods | |
|---|---|---|---|---|---|
| | | | | Observation | Reference |
| Jin and Meng (2011) | - Drag force increases linearly with increase in inundated depth of superstructure.<br>- Linear decrease in pressure exists between storm water level and wave crest.<br>- Inviscid flow.<br>- Incompressible fluid.<br>- Irrotational flow. | - Covers wide ranges of seawater levels.<br>- Explicitly relates effect of superstructure width to magnitude of forces. | - Based on two-dimensional model, which does not consider exact effect of air entrapment. | - Smaller uplift and drag forces by up to 10% and 36% than McConnell's (2004) method, respectively.<br>- AASHTO (2008) equations show larger total uplift forces by about 67%. | Jin and Meng (2011) |
| McPherson (2008) | -Forces mainly based on hydrostatic pressure and partially dependent on wave height.<br>- Effect of wave height on uplift forces decreases with increase in water depth. | - Provides more accurate estimation than Douglass et al's. (2006) method in terms of effect of backside and overtopping water effects.<br>- Explicitly considers effect of air entrapment on buoyant forces. | - Prediction of forces is limited to hydrostatic element. | - Uplift forces are larger than Douglass et al's. (2006) method by about 12%.<br>- Drag forces are smaller than Douglass et al's. (2006) method by about 271%. | McPherson (2008) |
| Douglass et al. (2006) | - Linear relationship exists in front of bridge deck between magnitude of loads and hydrostatic pressure when there is air at the backside.<br>- Magnitude of forces is directly related to difference in crest and deck bottom and centroid of front deck side. | - Conservative and can be applied on all bridges.<br>- Does not require much information about wave types and bridge geometry compared with other methods.<br>- Considered as basic method for further development when more data are available. | - Based on hydrostatic element of forces. | - Shows close values of drag forces to Guo et al's. (2015) measurements at low submergence for low values of empirical coefficient ($c_{h\text{-}va}$) used in equation.<br>- Over-estimates horizontal slamming forces when empirical coefficient ($c_{h\text{-}va}$) values are close to 6.0.<br>- Horizontal forces are over-estimated at clearance of zero. | Guo et al. (2015) |
| AASHTO (2008) | - Non-breaking waves act on bridge at time water impacts deck. | - Method equations validated with data from experiments and field measurements. | - Based on angle of attack of only $0^o$. | Guo et al. (2015):<br>- May over-estimate uplift forces at high wave heights, while it | Azadbakht and Yim |

| | | | | | |
|---|---|---|---|---|---|
| | | - Extension of widely-used equations for offshore structures by Kaplan (1992), Kaplan et al. (1995) and Morison et al., (1950). Modifications on effect of thickness, air entrapment and integration of forces over inundated part of superstructure width made to match bridge geometry. | - Method still lacks accuracy related to complex interaction between wave forces and relatively large-scale bridge models. This is particularly important in entrapped air problem.<br>- Uplift quasi-static forces do not explicitly consider the width of deck. | under-estimates forces at small wave heights.<br>- Close values of forces obtained when clearance is zero.<br>- Over-estimates force in large submergence cases.<br><br>Azadbakht and Yim (2016):<br>- Effect of maximum air entrapment can lead to under-estimation of uplift forces by 200% at small wave heights.<br>- Over-estimates horizontal forces at small wave periods. | (2016), Guo et al. (2015) |
| Xu et al. (2017) | - Hydrostatic and hydrodynamic forces are larger than inertia force. | - Modification of McPherson (2008) incorporating hydrodynamic elements, i.e. drag and lift forces, deck elevation factor and height of water from storm water level at landward side of deck. | - The method is based on two-dimensional models.<br>- The method still needs to be examined for larger wave heights or non-breaking waves.<br>- The method results are sensitive to the new proposed parameters, which requires further investigation. | - Provides better prediction of forces than McPherson's (2008) method. | Xu et al. (2017) |
| Azadbakht and Yim (2014) | - Full bridge inundation stage is reached at certain level of the front (seaward) side, regardless of small variation over deck width.<br>- Resistance from bridge railing is neglected. | - First method proposed specifically for tsunami-generated wave forces. | - Its accuracy is sensitive to value of tsunami inundation level. | - Provides estimation with accuracy of about 10% and 25% for drag and downward forces, respectively. | Azadbakht and Yim (2014) |

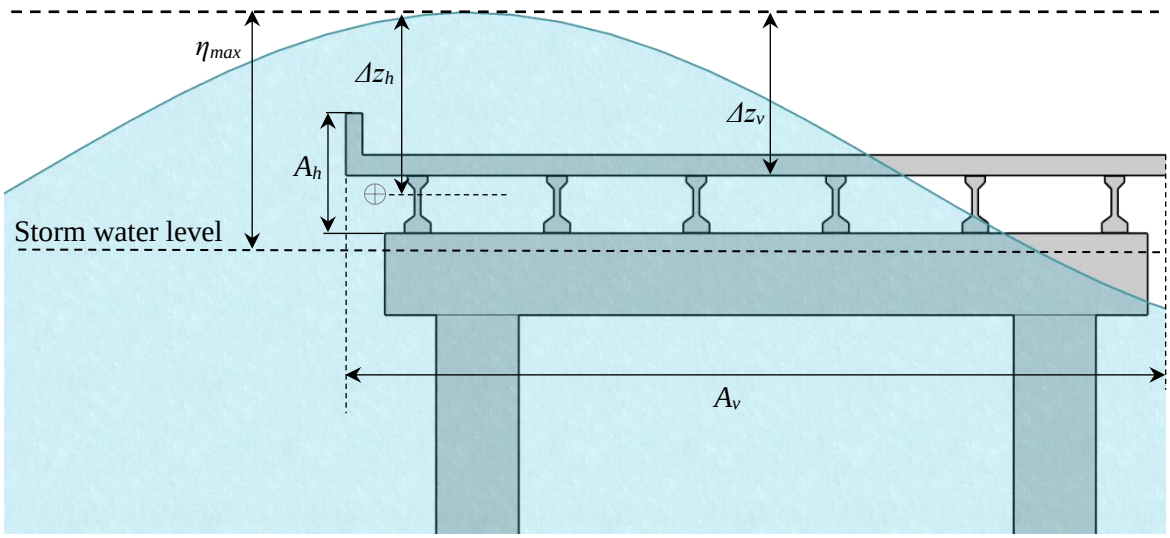


**Figure 2-4.** Schematic of uplift force main parameters in the method proposed by Douglass et al. (2006).

Later, McPherson (2008) reported that overtopping water creates a downward force ($F_w$) that needs to be deducted from the total uplift force predicted by Douglass et al. (2006). The effect of overtopping water can be explained by a triangular distributed load, which is added to a parallelepiped in case the water level rises above the deck surface. McPherson (2008) suggested the following main equations to calculate the total uplift ($F_{v,total}$) and drag ($F_{h,total}$) forces:

$$F_{v,total} = [\gamma \delta_z A - F_w] + [\gamma Vol_{Bridge}] + [(n\text{-}1)0.5\gamma \delta_G A_G] \quad (2\text{-}6)$$

$$F_{h,total} = F_{Hydrostatic\_Front} - F_{Hydrostatic\_Back} \quad (2\text{-}7)$$

Figure 2-5 shows a schematic of the main uplift force parameters. The spacing between girders is included in the calculation of the volume of displaced water ($Vol_{Bridge}$) to add the effect of entrapped air. The uplift force is estimated based on the horizontal projected area

($A$) and the height between the deck surface and wave crest ($\delta_z$), while the water force at the backside girder ($F_{Hydrostatic\_Back}$) is deducted from the drag force ($F_{Hydrostatic\_Front}$) at the front of the superstructure. Figure 2-6 shows a schematic of the drag force profile. Furthermore, it is suggested to deduct the hydrostatic water pressure applied on the landward side of the deck when the storm water level is above the bottom of the girders. The effect of air entrapment between girders is also included by calculating the total volume of the cross-sectional areas ($A_G$) of the spacing between girders. In Equation 2-6, $\gamma$, $\delta_G$ and $n$ refer to the density of water, girder height and number of girders, respectively.

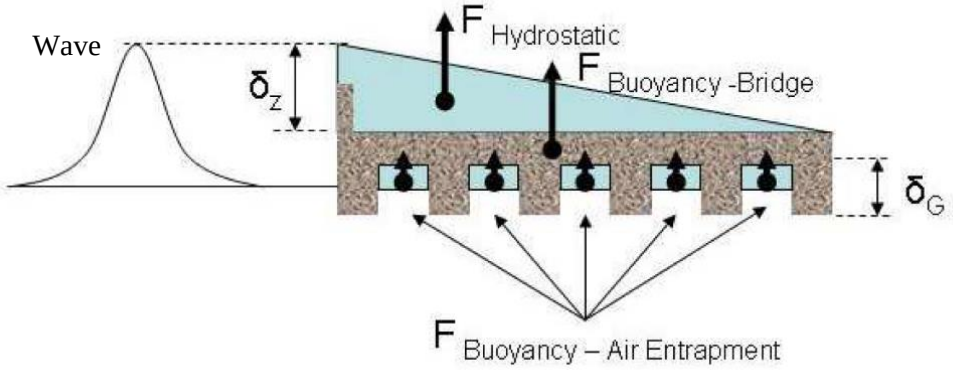


**Figure 2-5.** Schematic of uplift force main parameters in the method proposed by McPherson (2008). Adapted from McPherson (2008).

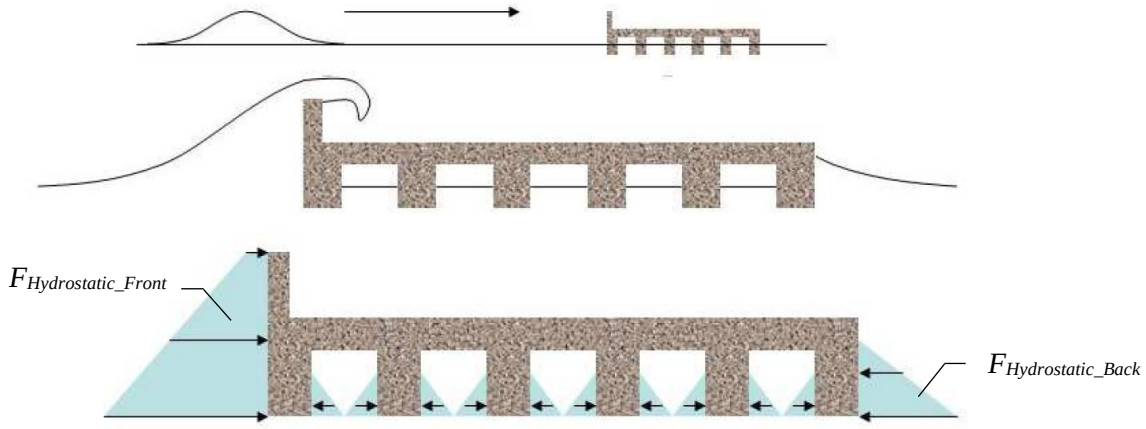


**Figure 2-6.** Schematic of drag force profile proposed by McPherson (2008). Adapted from McPherson (2008).

More recently, Xu et al. (2017) suggested the consideration of the hydrodynamic uplift ($F_L=0.5\rho C_L A u^2$) and drag ($F_D=0.5\rho C_D A_h u^2$) forces, the overtopping water ($C_w$) and the water height at the deck landward side ($h_{back}$) in McPherson's (2008) method. The method is based on the assumption that the hydrodynamic and hydrostatic forces are larger than the inertia force, and its main equations for the uplift ($F_v$) and drag ($F_h$) forces can be expressed as follows (Xu et al., 2017):

$$F_{v,total} = [\gamma \delta_z A - F_w] + [\gamma Vol_{Bridge}] + [(n\text{-}1)0.5\gamma \delta_G A_G] + 0.5\rho C_L A u^2 \quad (2\text{-}8)$$

$$F_{h,total} = F_{Hydrostatic\_Front} - F_{Hydrostatic\_Back} + 0.5\rho C_D A_h u^2 \quad (2\text{-}9)$$

In Equations 2-8 and 2-9, the hydrodynamic forces drag ($C_D$) and uplift ($C_L$) coefficients are kept at 1; and $A_h$ refers to the vertical projected area. The parameter $C_w$ defines the ratio of water weight on the deck to the weight induced by the distributed water surface, while $h_{back}$ is added to the height of the storm water level in the hydrostatic pressure. The wave force equations provided by the American Association of State Highway and Transportation

Officials (AASHTO) specifications for the vulnerability of bridges to coastal storms (AASHTO, 2008) consider three cases based on the peak applied force and type of failure mechanism. The method is considered as an extension of the widely-used equations by Kaplan (1992), Kaplan et al. (1995) and Morison et al. (1950) for offshore structures, and it was validated using data from field measurements and experiments. The effect of thickness, air entrapment and the integrated forces over the inundated part of the superstructure were made to match the coastal bridges geometry (AASHTO, 2008). The first case assumes that the peak applied force on the deck is the uplift force, and the drag and bending moment are the associated forces acting on the structure in that instance. The main expressions for the uplift ($F_{V\text{-}MAX}$), drag ($F_{H\text{-}AV}$), slamming ($F_s$), and moment ($M_{T\text{-}AV}$) of the first case of the AASHTO (2008) method can be written as follows:

$$F_{V-MAX} = \gamma_w \overline{W} \beta b_1 \left( -1.3 \frac{H_{\max}}{d_s} + 1.8 \right) \left[ 1.35 + 0.35 \tanh\left(1.2\left(T_p\right) - 8.5\right) \right] (TAF) \tag{2-10}$$

$$F_{H-AV} = \gamma_w H_{\max}^2 \, a_1 \, a_2 \tag{2-11}$$

$$F_s = A \gamma_w H_{\max}^2 \left( \frac{H_{\max}}{\lambda} \right)^B \tag{2-12}$$

$$M_{T-AV} = a_3 \left[ F_{V-MAX} W^* + F_{H-AV} (d_b + r) \right] + 2 F_s W^* / 3 \tag{2-13}$$

In Equations 2-10, 2-11 and 2-13, $b_1$, $a_1$, $a_2$ and $a_3$ are abbreviated equations of coefficients defined based on the wave parameters and geometry of the superstructure, such as wave length, maximum wave crest elevation, clearance, girder depth, height of railing ($r$) and total height of girder and deck thickness ($d_b$). The parameters $\overline{W}$ , $W^*$ , $\beta$, $B$ and $A$ are defined based on wave parameters such as clearance, wave length, maximum wave crest elevation

and superstructure width. Figure 2-7 shows the main force parameters. The detailed expressions of the coefficients and parameters can be found in AASHTO (2008). In Equation 2-10, $\gamma_w$, *TAF* and $d_s$ are the unit weight of water, air entrapment factor and level of storm water, respectively. This case is particularly important for the design of the resistance of the deck to movement by the substructure. In the second case defined by AASHTO (2008), the drag is the peak force that acts on the deck, and other associated forces are obtained in a similar method to that used in the first case. The main expressions for the uplift ($F_{V\text{-}AH}$), drag ($F_{H\text{-}MAX}$), and moment ($M_{T\text{-}AH}$) of the second case of AASHTO (2008) method can be written as follows:

$$F_{H-MAX} = \left[ \gamma_w \pi (d_b + r)(\omega + 0.5 H_{\max}) \left( \frac{H_{\max}}{\lambda} \right) \right] e^{\left[ -3.18 + 3.76 e^{\left( -\frac{\omega}{\lambda} \right)} - 0.95 \left[ \ln \left( \frac{\eta_{\max} - Z_c}{d_b + r} \right) \right]^2 \right]} \tag{2-14}$$

$$F_{V-AH} = \left[ \gamma_w \alpha (\eta_{\max} - Z_c) \right] e^{\left[ -0.30 + 2.04 e^{\left( -9.01 \frac{\alpha}{\lambda} \right)} - 0.16 \left( \frac{\eta_{\max} - Z_c}{d_b} \right) \right]} TAF \tag{2-15}$$

$$M_{T-AH} = \left[ F_{H-MAX} (d_b + r) + \frac{2}{3} (F_{V-AH} + F_s) W \right] 1.37 \tanh \left( \frac{d_b}{\eta_{\max} - Z_c} \right) \tag{2-16}$$

In Equations 2-14 and 2-15, $Z_c$ refers to the clearance; while $\omega$ and $\alpha$ are defined based on clearance, wave height, wave length and superstructure width. The second case is usually used to design the substructure against significant lateral displacements. The third case assumes that both the first and second cases are applied as pro-rated distributed loads on the seaward overhang of the deck.

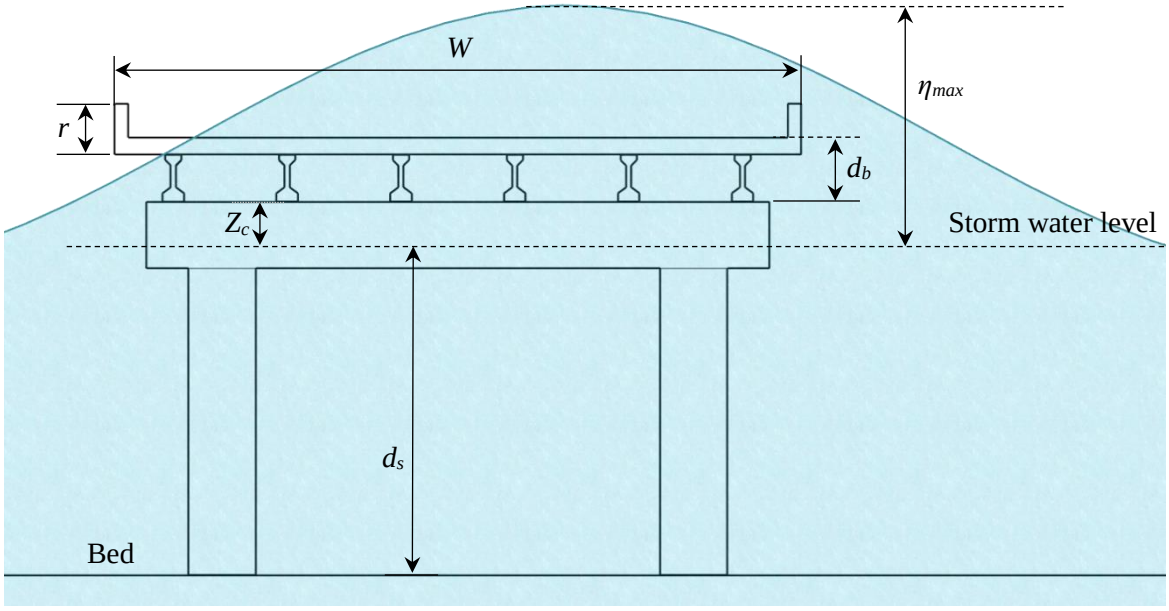


**Figure 2-7.** Main force geometrical parameters used in the method proposed by AASHTO (2008).

Jin and Meng (2011) suggested a simplified approach in a parametric study on wave heights, wave periods and inundation levels, and the main equations of the uplift ($F_{v0}$) and drag ($F_{h0}$) forces are expressed as follows:

$$F_{v0} = F_b + 2\rho g \eta_{max} L_x L_y C_v(T) \quad (2\text{-}17)$$

$$F_{h0} = 2\rho g \eta_{max} L_y L_z C_h(T) \quad (2\text{-}18)$$

In Equations 2-17 and 2-18, $L_x$, $L_y$ and $L_z$ are the deck length, width and depth, respectively. The coefficients $C_h(T)$ and $C_v(T)$ are provided to account for the effect of wave period, and $F_b$ is the buoyant force. The two main stages in the method were defined by the elevation of the storm water level above the deck surface. The method assumes that a linear increase exists between the drag force and inundation depth. It is also assumed that there is a linear decrease in the pressure between the storm water level and the wave crest. The method also

relates the effect of superstructure width to the amount of forces, and it covers a wide range of seawater levels. Azadbakht and Yim (2014) developed a method for tsunami-generated wave forces that is based on two main stages: a) initial impact, and b) full inundation, and its main equations for estimating the uplift ($F_{UPmax}$), drag ($F_{Hmax}$) and downward forces ($F_{DVmax}$) can be written as follows:

$$F_{UPmax} = C_{UP}\,(F_b + F_l) \tag{2-19}$$

$$F_{Hmax} = F_{h\_hs} + F_d \tag{2-20}$$

$$F_{DVmax} = C_{DV}\,(F_{v\_hs} + F_{v\_s}) \tag{2-21}$$

In Equations 2-19, and 2-21, $C_{UP}$ and $C_{DV}$ are empirical uplift and drag coefficients, respectively; while $F_b$, $F_l$, $F_{v\_hs}$ and $F_{v\_s}$ are the buoyant, uplift, downward vertical (hydrostatic) and slamming vertical forces, respectively. The maximum drag force ($F_{Hmax}$) in Equation 2-20 is the summation of horizontal hydrostatic force ($F_{h\_hs}$) and drag ($F_d$) forces. The method ignores the effect of the railing, and it assumes that the full inundation of a bridge is reached when the water depth crosses a certain level of the front (seaward) side, regardless of the variations that may exist in deck width. It is also assumed that the downward force is dominant in the initial stage, while the buoyant uplifts are the dominant forces in the full inundation stage, accompanied by slamming forces occurring at the landward side of the bridge. Additional detailed theoretical and experimental discussion on the methods used to develop the above approaches can be found in Refs. Hayatdavoodi and Ertekin (2016); Marin and Sheppard (2009); Sheppard and Marin (2009), among others. Hayatdavoodi and Ertekin (2016) reported that empirical methods can provide satisfactory predictions of forces when the deck is higher than the sea water level, whereas their accuracy reduces at relatively small wave length-to-deck width ratios, and due to the effect of air

entrapment. In addition, the study by Guo et al. (2015) showed that the Douglass et al. (2006) method over-estimates the drag forces for low values of the empirical coefficient ($c_{h\text{-}va}$) under zero clearance and relatively small inundation conditions. The slamming horizontal forces also show higher magnitudes when the $c_{h\text{-}va}$ values are close to 6.0. Despite the fact that the method provided by AASHTO (2008) covers a large range of parameters and takes into account different storm wave conditions, the method still lacks the accuracy needed for more complex wave-structure interactions, particularly the air entrapment effect. Azadbakht and Yim (2016) reported an over-estimation of the uplift forces by the AASHTO (2008) method of up to 200% for small wave heights when 100% air entrapment is considered. They also reported an over-estimation of the drag forces for small periods of waves at 100% air entrapment. Furthermore, the predictions of Xu et al's. (2017) method were found to be sensitive to the $C_w$ and $h_{back}$ parameters. This is attributed to the fact that the estimation of weight of water on the deck can be difficult because of the wave disturbance at the moment it impacts the deck, as well as the diffraction of waves at clearances close to zero (Xu et al., 2017). This sensitivity in parameters was also reported by Azadbakht and Yim (2014) for tsunami-generated wave forces. They found that the inundation depth has a non-uniform distribution throughout the width of the deck. Hence, assuming a constant value for the inundation depth can lead to larger values of downward forces. Most of the existing methods cover the forces initiated on superstructure.

## 2.3 Structural Response Analysis

### 2.3.1 Engineering Demand Parameters

The second phase of resilience is structural response analysis, which focuses on providing a probabilistic description of the response of structures to the various magnitudes and characteristics of hazards. The response quantities, denoted as engineering demand parameters (EDPs), are captured either at the local or global levels through time-history analysis which considers the uncertainties in the parameters related to the equations of motion such as mass, damping, stiffness, strength and external forces. Examples of local EDPs include element forces, curvature ductility and displacements, while global EDPs include the deck or floor drifts, displacements and accelerations (Günay and Mosalam, 2013; Nielson and DesRoches, 2007; Padgett and DesRoches, 2008; Zhang et al., 2008). Most of the available studies on bridge responses have particularly focused on simply supported decks subjected to hurricane- and tsunami-generated waves. The investigations of deck displacements include numerical models that apply the waves in the form of simplified forces (static or dynamic) and fluid structure interactions (Ataei et al., 2010; Salem and Helmy, 2014; Salem et al., 2014; Salem et al., 2016), while the only available experimental investigation focused specifically on the effect of anchorages between the girders and substructures (Lehrman, 2010; Lehrman et al., 2011).

### 2.3.2 Simply Supported Bridges

One of the first studies of the response of bridges under hurricane-generated waves is the computational work conducted by Ataei et al. (2010) using Open System for Earthquake

Engineering Simulation (*OpenSees*). They proposed a sinusoidal dynamic force with peak magnitudes and periods estimated using AASHTO (2008) equations. The dynamic force was applied on a simply-supported deck in a typical multi-span concrete girder bridge. The superimposed slamming force was assumed to have a period of 5/8 of the wave period ($T_p$ = 6 sec.). This ratio was adopted based on the mathematical formulations by Marin and Sheppard (2009), which were validated by experiments on wave-tank models of the old I10-Escambia Bay Bridge in Florida. It was found that the uplifting of the deck, after the initial slamming of waves, permitted a further increase in the lateral displacements. The sequential uplifting and slamming of decks increased significantly the moments on the piers. Ataei and Pagett (2015b) conducted a fluid-structure interaction study on a simply-supported deck of a three-span concrete girder bridge. The bridge was subjected to three wave conditions: (a) $H$=1.8 m, $T_p$=5.0 sec., $d$=6.0 m, $z$=0.0 m, (b) $H$=3.2 m, $T_p$=6.0 sec., $d$=6.0 m, $z$=0.0 m, and (c) $H$=4.2 m, $T_p$=6.0 sec., $d$=7.5 m, $z$=-1.5 m. The second and third conditions were selected to produce uplift forces higher than the deck self-weight based on AASHTO (2008) equations. The results showed that the impact of the wave crest caused a significant increase in the drag force when the water level was at the deck (clearance = 0 m). In comparison with the first and second conditions (partial inundation), the third condition (full inundation) showed that the deck undergoes larger vertical displacement and significant rotations.

### 2.3.3 Deck Connections

The role of anchorages and bearings in investigating the response of decks under wave forces has recently been highlighted by some notable studies. Table 2-4 presents the details and responses of deck connections for bridges under extreme waves. Lehrman (2010) and

Lehrman et al. (2011) studied the behaviour of steel anchors on AASHTO girders using static and dynamic loadings. The loading cases adopted were static uplift, static drag, combined static uplift and drag, and combined dynamic uplift and drag. In the combined loading cases, the magnitude of static uplift was twice the drag force. The results showed that in combined loading cases, the drag force provided a compressive effect that increased the uplift capacity of the connections. Further, a numerical approach was suggested by Salem et al. (2014, 2016) using the discrete cracking method to capture the movement of decks under tsunami-generated wave forces. The bearing connection was modelled using two plates, at the top (sole) and bottom (bed), attached together using a friction coefficient of 0.6. Two blocks were fixed at the sides of the bearing plates to prevent their lateral movement. The velocity was assumed to have a linear increase with the percentage of air entrapment. This linear increase is up to a velocity of 3.13 m/s, which corresponds to air entrapment over the full depth of the girders. In addition, the drag force applied on the deck was adjusted to take into account the change in wave velocity due to the movement of the deck. The lateral movement of decks was found to occur at air entrapment of 75% and 100% of the girder's depth. More recently, the forces in flexible and rigid support bearings were studied by Cai et al. (2017). The flexible bearing was modelled using non-linear vertical spring elements, whereas the rigid bearing supports were modelled using linear elements. In the flexible deck, the onshore girder bearing was kept vertically rigid to initiate the rotation. It was reported that the deck rotation is mainly related to drag forces. The peak rotating moment was found to occur in an opposite direction to that recommended by the AASHTO (2008) equations. In addition, the bearings showed high tensile and compressive stresses at an inundation ratio of -0.5. Cai et al. (2017) reported that the maximum uplift movement of the deck corresponded to the case where the water level was at the girder soffit (zero

clearance). In contrast, the study discussed above by Ataei and Padgett (2015b) concluded that for the same case, maximum lateral displacements occur. Furthermore, a comparative study was conducted by Ataei (2013) on the effectiveness of shear keys, restrainer cables and high-strength bars for preventing large displacements of the deck. Shear keys were found to be the most effective measure for preventing lateral displacement without significant force transfer to the substructure. The lateral movement of the deck was reduced by up to 11 times, but this led to an increase in uplift force by about 60%. Furthermore, non-linear static analyses that adopt simplified load patterns distributed over vertical elements have recently been implemented in frame structures to provide an adequate evaluation of the structural response. Further discussion on the load patterns, load discretization methods and pushover analyses for structures subjected to extreme waves can be found in Refs. AASHTO (2008); Alam et al. (2017); Ataei and Padgett (2013b); FEMA (2008); Foytong et al. (2013); Foytong et al. (2015); Fukuyama et al. (2011); Macabuag and Rossetto (2014); Macabuaget al. (2014); Nanayakkara and Dias (2016); Petrone et al. (2017).

**Table 2-4.** Details and response of deck connections in recent investigations for bridges subjected to extreme wave forces.

| Connection | Details | Response/failure | Remarks/details | Reference |
|---|---|---|---|---|
| Clip bolt | Steel angle (mm): 203×152×25<br>Connected to bottom flange using four bolts inserted into pre-fabricated threads. | Static uplift and drag: separation of concrete around the strands.<br>Combined uplift and drag: external strands appeared along 610 mm of girder and pullout of inserts was observed at flanges. | Has lowest capacity compared to headed stud and through-bolt. | Lehrman (2010), Lehrman et al. (2011) |
| Headed stud | Steel plate positioned at bottom of girder with welded headed stud anchor 16 mm in diameter and 152 mm long. Plate connected to substructure by expansion anchor. | Static uplift: yielding and rupture of both stud and plate.<br>Static drag: plate underwent plastic deformations without slip in strand.<br>Combined uplift and drag: fracture of seaward stud. | Connection has greatest strength. Yielding failure can be utilized in practical design of connection to limit transfer of forces to substructure. | |
| Through-bolt | Steel angle (mm): 203×152×25<br>Connected to bottom flange using two 25 mm diameter bolts. | Static uplift: initiation of cracks and strand slip. Cracks further propagated at girder soffit until exposure of strands.<br>Static drag: further increase in capacity due to compressive effect of uplift forces at seaward side.<br>Combined uplift and drag: cracks at bolt locations after exceeding self-weight of girder.<br>Combined cyclic uplift and drag: significant cracks and banding followed by pull down of prestressing strands. | Compression from drag enables connection to sustain higher loads under combined static loads.<br>Large increase in deformation at small change in load due to rapid propagation of crack from seaward to landward side at combined static loads.<br>Connection failed due to combined tension from uplift and drag. | |
| Fixed and movable bearing | Bottom and top plates with specified contact friction. Friction coefficient zero for movable bearing and 0.6 for fixed bearing. Lateral movement prevented using bolts fixed at sides. | All simply-supported decks on bearings showed overturning and sliding failure modes. | Bearing plates experienced failure due to movement of side block and top plate. | Salem et al. (2014, 2016) |
| Bearing fixed and movable | First deck modelled to allow movement in horizontal direction only. Linear vertical spring elements used to model girder | Ultimate vertical displacement of deck occurs at zero clearance. | Positive (clockwise) overturning moment was found to be the ultimate moment, which contradicts | Cai et al. (2017) |

| | | | | |
|---|---|---|---|---|
| in vertical direction | support. Spring elements can deform in tension and compression.<br>Second deck modelled with linear vertical spring elements only at last girder at onshore side of deck. Non-linear vertical spring elements used for rest of girders, which can deform only in compression. This model allows both rotation and horizontal movement of deck. | At inundation ratio of -0.5, larger uplift force and lower moment in interaction diagram (moment-uplift force) observed. Bearings show high tensile and compressive stresses.<br>At inundation ratio of 0.5, negative moment occurs. | AASHTO (AASHTO, 2008) method which assumes that negative moment is the ultimate. | |
| Simplified interface friction | Interface coefficient of friction of 0.6 used between deck and substructure. | High deck vertical displacements at larger inundation accompanied by larger moments and rotations.<br>Horizontal displacements are high at zero clearance. | Resistance of deck to horizontal movement reduces with uplift movement. | Ataei and Padgett (2015b) |

## 2.4 Vulnerability Assessment

### 2.4.1 Definition of Fragility Functions

The third phase of resilience is damage analysis. Fragility functions are typically used to determine the likelihood of reaching or exceeding the level of damage at a given intensity measure (IM). The level of damage is often expressed in terms of a damage measure (*DM*) that corresponds to the repair method required to restore the structure to its initial "undamaged" condition (Moehle and Deierlein, 2004; Porter, 2003). For example, the HAZUS (FEMA, 2012) methodology for earthquake hazards defines damage to bridges as slight, moderate, extensive and complete for minor spalling, shear cracks with spalling, shear failure and collapse, respectively. Figure 2-8 shows an example of fragility functions at two damage states. The damage measure can also be quantitively defined as a function of the structural response thresholds, i.e., EDPs derived from experimental results for the physical damage of bridge components (Nielson, 2005).

Different methodologies for constructing fragility functions for structures subjected to extreme waves are available in the literature, and they are classified into four main types (Ataei and Padgett, 2015a; Attary et al., 2016; FEMA, 2017; Koshimura et al., 2009a; Koshimura et al., 2009b; Padgett, 2007): (a) expert opinion (heuristic) methods based on survey responses of experts who provide their opinion on the damage probability of the structure at the various levels of hazard, (b) empirical methods that use statistical data on bridge damage from post-hazard field surveys, (c) integration of remote sensing and hazard modelling methods using satellite images and simulation of waves; and (d) analytical methods that use numerical models of the structure to estimate its response. The first three methods suffer from a number of shortcomings. For example, expert opinion methods

provide highly subjective data, and obtaining high response rates to surveys is often challenging (Padgett, 2007). In addition, fragility functions for empirical and remote sensing methods are based on specific types or classes of bridges and damage levels (Alam et al., 2017; Gidaris et al., 2017). The use of analytical fragility methods has recently gained significant attention for the assessment of the vulnerability and resilience of bridges located in at-risk regions. Analytical fragility curves can be incorporated in different hazard environments and implemented to the various classes of bridges, and hence, most of the drawbacks associated with the other three methods can be overcome (Gidaris et al., 2017; Padgett, 2007).

The different components of the bridge usually experience different damage measures (Zhang and Huo, 2009). Hence, the description of the global damage to a bridge using a single component damage measure becomes difficult. A number of methods are implemented to relate the component damage measures to a comprehensive damage measure at the system-level of the bridge. System-level fragility can be computed by combining the probability of failure of the different components, assuming that bridges operate as a serial or parallel system of components (Dueñas-Osorio and Padgett, 2011). In the serial system assumption, each component independently plays a crucial role, and the occurrence of any damage at the component level results in damage to the bridge at the exact same level (Nielson and DesRoches, 2007; Zhang and Huo, 2009). This implies that the largest damage measure at the component level determines the system-level damage measure. With the parallel system assumption, the global damage is determined when all components reach the same damage measure (Lupoi et al., 2006; Zhang and Huo, 2009). Other methods include post-hazard estimation of the functionality of the components that experienced the most severe damage and the repair required that may lead to the closure of the bridge (Mackie and

Stojadinović, 2005). The literature shows that long-term deterioration and bridge characteristics have a considerable effect on the fragility of bridges, e.g., Refs. Agrawal et al. (2011); Choe et al. (2010); Choe et al. (2008, 2009); Gardoni and Rosowsky (2011); Ghosh and Padgett (2010); Zhang et al. (2008); Zhong et al. (2012), among others. However, the application of fragility is usually limited to the intensity measure due to the lack of deterioration data and modelling constraints associated with the incorporation of the different bridge parameters (Agrawal et al., 2011; Gidaris et al., 2017; Zhang et al., 2008). Hence, the fragility function expression can be abbreviated as follows (Attary et al., 2016; Ellingwood, 2001; Koshimura et al., 2009a; Rosowsky and Ellingwood, 2002; Shinozuka et al., 2000):

$$Fr(IM) = P[DM \mid IM, X, t] = P[DM \mid IM] = \Phi\left[\frac{\ln(IM) - \mu}{\sigma}\right] \tag{2-22}$$

where, $\Phi(\cdot)$ is the standard normal cumulative distribution function; $\mu$ is the mean; $\sigma$ is the standard deviation; $t$ is the time vector; and $X$ is the structural parameters vector. Table 2-5 presents a synopsis of the fragility models for bridges subjected to extreme wave hazards.

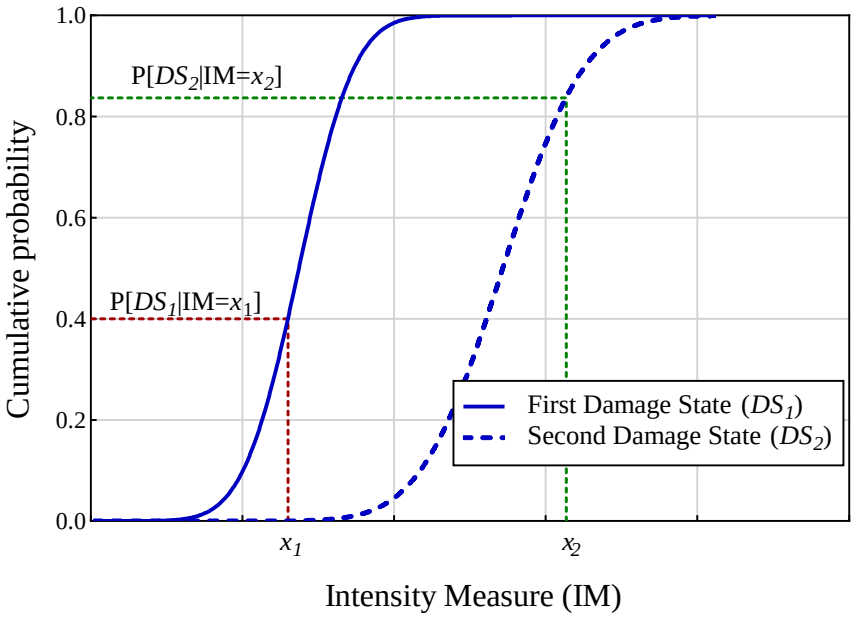


**Figure 2-8.** Example of a fragility function for two different damage states.

**Table 2-5.** Synopsis of bridge fragility curves under extreme wave hazards.

| Authors | EDP | IM | Methodology | Random variables (structural) | Remarks |
|---|---|---|---|---|---|
| Ataei and Padgett (2015a) | Deck lateral displacement (>0.6 m) | Clearance and wave height | Fluid structure interaction Modified empirical methods of AASHTO (2008) and Douglass et al. (2006) | Concrete strength; steel strength; concrete density; coefficient of friction. | Statistical learning techniques employed over range of clearance (2 to -2 m) and wave heights (0 to 5 m) from model to reduce computational cost. |
| Ataei and Padgett (2012) | Connection strength (pullout + breakout + steel yield) and bridge self-weight | Clearance and wave height (wave period) correlated to wave height using Longuet-Higgins (1983) joint probability | Simplified model based on AASHTO (2008) total uplift force | Deck thickness; concrete strength; steel strength; concrete density; steel density; anchor breakout and pullout strengths. | Mainly proposed to capture failure due to deck displacement within an inventory. |
| Ataei and Padgett (2013a, 2013b) | Lateral strength (>15%) and lateral stiffness (>40%) | Clearance and wave height | Nonlinear static pushover | Concrete strength; steel strength; concrete density; steel density; shear strength | Mainly for bridges with strong connections between deck and substructure. |
| Ataei and Padgett (2011) | Curvature ductility of column (>cracking force for major damage; >ultimate force for complete damage) Deformation of dowel bars (>yield deformation for major damage; >fracture deformation for complete damage) | Clearance and wave height | Dynamic sinusoid load with peak values extracted from AASHTO (2008) method | Deck thickness; concrete strength; steel strength; concrete density; steel density | Fragility analysis showed that global performance of case study bridge mainly influenced by tensile force in column. |
| Akiyama et al. (2013) | Deck weight, horizontal resistance and capacity of pier | Wave height | Simplified method relating amount of force to resistance of bridge (total | Concrete strength; steel yielding strength; uplift force model error; drag | Bridges with shorter piers are more vulnerable to tsunami-generated waves |

| | | | | | |
|---|---|---|---|---|---|
| | | | uplift and total drag against bridge resistance to vertical and horizontal movements) | force model error; coefficient of friction | due to additional force generated on bridge deck. |
| Shoji and Moriyama (2007) | Ranks of damage based on field observations:<br>A: fall-down and wash-out of deck<br>B: deck displacement, abutment damage and scouring and erosion and scouring of abutment embankment soil<br>C: deck attachment damage<br>D: No damage | Inundation depth | Empirical, based on statistical analysis of damage data and field measurements | N/A[a] | For data collected on bridge damage in Sumatra, probability of failure of more than 0.5 obtained for inundation depths larger than 20 m. Probability of failure of bridges in Sri Lanka up to 0.4 at inundation depth of about 10 m. |
| Kameshwar and Padgett (2014) | Deck unseating | Clearance and wave height | Sinusoid dynamic load uniformly distributed on deck. | N/A[a] | Parametrized fragility functions for different bridge height, wave height and clearance proposed for hurricane-generated waves. |

[a] No information was provided on the random variables.

Note: EDP: Engineering demand parameter; IM: Intensity measure

### 2.4.2 Tsunami Waves Fragility Functions

The existing research efforts on fragility models of tsunami-generated waves are mainly devoted to bridges subjected to Indian Ocean (2004) and Tohoku (2011) tsunamis in Southeast Asia and Japan. Shoji and Moriyama (2007) developed empirical fragility models for bridges located in Sumatra and Sri Lanka during the Indian Ocean tsunami (2004). Damage to bridges based on post-hazard surveys was measured and ranked A, B, C and D for complete collapse of deck, deck displacement with abutment damage, deck attachment damage (e.g. railing), and no damage, respectively. The inundation depth was considered as the only intensity measure, and it was defined as the measured height from the still water level at the bridge location to the line marks on the surrounding structures. It was found that for bridges located in Sri Lanka, the probability of failure reached up to 0.4 at an inundation depth of about 10 m, while it was about 0.5 at an inundation depth of 20 m for bridges located in Sumatra. Akiyama et al. (2013) proposed a methodology for developing the fragility of concrete girder bridges under tsunami-generated waves using a simplified approach similar to the framework developed by Ataei and Padgett (2012). However, Akiyama et al's. (2013) approach considered both the uplift and the lateral capacity of the Tsutanigawa Bridge, which was damaged by the Tohoku tsunami (2011). Lateral capacity was defined by the resistance of the deck to horizontal movement and pier flexural and shear strengths, while the uplift capacity was controlled mainly by the deck self-weight. Wave height was used as the only intensity measure. It was reported that the vulnerability of the bridge increased with the reduction in pier height due to the additional drag force developed on the decks in piers with smaller heights. The bridge with strengthened piers showed a reduction in failure probability in 50 years of tsunami hazard by up to 18 times. The HAZUS (FEMA, 2013) methodology for tsunami hazards proposes an expert opinion method for estimating the

fragility of bridges. The proposed method uses flow rate as an intensity measure to consider the effect of debris and flow velocity. The existence of debris and high flow rates are incorporated in the fragility function by increasing the logarithmic standard deviation of the demand (i.e. intensity measure). Higher flow rates were found to increase the vulnerability of bridges (Gidaris et al., 2017).

### 2.4.3 Hurricane Waves Fragility Functions

Analytical fragility frameworks have been recently developed for bridges subjected to hurricane-generated waves in the United States (Ataei and Padgett, 2012, 2015a; Kameshwar and Padgett, 2014), following the earlier studies on empirical methods for predicting wave forces (AASHTO, 2008; Douglass et al., 2006). Ataei and Padgett (2012) developed a methodology for the estimation of the fragility of deck unseating failure mode under hurricane-generated waves using a simplified approach based on the uplift capacity exceedance conditioned on the total uplift force. Wave height and clearance were used as the intensity measures. To account for other wave parameters that affect the magnitude of the uplift force, the wave period was correlated to the wave height using a Longuet-Higgins joint probability density function (Longuet-Higgins, 1983). The proposed methodology was implemented on the bridge inventory of the Houston/Galveston Bay region in the US. A generic metric for classifying bridges with different properties based on deck span mass per unit length was used. Later, Kameshwar and Padgett (2014) provided a multi-hazard probabilistic framework to model deck unseating failure caused by earthquakes and hurricanes conditional on wave height and clearance. In this approach, an approximation of the structural response is obtained using metamodel functions for bridges with different

characteristics (e.g. strength, pier height, steel yield strength and reinforcement ratio). The framework was applied to multi-span simply-supported concrete girder bridges that are subjected to earthquakes and hurricanes in South Carolina in the US. The wave was applied on the bridge deck as a uniformly-distributed dynamic sinusoidal load. System-level fragility was estimated by assuming that the bridge is a serial system of components, and the collapse of any of the bridge components determines the collapse of the bridge. The probability of failure under hurricane hazard can be expressed in terms of wave height, clearance and bridge height. Ataei and Padgett (2015a) employed statistical learning techniques, such as support vector machines and random forests, to develop surrogate fragility models for bridges subjected to hurricane-generated waves (Ataei and Padgett, 2015a). Surrogate models were used to examine the efficiency of using the simplified wave load approaches of AASHTO (2008) and Douglass et al. (2006) in probabilistic models. It was found that simplified approaches can be used to predict deck unseating failure, despite a reduction in accuracy of about 13%. This is more practical than the fluid-structure interaction models for fast screening applications for bridges subjected to extreme wave hazards.

## 2.5 Post-Disaster Recovery

The last phase of resilience is the loss analysis, where the results of the damage analysis in the previous phase are translated into structural risk indicators that are termed as decision variables (*DVs*). The common decision variables used in the loss analysis phase include the fatalities, economic losses (due to bridge network downtime and dislocation of population) and repair losses (due to hazard-induced damage) (Attary et al., 2017; Günay and Mosalam, 2013). These decision variables can be used by structural engineers, community managers

or stakeholders to assist in risk-informed decisions and post-hazard strategic planning (Porter, 2003). In the post-hazard recovery stage, the quantification of resilience becomes necessary to ensure an acceptable level of performance of bridges when different retrofitting and risk mitigation schemes are considered. By definition, the resilience of a structure under an extreme hazard has two main elements (Bocchini et al., 2013): (a) robustness, which is the ability of the structure to resist significant forces, and (b) rapidity, which is the ability of the structure to recover quickly from the damage induced by the forces. Bruneau and Reinhorn (2007) expanded the definition to include two more elements: (c) resourcefulness, which is the ability to recognize problems, manage resources and determine priorities in the recovery process, and (d) redundancy, which is the ability to provide alternative elements or resources in the analysis to maintain the performance of the structure or system.

With the recent increase in the popularity of the resilience concept for infrastructures, some research studies have been published on the resilience restoration of bridges under extreme loads (Bocchini and Frangopol, 2012; FEMA, 2012; Padgett and DesRoches, 2007). Restoration models for bridges can be generally categorized into two main types based on the damage state and time after the occurrence of the event (Bocchini et al., 2012; Bocchini and Frangopol, 2012; Gidaris et al., 2017; Padgett and DesRoches, 2007; Shinozuka et al., 2003). The first type provides a probabilistic description of the reparability of the bridge given the damage state and time after the event, while the second type provides a quantification of the performance percentage of the bridge. Expert opinion data have been used by HAZUS (FEMA, 2012) and Padgett and DesRoches (2007) to provide a functional form of the probability of the restoration in the performance of a bridge after the occurrence of a hazard. Bocchini et al. (2012) recently proposed a more versatile model that considers different restoration shapes (e.g. trigonometric or linear) through a sinusoidal process.

However, the calibration of the parameters used in the model can be difficult, as they rely on a number of factors such as the collection of data at the post-hazard stage, the availability of resources, and prioritization of the critical infrastructure components (Gidaris et al., 2017). Later, Decò et al. (2013) developed a probabilistic model of the resilience of bridges in the pre-event stage. The performance of the bridge over time is then estimated using a six-parameter sinusoidal function. The model considers the uncertainties associated with structural damage, the recovery process and the costs of rebuilding/rehabilitation. Chandrasekaran and Banerjee (2015) developed a multi-objective approach to provide an optimization tool for the selection of the optimum retrofit design schemes for bridges under seismic loads and scour effects. The developed tool, which was applied on different retrofitting materials, i.e., carbon fibre, steel and glass fibre, assists in maximizing the resilience of the bridge and minimizing the associated costs. The HAZUS (FEMA, 2013) methodology for tsunami hazards provides an estimation method for the loss in the performance of bridges in terms of damage states based on expert opinion data. However, the restoration time given only corresponds to full performance, unlike the restoration models discussed above, for which different performance stages can be calculated (Gidaris et al., 2017).

## 2.6 Discussion and Gaps in Knowledge

This chapter presented a review of the four modules of the resilience assessment of bridges subjected to extreme wave forces. The background of the research efforts in the areas of extreme wave forces, bridge response, vulnerability modelling and post-disaster recovery

are presented in this chapter. Based on the discussion of the four modules, the limitations of current studies and suggestions for future research needs are addressed in this section.

In terms of forces, the wave height and storm water level are among the main controlling parameters of the magnitude of forces. The maximum values of wave forces correspond to subaerial conditions (low clearance) and large wave heights (Guo et al., 2015; Xu et al., 2015). The overtopping of wave and air pockets initiate downward forces, which leads to a reduction in the magnitude of forces (Azadbakht and Yim, 2014; Ataei, 2013). In addition, the contribution of the inertia forces on total drag force becomes more significant with the decrease in the lateral rigidity of the decks (Xu and Cai, 2015, 2017). Further research is required to investigate the effect of inertia on decks with different supports conditions (i.e., lateral stiffness) (Xu et al., 2017). The air entrapment has a significant effect on the magnitude of hydrodynamic and impact (slamming) forces (Cuomo et al., 2009; Guo et al., 2015). The change in the redistribution of the pressure between girders can influence these forces, which can be supported by more studies that can specifically focus on the effect of girders spacing and air vents (Xu et al., 2016). In particular, the reduction in impact forces resulting from air entrapment below deck (the cushioning effect) needs to be further examined in both individual elements and complete superstructure models (Cuomo et al., 2009). A number of design-type empirical methods for predicting the magnitude of wave forces have been recently proposed, which provided a fundamental advancement in the design and risk assessment schemes for bridges subjected to extreme wave hazards. However, significant improvements are still needed to expand the applicability of these methods to a wider range of bridge classes and hazard type. For instance, the consideration of the angle of attack, the effect of scale and the inclusion of hydrodynamic force elements have not been covered in detail (AASHTO, 2008; Mazinani et al., 2015; Xu et al., 2017).

Although there have been recent attempts to address these factors through more advanced large-scale wave-structure interaction models, further research studies are still required to improve the understanding of the deck response to wave breakings. In addition, limited research has been reported on the effect of factors such as parapet configuration, deck inclination and nearby structures. Deck inclination and parapets have been found to play a major role in drag force variations (Lau et al., 2010; Xu et al., 2015). While the effect of nearby bridges has been reported, the effect of other types of structures with different sizes and at different distances can be further investigated.

Regarding the bridge response, the unseating of simply-supported decks and decks with limited connection to the substructure have been mainly addressed in recent studies. In integral bridges or bridges with strong deck connectivity, significant damage can result in piers due to the force transfer. The strong connection of the deck to the substructure enhances both its energy dissipation and resistance to lateral displacement (CALTRANS, 2013; Priestley et al., 1996). In this case, the demands that result from moments and uplift forces on the deck are further transmitted to the piers and foundations. Possible retrofitting methods for simply support decks have been recently suggested, such as restrainer cables and high strength bars. The response of bridges with different deck connectivity that can result from these methods can be examined through numerical models. In addition, multi-axial hybrid testing has recently emerged as an advanced technique for testing the critical components of a full-scale model of a structure (Hashemi et al., 2017; Hashemi et al., 2015; Hashemi and Mosqueda, 2014). The method can capture the complex non-linear behaviour of decks with strong connections with the substructure to overcome the simplifications usually made in numerical simulations. The existing studies regarding analytical fragilities consider wave height and clearance as intensity measures for bridges subjected to hurricane- and tsunami-

generated waves. In theory, the hydrodynamic force component is mainly affected by the inundation depth ($h$) and velocity ($u$), and it has a linear relationship with the momentum flux ($hu^2$) (Attary et al., 2016). Hence, the use of velocity or depth as independent intensity measures leads to a scatter in the fragility data. Recent studies have adopted momentum flux and moment of momentum flux ($h^2u^2/2$) as possible intensity measures that combine both the inundation depth and velocity, e.g., Refs. Alam et al. (2017); Attary et al. (2016); Park et al. (2013); Park et al. (2014). The use of vector intensity measure that combines these intensity measures and flow rate can be examined on bridges. Furthermore, most current fragility models are based on damage states for individual bridge elements, whereas system-level fragility models are often required in resilience assessment (Gidaris et al., 2017). Hence, future research endeavours can be devoted to efficient definitions of system-level damage states that can be used in restoration models for extreme wave hazards. Most of the current parametrized fragility functions are limited to concrete girder bridges subjected to hurricane hazards (Kameshwar and Padgett, 2014). Further research can focus on expanding these models to include more bridge classes and wave types.

The resilience metric has recently been incorporated in the PBEE methodology as a decision variable in the loss analysis stage (Broccardo et al., 2017; Broccardo et al., 2015). The proposed framework consists of five main analysis stages: (a) hazard (describes the mean annual exceedance rate), (b) vulnerability (describes the fragility functions), (c) absorption (describes the performance drop at a specific damage state), (d) restoration (describes the recovery time at a specific performance drop) and (e) recovery strategies (describes the form of recovery function) (Broccardo et al., 2017). While these studies focused specifically on earthquake hazards, future research can include extreme wave hazards by taking into account the variations in the above analysis stages, e.g., hazard characteristics. In addition, the use

of suitable acceptance limits in the validity criteria of the framework and modified reliability approaches (e.g. time-variant analysis) to describe the range of occurrence of the significant interaction between consecutive hazards (defined as “resilience breaking points”) can be expanded to include extreme waves and multi-hazard conditions (Broccardo et al., 2015). Existing investigations of performance restoration models for bridges under extreme waves are limited. Restoration models can be developed for different retrofitting schemes, particularly for simply-supported decks that have limited connectivity to the substructure. The available performance models for seismic hazards can be modified to include larger groups of bridges and infrastructure system networks subjected to extreme waves. The reliability of these models can be further improved using expert opinion and past hazard data.

The majority of empirical methods for the estimation of wave forces are limited to hurricane-generated waves for bridges located in North America. Despite the variations in wave and infrastructure characteristics that may exist as a result of the differences in topography or climate among the geographic regions around the world, the empirical formulas discussed above are still applicable to a range of wave and bridge parameters. Hence, these methods can be used for bridges in Australia that are subjected to extreme wave forces, provided that the properties of hazards and bridges are similar to the case studies conducted in North America. For instance, most of these methods can be applicable to concrete girder bridges subjected to cyclone waves (a common hazard in Australia), since they fall under the same hazard category as hurricanes. In particular, the two main differences in the hazard characterization phase that may need attention when applying the methods are the variations in the annual probability of exceedance and the upper and lower bounds of the wave parameters in each method. In addition, the structural response and damage analysis depend

mainly on the variations in the provisions provided by the design standards (e.g., shear and torsion of piers). Finally, the decision-making of stakeholders in the loss analysis stage can be influenced by the variation in economic and societal decision variables, such as the impacts of fluctuations in the prices of the market and disruption of services due to bridge closure (Günay and Mosalam, 2013).

## 2.7 Summary

Recent studies have revealed growing worldwide attention to the resilience of bridges under extreme waves. This is mainly driven by current concerns of the consequences of climate change and its effects on the intensity of weather hazards. The response of bridges under extreme wave conditions is currently being researched in different specialty areas to develop tools for quantifying and enhancing their resilience. Hence, this chapter contributes to the topic by providing a detailed discussion of the resilience of bridges and their restoration based on a multi-phase assessment method. The following are the main findings and outlook identified from this chapter:

- Wave height and storm water level are the most influential parameters affecting wave forces. In particular, wave forces reach their peak values at relatively small clearance values (sub-aerial conditions) and at large wave heights, and they reduce with the increase in inundation depth due to the effect of downward forces initiated by the wave overtopping and the presence of air pockets. In addition, although it has been mentioned in several studies that the effect of inertia is minimal compared to other forces, this assumption needs to be supported by further research, taking into account changes in the lateral rigidity of decks.

- The effect of air entrapment was also found to be influential on both hydrodynamic and impact (slamming) forces. The magnitude of these forces is directly affected by the change (redistribution) of pressure between girders, which needs to be further confirmed by studying the effect of geometrical parameters such as girder spacing and air openings.
- Empirical methods of calculating wave forces provide the fundamental step for the design and retrofitting of bridges located in hazard-prone regions. However, the simplifications and assumptions associated with these methods limit their applicability over a wide range of typical bridge classes and wave types. The assumptions include the consideration of the hydrodynamic elements of the force, angle of attack and effect of scale. Recently published methods for estimating wave forces have attempted to resolve some of the issues by providing three-dimensional large-scale wave-structure interaction models. These may be further explored by capturing deck responses to wave breaking, which will provide better insights.
- Most of the current studies concern exclusively simply-supported decks or decks with limited connectivity to the substructure. A few notable studies have addressed the potential failure of piers resulting from force transfer in decks with strong connections. Numerical models for bridges with different connection strengths can be developed, especially when high strength steel bars and restrainer cables are adopted as possible retrofitting schemes.
- Recently, parametrized fragilities have been developed as a versatile approach for a range of bridge characteristics. However, these models are limited mainly to concrete girder bridges and hurricane-generated waves. This underlines the need for future research studies that can improve current models to cover more bridge topologies

with different damage measures, as well as other hazards such as coastal surges and tsunamis.

- The existing analytical fragilities consider wave height and clearance as intensity measures for bridges subjected to hurricane- and tsunami-generated waves. Recent research on framed building structures subjected to tsunami waves shows the efficiency of the use of momentum flux and moment of momentum flux as intensity measures that combine both inundation depth and velocity. Future research can adopt these new intensity measures on bridges with the addition of flow rate as a vector intensity measure.
- The existing investigations of post-disaster recovery and restoration models for extreme wave hazards are limited. Restoration models can be developed for different retrofitting strategies (e.g., deck restraints and FRP jackets for piers) of the bridges damaged by extreme wave hazards.

Furthermore, the resilience quantification requires understanding for the practical aspects of post-disaster recovery. Chapter 3 presents a new concept that considers the effect of resources on recovery time is proposed to assist in the evaluation of resilience by comparing different recovery options and demonstrates the application of the concept using an example. The outcome of vulnerability modelling can be linked to the resilience quantification through the proposed methodology. In Chapters 4 to 6, a complementary research program on fragility analyses of bridges is presented to address the research questions and objectives.

# CHAPTER 3

# RESILIENCE QUANTIFICATION

## 3.1 Introduction

Resilience generally refers to the ability to regain the strength of a system quickly after a shock. In the structural engineering field, the shock often refers to the extreme forces that result from the extreme events (e.g. earthquakes and extreme waves). Hence, the decision on viability of the different rehabilitation strategies after the extreme event is determined by the time taken to restore the full performance. However, this concept assumes that the time taken to complete the project is the most important element for the project. However, priorities specified by the stakeholders based on different constraints (e.g. allocated resources) play a significant role in their decision. Hence, this chapter introduces a unified definition of resilience that takes into account the resources and environmental impacts based on their level of importance to the decision maker. The resilience quantification concept is introduced in this chapter. The effect of resources is shown using two different approaches, namely, the conservative approach (products of time and resources resilience) and the resilience based on importance factors. These new indices are further expanded to include the effect of environmental impact of the different retrofit options. The resilience indices are demonstrated using a real highway project example from the engineering area that adopts realistic resources (cost)-time relationship.

### 3.2 Effect of Resources

The *resilience triangle* concept has been introduced by a number of researchers as a versatile approach for estimating resilience, and it can be expressed as follows (Bocchini and D. Frangopol, 2011; Bruneau et al., 2003; Cimellaro et al., 2010):

$$R_1 = \frac{1}{t_h} \int_{t_o}^{t_o+t_h} Q(t)\ dt \qquad (3\text{-}1)$$

where $R_1$ is the normalized resilience factor; $Q$ is the performance; $t_o$ is the time of occurrence of the extreme event; and $t_h$ is the specific time horizon (measured from $t_o$). Performance ($Q$) can be defined based on different indicators, such as the performance of the network (the ratio of total time over travel distance in a pre-defined timeframe) (Bocchini and Frangopol, 2010b; Frangopol and Bocchini, 2011). A schematic illustration of the resilience triangle concept is shown in Figure 3-1(a).

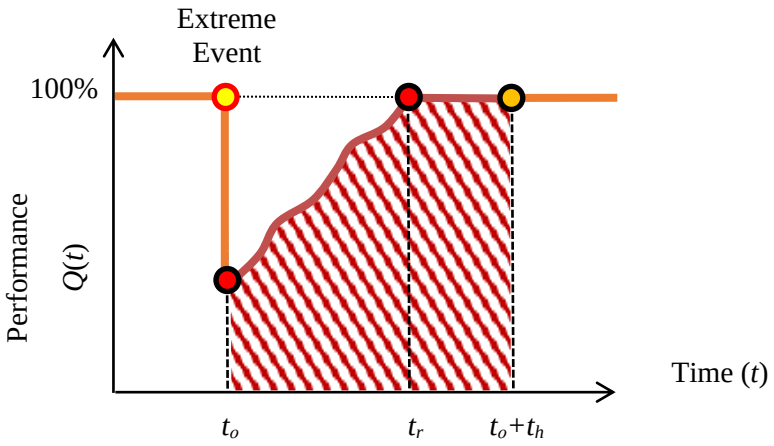


(a)

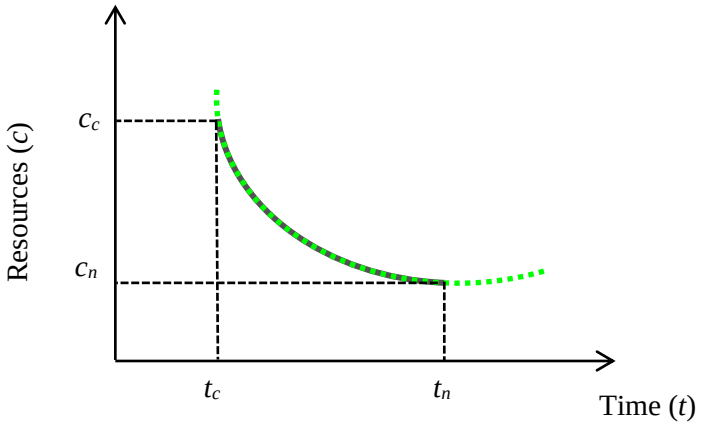


(b)

**Figure 3-1.** Quantification of resilience: (a) definition of resilience triangle concept; and (b) resources (cost)-time relationship.

In post-hazard recovery, the ability to mobilize different resources, either monetary, human or technological, is an essential element for the achievement of the established aims and priorities. Hence, the rapidity of recovery of the original performance of the infrastructure is a function of the availability of resources (Bruneau and Reinhorn, 2007; Cimellaro et al., 2010). A new form of resilience is used here to combine the effect of resources (cost) and time of recovery in one index. The new index facilitates the study of resilience, as it compares different recovery options by considering the amount of resources that needs to be spent to restore performance in a specific period of time. The inter-relationship between the construction resources (cost) and time (duration) can be presented by a polynomial form that has two main points: (a) crash point and (b) normal point (Shr and Chen, 2004; Shuka, 2017). Figure 3-1(b) shows a schematic example of the resources-time relationship. The crash point represents the duration (crash time) that requires the largest amount of resources (crash cost),

while the normal point defines the case where construction duration (normal time) corresponds to the lowest possible resources (normal cost). In other words, the normal time ($t_n$) defines the maximum possible time to complete the project with the lowest amount of resources ($c_n$), while the crash time ($t_c$) refers to the minimum possible time to finish the project with the largest amount of resources ($c_c$). Hence, the time required to restore the targeted performance typically decreases from the normal to the crash duration with the increase in resources from normal to the crash point. The further increase in construction duration beyond the normal time leads to an increase in the required resources resulting from the additional indirect costs such as delay penalties and revenue loss (Shuka, 2017). In theory, an infinite increase in resources should lead to 'zero' time required to achieve the targeted performance. However, human limitations usually impose a practical limit, after which the increase in resources does not lead to a significant reduction in time (Bruneau and Reinhorn, 2007). This includes the constraints on the number of simultaneous recovery operations, recovery rate and maximum available funding (Bocchini and Frangopol, 2011; Bocchini and Frangopol, 2010b). In addition, the capping of resources cannot be infinite, and it needs to be defined appropriately, based on factors such as the budget allocated by the government and the type and importance of a structure. In this study, the decrease in restoration time with the increase in resource capacities is represented by the region between the crash and the normal point.

Accordingly, the resilience triangle can be considered not only for time of recovery but also for the resource (cost) of recovery. This is particularly important, as an option with a faster recovery time may actually produce a more significant shock in the available resources. For example, Figure 3-2 shows the resilience triangles of two restoration strategies in terms of restoration time and capacity of resources of an infrastructure facility, e.g., a bridge. The two

resource capacities in Figure 3-2(b), denoted as $c_{r1}$ and $c_{r2}$, are meant to be fully utilized to achieve full performance at restoration time of $t_{r2}$ and $t_{r1}$ in Figure 3-2(a), respectively. A fixed resource capping ($c_h$), measured from the initial resource capacity ($c_o$), at the instant of an extreme event, is used in Figure 3-2(b) to obtain the resilience from the area under the performance $Q(c)$, similar to the specific time horizon ($t_o+t_h$) defined in Equation 3-1.

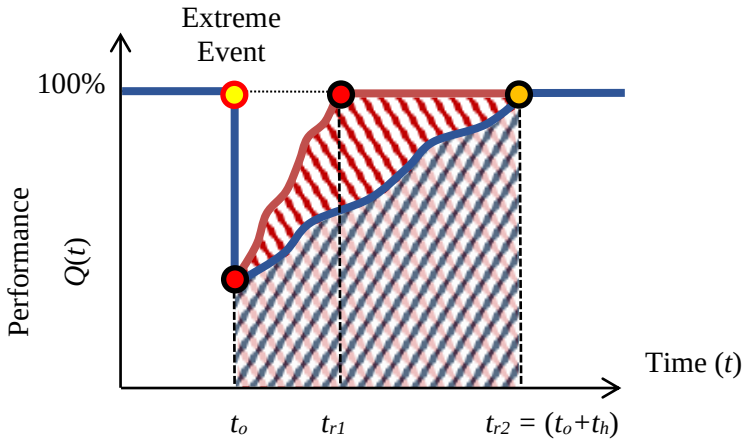


(a)

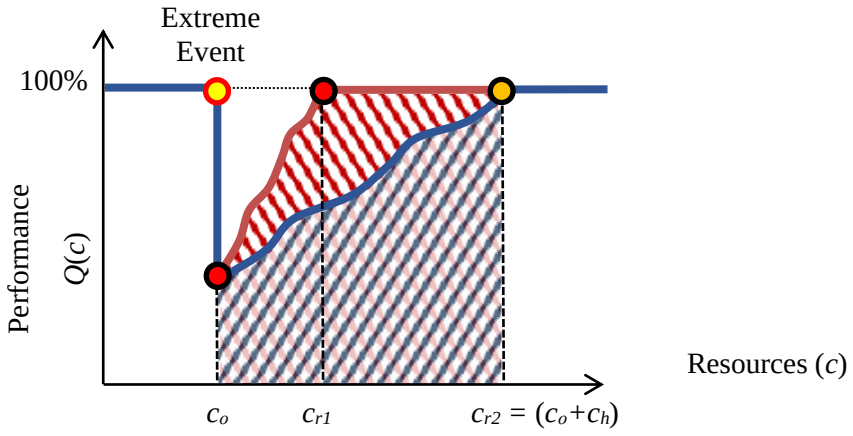


(b)

**Figure 3-2.** Resilience triangles: (a) time; and (b) resources (cost).

By combining the relationship between time and cost (Figure 3-1(b)) and the triangles of resilience associated with the time and cost (Figure 3-2), one can define a new index for resilience that accounts for both parameters. As illustrated in Figure 3-3, the performance of two recovery strategies as a function of both time and resources can be presented in one plot. For example, the two restoration strategies presented are assumed to have resource capacities equal to the crash ($c_{r2}=c_c$) and normal ($c_{r1}=c_n$) points necessary to complete the project at the crash ($t_{r1}=t_c$) and normal ($t_{r2}=t_n$) time, respectively (see Figures 3-3(a) and (b)). The change in restoration rate resulting from the variation in resources leads to different forms of resource performance at a specific restoration time, $Q(t_c,c)$ and $Q(t_n,c)$, and time performance at specific resource capacity, $Q(c_n,t)$ and $Q(c_c,t)$. Consequently, the strategy with greater availability of resources ($c_c$) meets full performance in a shorter time ($t_c<t_n$) than that with lower availability of resources ($c_n$). Hence, the increase in resources resilience is associated with a drop in time resilience, and vice-versa.

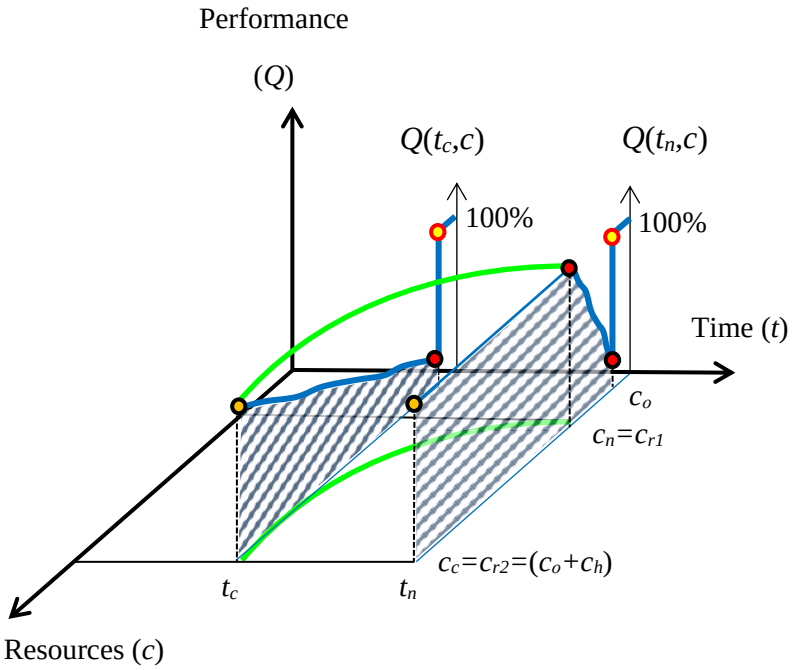
Performance
(Q)
Q(tc,c)
Q(tn,c)
100%
100%
Time (t)
co
cn=cr1
cc=cr2=(co+ch)
tc
tn
Resources (c)

(a)

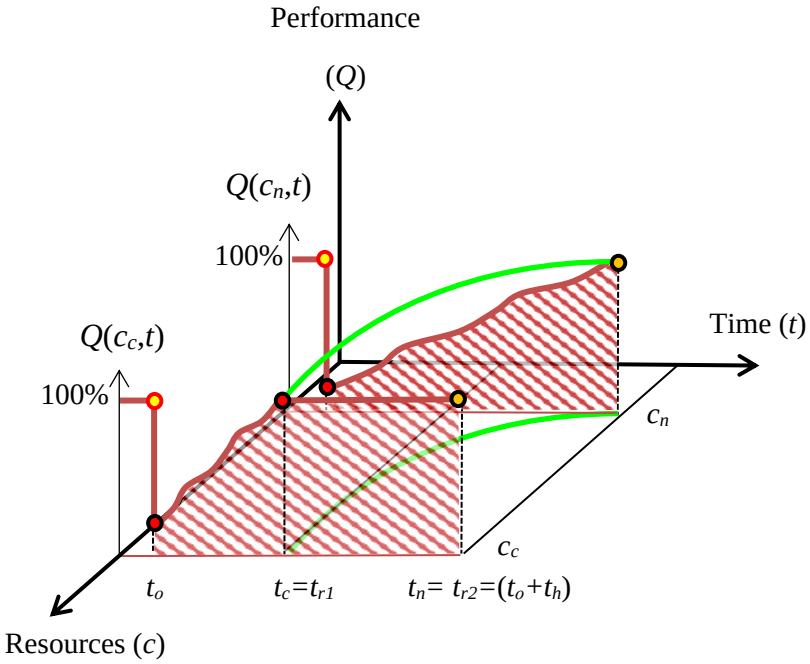
Performance
(Q)
Q(cn,t)
100%
Q(cc,t)
100%
Time (t)
cn
cc
to
tc=tr1
tn= tr2=(to+th)
Resources (c)

(b)

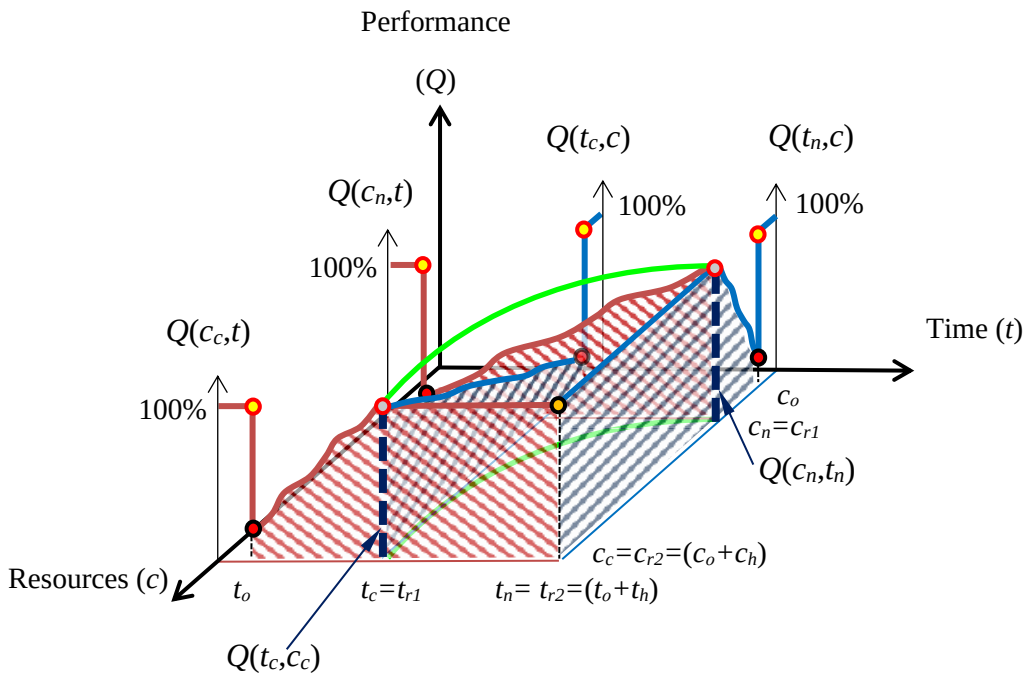


(c)

**Figure 3-3.** Resilience estimation by including the effect of resources (cost): (a) resilience triangles of resources (cost) at $t_c$ and $t_n$; (b) resilience triangles of restoration time at $c_c$ and $c_n$; and (c) performance ($Q$) as a function of both resources (cost) and time.

Figure 3-3(c) shows the full performance at crash and normal points, $Q(t_c,c_c)$ and $Q(c_n,t_n)$, where the unified resilience indices can be estimated. In this study, the unified resilience index is estimated using two proposed methods. The first method is the direct multiplication of the independent resilience indices associated with time and resources, respectively. It can be expressed as follows:

$$R_2 = R_t \cdot R_c \tag{3-2}$$

In Equation 3-2, $R_2$ is the unified normalized resilience factor; $R_t$ is the normalized resilience factor calculated from the performance-time relationship; and $R_c$ is the normalized resilience factor calculated from the performance-resources relationship. The fixed resource capping and time horizon are taken to be equal to the largest time ($t_{r2}$) and resources ($c_{r2}$) to facilitate the comparison between resilience factors in strategies that have close time or resource values at full performance. The resilience measure obtained from this method is conservative, since for instance, in the case of equal $R_t$ and $R_c$ the calculated index is lower than both cases.

The second proposed method is the summation of the independent resilience indices associated with time and cost using importance factors. It can be expressed as follows:

$$R_3 = R_t \cdot I_t + R_c \cdot I_c \tag{3-3}$$

In Equation 3-3, $R_3$ is the unified normalized resilience factor; and $I_t$ and $I_c$ are the importance factors for time and resources, respectively. These factors define the relative importance of the resilience element for the decision maker, and hence their summation is always equal to 1.

The resilience forms discussed above are applied to restoration options for a hypothetical bridge damaged by an extreme event. The overall performance of the highway segment, where the bridge is located, at the instant of extreme event is assumed to drop to 45%. The performance with respect to time $Q(t)$ is estimated using the network performance index ($\Gamma$) proposed by Bocchini and Frangopol (2010a). The index is based on the total travel time (*TTT*) and distance (*TTD*), and it can be expressed as follows (Bocchini and Frangopol, 2010a; Bocchini and Frangopol, 2010b; Bocchini and Frangopol, 2012):

$$\Gamma(t) = \frac{1}{\gamma_T \cdot TTT(t) + \gamma_D \cdot TTD(t)} \tag{3-4}$$

In Equation 3-4, $\gamma_T$ and $\gamma_D$ are balancing factors for the total travel time and distance, respectively. The balancing factors are taken in this study to be 0.5 (measured in 1/time and 1/length for $\gamma_T$ and $\gamma_D$, respectively (Bocchini and Frangopol, 2010b)). Using the performance index for the two main cases, total closure of all bridges ($\Gamma^0$), and all are in full service ($\Gamma^{100}$), the bridge performance can be expressed as follows (Bocchini and Frangopol, 2010b; Bocchini and Frangopol, 2012):

$$Q(t) = \frac{\Gamma(t) - \Gamma^0}{\Gamma^{100} - \Gamma^0} \times 100\% \tag{3-5}$$

The total travel time and distance are estimated using the time needed to cover the specific highway segment, the length of the segment and traffic flow. A detailed discussion of the analysis of traffic flow is beyond the scope of this research and can be found in Refs. Bocchini and Frangopol (2010a, 2010b, 2011, 2012), among others.

At the instant of an extreme event ($t_o$), each of the total travel time (*TTT*) and distance (*TTD*) is assumed to be about 1.93 times its value under normal conditions. This leads to a drop in the performance index to 52% of the normal condition, i.e., $\Gamma(t_o) = 0.52\ \Gamma^{100}$, according to Equation 3-4. The performance index when all bridges are closed ($\Gamma^0$) is taken as one-eighth the normal condition, i.e., $\Gamma^0 = 0.125\ \Gamma^{100}$. Hence, according to Equation 3-5, this results in a performance of 45% at the instant of an extreme event ($t_o$).

The performance index with respect to resources, $\Gamma(c)$, can be directly linked to the restoration time, or it can be calculated using the same assumptions used for the time index $\Gamma(t)$. The variation in restoration time ($t_r$) with the required resources cost are assumed to

have the polynomial relationship shown in Figure 3-4. The relationship is taken from the study by Shuka (2017) for the construction cost and duration of highway projects in Florida, the United States. The resilience factors, expressed as percentages, for the different recovery strategies are summarized in Table 3-1. The total cost of resources is assumed to include the estimated unit, construction and removal costs. The fixed time horizon ($t_o$+$t_h$) and resources capping ($c_o$+$c_h$) are taken to be equal to the normal time ($t_n$ = 80 days) and crash resources ($c_c$ = \$223×$10^4$), respectively. The unified resilience $R_2$ shows an overall decrease from the independent factors of time ($R_t$ and $R_1$) and resources ($R_c$) alone. For instance, the resilience factor $R_1$ at a restoration time ($t_{r1}$) of 40 days is 88.2%, whereas $R_2$ showed a value of 64% (a reduction by about of 27% from $R_1$) at the corresponding resources ($c_{r1}$=\$223×$10^4$). However, the main limitation of the resilience factor $R_2$ is that it does not indicate specifically the relative importance of the cost and time in every project, which can vary widely depending on the different perspectives of stakeholders. The unified resilience values of $R_3$ estimated using Equation 3-3 are presented in Table 3-1 with importance factors of 0, 0.25, 0.5 and 1 for resources and time. For a restoration strategy, the restoration time may be identified as not a priority ($I_t$=0.25), and the resources may be considered as very important for the project ($I_c$=0.75) due to limitations in the allocated budget. The minimum unified resilience index was specified by the government to be $R_{min.}$=80% to ensure the highest possible quality of completing the work based on the project limitations. In this case, the decision maker might choose the closest resilience value of $R_3$ to the specified $R_{min.}$ for $I_t$=0.25 and $I_c$=0.75, which is 76.6% (see Table 3-1). Hence, the time and resources that match the identified priorities of the project are $t_{r2}$ = 53 days and $c_{r2}$ = \$211×$10^4$, respectively.

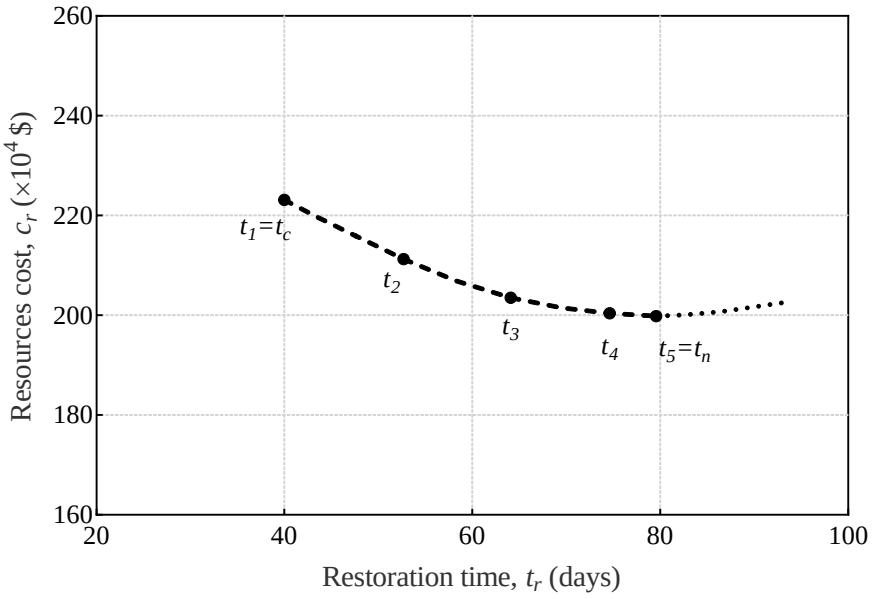


**Figure 3-4.** Cost-time relationship for a highway project. Adapted from Shuka (2017).

**Table 3-1.** Resilience assessment of a bridge restoration project after an extreme event based on time and resources.

| Time at full performance restoration ($t_r$) (days) | Resources at full performance restoration ($c_r$) [a] (×10$^4$ $) | Resilience factors (%) | | | | | | | | |
|---|---|---|---|---|---|---|---|---|---|---|
| | | $R_t$ | $R_c$ | $R_1$ | $R_2$ | $R_3$ [b] | | | | |
| | | | | | | $I_t$=0; $I_c$=1 | $I_t$=0.25; $I_c$=0.75 | $I_t$=0.5; $I_c$=0.5 | $I_t$=0.75; $I_c$=0.25 | $I_t$=1; $I_c$=0 |
| $t_{r1}$ = $t_c$ = 40 | $c_{r1}$ = $c_c$ = 223 | 88.2 | 72.5 | 88.2 | 64.0 | 72.5 | 76.4 | 80.4 | 84.3 | 88.2 |
| $t_{r2}$ = 53 | $c_{r2}$ = 211 | 83.1 | 74.4 | 83.1 | 61.8 | 74.4 | 76.6 | 78.8 | 80.9 | 83.1 |
| $t_{r3}$ = 64 | $c_{r3}$ = 205 | 78.8 | 75.4 | 78.8 | 59.4 | 75.4 | 76.2 | 77.1 | 77.9 | 78.8 |
| $t_{r4}$ = 75 | $c_{r4}$ = 201 | 74.5 | 76.0 | 74.5 | 56.6 | 76.0 | 75.6 | 75.2 | 74.8 | 74.5 |
| $t_{r5}$=$t_n$ = 80 | $c_{r5}$ = $c_n$ = 200 | 72.5 | 76.2 | 72.5 | 55.2 | 76.2 | 75.2 | 74.3 | 73.4 | 72.5 |

[a] The corresponding cost values from Figure 3-4.

[b] $I_t$ and $I_c$ are importance factors of time and resources, respectively.

Notes: Time at extreme event ($t_o$) = 10 days. Initial resource capacity ($c_o$) at the instant of extreme event = \$40×10$^4$.

### 3.3 Linking Resilience to Sustainability

Another noteworthy area of research in the life-cycle management of infrastructure is the consideration of both resilience and sustainability concepts in one framework. Sustainability defines the impacts on society, the economy and the environment during the whole life cycle of infrastructure, such as maintenance costs based on degradation curves, while resilience addresses the significant impacts that occur on the infrastructure during extreme events, such as the damage/repair cost of earthquakes or hurricanes (Bocchini et al., 2013; Rodriguez-Nikl, 2015). A study by Bocchini et al. (2013) addressed resilience and sustainability as parallel concepts that have many similarities. In addition, risk analysis approaches that rely on both concepts have been proposed, e.g., (Bocchini et al., 2013; Rodriguez-Nikl, 2015). However, despite the fact that the probability of occurrence of extreme events is relatively low, their impact on structures is significant and cannot be ignored in the assessment of their whole life cycle (Comber et al., 2012; Court et al., 2012; Rodriguez-Nikl, 2015; Tapia et al., 2011). Hence, resilience needs to be adopted as a sub-section of sustainability to measure both ordinary (low consequences) and extreme (high consequences) events. Therefore, the information collected thus far in this chapter on resilience estimation needs to be integrated into a global sustainability assessment framework to take into account the total societal, economic and environmental impacts that result from various events during the lifetime of bridges. The resilience indices presented in Equations 3-2 and 3-3 focus mainly on the time (societal aspect) and cost (economic aspect) of recovery after extreme events. However, to account for the significant energy consumption and gas emissions associated with rehabilitation activities such as structure repair and retrofitting, or demolition, debris removal and reconstruction (Wei et al., 2015), a new resilience index can be proposed. Using

the concept of resilience triangles adopted earlier for time and resources, the performance-environmental impact relationship can be defined (see Figures. 3-5(a) and (b)). Hence, Equations 3-2 and 3-3 can be extended to provide more generic resilience indices, which can be expressed as follows:

$$R_4 = R_t \cdot R_c \cdot R_e \tag{3-6}$$

$$R_5 = R_t \cdot I_t + R_c \cdot I_c + R_e \cdot I_e \tag{3-7}$$

In Equation 3-6, $R_4$ is the unified normalized resilience factor; $R_e$ is the normalized resilience factor calculated from the performance-environmental impact relationship (see Figure 3-5(a)). In Equation 3-7, $R_5$ is the unified normalized resilience factor; and $I_e$ is the importance factor for the environmental impact.

The selection of correct environmental impact values requires a comprehensive study to compare the energy consumption and gas emissions associated with each recovery option with a specific time and cost (see Figure 3-5(b)). In this study, for the bridge example presented in the previous section, it is assumed that the environmental impact is proportional to the restoration time. The resilience calculations considering the environmental impact are shown in Table 3-2. Hence, the shortest restoration duration is assumed to be associated with greater energy consumption and gas emissions due to the use of more equipment and transportation. The fixed environmental impact value ($e_h$) measured from the initial value ($e_o$) is taken as the value that corresponds to the crash time ($0.9\times10^6$ kg). The effect of the reduction in environmental impact on unified resilience $R_5$ is obvious at the larger restoration time (see Table 3-2).

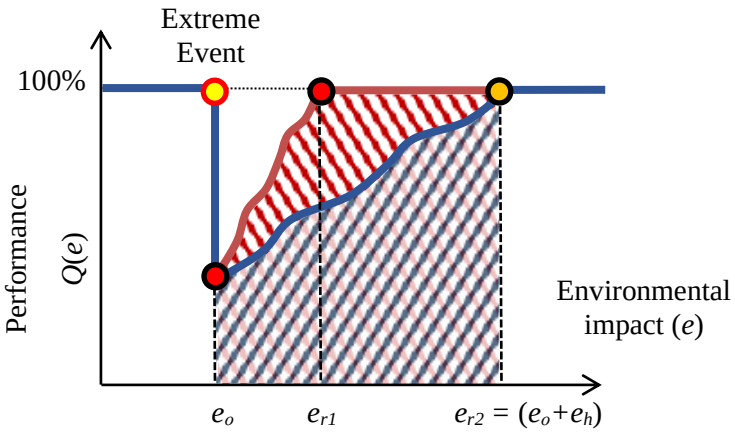


(a)

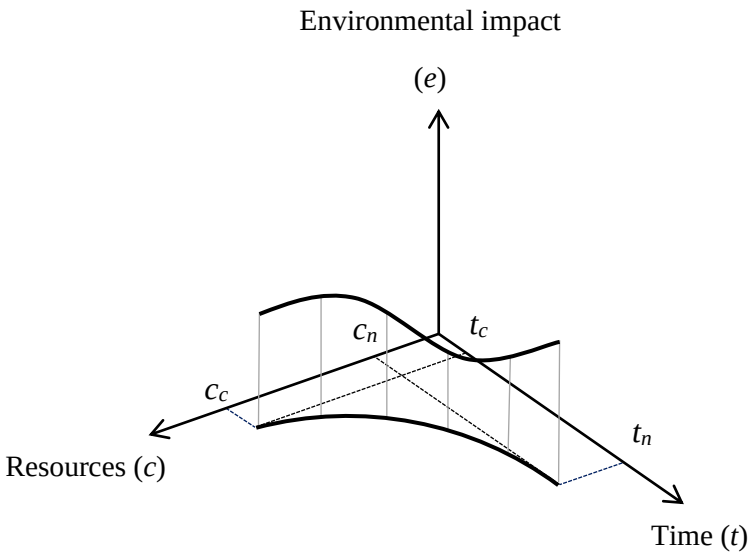


(b)

**Figure 3-5.** Resilience estimation considering the effect of environmental impact: (a) resilience triangle; and (b) variation of environmental impact, resources (cost) and time.

**Table 3-2.** Resilience assessment of a bridge restoration project after an extreme event based on time, resources and environmental impact.

| Time at full performance restoration ($t_r$) (days) | Resources at full performance restoration ($c_r$) ($\times 10^4$ \$) | Environmental impact at full performance restoration ($e_r$) [a] ($\times 10^6$ kg) | Resilience factors (%) | | | | | | | | | | | | |
|---|---|---|---|---|---|---|---|---|---|---|---|---|---|---|---|
| | | | $R_t$ | $R_c$ | $R_e$ | $R_1$ | $R_4$ | $R_5$ [b] | | | | | | | |
| | | | | | | | | $I_t$=0; $I_c$=1; $I_e$=0 | $I_t$=1; $I_c$=0; $I_e$=0 | $I_t$=0; $I_c$=0; $I_e$=1 | $I_t$=0.67; $I_c$=0.33; $I_e$=0 | $I_t$=0; $I_c$=0.67; $I_e$=0.33 | $I_t$=0.67; $I_c$=0; $I_e$=0.33 | $I_t$=0.33; $I_c$=0.33; $I_e$=0.33 | $I_t$=0.33; $I_c$=0; $I_e$=0.67 |
| $t_{r1} = t_c = 40$ | $c_{r1} = c_c = 223$ | $e_{r1}$= 0.9 | 88.2 | 72.5 | 72.5 | 88.2 | 46.4 | 72.5 | 88.2 | 72.5 | 83.0 | 72.5 | 83.0 | 77.0 | 77.7 |
| $t_{r2}$ = 53 | $c_{r2}$ = 211 | $e_{r2}$= 0.68 | 83.1 | 74.4 | 81.1 | 83.1 | 50.2 | 74.4 | 83.1 | 81.1 | 80.2 | 76.6 | 82.5 | 78.8 | 81.8 |
| $t_{r3}$ = 64 | $c_{r3}$ = 205 | $e_{r3}$= 0.56 | 78.8 | 75.4 | 85.9 | 78.8 | 51.0 | 75.4 | 78.8 | 85.9 | 77.7 | 78.8 | 81.1 | 79.2 | 83.5 |
| $t_{r4}$ = 75 | $c_{r4}$ = 201 | $e_{r4}$= 0.48 | 74.5 | 76.0 | 89.0 | 74.5 | 50.4 | 76.0 | 74.5 | 89.0 | 75.0 | 80.3 | 79.3 | 79.0 | 84.2 |
| $t_{r5}$=$t_n$ = 80 | $c_{r5} = c_n$ = 200 | $e_{r5}$= 0.45 | 72.5 | 76.2 | 90.2 | 72.5 | 49.8 | 76.2 | 72.5 | 90.2 | 73.7 | 80.8 | 78.3 | 78.8 | 84.3 |

[a] Estimated based on carbon dioxide emission.

[b] $I_e$ is the importance factor of environmental impact.

Notes: Environmental impact at extreme event ($e_o$) = 0.2 $\times 10^6$ kg.

### 3.4 Summary

Indices of resilience were presented in this study for measuring the effectiveness of the usage of recovery elements based on the priorities determined by stakeholders. The indices were adopted using the 'resilience triangle' concept, which is a widely-used approach to the evaluation of the resilience of bridges for a specific recovery option, and it is commonly expressed in terms of the improvement of performance with time (Bocchini and Frangopol, 2011; Bruneau et al., 2003; Bruneau and Reinhorn, 2007). Future research can focus on expanding the resilience forms to include the effect of redundancy, as a fourth resilience element, in the system to examine its impact on rapidity, robustness and resources (Bruneau et al., 2003; Bruneau and Reinhorn, 2007). For instance, the existence of functional bridges within a region may facilitate the rehabilitation activities on the damaged bridges, which can consequently reduce the cost and shorten the recovery time. Therefore, such forms can provide more efficient and holistic evaluation methods for the various recovery options.

The subsequent chapters focus on fragility analysis of bridges, which can quantify the probability of a given damage state of bridge under a given level of intensity measure (IM). The typical recovery costs can be calculated once the level of damage with a high (threshold) probability is established.

# CHAPTER 4

# FRAGILITY ASSESSMENT METHODOLOGY

## 4.1 Introduction

Fragility describes the probability of exceeding a certain limit state at a given hazard intensity level. As discussed in Chapter 2, the use of analytical fragility functions (i.e. based on structural models) can be expanded to include a wide range of bridge classes and hazard types. They also facilitate the evaluation of different retrofit measures for reducing or preventing damage. The available literature on analytical fragility functions has focused mainly on simply supported bridges. However, the enhancement of the connectivity between deck and substructure results in transfer of forces to the substructure. This requires fragility functions that can provide an accurate evaluation of probability of failure considering the connectivity. Hence, the objective of this chapter is to develop a comprehensive fragility analysis methodology for integral bridges, and bridges with strong connection between super- and sub-structure, subjected to extreme hydrodynamic forces. The developed methodology is considered general and can be used for ay IM combination and proposed strengthening schemes for bridge piers. The magnitude of hydrodynamic force and its distribution over the height of bridge is first discussed. This includes the different parameters (e.g., force coefficient) used in estimating its magnitude. The uncertainties in structural and demand parameters considered in the proposed methodology are presented. The steps involved in the procedure adopted for the proposed methodology are then explained. The methodology is broadly divided into two different analysis types, namely, static and time-history. The main aim of the static analysis is to develop capacity curves at the inundation levels and identify the performance levels. The time-history analysis is utilized to capture

the maximum engineering demand parameter (i.e., pier drifts) and compare it with the damage states defined in the static analysis.

### 4.2 Wave-Induced Hydrodynamic Forces

As discussed previously, the extreme wave-induced forces generated on bridges are mainly classified as: (1) hydrostatic forces; (2) hydrodynamic forces; and (3) impact forces. The magnitude of force responsible for the major damage of structures during extreme wave events is dominated by the hydrodynamic force element (Attary et al., 2016). In addition, most of the previous studies have been devoted to cover the deck unseating failure, which is unlikely to occur in integral bridges. As the wave impacts the bridge, the abutments can be washed away, and hence the demand can be completely transferred to piers. Hence, piers can be subjected to significant damage, which has been shown in field observations and numerical simulations of case study bridges (Maruyama et al., 2012; Salem et al., 2016). With the increase in research efforts on strengthening the deck and substructure connections (Ataei, 2013; Lehrman et al., 2011), these types of failure become more predominant and require fragility models that can provide reliable estimation of the level of damage. Therefore, the drag force component initiated by steady flows and causes the significant lateral displacement of piers is specifically adopted in the analysis presented in this study. The failure of foundation and deck connection is not considered in this study. Future research can include stability-related failures and the other wave-induced forces when more data become available. The hydrodynamic forces are applied in this study in the form of a pressure ($p_w$) distributed over the height of the structural element. However, there is insufficient understanding of the most suitable distribution pattern that can provide accurate

representation of the hydrodynamic forces. For instance, the experimental investigations by Shafiei et al. (2016) and Palermo et al. (2012) showed that the pressure distribution from tsunami-generated waves is similar to the hydrostatic pressure (triangular pattern). However, Chinnarasri et al. (2013) reported that the pressure distribution is uniform until a certain depth where it decreases linearly to zero (trapezoidal pattern). In addition, the recent study by Nasim et al. (2019) examined the pressure distribution on bridge piers using finite volume method. The investigation was conducted on both circular and rectangular pier cross-sections of a U-slab bridge case study. The results showed that the pressure distribution is uniform along the pier height for both cross-sections with slight variation at the bottom and top. It was also reported that the distribution pattern is not affected by the flow velocity. Furthermore, the study by Petrone et al. (2017) on the fragility of building structures reported that the use of different distribution patterns provided similar results. Hence, in this study, the uniform distribution of hydrodynamic load on structures is used. This pattern is adopted by the ASCE 7-16 (ASCE, 2016), and it has been used in recent fragility studies for bridges and other structures subjected to extreme wave forces (Alam et al., 2017; Ataei and Padgett, 2013b; Attary et al., 2016). The magnitude of hydrodynamic force is controlled by the flow velocity, projected (tributary) area of element and the uplift or drag force coefficients that depend on the cross-sectional shape of the structural element (see Figure 4-1). The magnitude of hydrodynamic force is expressed using the following equation (ASCE, 2016):

$$F = 0.5\rho_s C b h u^2 \tag{4-1}$$

In Equation 4-1, $\rho_s$ is the water density (usually taken as 1200 kg/m$^3$); $C$ is the force coefficient; $b$ is the width (or diameter) of structural element; $h$ is the overall inundation height; and $u$ is the flow velocity.

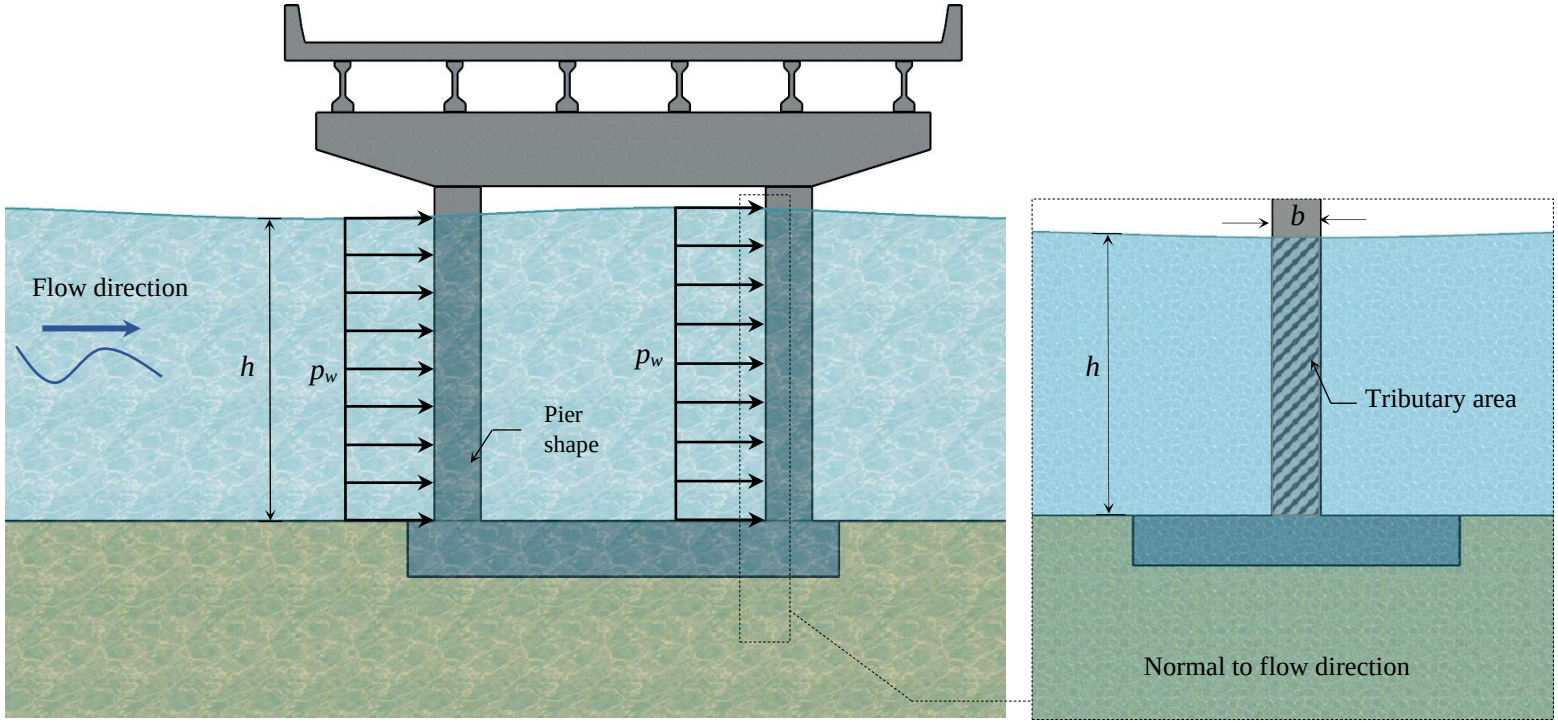


**Figure 4-1.** Illustrative diagram for the distribution of hydrodynamic force pressure on bridge and the main geometrical parameters. (Note: the force coefficients are defined based on the pier shape).

### 4.3 Uncertainty of Input Parameters

#### 4.3.1 Wave Load Parameters

The variation in extreme wave demand needs to be considered in probabilistic models by identifying the inherent aleatory (based on nature) and epistemic (based on knowledge) uncertainties in the realizations of the modeling parameters. Examples of wave hazards aleatory uncertainties include the change in wave height with time and dip angle, while epistemic uncertainties include instrument imperfection (e.g., errors in significant wave height measurement) and sampling variability (Bitner-Gregersen et al., 2014; Thio, et al., 2010). The further statistical characterization of hazard IMs requires numerical models for wave propagation using topographic and bathymetric data for the location of bridge. Numerical simulations have been recently adopted due to the difficulties in obtaining site-specific historical data (Burbidge et al., 2008; Geist and Parsons, 2006). The results of these models are the annual rate of occurrence of the exceedance of selected IMs (e.g., inundation depth) (Attary et al., 2017). However, compared to earthquake hazards, probabilistic methods that incorporate the uncertainties of wave hazards demands are limited (Bradley, 2010; Cornell et al., 2002; Mangalathu et al., 2018; Padgett and DesRoches, 2007). Ataei and Padgett (2012) employed Longuett-Higgins (1983) density function for joint probability to correlate the wave period to the maximum wave height. The probability distribution of maximum wave height and wavelength was taken as a function of significant wave height and wave period, respectively. De Risi et al. (2017) used Bayesian statistical approach to account for the uncertainty in the inundation depth input data. It was reported that the consideration of the uncertainty in the inundation depth enhanced the reliability of the proposed damage assessment method by reducing the residuals between fragility models and

observed data. Recent studies have suggested the use of hydrodynamic force parameters (e.g., force coefficients) to account for the demand uncertainties in the fragility models (Alam et al., 2017; Attary et al., 2016). The variation in force coefficients depends on the shape of structural elements (Kerenyi et al., 2009). The ASCE 7-16 (ASCE, 2016) provided a range of 1.2 to 2 for drag coefficients for different structural element sections. In particular, a value of 1.75 was suggested for round columns, while 2.25 was given for square columns. Figure 4-2 shows the main steps of the fragility functions development methodology and the adopted random variables. In this study, the uncertainties in the computation of IMs was considered by adopting a uniform probability distribution of the drag coefficient of the hydrodynamic force (see Figure 4-2). The variation in water density at the location of bridge is less than 10% (Attary et al., 2016), and hence it was taken as a deterministic value.

### 4.3.2 Material Parameters

The uncertainties in the structural capacity was considered by taking into account the ultimate compressive strength of concrete and yield strength of steel as random variables. A normal probability distribution of the concrete was assumed, while a lognormal distribution was used for the steel yield strength (see Figure 4-2). The concrete elastic and shear moduli are assumed to be a function of concrete compressive strength. The errors due to construction and workmanship were not taken into account as most of bridge components are assumed to be precast. Hence the geometrical parameters of bridge components were taken as deterministic. It should be mentioned that all these assumptions and considerations can be adjusted for other types of structures and fragility capacity models.

| Step | | Illustration |
|---|---|---|
| 1 | Select **velocity ($u_i$)** and **inundation depth ($h_i$)** ranges | 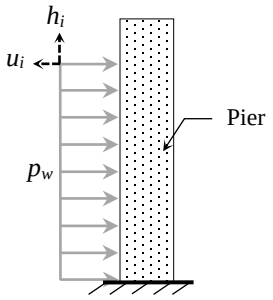 |
| 2 | **Estimate demand** considering the uncertainty in hydrodynamic force coefficients | 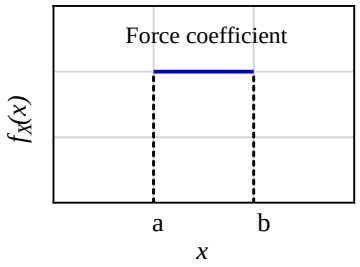 |
| 3 | **Estimate capacity** and generate structural models using random variables of steel and concrete | 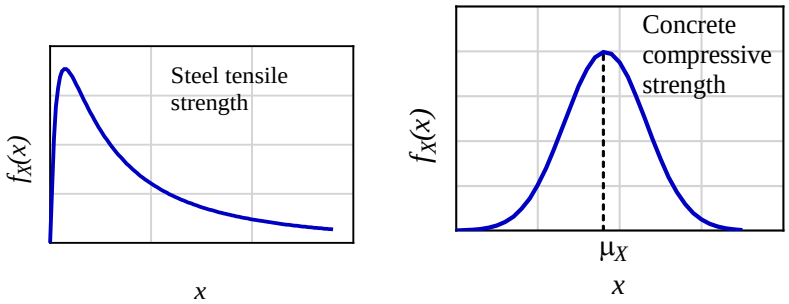 |
| 4 | **Check EDP (drift) exceedance** with damage state (*DS*) and **compute fragility function** | 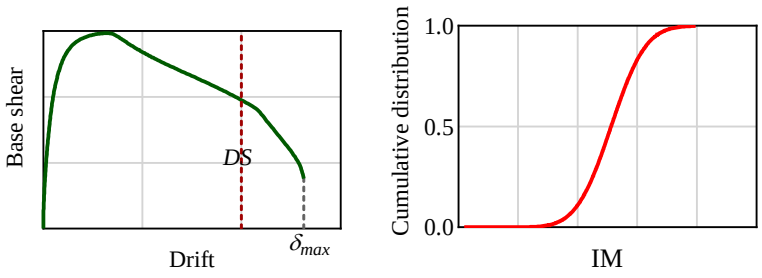 |

**Figure 4-2.** Generic procedures of the proposed methodology for developing fragility functions. Notes: $X$ is the random variable; $x$ is random variable realization (specific value) (Nowak and Collins, 2013); $f_X(x)$ is the probability density function (Nowak and Collins, 2013); $\mu_X$ is the mean of random variable; and [a,b] is the uniform distribution range.

## 4.4 Fragility Functions Derivation Methodology

### 4.4.1 Main Procedures and IM Ranges

The fragility of a structure defines its potential response and the uncertainty in its safety above a specific hazard level (Tekie and Ellingwood, 2003). A fragility model is represented by a function (or curve) that states the probability of reaching or exceeding a certain damage level at a given intensity measure (Jeong and Elnashai, 2007), and it is expressed as $P[DM|\mathrm{IM}=x]$, where $DM$ is the damage measure and $x$ is the demand variable. The proposed methodology for developing fragility functions for bridges subjected to extreme hydrodynamic forces is based on Monte Carlo Simulation (MCS) (Melchers, 1999), and it comprises mainly of two phases, static and time-history analyses. The main steps of the methodology procedure are schematically presented in Figure 4-3. The uncertainties in demand and capacity are considered in the time-history analysis phase. The initial step of the methodology is the generation of inundation depths from 0 to maximum depth ($h_{max}$). The selection of the ranges of inundation depth depends on factors such as the observed inundation marks at the location of bridge in the post-hazard inspection or the estimated largest storm water level. For each inundation depth, a range of velocities, from 0 to maximum velocity ($u_{max}$), is determined. A constant value of Froude number, denoted as $Fr_{limit}$, is used to determine the realistic ranges of velocity, $u_i$ and inundation depth, $h_j$ combinations, where $i=1,2,3,\ldots,i_{max}$ and $j=1,2,3,\ldots,j_{max}$. Based on historical extreme wave records, $Fr_{limit}$ is taken in this study as 2 (Matsutomi and Okamoto, 2010).

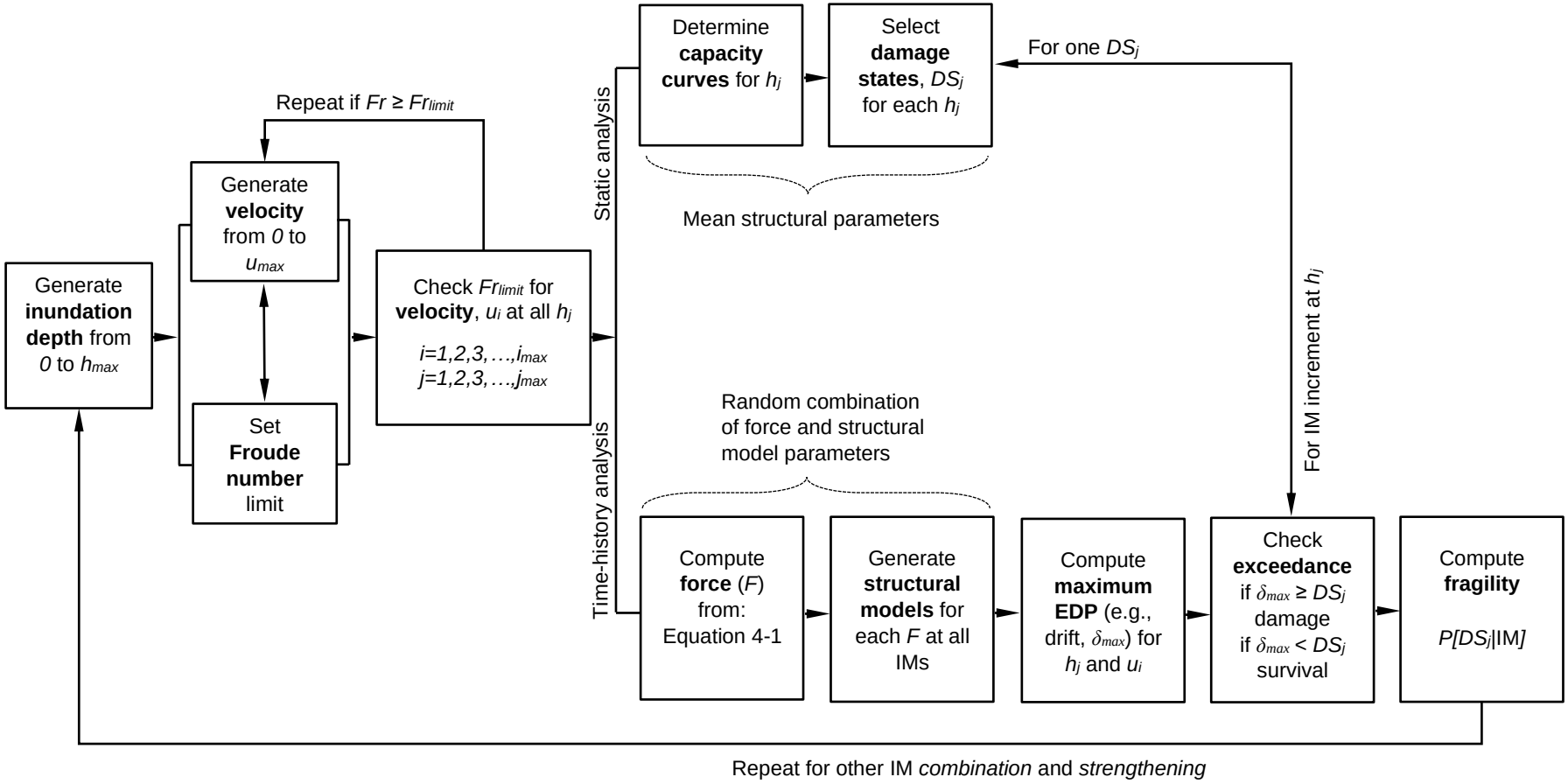


**Figure 4-3.** Integrated framework for developing fragility functions of integral bridges subjected to hydrodynamic forces.

### 4.4.2 Static Analysis

The nonlinear static pushover analysis is adopted to obtain the capacity curves for all inundation depths using the mean structural parameters. In this type of analysis, a static incremental lateral load is applied on the structure until the final failure using displacement-controlled procedure, which is widely adopted in earthquake engineering area (Ghobarah, 2001). It has also recently been used in fragility assessment of structures subjected to extreme waves, e.g., Refs. Attary et al., (2016); and Petrone et al., (2017). The method assumes that the structural response has a single mode with a constant shape throughout its time-history (Krawinkler, 1996). Hence, the structural performance can be evaluated based on the relevant parameters of demand and capacity, such as drift ratios and internal forces. Figures 4-4(a and b) illustrates the pushover analysis adopted in the methodology for three different inundation depths $h_1$, $h_2$ and $h_3$. In theory, the increase in inundation depth (i.e., the distributed load) over the height of a cantilever column results in a decrease in its load carrying capacity ($P$) and stiffness. In pushover analysis, the load carrying capacity is measured in terms of the base shear reaction (see Figure 4-4(a)) of bridge piers. For each inundation, six performance levels and their corresponding damage states ($DS$) are considered (see Figure 4-4(b)). The first three damage states $DS_1$, $DS_2$ and $DS_3$ represent the first crack ($P_{crack}$), yield ($P_{yield}$) and peak ($P_{peak}$) capacities, respectively. The pre-cracking stage in the capacity curve defines the full elastic behavior of column where the ultimate tensile stresses are lower than concrete flexural strength (Nawy, 2000). After the initiation of first crack at $P_{crack}$, the contribution of concrete to the overall stiffness reduces significantly, which results in a drop in flexural rigidity, and hence the slope of the capacity curve reduces (Janoyan et al., 2006). As the lateral load increases beyond the yield capacity ($P_{yield}$), the strains in the steel reinforcement exceed the steel yield strain and the stiffness of

the capacity curve drops further due to the widening of cracks. The remaining three damage states $DS_4$, $DS_5$ and $DS_6$ represent the post-failure performance defined by the drop in peak capacity ($P_{peak}$) at 10%, 20% and 50%, respectively. The consideration of the degradation in capacity is important for identifying the reserve strength (ductility) of structures overloaded by wave-generated forces (Hashemi et al., 2019). Hence, a nonlinear time-history analysis approach is adopted in this methodology to provide a full evaluation of the response through the maximum forces and displacements obtained from the time-varying solution.

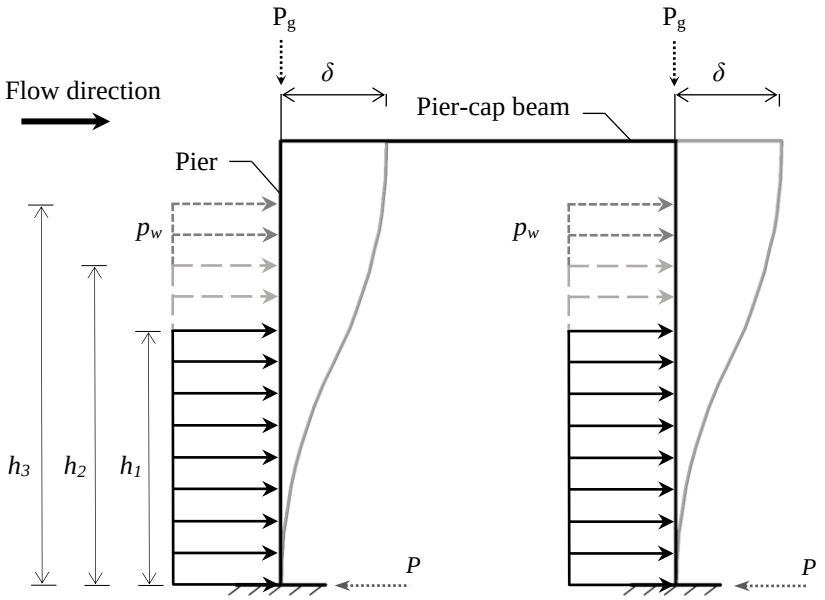


(a)

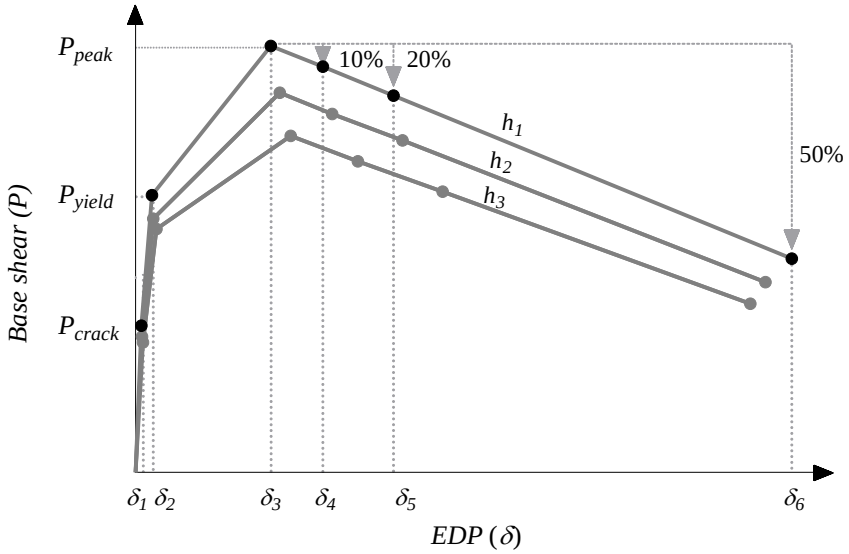


(b)

**Figure 4-4.** Static analysis of bridge under hydrodynamic force: (a) idealized two-dimensional bridge headstock frame under different inundations depths ($h_1$, $h_2$ and $h_3$); and (b) performance curves for different inundation depths and illustration of performance levels for one depth ($h_1$). Notes: $P$ = base shear reaction; $P_g$ = superimposed dead (gravity) load; and $\delta$ = pier drift.

### 4.4.3 Time-History Analysis

A series of time-history models is developed based on the random variables of wave force and structural parameters. However, the direct method for generating random samples for probabilistic models requires a large number of simulations to obtain a reasonable estimation of the damage probability, and the required time to complete one run of non-linear time-history analysis is relatively long. This is computationally impractical considering the hundreds or thousands time-history simulations needed to construct a fragility function. Hence, this study utilizes the Latin Hypercube Sampling (LHS) technique to generate the combinations of random variables (Nowak and Collins, 2013). The basic idea of this

technique is based on the "Latin square" concept, in which for an $n \times n$ matrix that contains $n$ samples, only one sample exists in each row and each column (Sheikholeslami and Razavi, 2017). The probability distribution region for the range of each possible samples of random variable is partitioned into equal intervals (strata), and a representative single sample is randomly selected from each interval (Park et al., 2009). The selected samples for each random variable are randomly combined without replacement. In this combination, each representative sample for each random variable is considered in the analysis only once (Nowak and Collins, 2013). As a result, all possible ranges of the random variables are taken into account in the probabilistic model. Figure 4-5 shows an illustrative example of the LHS method for two variables ($X_1$ and $X_2$) that have normal distribution. As can be seen, the cumulative probability distribution is partitioned into five equal intervals, and one sample is randomly selected from each interval. The five random samples for each variable are randomly combined to form a Latin square (Minasny and McBratney, 2006).

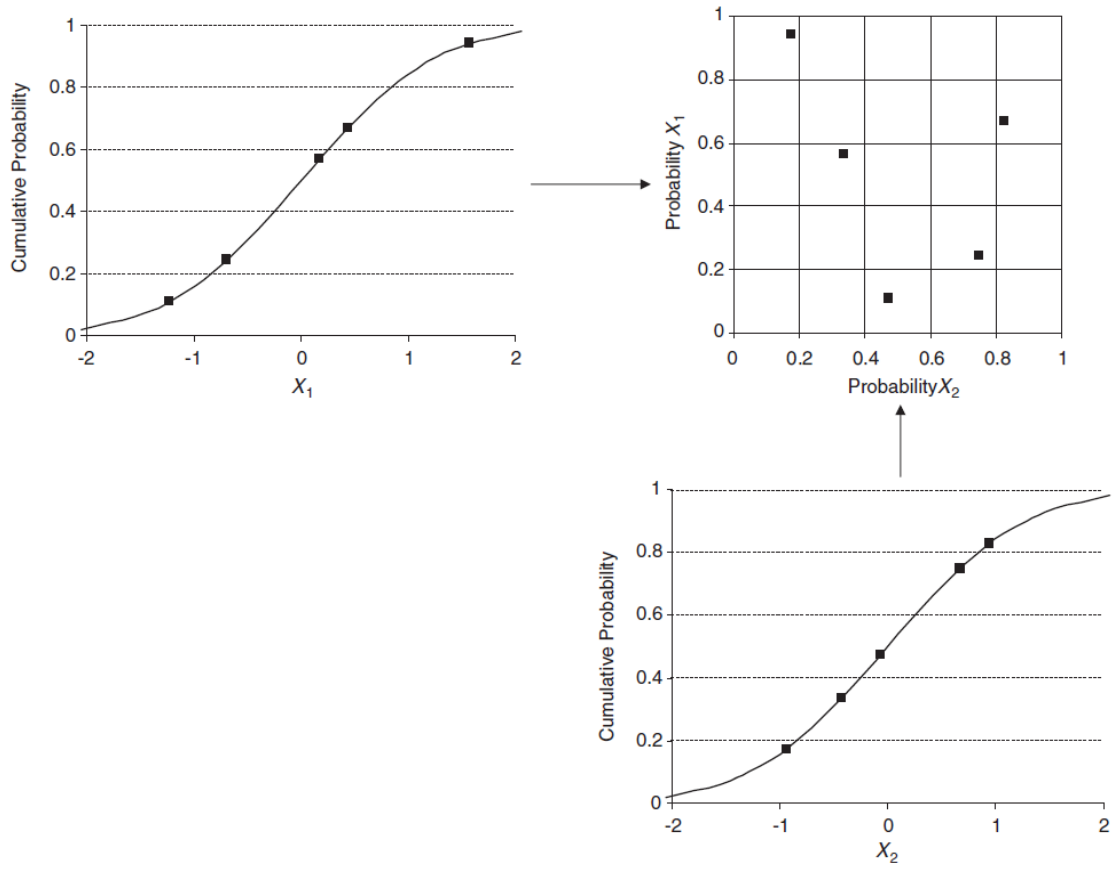


**Figure 4-5.** Example of Latin Hypercube Sampling (LHS) technique using five samples for two variables (Minasny and McBratney, 2006).

The estimation accuracy of the probability of failure can be improved by using variance reduction methods (Baji and Ronagh, 2014). In this study, the Antithetic Variates (AV) technique (Ayyub and Haldar, 1984) is utilized in conjunction with the LHS to reduce the variance of the estimated value of mean by introducing a negative correlation between the different simulation cycles. According to Ayyub and Lai (1991), if $V$ is a random number that has a uniform distribution over the interval [0,1], and it is used in an analysis run to obtain the failure probability $(P_{f_i}^{(1)})$, the random number 1-$V$ can be used in the second simulation run to obtain the failure probability $(P_{f_i}^{(2)})$. The random number 1-$V$ is also

uniformly distributed over the same interval [0,1] (Ayyub and Haldar, 1984). Hence, the failure probability ($P_{f_i}$) of the *i*th cycle and the variance (*Var*) of the mean value of failure probability ($\overline{P}_f$) of *N* cycles of simulation can be written as follows (Ayyub and Lai, 1991):

$$P_{f_i} = \frac{P_{f_i}^{(1)} + P_{f_i}^{(2)}}{2} \tag{4-2}$$

$$Var(\overline{P}_f) = \frac{Var[P_{f_i}^{(1)}] + Var[P_{f_i}^{(2)}] + 2Cov[P_{f_i}^{(1)}, P_{f_i}^{(2)}]}{4N} \tag{4-3}$$

In Equation 4-3, the covariance (*Cov*) of failure probabilities $P_{f_i}^{(1)}$ and $P_{f_i}^{(2)}$ is negative, which results in a reduction of the variance of $P_{f_i}$.

The common engineering demand parameter (EDP) used in structures damaged by lateral inertial forces initiated during earthquakes are the columns or piers drifts. The hydrodynamic force adopted in this analysis is the drag force component that causes significant lateral displacement. Hence, pier drift ($\delta$) can be a reasonable estimate for the global damage of the bridge, and it has been recently adopted for other structures subjected to extreme waves (Park et al., 2012). However, if the elements local failure needs to be considered, detailed structural analysis (e.g., progressive damage) is required to define different performance levels and their EDPs (Attary et al., 2017), which is beyond the scope of this study. Thus, six drifts ($\delta_1$ to $\delta_6$) are obtained for the six damage states discussed above at each depth in the static analysis (see Figure 4-4(b)). The force time-history of the extreme wave was represented by a triangular pattern with an amplitude equal to the hydrodynamic load and a period of 4 seconds. It should be mentioned that this pattern was selected as an example of extreme wave scenario, as it was found suitable for estimating the dynamic response of bridge with acceptable computational time. However, further research is needed if the effect

of the nature of applied forces generated by different wave types on bridge response is specifically examined to provide more accurate estimation of the exact pattern of the force time-histories.

### 4.4.4 Calculation of Cumulative Damage Probability

The typical dynamic response of the bridge under three different hydrodynamic forces ($F_a$, $F_b$ and $F_c$) at a single inundation depth is shown in Figure 4-6(a). A sample base shear-drift response from time-history analysis is shown in Figure 4-6(b). When the hydrodynamic force is relatively low ($F_a < P_{peak}$), the bridge deflects until $\delta_{a,max}$, and it then oscillates back to rest with some residual drift. The increase in force ($F_b > P_{peak}$) increases further the maximum drift ($\delta_{b,max}$), and it is followed by oscillation to rest at larger residual drift than the first case. However, as the hydrodynamic forces become significantly larger than the peak capacity (i.e., $F_c >> P_{peak}$), the bridge shows a complete failure at significantly large drift ($\delta_{c,max}$) without oscillation as in the first two cases. The recorded maximum drift is then checked with the corresponding six damage states ($DS_j$), and the process is repeated until all $h_i$ and $u_i$ combinations are considered. The cumulative probability distribution is computed by averaging the number of cases that exceed the certain damage state by the total number of cases for each IM combination. In addition, a preliminary convergence check was conducted to determine the number of samples needed to obtain sufficiently accurate results (see Figure 4-7). At a single IM, a number of simulations were performed using the random variables combinations with number of samples trials between 4 and 1000, and the mean drift was computed for each trial. The results indicated that the mean drift reaches a degree of stability at relatively large number of samples (higher than 100), while the computational

time significantly increases for number of samples higher than 20. The mean drift obtained from 10 samples was found to show an error of about 0.6% from the 1000 samples, but with significantly lower computational time. Therefore, non-linear time-history simulation process was conducted using 10 samples for all random variables.

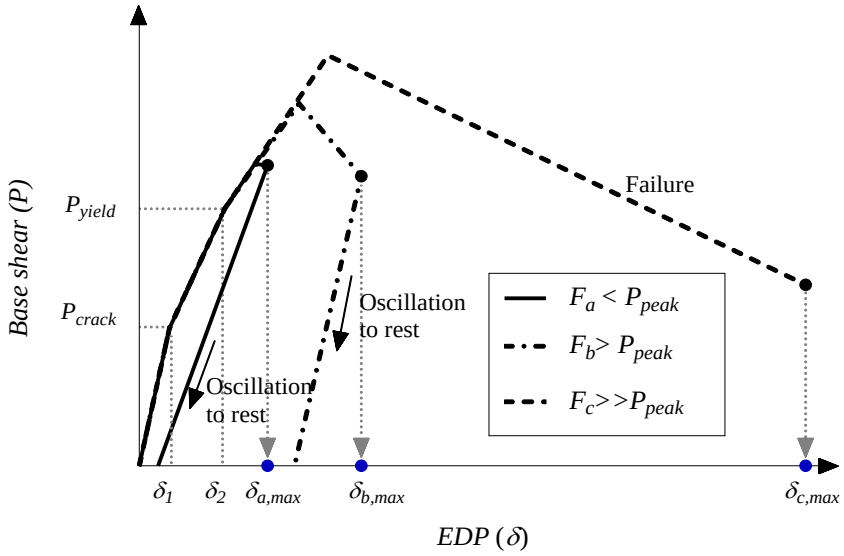


(a)

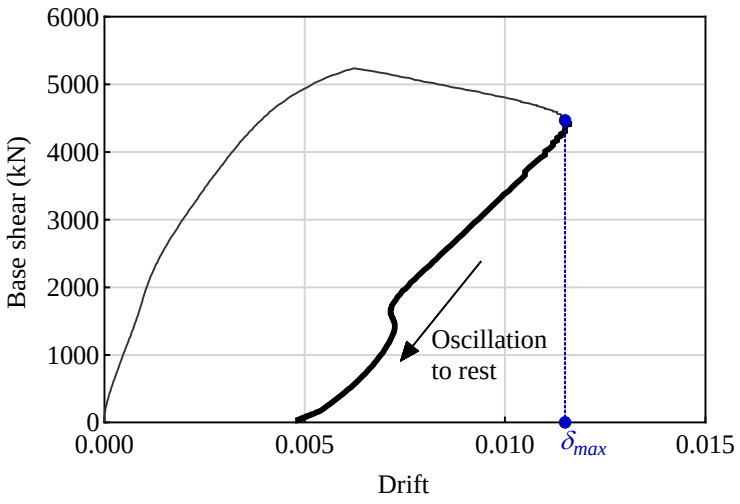


(b)

**Figure 4-6.** Evaluation of the response of bridge using time-history analysis: (a) typical dynamic response of bridge for different applied forces; (b) sample base shear-drift relationship from time-history analysis.

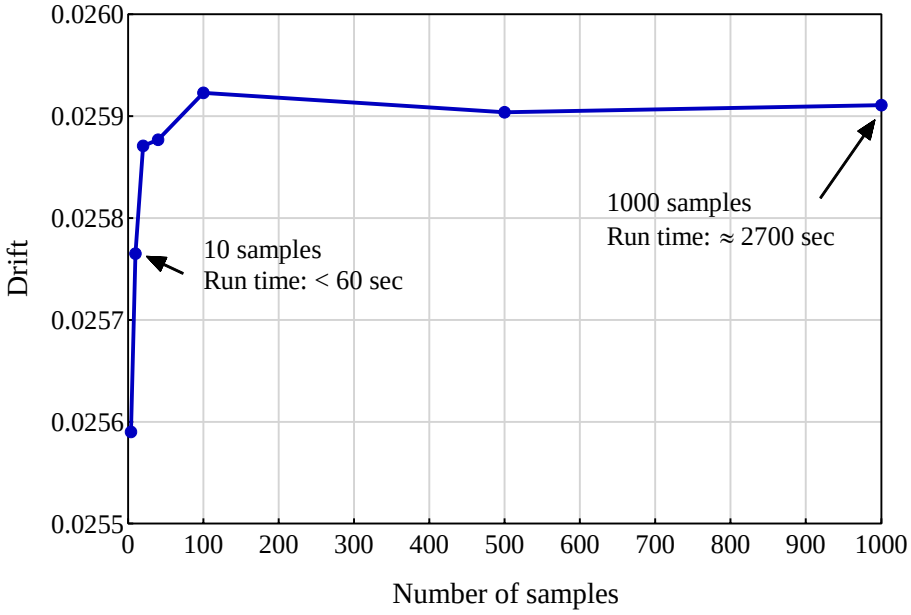


**Figure 4-7.** Convergence check of pier drifts with the increase in sample size.

### 4.4.5 Adopted IMs for Fragility Analyses

Most of the existing fragility studies on extreme wave forces have adopted the inundation depth as the intensity measure (Dias et al., 2009; Suppasri et al., 2011). This is due to the fact that the inundation depth can be easily measured by observing the remaining marks on the structures, and it can be accurately predicted from numerical simulations compared to other wave parameters, e.g., velocity (Charvet et al., 2017). However, the existence of a range of velocities at each inundation depth leads to a significant dispersion of the predicted response. Recent research efforts have attempted to provide IMs that combine both inundation depth and flow velocity, such as momentum flux and moment of momentum flux. The momentum flux ($hu^2$) changes linearly with the magnitude of hydrodynamic force, and hence it can provide a stronger correlation between the structural response and hazard intensity (Park et al., 2013; Park et al., 2014). However, a single value of $hu^2$ can be a product of either large velocity and small depth or small velocity and large depth, which leads to two different responses of bridge (Attary et al., 2016). In addition, different structural response results at different heights of the uniformly distributed load (UDL) as discussed above and shown in Figures 4-4(a and b). The moment of momentum flux ($h^2u^2/2$) has recently been proposed to include the effect of inundation depth by considering the distance between resultant force location ($h/2$) and the pier base (see Figure 4-8) (Alam et al., 2017; Attary et al., 2016; Onai and Tanaka, 2015). To illustrate further the difference in structural response with the use momentum flux and moment of momentum flux IMs, Table 4-1 presents three cases of inundation depth and velocity combinations. The first case represents an inundation depth of 9 m, while the second and third cases represent an inundation depth of 9.46 m. The combinations of velocity and inundation depth in the second and third cases provide the same momentum flux and moment of momentum flux values as the first case, respectively.

This can show the effect of the increase in inundation depth for a single IM. The same value of momentum flux results in the same magnitude of hydrodynamic force (first and second case) as shown in Table 4-1. However, the consideration of the inundation depth leads to different magnitudes of forces for the same value of moment of momentum flux (first and third case). The drift-time histories for a sample cantilever column are shown in Figure 4-9 for the three cases. The increase in inundation depth (from 9 to 9.46 m) for a single IM value results in a large increase in the drift for the momentum flux compared to the moment of momentum flux. The maximum drifts showed an increase of about 8.53% for the same momentum flux values, while it was only about 0.47% for the same moment of momentum flux values (see Table 4-1). This is attributed to the fact that in the case of momentum flux, the decrease in the initial stiffness with the increase in inundation depth results in larger drifts (deflections) for a single magnitude of force. However, the consideration of the inundation depth in the moment of momentum flux provided lower values of the magnitude of forces at the larger inundation depth (third case). Hence, the resulting lower drifts minimized the difference in drifts between the two inundation depths (9 and 9.46 m). The reduction in the difference between the drifts for the same value of moment of momentum flux IM at different inundation depths would lead to a significant reduction in scatter of fragility data. The methodology discussed in this chapter utilizes the above intensity measures, i.e., inundation depth, flow velocity, momentum flux and moment of momentum flux to present the fragility functions, and it examines their efficiency for providing accurate prediction of the fragility of bridge.

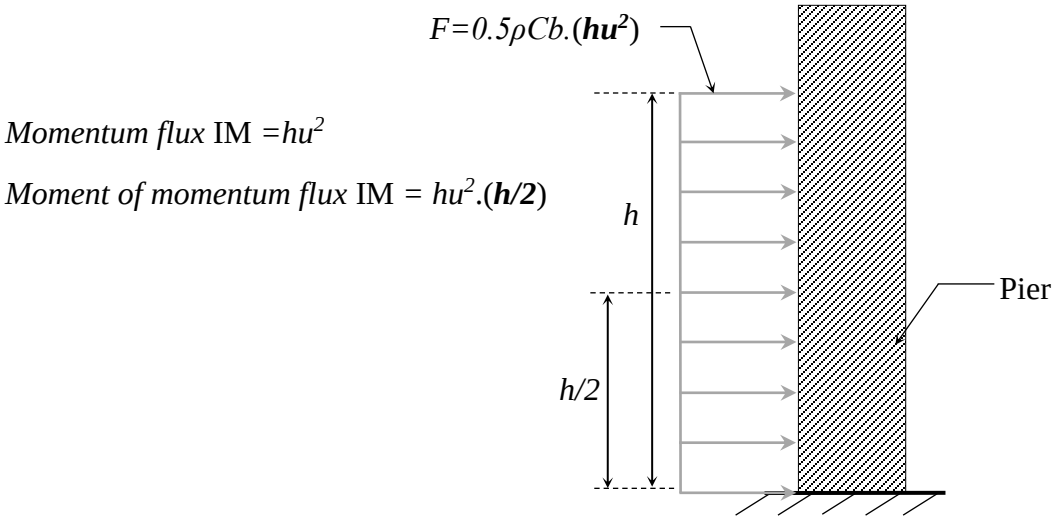


**Figure 4-8.** Illustrative diagram of momentum flux and moment of momentum flux IMs.

**Table 4-1.** Illustration of the momentum flux and moment of momentum flux IMs.

| Case | $h$ (m) | $u$ (m/s) | $Fr$ | $hu^2$ ($m^3/s^2$) | $h^2u^2/2$ ($m^4/s^2$) | $F$ ($\times 10^6$ N) | Maximum drift | % increase in drift in relation to Case 1 |
|---|---|---|---|---|---|---|---|---|
| 1 | 9 | 12 | 1.28 | **1296** | **5832** | 2.37 | 0.0012633 | - |
| 2 | 9.46 | 11.7 | 1.22 | **1296** | 6130.08 | 2.37 | 0.001371 | 8.53 |
| 3 | 9.46 | 11.42 | 1.19 | 1232.98 | **5832** | 2.15 | 0.0012693 | 0.47 |

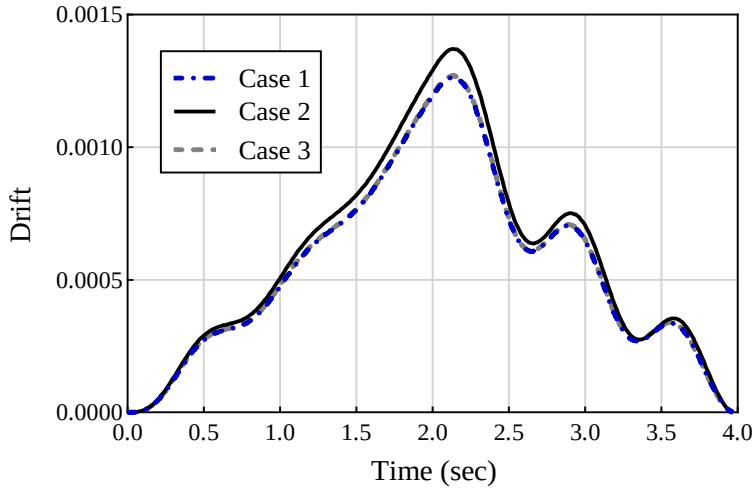


**Figure 4-9.** Drift-time histories for a pier based on three cases of IMs and forces.

## 4.5 Summary

This chapter explained the fragility functions development methodology for bridges subjected to extreme wave hazards. The methodology comprises mainly of static and time-history history analysis phases. The uncertainties associated with concrete, steel reinforcement and hydrodynamic forces are considered in the analysis. The non-linear static pushover method is adopted to determine the capacity curves of bridges at different inundation levels. Six performance levels and their corresponding damage states are adopted at each inundation depth. The damage states represent the behavior of bridge at both pre- and post-peak stages. In the time-history analysis, the bridge is subjected to a sinusoidal load, and the maximum drift is recorded and compared with the damage states. The fragility of bridge is constructed using the average number of cases that exceed the damage states. The use of different intensity measures combinations is considered to examine their

efficiency in the proposed methodology for providing accurate estimation of the damage of bridge.

# CHAPTER 5

# STRUCTURAL ANALYSIS AND NUMERICAL MODEL VALIDATION OF A CASE STUDY BRIDGE

## 5.1 Introduction

In this chapter, a concrete girder bridge is used as a case study to demonstrate the procedures of the fragility analysis methodology discussed in Chapter 4 and provide more details on the proposed framework. Some assumptions were made on the bridge properties for this study, such as the connection between super- and sub-structure and pier details. The superstructure is assumed to have strong connections to the headstock to transfer the demands completely to the substructure. The bridge was modelled using the Open System for Earthquake Engineering Simulation (*OpenSees*). The superstructure was represented by a spine that is modelled using elastic elements, in which the section properties of the composite deck and girders are defined. Rigid links were used to link the pier to pier-cap beam, and to link the superstructure spine to the pier-cap beam at each headstock. Circular pier model was selected from the available literature to validate the modelling procedures and assumptions. The piers were modelled using displacement-based beam-column elements with fiber section. The cyclic load envelopes in the push region were compared with the pushover curves. The pier models were then converted to full scale and added in the bridge model to conduct the static and time-history analysis. The response of bridge system with piers strengthened using FRP jackets was examined. The static and time-history analysis results showed that the strengthening of bridge piers with FRP jackets enhances the bridge ductility and capacity significantly.

## 5.2 Case Study Bridge Description

A three-span concrete girder bridge over Tenthill Creek in Queensland, Australia, is selected as a case study in this study to illustrate the methodology discussed above for developing fragility functions and provide further information on the main aspects of the proposed approach. Figure 5-1 shows the elevation views of the evaluated bridge and pier details. The bridge was selected because it is located in a region that has experienced significant floods and cyclones in recent years (Wahalathantri et al., 2015). It has also been adopted as a case study for different retrofitting schemes to overcome the reduction in strength due to deterioration (Setunge et al., 2002). The bridge was constructed in 1970s, and it has a total length and width of 82.2 and 8.6 m, respectively (QDMR, 2003; Nezamian and Setunge, 2007). The superstructure has twelve pre-cast prestressed concrete girder beams that are 27.4 m long and spaced at 2.6 m center-to-center with a concrete deck on top as shown in Figures 5-1(a and b). The superstructure is supported by two abutments and two headstocks. Each headstock consists of two piers, each has a rectangular cross-section with a depth and width of 1.524 and 0.7 m, respectively. However, the geometry of piers and pier-cap beams is modified in this study in order to validate the modelling procedures and assumptions of piers based on available data in the literature as discussed in the following sections. Hence, circular piers with a height of 9.46 m and a diameter of 1.52 m are considered (see Figures 5-1(b and c)). The modified pier has a longitudinal reinforcement of 14 bars with 65 mm diameter, and the transverse reinforcement consists of gage wire hoops with a diameter of 18 mm and spacing of 445 mm center-to-center. The modified pier-cap has a rectangular cross-section with a depth and width of 1.68 and 2.05 m, respectively. The bridge superstructure is assumed to have a strong connection to the substructure. This can be in the form of high-strength dowel bars, headed stud anchorages, retainer cables or shear keys that

can completely prevent the vertical and horizontal movements due to uplift and drag hydrodynamic forces. Such measures have been addressed in the recent studies for retrofitting bridges subjected to extreme waves (Ataei, 2013; Lehrman et al., 2011). In addition, it is assumed that the piers footings are supported by multiple piles that provide larger lateral strength than pier columns. Consequently, large demands are expected to be transferred to piers leading to extensive damage, e.g., flexural failure due to significant lateral displacements.

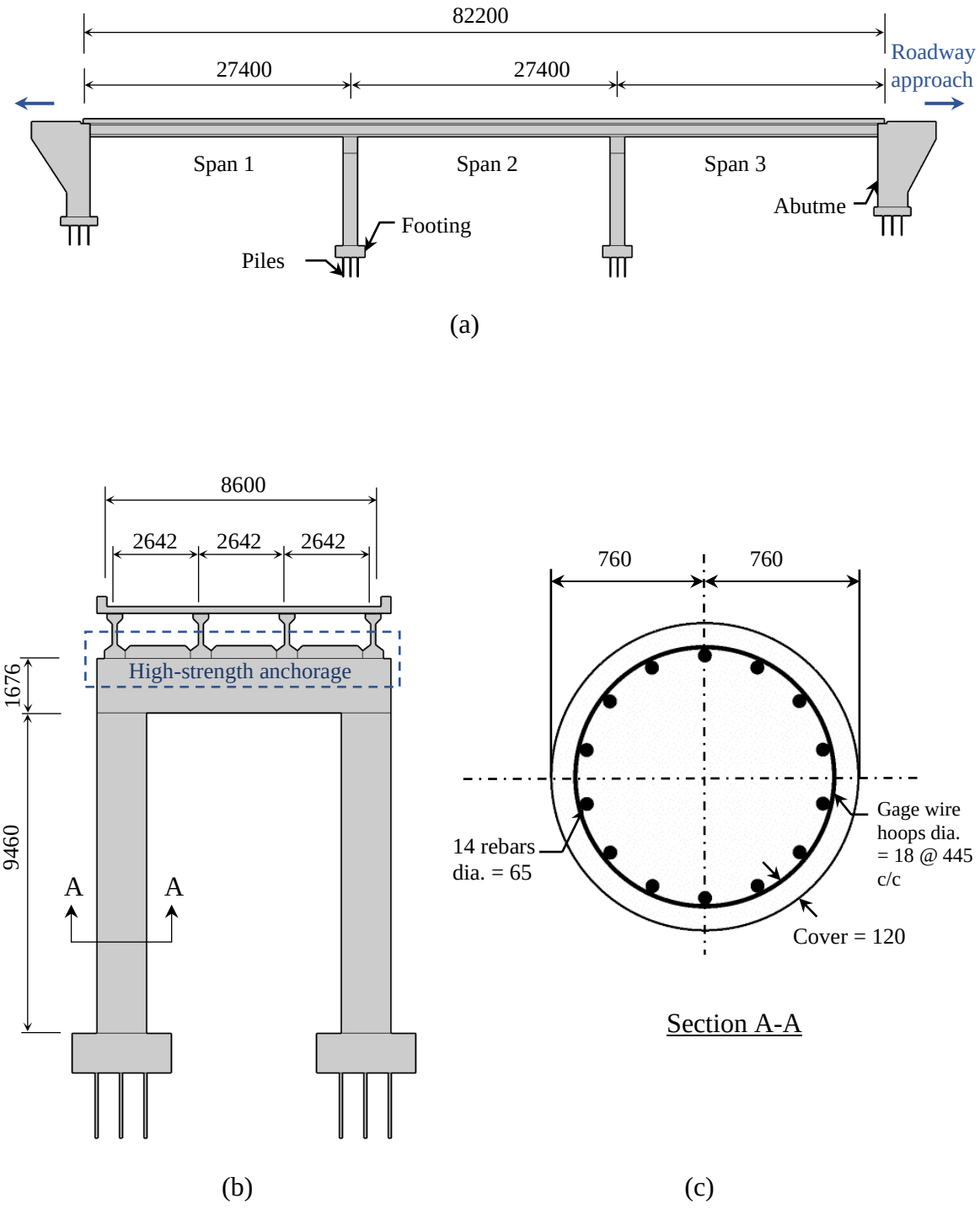


**Figure 5-1.** Application example bridge: (a) elevation (side) view; (b) headstock elevation; and (c) pier details. All dimensions are in mm.

## 5.3 Numerical Modelling

### 5.3.1 The Use of *OpenSees* Platform for Analysis

This study focusses on the performance of a bridge that has a strong connectivity between deck and substructure. Hence, a full-scale model needs to be developed for the bridge to analyze the global response. Typical finite element platforms that adopt solid elements require large computational time for the hundreds or thousands of simulations required to construct a fragility curve. Hence, the Open System for Earthquake Engineering Simulation (*OpenSees*) (McKenna et al., 2013) is considered the most suitable software for modelling the case study bridge. This open source platform is widely used in earthquake engineering area for fragility analyses of full-scale structures. This is because it uses cooperating modules to construct structural models, and it allows scripted automated routine operations for different structural and demand parameters required for the development of fragility functions (Scott et al., 2008). The specification of model properties and analyses are usually conducted using the fully programmable Tool Command Language (Tcl). The bridge components are modelled using the one-dimensional line elements that can have three-dimensional behavior, and they can be used in the three-dimensional domain (Priestley et al., 1996). The analysis of the nonlinear response of line elements is subdivided into two main types: (a) concentrated plasticity and (b) distributed plasticity. In the concentrated plasticity approach, the nonlinear behavior is represented by rotational springs that are located at the ends of linear elastic member, while in the distributed plasticity approach the plastic hinges are allowed to form at any position along the member length (Scott and Fenves, 2006). Two main types of beam-column elements are adopted for the distributed plasticity models: (a) displacement-based elements and (b) force-based elements. The

displacement-based beam-column elements are based on the common procedures of finite element method, in which the nodal displacements are used to define an approximated displacement field of the element (Scott and Fenves, 2006). In the force-based elements, the equilibrium in the nonlinear response range of material is achieved by interpolating the section basic forces (Spacone et al., 1996). In the displacement-based elements, the representation of deformation distribution in the plastic hinge area requires several elements (refined mesh) along the length of structural member (Scott et al., 2004). In contrast, the force-based elements require only one element to estimate the nonlinear response of member, and hence the number of degrees of freedom can be significantly reduced (Neuenhofer and Filippou, 1997). The section of the member is discretized into filaments or layers, from which the moment-curvature behavior is estimated at specific locations that are known as "integration points" (Kashani et al., 2016). The layer discretization is suitable when the section bending is only in one direction, while the filament discretization is used when the direction of load changes and in members that have arbitrary geometry (Priestley et al., 1996). Each layer or filament is considered as a uniaxial member with specified uniaxial constitutive properties (Sedgh et al., 2015). The constitutive laws of the fiber section uniaxial materials can only capture the bending and axial behavior, and the behavior of shear and torsion can be included by aggregating their force-deformation relationships to the previously defined section at the specific degree of freedom (Cardone and Flora, 2016; Rajeev and Tesfamariam, 2012).

### 5.3.2 Modelling of Superstructure Components

Figure 5-2 shows a representative model of the case study bridge. The superstructure components, which consist mainly of deck and girders, remain elastic under wave loading. Hence, the superstructure was modelled as a spine with linear elastic beam-column elements located at the section center of gravity along the bridge length. Table 5-1 presents the main section properties (uncracked) used to define the elastic beam-column elements. The lateral response of bridge is not affected by the stiffness of the superstructure. This is because the stiffness of the composite section of deck and girders is significantly larger than the other bridge components, and it typically acts like a rigid link (Nielson, 2005). The pier-cap beam acts monolithically with the superstructure due to the strong connection between deck and headstock, and hence it was modelled in this study using elastic beam-column elements located at its center of gravity (Kaviani et al., 2012). Rigid links were used to connect the pier column to the pier-cap beams (Nielson, 2005). In simply supported bridges, or bridges with limited connectivity between the super- and sub-structure, bearings are usually modelled to link the superstructure to the pier-cap beam (Siqueira et al., 2014; Tavares et al., 2012). In this study, transverse and vertical rigid links at pier headstocks are used to represent the strong deck connection and distribute the demands to the rest of structure (see Figure 5-2). To provide a sufficient representation of the mass, which is mainly contributed by the superstructure, four elements were used for each span (CALTRANS, 2013; Imbsen, 2007), and the mass was applied in the form of lumped translational masses at each node. The rotational masses are not included in the model as the bridge has two-column headstocks, and the effect of rotational inertia about the longitudinal axis is not significant as in the single-column headstocks (Priestley et al., 1996).

**Table 5-1.** Section properties for elastic bridge elements.

| Component | $I_z$[a] ($m^4$) | $I_y$[a] ($m^4$) | Area ($m^2$) |
|---|---|---|---|
| Superstructure [b] | 1.68 | 43.7 | 6.207 |
| Pier-cap beam | 0.804 | 1.203 | 3.436 |
| Rigid links for piers | 0.265 | 0.265 | 1.827 |

[a] Second moment of area about local *z*- and *y*-axes.

[b] Composite deck and girders.

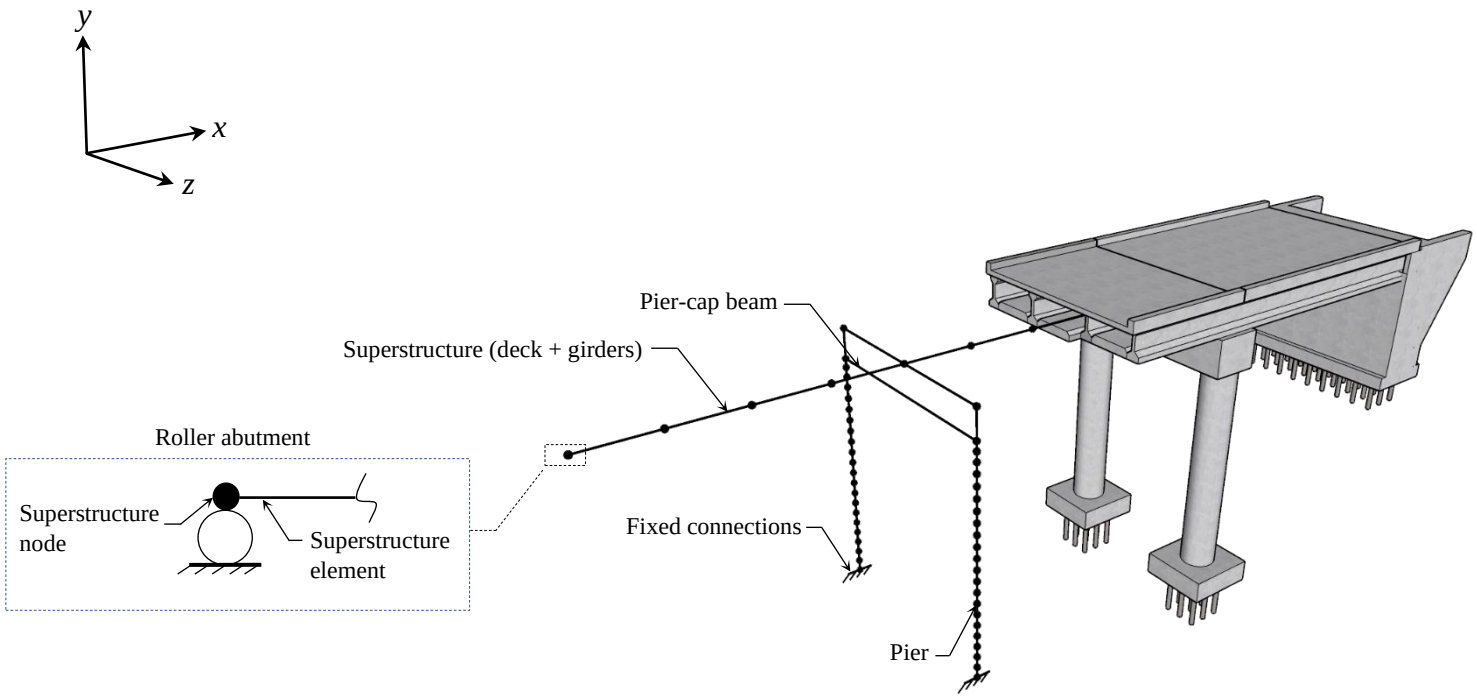


**Figure 5-2.** Numerical model of case study bridge.

### 5.3.3 Modelling of Substructure Components

Several abutment models are available in the literature to provide realistic response in the longitudinal and lateral directions of bridge (Mangalathu et al., 2017). As discussed, this study considers the case where the demand from the drag hydrodynamic forces are completely transferred to the piers, and abutment components (i.e., shear keys and wing walls) do not provide strong restraints to the large lateral displacements. Hence, roller abutment model is adopted in this study, which is mainly based on a single constraint in the vertical (*y*-axis) direction, as shown in Figure 5-2. This model provides a lower-bound estimation of the transverse response of the bridge, and its failure is mainly controlled by the formation of plastic hinges in the piers (Aviram et al., 2008). A damping coefficient of 0.05 was used for the bridge (Xu and Cai, 2015, 2017). Figures 5-3 shows the arrangement of elements and nodes of pier model (Figure 5-3(a)) and fiber section discretization (Figure 5-3(b)). As discussed in Section 5.3.1, the piers are modelled using fiber-section non-linear displacement-based beam-column elements, which allow the spread of inelasticity along the element (distributed plasticity model) (Spacone et al., 1992; Spacone et al., 1991). The mechanical properties of the materials adopted for piers model are summarized in Table 5-2. Figures 5-4 and 5-5 show the stress-strain relationships of concrete and steel. The analytical model proposed by Braga et al. (2006) was used to represent the uniaxial constitutive laws of concrete (*ConfinedConcrete01* in *OpenSees* library). The model was adopted because it allows the input of the section and confinement parameters, thus making it appropriate for calibration and optimization of the confinement reinforcement. The tensile stress-strain data for transverse reinforcement is not available, and hence an elastic-perfectly plastic behavior with zero hardening ratio was assumed. The model does not include any failure mechanism of the confined concrete, and the failure strain was estimated using the

model proposed by Scott et al. (1982) based on the rupture of first hoop. The Giuffré-Menegotto-Pinto (GMP) (Menegotto and Pinto, 1973) model (*Steel02* in *OpenSees* library) is adopted for the longitudinal steel reinforcement to describe the change in material behavior between the initial elastic and the strain hardening post-yield (plastic) phase. The elastic modulus of longitudinal steel was taken as 200 GPa. The parameters that control the transition from elastic to strain hardening stage are defined as follows: $R_o$ = 20, $cR_1$ = 0.925, $cR_2$ = 0.15 (Filippou et al., 1983; Lu and Panagiotou, 2013). A strain hardening ratio ($b_{sh}$) of 0.01 is considered a reasonable estimation for steel bars, as there is no data available on the ultimate strength. The bond-slip between the concrete and reinforcing bars and the effects of strain penetration in the pier base are not taken into account in this study. Fixed connections are defined at the pier base to represent the strong piles foundation.

**Table 5-2.** Mechanical properties of materials used for pier model.

| Material | Ultimate strength (MPa) | Elastic modulus (GPa) | Yield strength (MPa) | Ultimate strain |
|---|---|---|---|---|
| Compressive | | | | |
| Unconfined concrete | 31.03 | 28.8 | N/A[a] | 0.017 |
| Confined concrete | 32.2 | 28.8 | N/A[a] | 0.03 |
| Tensile | | | | |
| Longitudinal Steel | N/A[b] | 200.0 | 358.0 | N/A[b] |
| FRP | 532.0 | 17.755 | N/A[a] | 0.03 |

[a] Not applicable

[b] No specific ultimate strength and strain can be given as Giuffré-Menegotto-Pinto Model (Menegotto and Pinto, 1973) (*Steel 02* in *OpenSees* library) was used for steel.

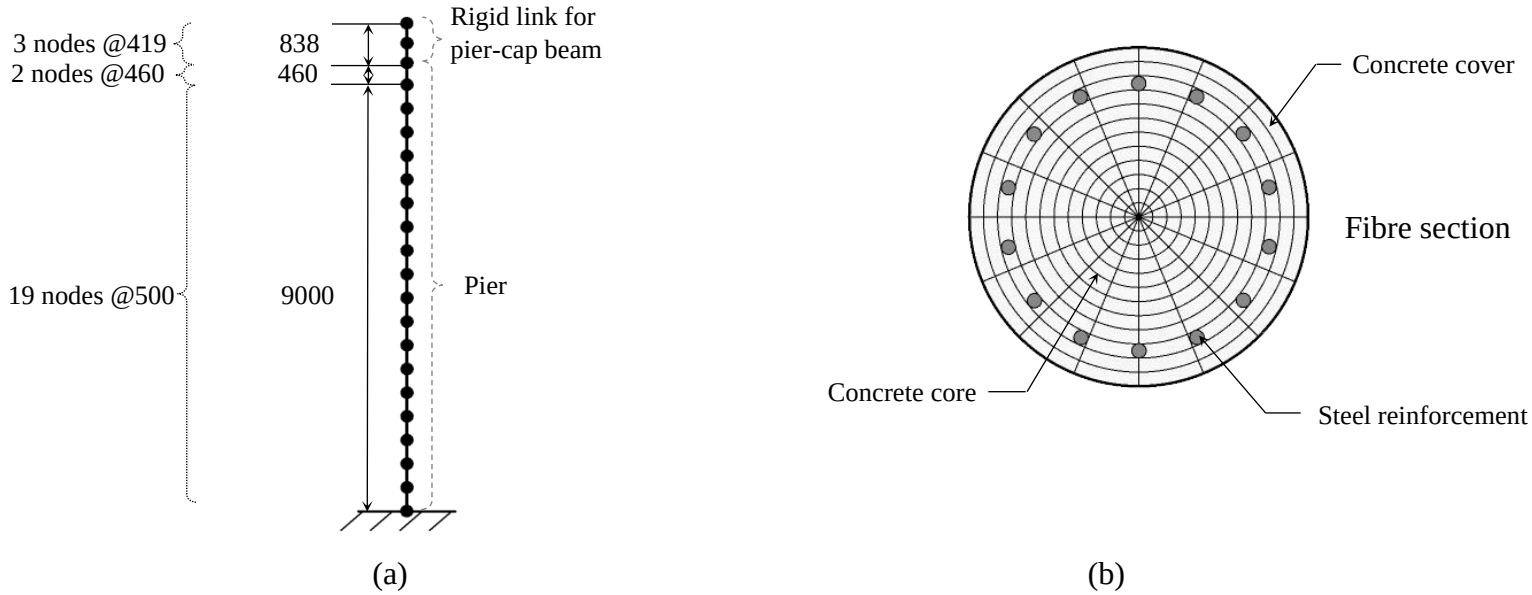


**Figure 5-3.** Numerical model of case study bridge: (a) pier model details; and (b) fibre discretization of circular cross-section of pier. All dimensions are in mm.

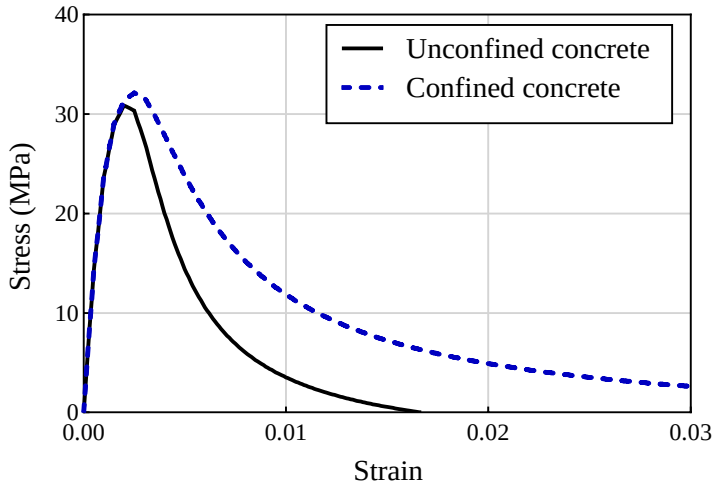


**Figure 5-4.** Stress-strain relationship of concrete obtained using Braga et al. (2006) model.

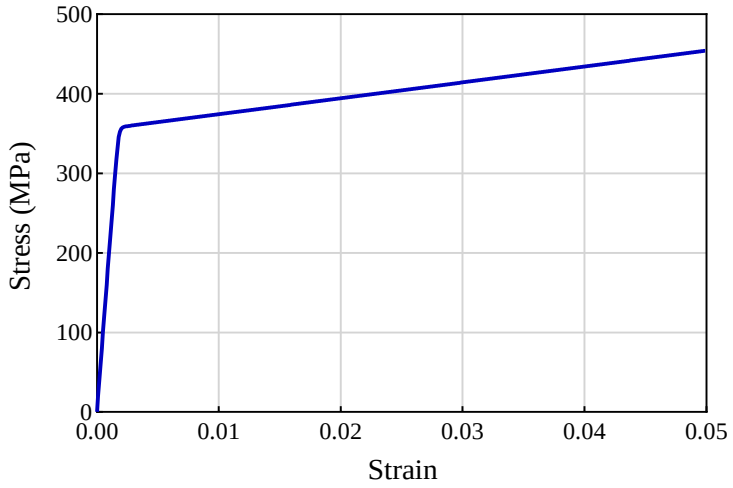


**Figure 5-5.** Stress-strain relationship of longitudinal steel reinforcement obtained using Giuffré-Menegotto-Pinto (GMP) (Menegotto and Pinto, 1973) model.

### 5.3.4 Pier Model Validation

To evaluate the accuracy of piers model and validate the adopted approach and failure criterion, two pier specimens, initial (un-strengthened) and confined with FRP jackets, were selected from the available literature and modelled using the procedures discussed above.

Saadatmanesh et al. (1997) tested four one-fifth scale pier specimens of a prototype bridge. The study examined the performance of piers retrofitted with FRP jackets and subjected to lateral reverse cyclic loading. In this study, the circular specimens, C-2 (initial) and C-2/R (FRP-confined) were considered in the verification model. Figure 5-6 shows the test specimen details. The specimens had a total height of 2.4 m. The height between the point of lateral load and the top of footing was 1.892 m. The total diameter of the pier was 305 mm, and it had concrete cover of 24 mm. The longitudinal reinforcement of piers consisted of 14 bars with 13 mm diameter. This study was selected because it addressed specifically piers that have limited ductility due to factors such as inadequate transverse reinforcement. Gage wires with a diameter of 3.5 mm and spacing of 89 mm were used. The specimens had a concrete cylindrical strength of 36.5 MPa, and the yield strength of the longitudinal and transverse steel reinforcement was 358 and 301 MPa, respectively. The FRP jackets had tensile strength and elastic modulus of 532 MPa and 17.755 GPa, respectively. An axial load of 445 kN was applied on piers top to represent the superimposed dead (gravity) load. The specimen failure at the end of test is shown in Figure 5-7. More recently, D'Amato et al. (2012) conducted an extensive numerical verification of columns subjected to reverse cyclic loading, including the pier specimens C-2 and C-2/R tested by Saadatmanesh et al. (1997). It was reported that the load-deformation results of the modelled piers compared well with Saadatmanesh et al. (1997). However, the piers model showed slightly larger stiffness than the experiment, which is attributed to factors such as the effect of bond-slip between reinforcement bars and concrete. The cyclic load-deformation relationships reported by D'Amato et al. (2012) are taken further in the analysis presented in this study as similar model assumptions and simplifications are adopted, which can facilitate the comparison of results and validation of the model. A monotonic (pushover) analysis was conducted in this

study to obtain the load-deformation relationships of initial and FRP-confined piers. In Figure 5-8, the pushover curves obtained for both pier specimens are compared with the strength envelope (or backbone curve) in the push region. It should be mentioned that the comparison between the strength envelopes and pushover curves is limited to the models that do not consider the $P$-$\Delta$ effects. The piers modelled with $P$-$\Delta$ effects are included in Figure 5-8, as they are considered in the subsequent analysis of the bridge to provide more reasonable estimate of the effective capacity at large lateral deformations. The strength envelope of cyclic response defines the monotonic response and the boundaries of the load-deformation relationship (Ibarra and Krawinkler, 2005). The initial and hardening stiffness branches of the strength envelope are considered in the comparison as they theoretically match with the pushover curve. Figures 5-8(a and b) show that the pushover analysis results show good agreement with the strength envelops of both initial and FRP confined piers. The initial and hardening stiffness matched well with the strength envelopes. The discrepancies between the curves are expected after the yielding stage. Table 5-3 presents a summary of the results obtained from the piers model verification. The results are compared at the first crack and yielding loads and their corresponding displacements. The comparison shows that the adopted models can predict the response of piers with satisfactory accuracy, which confirms that the adopted modelling approach and procedures were acceptable.

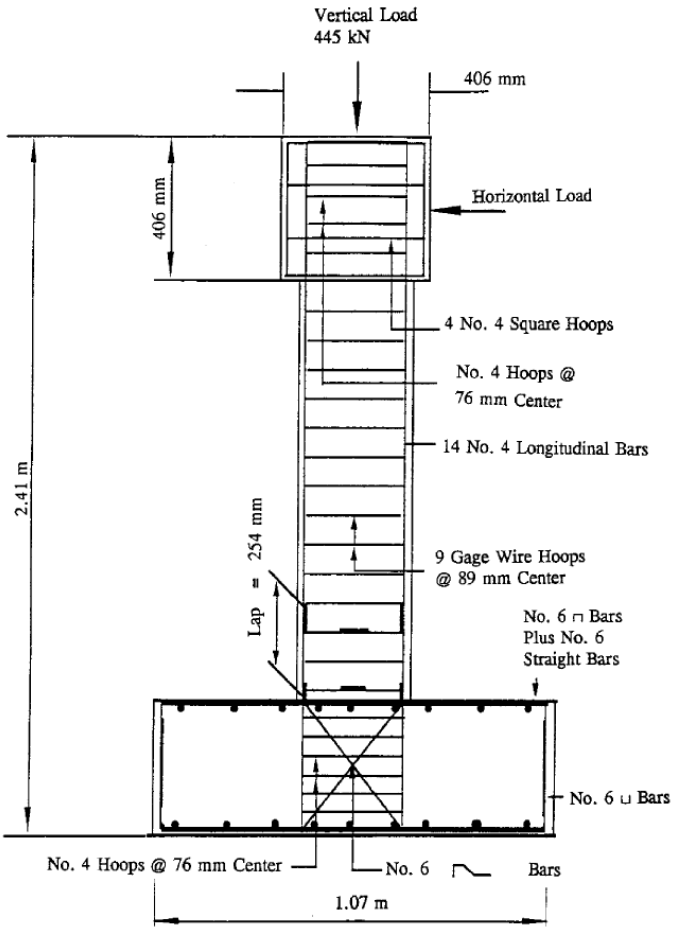


**Figure 5-6.** Test pier details used in the validation model (Saadatmanesh et al., 1997).

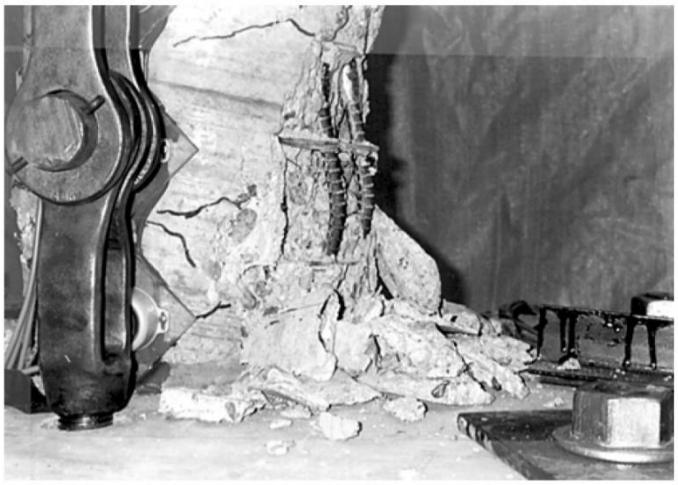

**Figure 5-7.** Failure of pier specimen C-2 (Saadatmanesh et al., 1997).

**Table 5-3.** Summary of numerical simulations verification results: pushover analysis (without *P*-Δ effects) in comparison with cyclic load envelopes in push region.

| Case | $P_{cr}$ (kN) | $\Delta_{cr}$ (mm) | $P_y$ (kN) | $\Delta_y$ (mm) |
|---|---|---|---|---|
| Unconfined (C-2) | | | | |
| Strength envelope from D'Amato et al. (D'Amato et al., 2012) | 20.27 | 3.35 | 35.36 | 7.4 |
| Pushover (linear) | 20.14 | 3.25 | 35.29 | 8.1 |
| Pushover/ envelope | 0.99 | 0.97 | 0.99 | 1.09 |
| FRP-confined (C-2/R) | | | | |
| Strength envelope from D'Amato et al. (D'Amato et al., 2012) | 25.73 | 4.6 | 49.53 | 12.8 |
| Pushover (linear) | 25.24 | 4.65 | 49.04 | 13.95 |
| Pushover/ envelope | 0.98 | 1.01 | 0.95 | 1.09 |

Note: $P_{cr}$ = cracking load; $\Delta_{cr}$ = lateral displacement at first crack; $P_y$ = yielding load; and $\Delta_y$ = lateral displacement at yielding.

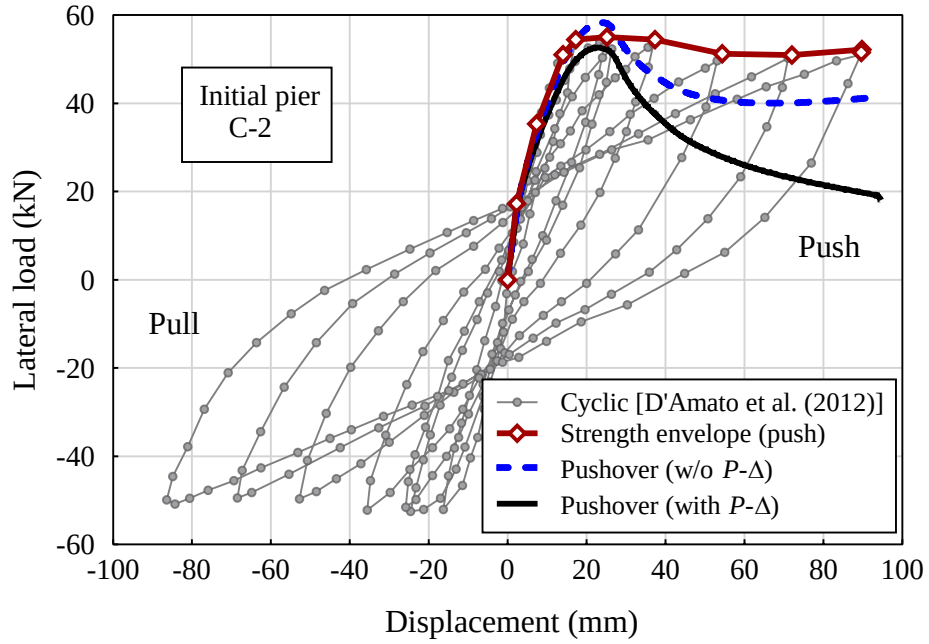


(a)

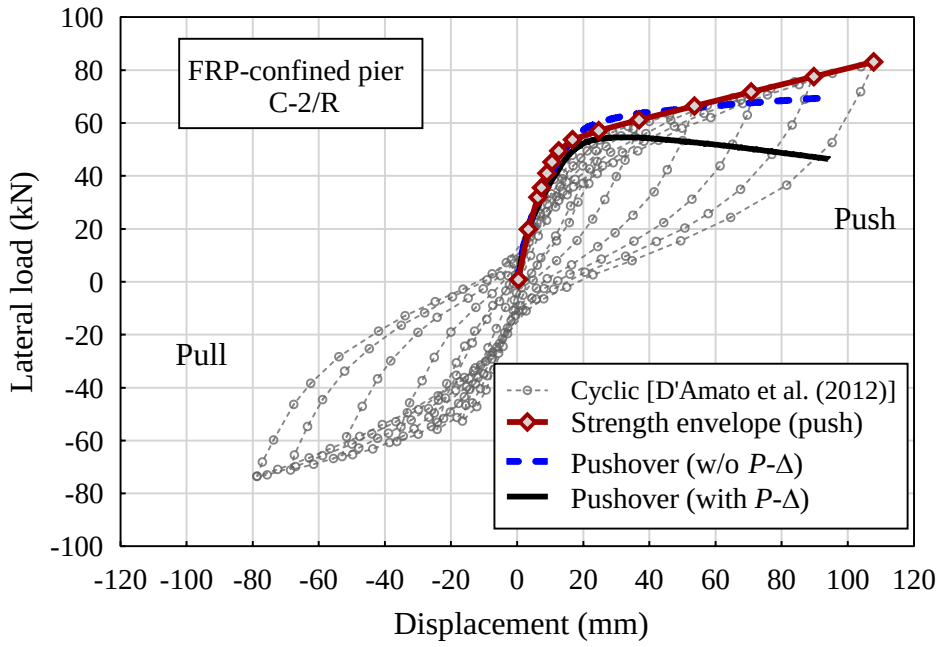


(b)

**Figure 5-8.** Comparison of the cyclic load strength envelope (push region) developed by D'Amato et al. (2012) of piers tested by Saadatmanesh et al. (1997) and static pushover curves: (a) initial pier; and (b) pier strengthened with FRP jackets.

## 5.4 Structural Response Analysis

### 5.4.1 Full-Scale Initial Bridge

The one-fifth scale pier models discussed in the previous section are converted to full scale bridge piers using the similitude law (Harris and Sabnis, 1999). Table 5-4 summarizes the main properties of pier specimens (C-2 and C-2/R) and bridge piers. The total axial load applied on piers was taken in this study as the superimposed dead load for the bridge. Figure 5-9 shows the pushover analysis results in terms of base shear normalized by the superimposed dead load and drift ratio for the pier specimens and bridge system. The results are presented for two loading cases, point load at top and UDL at a height of 10.298 m. In the case of UDL, the location of resultant force is closer to the pier base, which leads to a larger initial stiffness than the case of point load at top. In addition, the existence of rigid elements above the pier in the bridge provides constraints against rotation (double-curvature bending). This leads to a higher stiffness in comparison with the single pier specimen, which acts as a cantilever with a single-curvature bending.

**Table 5-4.** Main geometry details of pier models.

| Model | $L$ (mm) | $A_g$ (mm$^2$) | $c$ (mm) | Longitudinal steel | | Transverse steel | | FRP jacket | | | $P_g$ (kN) |
|---|---|---|---|---|---|---|---|---|---|---|---|
| | | | | $A_{sl}$ (mm$^2$) | $n$ | $A_{st}$ (mm$^2$) | $s$ (mm) | $n_p$ | $w_p$ (mm) | $t_p$ (mm) | |
| C-2 and C-2/R specimens | 1892 | 73061.7 | 24 | 132.7 | 14 | 9.6 | 88.9 | 6 | 151 | 0.8 | 445 |
| Bridge pier | 9460 | 1826541.6 | 120 | 3318.3 | 14 | 240.5 | 444.5 | 6 | 755 | 4 | 11125 |

Note: $L$= pier height; $A_g$ = total gross-sectional area of pier; $c$ = concrete cover thickness; $A_{sl}$ = cross-sectional area of longitudinal steel reinforcement; $n$ = number of longitudinal steel reinforcement; $A_{st}$ = cross-sectional area of transverse reinforcement; $s$ = spacing of transverse reinforcement; $n_p$ = number of FRP layers; $w_p$ = width of FRP jackets; and $t_p$ = thickness of one FRP layer.

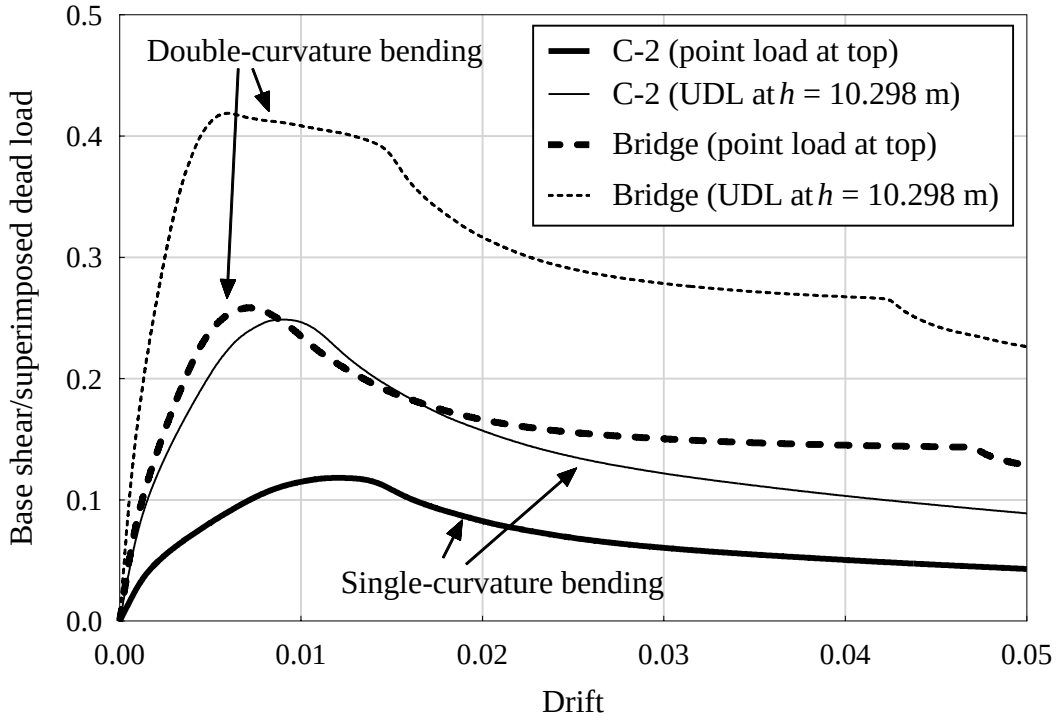


**Figure 5-9.** Results of non-linear static pushover analyses including pier shear normalized by the total superimposed dead load versus drift ratios for single piers and the bridge system.

### 5.4.2 Strengthening of Bridge Piers Using FRP Jackets

A comparative analysis of the response of the initial and strengthened (piers confined by FRP jackets) bridge is conducted. Figure 5-10 presents the schematic of strengthening of bridge piers. The strengthening details of piers included six continuous layers of FRP with a total thickness of 24 mm applied over the height between the footing top to the soffit of pier-cap beam. The analytical peak axial load-moment interaction diagrams for the initial and FRP-confined piers obtained from section analysis are shown in Figure 5-11(a). As the figure shows, the use of FRP jackets improved the sectional moment capacity by about 24% at the applied axial superimposed dead load. It should be mentioned that the effect of the direction of strengthening (transverse and longitudinal) is beyond the scope of this study. Further discussion on the use of different FRP schemes to enhance the axial load and moment capacity of columns can be found in the study by Sadeghian and Fam (2014), among others. Figure 5-11(b) shows the pushover analysis results at an inundation of 10.298 m for the initial and strengthened bridge, and their corresponding performance levels. The significant enhancement in strength and ductility level of bridge with FRP confined piers can be observed. For instance, the increase in peak strength and drift at collapse (50% drop in strength) for the strengthened bridge was about 26% and 111%, respectively.

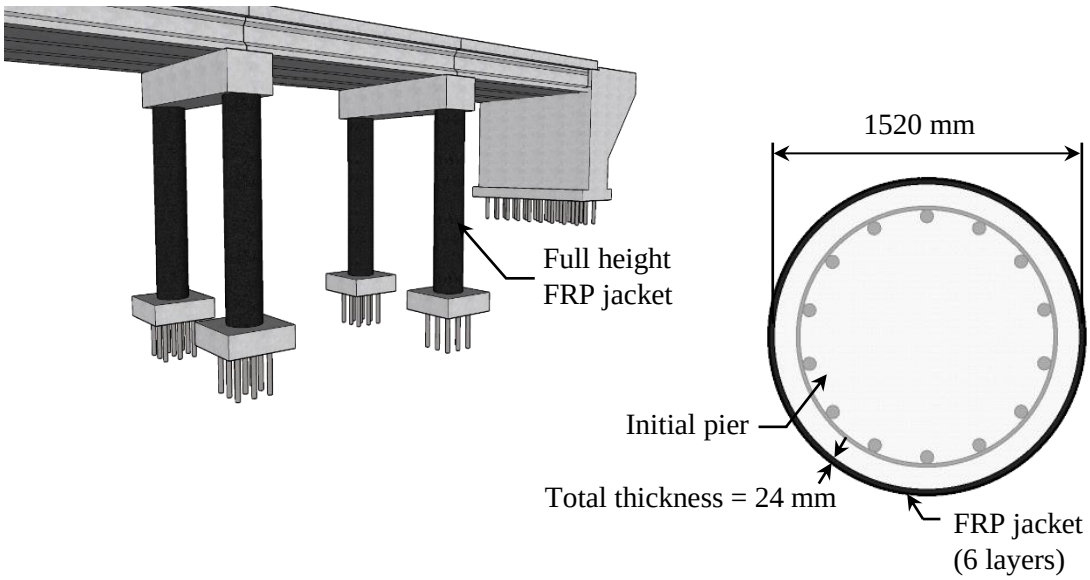


**Figure 5-10.** Schematic of strengthening of bridge piers using FRP jackets.

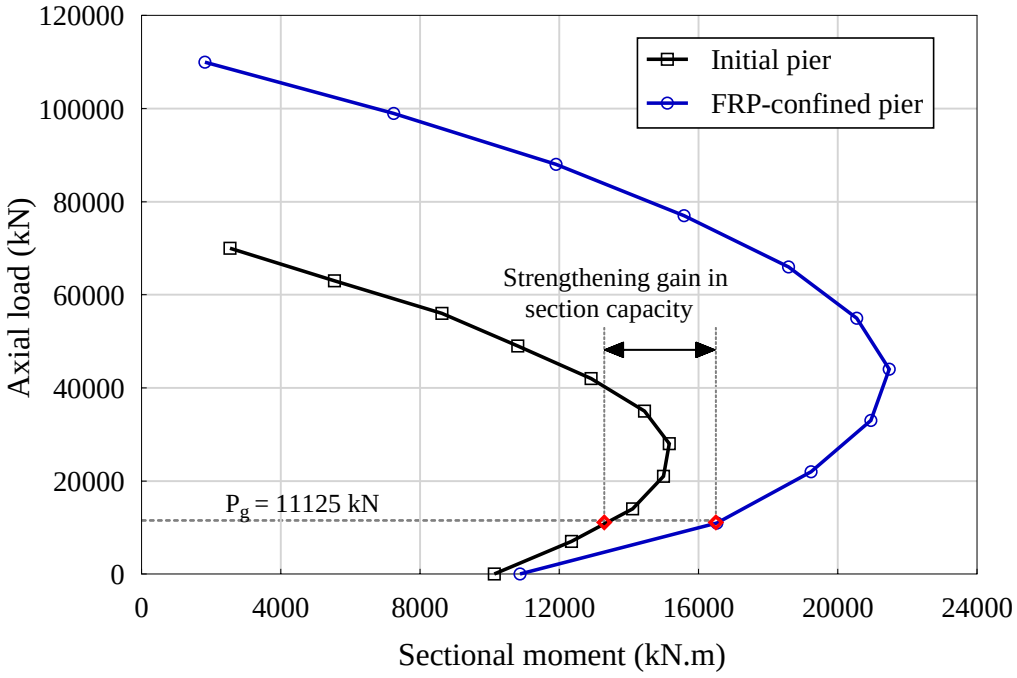


(a)

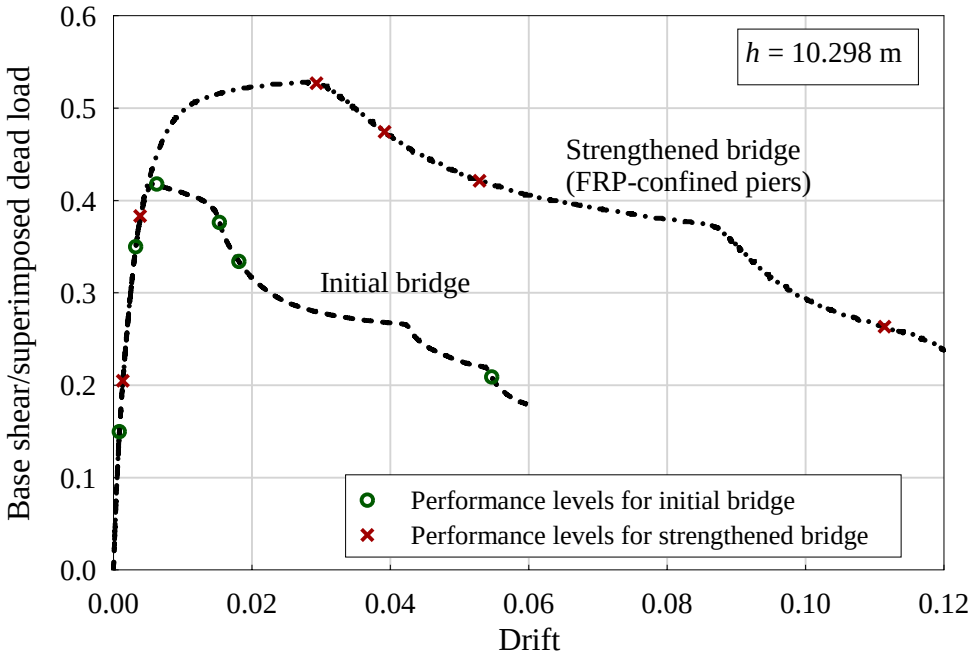


(b)

**Figure 5-11.** Strengthening of bridge piers using FRP jackets: (a) interaction diagrams of piers; and (b) sample pushover analysis results of bridge at *h* =10.298 m.

### 5.4.3 Dynamic Response of Initial and Strengthened Bridge

Figures 5-12 to 5-14 show the time-history analysis results of bridge at an inundation of 10.298 m and four velocities 16, 17, 18, 19 and 20 m/s. The damage states, $DS_2$ (no collapse, yielding), $DS_5$ (collapse, 20% drop in strength) and $DS_6$ (collapse, 50% drop in strength) are presented to evaluate the response of bridge. As the applied load increases, the bridge shows larger base shear and drifts (see Figures 5-12 (a and b)). However. The increase in the drift is relatively significant, and it exceeds the damage state $DS_6$, particularly for velocities 18, 19 and 20 m/s (see Figures 5-12(b and c)). The strengthened bridge shows larger base shear values than the initial bridge as it has larger strength as shown in Figure 5-13(a)). In addition, the corresponding drift-time histories show lower values than the damage state $DS_6$ (see Figures 5-13(b and c)). Comparisons of the normalised base shear and drift ratios between the initial and strengthened bridges are presented in Figure 5-13(d), which show that the use of FRP jackets can prevent the total collapse under significant hydrodynamic forces. The analysis is expanded further to include the performance of initial and strengthened bridge for one velocity (18.5 m/s) and two inundation depths 10.298 and 9 m, and the results are shown in Figure 5-14. These combinations of velocity and inundation depth are selected in accordance with the $Fr_{limit} = 2$ adopted in this study. The large capacity at inundation depth of 9 m prevented the occurrence of significant lateral displacements, but the maximum drift still exceeds the damage state $DS_2$ as shown in Figure 5-14(a). This has been prevented in the strengthened bridge, which showed significant reduction in lateral displacement (see Figures 5-14(b and c)).

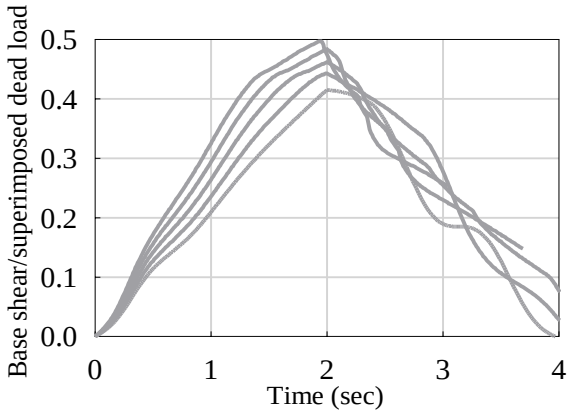


(a)

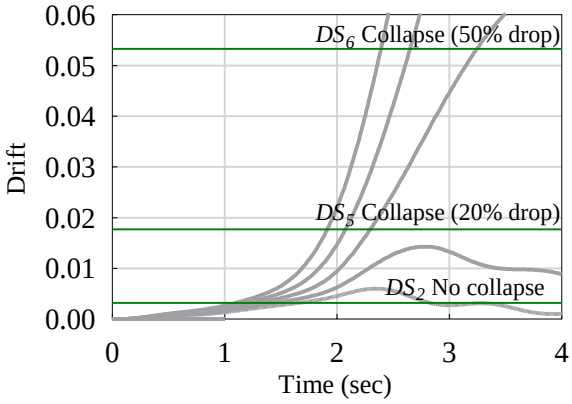


(b)

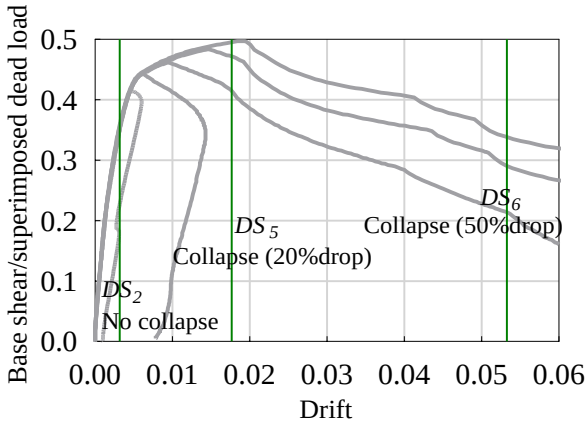


(c)

**Figure 5-12.** Results of non-linear time-history analysis for initial bridge at $u$ = 16, 17, 18, 19 and 20 m/s and $h$ = 10.298 m: (a) reaction force-time history; (b) drift-time history; and (c) drift-reaction force.

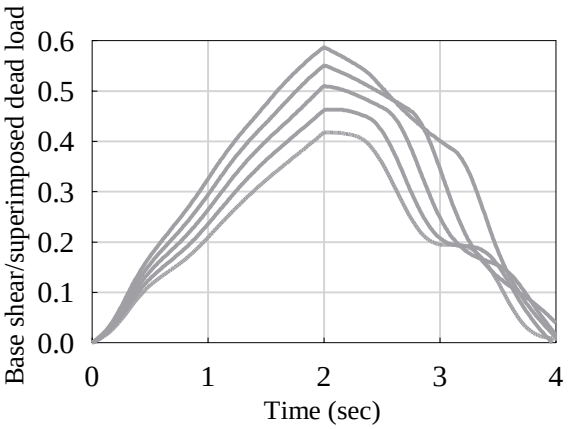
Base shear/superimposed dead load
0.6
0.5
0.4
0.3
0.2
0.1
0.0
0
1
2
3
4
Time (sec)

(a)

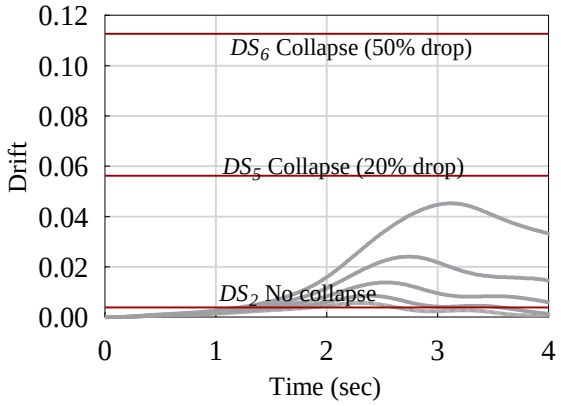
0.12
0.10
0.08
0.06
0.04
0.02
0.00
Drift
$DS_6$ Collapse (50% drop)
$DS_5$ Collapse (20% drop)
$DS_2$ No collapse
0
1
2
3
4
Time (sec)

(b)

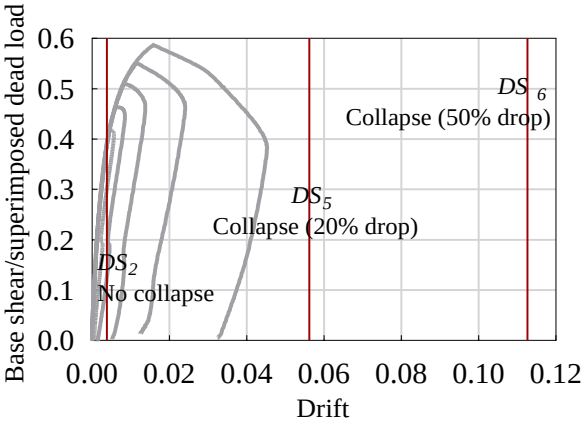
Base shear/superimposed dead load
0.6
0.5
0.4
0.3
0.2
0.1
0.0
$DS_6$
Collapse (50% drop)
$DS_5$
Collapse (20% drop)
$DS_2$
No collapse
0.00
0.02
0.04
0.06
0.08
0.10
0.12
Drift

(c)

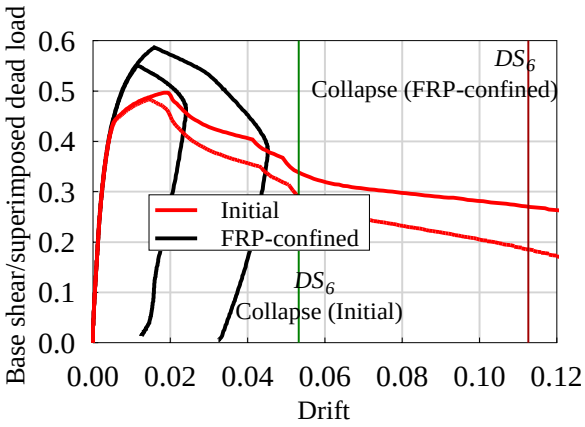


(d)

**Figure 5-13.** Results of non-linear time-history analysis of bridge with FRP-confined piers at $u$ = 16, 17, 18, 19 and 20 m/s and $h$ = 10.298 m: (a) reaction force-time history; (b) drift-time history; (c) drift-reaction force; and (d) comparison between initial bridge and bridge with FRP-confined piers drift-reaction force for $u$ = 19 and 20 m/s.

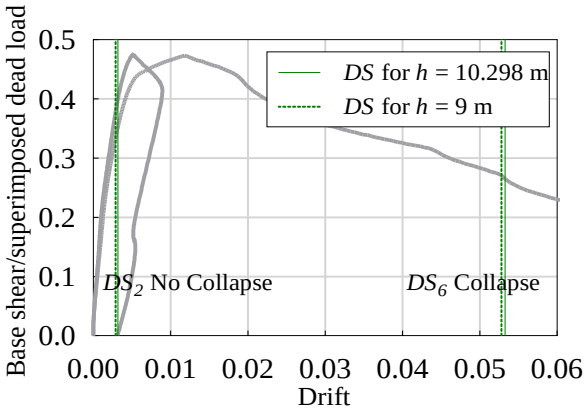


(a)

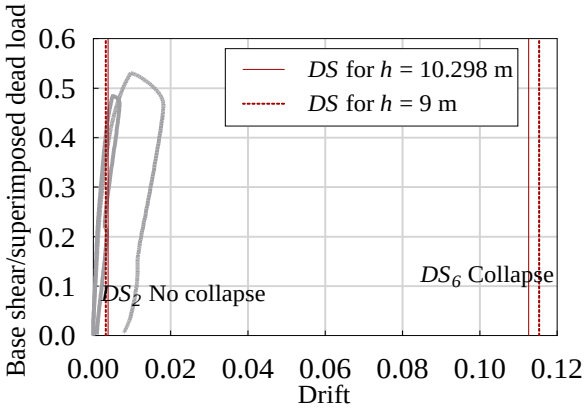


(b)

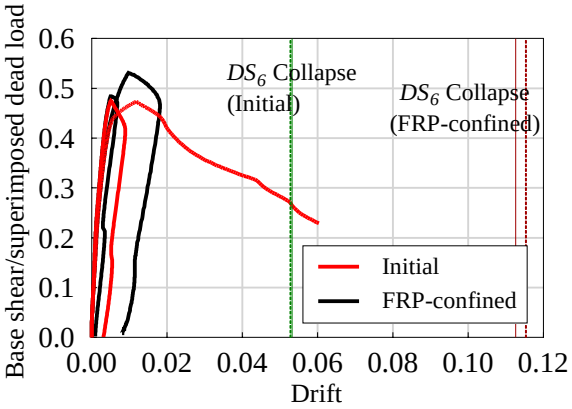


(c)

**Figure 5-14.** Results of time-history analysis at $h$ = 10.298 m and 9 m, for $u$ = 18.5 m/s: (a) initial; (b) FRP-confined; and (c) comparison between initial bridge and strengthened bridge.

## 5.5 Summary

This chapter presented the detailed numerical model of a case study bridge that was used as an illustrative example of the proposed fragility analysis methodology. The model was designed and detailed to suit the objective of this study. For instance, the response of bridge was mainly based on the pier performance. Hence, limited ductility pier specimens were adopted to examine the effectiveness of strengthening in enhancing their performance. Appropriate Concrete and steel models that can represent the failure criterion of structure were adopted. The results of pushover analysis showed satisfactory accuracy with the strength envelop in the push region of cyclic load. The initial bridge showed significant displacement at large load levels under time-history analysis, which was found to exceed the total collapse damage state (50% drop in peak strength). However, bridges with FRP strengthened piers could sustain the same load levels without showing a total collapse, which highlights the effectiveness of the use of FRP to enhance the performance of bridges subjected to extreme wave loads. Considering the uncertainties in the structural and force parameters, the data obtained from the time-history analysis were used to develop fragility models of the bridge.

# CHAPTER 6

# FRAGILITY ANALYSIS

## 6.1 Introduction

In this chapter, the numerical model discussed in Chapter 5 is utilized to construct fragility functions for a case study bridge to demonstrate the application of the proposed methodology. The time-history analyses were conducted at all the ranges of velocity and inundation depths, and the mean damage probability fractions were obtained. The methodology of developing the fragility function for a single inundation depth or velocity increment was first discussed. Then, the overall fragility function for the bridge was shown for the all IMs. The discrepancy in predicting the structural response, defined by the standard deviation of the damage probability, was discussed and compared for all IMs. In addition, the viability of the FRP jackets for reducing the vulnerability of bridges under extreme waves was discussed. In particular, the enhancement in the ductility capacity, represented by the damage states in the post-peak stage, was investigated. The efficiency of the single-(inundation depth and velocity) and two-parameter (momentum flux and moment of momentum flux) IMs in representing the enhancement of bridge capacity was addressed.

## 6.2 Computation of Fragility Data Using the Proposed Methodology

An illustration of the use of the proposed methodology discussed in Chapter 4 for developing fragility functions of the bridge is shown in Figure 6-1. The detailed calculation steps of the damage probability data are shown in Tables 6-1 to 6-3 for velocity, momentum flux and moment of momentum flux IMs. As can be seen, the initial step in the method is the

generation of the ranges of IMs. For instance, a maximum velocity values of 20 m/s were selected for this study. The maximum momentum flux and moment of momentum flux values were 4119.2 $m^3/s^2$ and 12872.5 $m^4/s^2$, respectively. As discussed, the inundation depth was increased with 0.5 m increments until an inundation depth of 9 m. Then, the increments were modified to 0.46 and 0.415 m until 10.298 m, which is equivalent to the pier-cap beam level. For the sake of illustration, the maximum inundation depth in the calculation examples shown in Tables 6-1 to 6-3 is taken as 9 m. For velocity IM, an increment of 0.5 m/s was used until the maximum velocity of 20 m/s. For momentum flux ($hu^2$) IM, an increment of 20.596 $m^3/s^2$ was used until the maximum value of 4119.2 $m^3/s^2$. The corresponding hydrodynamic forces at each $hu^2$ increment were obtained based on the back calculated velocities from IM each increment. For instance, the back calculated velocity increments for $hu^2$ increments of 20.596, 41.192 and 61.788 $m^3/s^2$ at inundation depth of 9 m are equal to 1.52, 2.14 and 2.62 m/s, respectively. In the moment of momentum flux ($h^2u^2/2$) IM, an increment of 51.49 $m^4/s^2$ was used until the maximum value of 12872.5 $m^4/s^2$. As in the momentum flux, the back calculated velocities of $h^2u^2/2$ were used to obtain the forces at each inundation depth. For example, for $h^2u^2/2$ increments of 51.49, 102.98 and 154.47 $m^4/s^2$ the back calculated velocities are 1.13, 1.6 and 1.95 m/s, respectively. Therefore, a total of 40 increments were used for velocity IMs, while 200 and 250 increments were used for momentum flux and moment of momentum flux IMs. The Froude number limit ($Fr_{limit}$) is then checked for the generated ranges, and the unrealistic values of velocity are excluded from the calculation. This leads to a reduction in the total increments with the increase in inundation depth, as the maximum realistic velocity becomes lower. For instance, the maximum realistic value for velocity IM at an inundation depth of 9 m is 18.5 m/s (37 velocity increments).

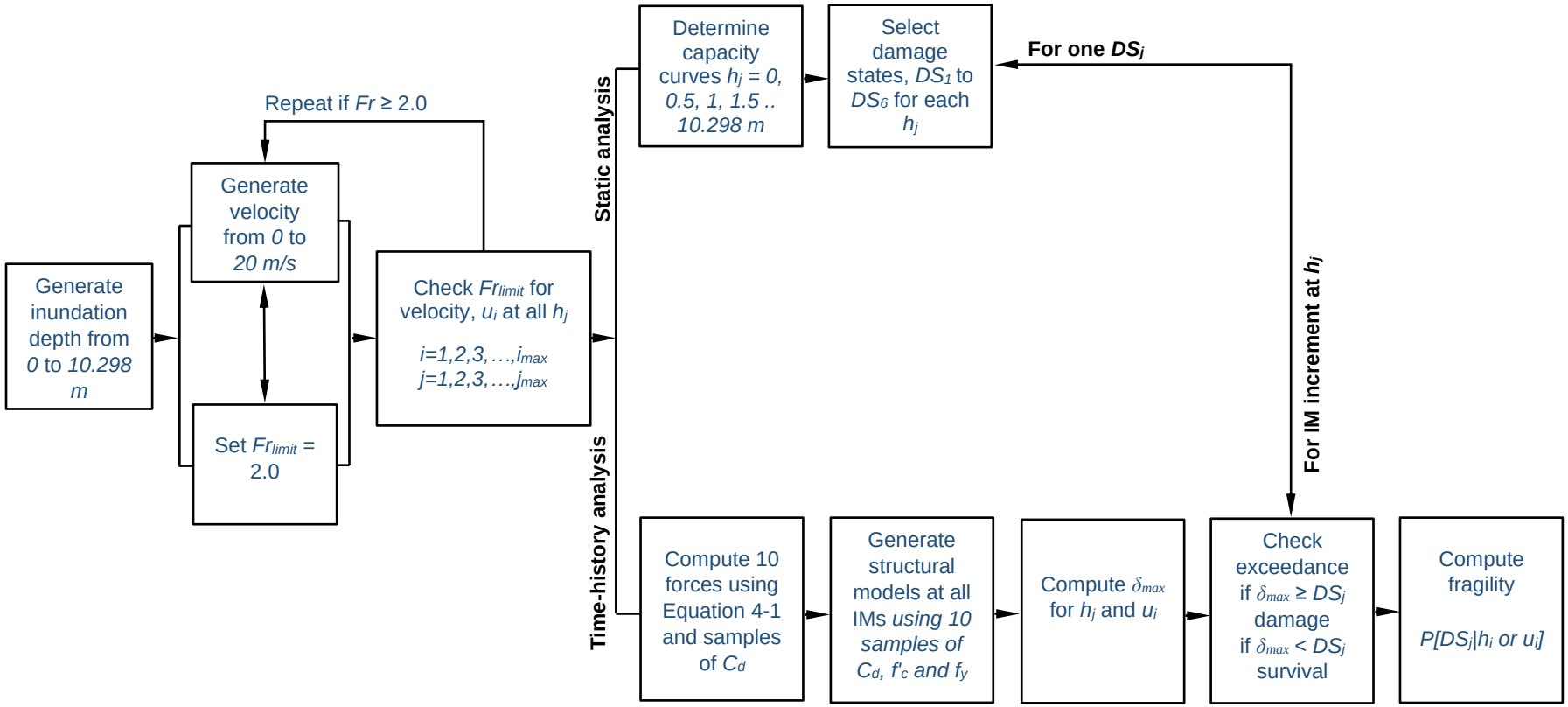


**Figure 6-1**. Illustration of the computation of fragility of bridge using proposed framework.

**Table 6-1.** Illustration of the application of the proposed fragility methodology for obtaining damage probability of bridge for velocity IM.

| Step | | Detailed calculation | |
|---|---|---|---|
| 1 | IM ranges | $h_{max}$ = 9 m<br>$h_i$ = 0.5, 1, 1.5, 2, 2.5, 3, 3.5, 4, 4.5, 5, 5.5, 6, 6.5, 7, 7.5, 8, 8.5, 9 (m)<br><br>$u_{max}$ = 20 m/s<br>$u_i$ = 0.5, 1, 1.5, 2, 2.5, 3, 3.5, 4, 4.5, 5, 5.5, 6, 6.5, 7, 7.5, 8, 8.5, 9, 9.5, 10, 10.5, 11, 11.5, 12, 12.5, 13, 13.5, 14, 14.5, 15, 15.5, 16, 16.5, 17, 17.5, 18, 18.5, 19, 19.5, 20 (m/s) | |
| 2 | $Fr_{limit}$ | $Fr_{limit}$ = 2 | |
| 3 | Revised velocity ranges<br>$u_i = Fr_{limit}.\sqrt{9.81h_i}$ | For $h$ = 9 m → $u_{max}$ =18.5 m/s<br><br>For $h$ = 8.5 m → $u_{max}$ =18 m/s | |
| Sample two inundation depths ($h_i$=8.5 and 9 m), and damage states ($DS_1$ *and* $DS_6$) and one velocity ($u_i$ = 18 m/s) | | | |
| 4 | Select damage states | For $h_i$ = 8.5 m<br><br>For $DS_1$:<br>P= 1818700 N<br>δ= 0.000878<br><br>For $DS_6$:<br>P= 2641960 N<br>δ= 0.0537 | For $h_i$ = 9 m<br><br>For $DS_1$:<br>P= 1790000 N<br>δ= 0.000877<br><br>For $DS_6$:<br>P= 2550000 N<br>δ= 0.0528 |
| 5 | Compute forces<br>(10 random samples of force coefficients) | For $h_i$ = 8.5 m and $u_i$ = 18 m/s<br>F = 454.21165, 462.18872, 564.21295, 393.72275, 520.02121, 509.28335, 501.30628, 399.28205, 569.77225, 443.47379 (N/mm) | For $h_i$ = 9 m and $u_i$ = 18 m/s<br>F = 454.21165, 462.18872, 564.21295, 393.72275, 520.02121, 509.28335, 501.30628, 399.28205, 569.77225, 443.47379 (N/mm) |
| 6 | Compute maximum drifts | For $h_i$ = 8.5 m and $u_i$ = 18 m/s<br>$\delta_{max}$ =<br>0.0024455, 0.0025007, 0.0047948, 0.0018843, 0.0034132, 0.0030749, 0.0029238, 0.0019537, 0.0056153, 0.0022816 | For $h_i$ = 9 m and $u_i$ = 18 m/s<br>$\delta_{max}$ =<br>0.0029758, 0.0030868, 0.010251, 0.0022856, 0.0046139, 0.0040627, 0.0036301, 0.0023748, 0.01555, 0.0027755 |
| 7 | Check exceedance and determine damage probability. | For $h_i$ = 8.5 m and $u_i$ = 18 m/s<br><br>For $DS_1$:1<br>For $DS_6$:0 | For $h_i$ = 9 m and $u_i$ = 18 m/s<br><br>For $DS_1$:1<br>For $DS_6$:0 |

**Table 6-2.** Illustration of the application of the proposed fragility methodology for obtaining damage probability of bridge for momentum flux IM.

| Step | | Detailed calculation | |
|---|---|---|---|
| 1 | IM ranges | $h_{max}$ = 9 m<br>$h_i$ = 0.5, 1, 1.5, 2, 2.5, 3, 3.5, 4, 4.5, 5, 5.5, 6, 6.5, 7, 7.5, 8, 8.5, 9 (m)<br><br>$(hu^2)_{max}$ = 4119.2 $m^3/s^2$<br>$(hu^2)_i$ = 20.596, 41.192, 61.788, 82.384, 102.98, 123.576, ……, 4119.2 ($m^3/s^2$) | |
| 2 | $Fr_{limit}$ | $Fr_{limit}$ = 2 | |
| 3 | Revised velocity ranges<br>$u_i = Fr_{limit}.\sqrt{9.81h_i}$ | For $h$ = 9 m → $u_{max}$ =18.7 m/s (back calculated from $hu^2$)<br><br>For $h$ = 8.5 m → $u_{max}$ =18.2 m/s (back calculated from $hu^2$) | |
| Sample two inundation depths ($h_i$=8.5 and 9 m), and damage states ($DS_1$ *and* $DS_6$) and one velocity $(hu^2)_i$ = 2821.652 $m^3/s^2$ | | | |
| 4 | Select damage states | For $h_i$ = 8.5 m<br><br>For $DS_1$:<br>P= 1818700 N<br>δ= 0.000878<br><br>For $DS_6$:<br>P= 2641960 N<br>δ= 0.0537 | For $h_i$ = 9 m<br><br>For $DS_1$:<br>P= 1790000 N<br>δ= 0.000877<br><br>For $DS_6$:<br>P= 2550000 N<br>δ= 0.0528 |
| 5 | Compute forces<br>(10 random samples of force coefficients) | For $h_i$ = 8.5 m and $(hu^2)_i$ = 2821.652 $m^3/s^2$<br>F = 465.36936, 473.54239, 578.07284, 403.39455, 532.79553, 521.79389, 513.62086, 409.09041, 583.7687, 454.36772 (N/mm) | For $h_i$ = 9 m and $(hu^2)_i$ = 2821.652 $m^3/s^2$<br>F = 439.5155, 447.23448, 545.95768, 380.98374, 503.19578, 492.80535, 485.08637, 386.36316, 551.33711, 429.12507 (N/mm) |
| 6 | Compute maximum drifts | For $h_i$ = 8.5 m and $(hu^2)_i$ = 2821.652 $m^3/s^2$<br>$\delta_{max}$ =<br>0.0025433, 0.0026059, 0.0054694, 0.0019578, 0.0036111, 0.0032499, 0.0030503, 0.002031, 0.0073714, 0.0023718 | For $h_i$ = 9 m and $(hu^2)_i$ = 2821.652 $m^3/s^2$<br>$\delta_{max}$ =<br>0.0028223, 0.0029063, 0.0075202, 0.00217, 0.0041519, 0.0037165, 0.003406, 0.0022531, 0.010998, 0.0026307 |
| 7 | Check exceedance and determine damage probability. | For $h_i$ = 8.5 m and $(hu^2)_i$ = 2821.652 $m^3/s^2$<br>For $DS_1$:1<br>For $DS_6$:0 | For $h_i$ = 9 m and $(hu^2)_i$ = 2821.652 $m^3/s^2$<br>For $DS_1$:1<br>For $DS_6$:0 |

**Table 6-3.** Illustration of the application of the proposed fragility methodology for obtaining damage probability of bridge for moment of momentum flux IM.

| Step | | Detailed calculation | |
|---|---|---|---|
| 1 | IM ranges | $h_{max}$ = 9 m<br>$h_i$ = 0.5, 1, 1.5, 2, 2.5, 3, 3.5, 4, 4.5, 5, 5.5, 6, 6.5, 7, 7.5, 8, 8.5, 9 (m)<br><br>$(h^2u^2/2)_{max}$ = 12872.5 $m^4/s^2$<br>$(h^2u^2/2)_i$ = 51.49, 102.98, 154.47, 205.96, 257.45, 308.94, ……, 12872.5 ($m^4/s^2$) | |
| 2 | $Fr_{limit}$ | $Fr_{limit}$ = 2 | |
| 3 | Revised velocity ranges<br>$u_i = Fr_{limit}.\sqrt{9.81h_i}$ | For $h$ = 9 m → $u_{max}$ =17.8 m/s (back calculated from $h^2u^2/2$)<br><br>For $h$ = 8.5 m → $u_{max}$ = 18.3 m/s (back calculated from $h^2u^2/2$) | |
| Sample two inundation depths ($h_i$=8.5 and 9 m), and damage states ($DS_1$ *and* $DS_6$) and one velocity ( $h^2u^2/2)_i$ = 12048.66 $m^4/s^2$ | | | |
| 4 | Select damage states | For $h_i$ = 8.5 m<br><br>For $DS_1$:<br>P= 1818700 N<br>δ= 0.000878<br><br>For $DS_6$:<br>P= 2641960 N<br>δ= 0.0537 | For $h_i$ = 9 m<br><br>For $DS_1$:<br>P= 1790000 N<br>δ= 0.000877<br><br>For $DS_6$:<br>P= 2550000 N<br>δ= 0.0528 |
| 5 | Compute forces<br>(10 random samples of force coefficients) | For $h_i$ = 8.5 m and $(h^2u^2/2)_i$ = 12048.66 $m^4/s^2$<br>F = 467.56732, 475.77895, 580.80311, 405.2998, 535.31196, 524.25836, 516.0467, 411.02257, 586.52588, 456.51372 (N/mm) | For $h_i$ = 9 m and $(h^2u^2/2)_i$ = 12048.66 $m^4/s^2$<br>F = 417.05851, 424.38308, 518.06204, 361.51742, 477.48505, 467.62551, 460.3009, 366.62198, 523.1666, 407.19897 (N/mm) |
| 6 | Compute maximum drifts | For $h_i$ = 8.5 m and $(h^2u^2/2)_i$ = 12048.66 $m^4/s^2$<br>$\delta_{max}$ =<br>0.0025628, 0.0026271, 0.005635, 0.0019724, 0.0036531, 0.0032867, 0.0030759, 0.0020464, 0.0077557, 0.0023897 | For $h_i$ = 9 m and $(h^2u^2/2)_i$ = 12048.66 $m^4/s^2$<br>$\delta_{max}$ =<br>0.0025939, 0.002654, 0.0052266, 0.001997, 0.0036342, 0.0032764, 0.0031012, 0.0020716, 0.0065304, 0.0024192 |
| 7 | Check exceedance and determine damage probability. | For $h_i$ = 8.5 m and $(h^2u^2/2)_i$ = 12048.66 $m^4/s^2$<br>For $DS_1$:1<br>For $DS_6$:0 | For $h_i$ = 9 m and $(h^2u^2/2)_i$ = 12048.66 $m^4/s^2$<br>For $DS_1$:1<br>For $DS_6$:0 |

The static pushover analysis is conducted for all inundation depths to obtain the capacity curves. The six performance levels are specified at each inundation depth, and the damage states that correspond to each performance level in the form of pier drifts are obtained. Figures 6-2 and 6-3 show the variation in capacity curves of initial and strengthened bridge with the increase in inundation depth. The details of the damage states used to develop the fragility functions are presented in Tables A-1 to A-12 in the Appendix. Table 6-4 presents the main random variables adopted in the fragility analysis for the case study bridge, and their probability distributions and defined parameters. The LHS and AV methods are then used to generate 10 samples for each random variable, which are used as input for the time-history analyses at each IM, as discussed in Chapter 4. The random samples of the force coefficients, concrete compressive strength and steel tensile strength are generated. The forces for all coefficients are calculated and applied on the bridge in the form of UDL. Table 6-5 shows the detailed calculation steps used to obtain the forces using 10 random samples of force coefficients. The bridge model parameters are specified, and the concrete compressive strength and steel tensile strength being are set as variables. The capacity curves for inundation depth of 10.298 m are shown in Figure 6-4(a) obtained from 10 random samples of concrete compressive strength and steel tensile strength. The 10 generated forces for each IM increment (e.g., velocity) at each inundation depth are applied on the bridge. The structural analyses are conducted for the 10 random samples of each of the concrete compressive strength and steel tensile strength. Figure 6-4(b) shows a sample of the response of bridge from the time-history analyses for 10 samples of force coefficients, concrete compressive strength and steel tensile strength at one inundation depth and velocity. The maximum drift from each model is computed and recorded. The procedures of the estimation of the maximum drift is explained in Table 6-6. This means that 10 maximum drifts are

obtained at each IM increment (e.g., velocity) at each inundation depth. The 10 maximum drifts are checked with the damage states obtained from the static analysis for each depth. The fragility damage probability is theoretically the ration of the number of maximum drifts that exceed a certain damage state to the total number of maximum drifts. For instance, if 4 maximum drifts exceed the damage state, then the damage probability would be equal to 0.4.

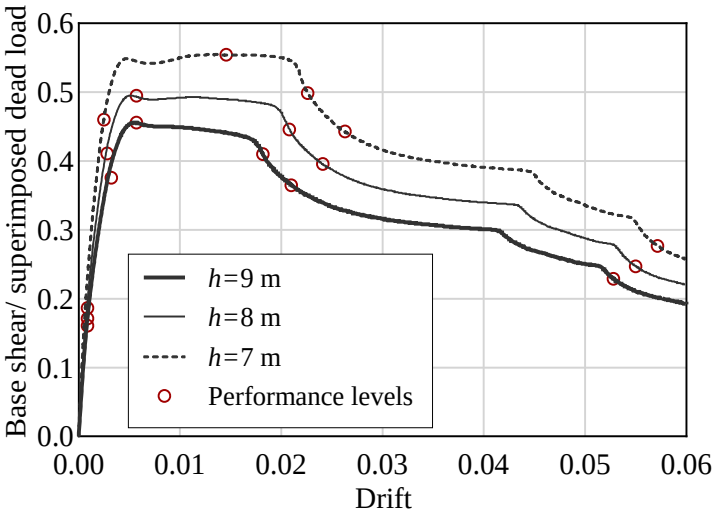


(a)

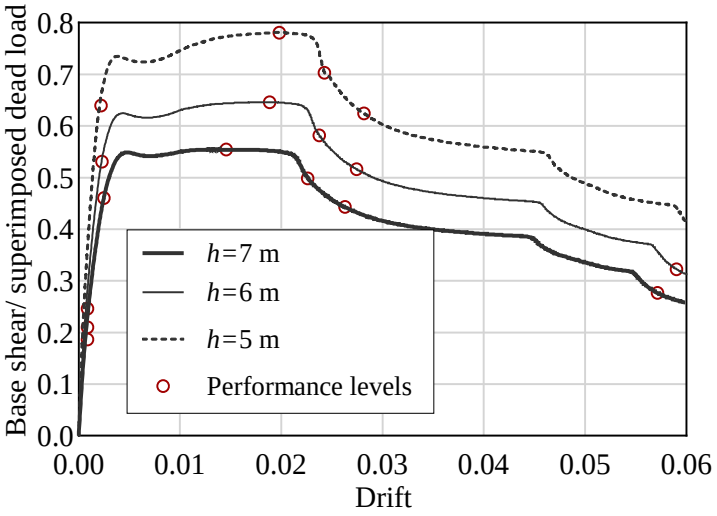


(b)

**Figure 6-2.** Capacity curves for different inundation depths for initial bridge: (a) 9 to 7 m; and (b) 7 to 5 m.

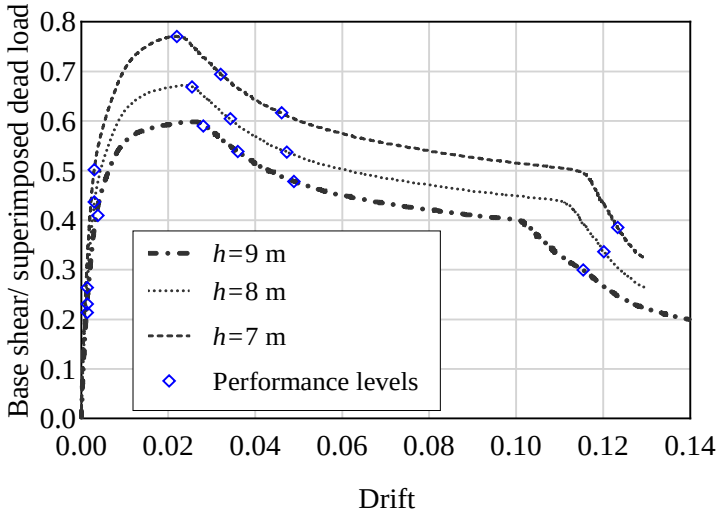


(a)

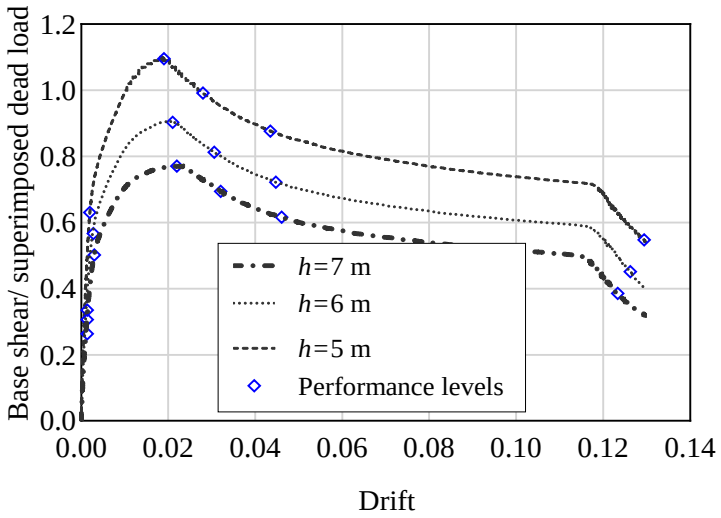


(b)

**Figure 6-3.** Capacity curves for different inundation depths for strengthened bridge: (a) 9 to 7 m; and (b) 7 to 5 m.

**Table 6-4.** Statistical characteristics of the random variables of capacity and demand estimation.

| Variable | Symbol | Distribution | Mean | COV | Range | Reference |
|---|---|---|---|---|---|---|
| Concrete strength | $f_c^{'}$ | Normal | 31.03 | 0.18 | N/A[a] | Bartlett and MacGregor, (1996) |
| Steel strength | $f_y$ | Lognormal | 358.0 | 0.11 | N/A[a] | Mirza and MacGregor, (1979) |
| Force coefficient | $C_d$ | Uniform | N/A[a] | N/A[a] | 1.25 to 2.0 | ASCE, (2016), Attary et al., (2016) |

[a] Not applicable. Note: COV= coefficient of variation.

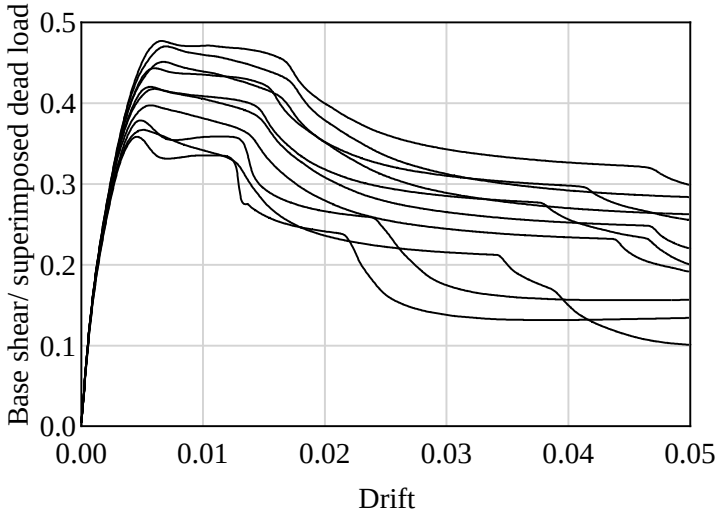


(a)

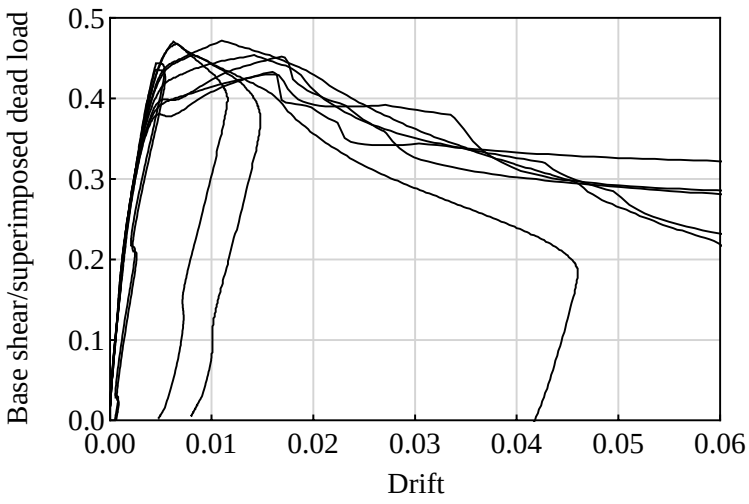


(b)

**Figure 6-4.** Effect of random variables samples on the response of bridge for inundation depth of 10.298 m: (a) capacity curves for the random combinations of $f_c^{'}$ and $f_y$; and (b) sample response from time-history analysis for all random combinations of $C_d$, $f_c^{'}$ and $f_y$ for $u$ =20 m/s.

**Table 6-5.** Procedures of the calculation of forces for all velocity ranges at each inundation depth.

| Parameter | | Calculation |
|---|---|---|
| 1 | The 10 force coefficients from 1.25 to 2. | For example: $C_d$ = 1.838604996, 1.964012577, 1.53150216, 1.672413832, 1.364007121, 1.411395004, 1.285987423, 1.71849784, 1.577586168, 1.885992879 |
| 2 | Velocity values | $u$ = 0.5, 1, 1.5, 2, 2.5, 3, 3.5, 4, 4.5, 5, 5.5, 6, 6.5, 7, 7.5, 8, 8.5, 9, 9.5, 10, 10.5, 11, 11.5, 12, 12.5, 13, 13.5, 14, 14.5, 15, 15.5, 16, 16.5, 17, 17.5, 18, 18.5, 19, 19.5, 20 (m/s) |
| 3 | Inundation depth | e.g., $h$ = 9 m |
| 4 | Pier diameter | $D$ = 1.525 m |
| 5 | Total tributary area of bridge | $A_{trib} = h \times D$ |
| 6 | Froude number limit | $Fr_{limit}$ = 2 |
| 7 | Revised velocity | $u$ = 0.5, 1, 1.5, 2, 2.5, 3, 3.5, 4, 4.5, 5, 5.5, 6, 6.5, 7, 7.5, 8, 8.5, 9, 9.5, 10, 10.5, 11, 11.5, 12, 12.5, 13, 13.5, 14, 14.5, 15, 15.5, 16, 16.5, 17, 17.5, 18, 18.5 (m/s) |
| 8 | Force | $u_1$ (0.5 m/s) $u_{37}$ (18.5 m/s)<br>$C_1$ = 0.35047195 N/mm . . . . . 479.7961 N/mm<br>. .<br>. .<br>. .<br>. .<br>. .<br>. .<br>. .<br>. .<br>$C_{10}$ = 0.34218656 N/mm . . . . . .468.45341 N/mm |

**Table 6-6.** Procedures of the calculation of bridge maximum drifts for all ranges of forces and uncertainties in structural parameters.

<table>
<tr><th colspan="2">Step</th><th>Details/illustrative examples</th></tr>
<tr><td>1</td><td>Input forces for all coefficients ($C_d$) at all IM increments.</td><td>Example input of triangular force pattern of peak = 1.0 N/mm<br><br>dt (sec) force (N/mm)<br>0.0 0.0<br>. .<br>. .<br>. .<br><br>2.0 1.0<br>. .<br>. .<br>. .<br>4.0 0.0<br><br>This input is repeated for each force coefficient.</td></tr>
<tr><td>2</td><td>Input 10 random samples of concrete compressive strength ( $f_c^{'}$ ) and steel tensile strength ($f_y$).</td><td>For example:<br>$f_c^{'}$ =36.87698741, 38.81443471, 31.80629998, 47.35484119, 27.22253786, 36.32301259, 34.38556529, 41.39370002, 25.84515881, 45.97746214<br><br>$f_y$=405.591471, 335.0978009, 287.5619654, 382.7849224, 359.435774, 312.2150361, 377.8949173, 440.3633686, 330.816989, 352.307046</td></tr>
<tr><td>3</td><td>Structural models</td><td>For each IM increment (e.g., $u$, $hu^2$, $h^2u^2/2$) 10 structural models are obtained for the following combinations (using LHS method) of structural and force parameters (rounded):
<table>
<tr><th></th><th>1</th><th>2</th><th>3</th><th>4</th><th>5</th><th>6</th><th>7</th><th>8</th><th>9</th><th>10</th></tr>
<tr><td>$C_d$</td><td>1.8</td><td>2.0</td><td>1.5</td><td>1.7</td><td>1.4</td><td>1.4</td><td>1.3</td><td>1.7</td><td>1.6</td><td>1.9</td></tr>
<tr><td>$f_c^{'}$</td><td>36.9</td><td>38.8</td><td>31.8</td><td>47.4</td><td>27.2</td><td>36.3</td><td>34.4</td><td>41.4</td><td>25.8</td><td>46.0</td></tr>
<tr><td>$f_y$</td><td>405.6</td><td>335.1</td><td>287.6</td><td>382.8</td><td>359.4</td><td>312.2</td><td>377.9</td><td>440.4</td><td>330.8</td><td>352.3</td></tr>
</table></td></tr>
<tr><td>4</td><td>Maximum drifts</td><td>Maximum drifts are recorded for the 10 random combinations at each IM increment, e.g.,<br>$\delta_{max}$ =<br>0.00017824, 0.00018109, 0.00022497, 0.00015385, 0.00021291, 0.00019996, 0.00019766, 0.00015621, 0.00023584, 0.0001733</td></tr>
</table>

## 6.3 Single-Parameter IM

### 6.3.1 Velocity

The fragility functions for the bridge are developed based on the damage probability data obtained from the time-history analyses considering all the uncertainties in force and structural parameters. The analysis was performed with a total of 21 inundation depth increments for each of the bridge models to provide a total inundation depth ($h_{max}$) of 10.298 m, which is equivalent to the pier-cap beam level. An inundation depth increment of 0.5 m was used up to a height of 9 m. Increments of 0.46 and 0.419 m were considered for the remaining height until 10.298 m. For each inundation depth, 40 velocity increments of 0.5 m/s were used, i.e. $u_{max}$ = 20 m/s. Figure 6-5 shows the fragility functions for a single increment of inundation depth or flow velocity for one performance level. A summary of some of the sample data used in the construction of the fragility functions is presented in Table 6-7. The damage fraction is the ratio of the number of damage cases, defined based on the selected damage state, to the total number of analyses at each IM increment. For the velocity IM, the damage probability data are computed at each velocity increment for all inundation depths and the fragility fitting curve is drawn, as shown in Figure 6-5(a) for $h$ = 7.5 m. Hence, the process of defining the fragility function for a single depth (see Figure 6-5(a)) is repeated for all velocity increments until $u_{max}$ = 20 m/s to develop the overall fragility function of the bridge. Figures 6-6 and 6-7 show the fragility functions for velocity IM for the six damage states. The dashed lines present the fragility function at each velocity increment for a single inundation depth. This means that the individual fragility functions representing each inundation depth show lower damage probability with the increase in inundation depth, as indicated in Figure 6-6(a). The mean damage probability data at each

velocity increment was calculated. The fragility trend line of the mean damage probabilities was drawn to facilitate the comparison between results. The scatter between the damage data is attributed to the difference in the hydrodynamic force at each combination of velocity and inundation depth. For instance, the mean damage probability of a velocity of 12 m/s is about 36% for $DS_1$ (see Figure 6-6(a)). This provides momentum flux ($hu^2$) values of 936 and 1482.9 $m^3/s^2$ for inundation depths of 6.5 and 10.298 m, respectively. Hence, the resulting variation in the response of bridge leads to a large scatter in the damage probability data (between 0 and 1) for most velocity increments. In addition, the effect of $Fr_{limit}$ on the fragility results at relatively large velocities and small inundation depths can be observed. For example, at a velocity of 15.5 m/s, and for an inundation depth of 6.5 m, the damage probability m was about 0.1. which is the threshold realistic case considered in the present analysis (see Figure 6-6(a)).

**Table 6-7.** Sets of sample data used for developing fragility functions for a single velocity/inundation depth increment of velocity, inundation depth and momentum flux IMs.

| IM level | $F_r$ | Total number of analysis trials | Number of damage cases | Damage probability | Fitted fragility function |
|---|---|---|---|---|---|
| Velocity (m/s) for $h$ = 7.5 m | | | | | |
| 12 | 1.40 | 10 | 0 | 0.00 | 0.01 |
| 13 | 1.52 | 10 | 1 | 0.10 | 0.09 |
| 14 | 1.63 | 10 | 4 | 0.40 | 0.35 |
| 15 | 1.75 | 10 | 7 | 0.70 | 0.71 |
| 16 | 1.87 | 10 | 10 | 1.00 | 0.93 |
| 17 | 1.98 | 10 | 10 | 1.00 | 0.99 |
| Inundation depth (m) for $u$ = 13 m/s | | | | | |
| 7.0 | 1.57 | 10 | 0 | 0.00 | 0.01 |
| 7.5 | 1.52 | 10 | 1 | 0.10 | 0.08 |
| 8.0 | 1.47 | 10 | 3 | 0.30 | 0.32 |
| 8.5 | 1.42 | 10 | 7 | 0.70 | 0.68 |
| 9.0 | 1.38 | 10 | 9 | 0.90 | 0.92 |
| 9.46 | 1.35 | 10 | 10 | 1.00 | 0.99 |
| Momentum flux ($m^3/s^2$) for $h$ = 8.5 m | | | | | |
| 1071.0 | 1.23 | 10 | 0 | 0.00 | 0.09 |
| 1215.2 | 1.31 | 10 | 3 | 0.30 | 0.27 |
| 1359.3 | 1.38 | 10 | 5 | 0.50 | 0.54 |
| 1503.5 | 1.46 | 10 | 8 | 0.80 | 0.79 |
| 1627.1 | 1.52 | 10 | 9 | 0.90 | 0.92 |
| 1771.3 | 1.58 | 10 | 10 | 1.00 | 0.98 |

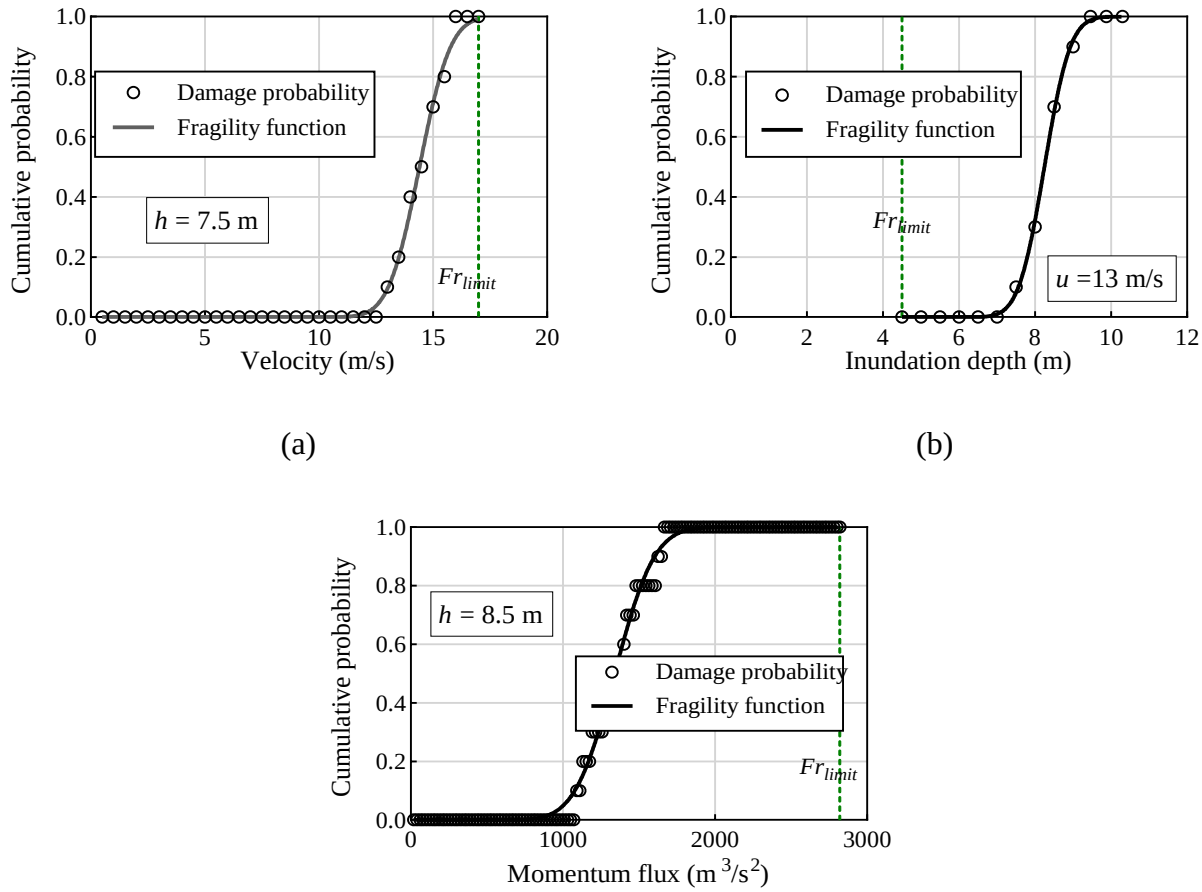


**Figure 6-5.** Illustration of fragility function fitting for one inundation depth/flow velocity increment of different IMs at $DS_1$: (a) velocity; (b) inundation depth; and (c) momentum flux.

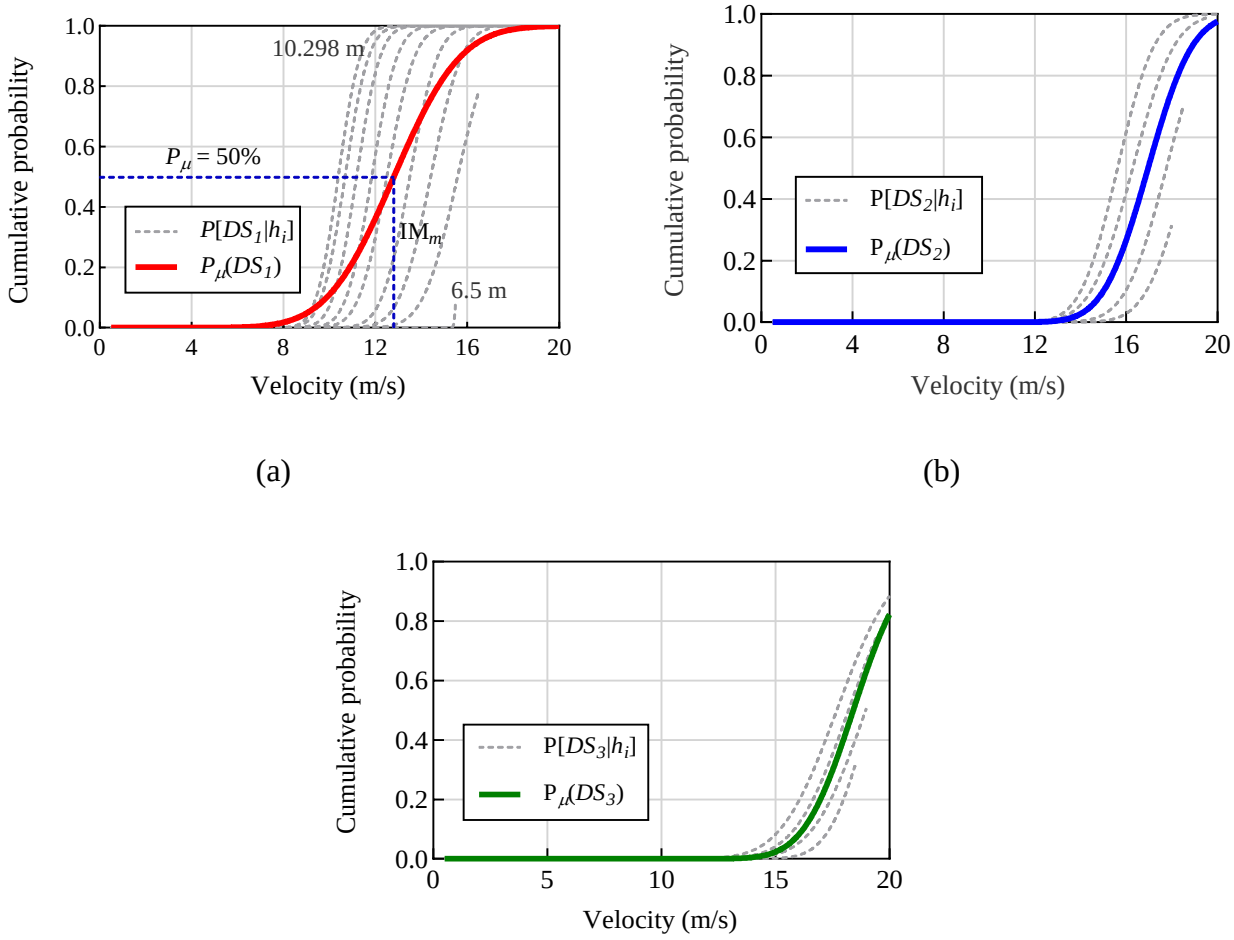


**Figure 6-6.** Fragility functions for velocity IM of the initial bridge: (a) *DS₁*; (b) *DS₂*; and (c) *DS₃*.

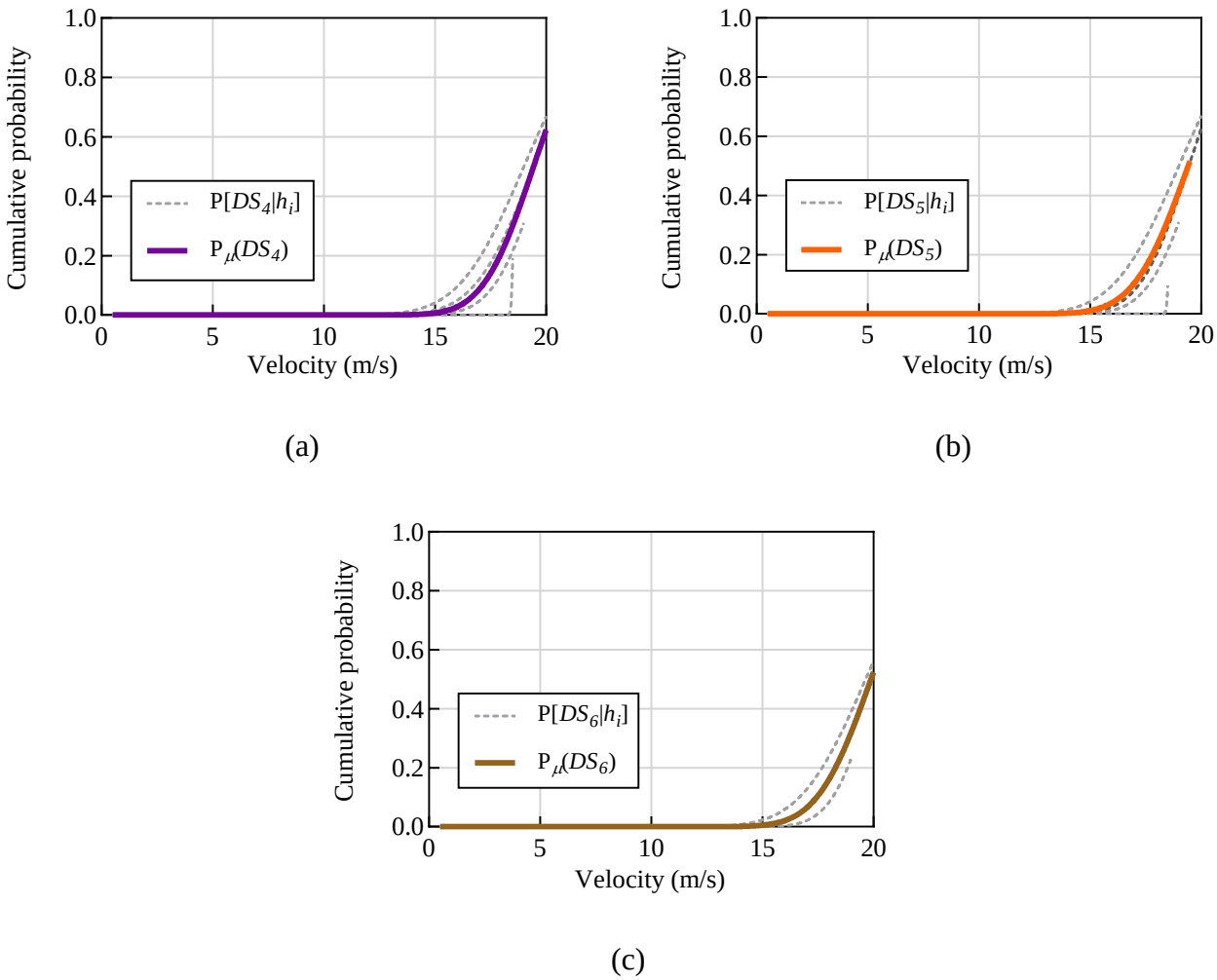


**Figure 6-7.** Fragility functions for velocity IM of the initial bridge: (a) *DS*$_4$; (b) *DS*$_5$; and (c) *DS*$_6$.

### 6.3.2 Inundation Depth

The fragility functions for the inundation depth IM is constructed by incrementing the inundation depth and computing the bridge response at all velocity ranges between 0.5 and 20 m/s for each inundation depth increment. Figure 6-5(b) shows the fragility function for inundation depth IM at a one velocity ($u$=13 m/s). The fragility functions for all inundation depth increments for the six damage states are shown in Figures 6-8 and 6-9. The discontinuity in the damage data at low inundation depth is due to $Fr_{limit}$. The fragility functions in Figures 6-6 to 6-9 show that the velocity and inundation IMs generally provide similar scatter in damage probability data, as they are obtained from the same combinations of velocity and inundation depth increments, and hence similar response of bridge is obtained. Figures 6-10 shows the fragility functions for all damage states for velocity and inundation depth IMs. The fragility functions of $DS_4$ were found to provide similar values to $DS_3$, and hence they were not included in the comparison. The use of different IMs provides different estimation of the damage probability of bridge as shown in Figures 6-10(a and b). For instance, the maximum damage probability for $DS_2$ is about 100% in the velocity IM, while it is below 80% in the inundation depth IM.

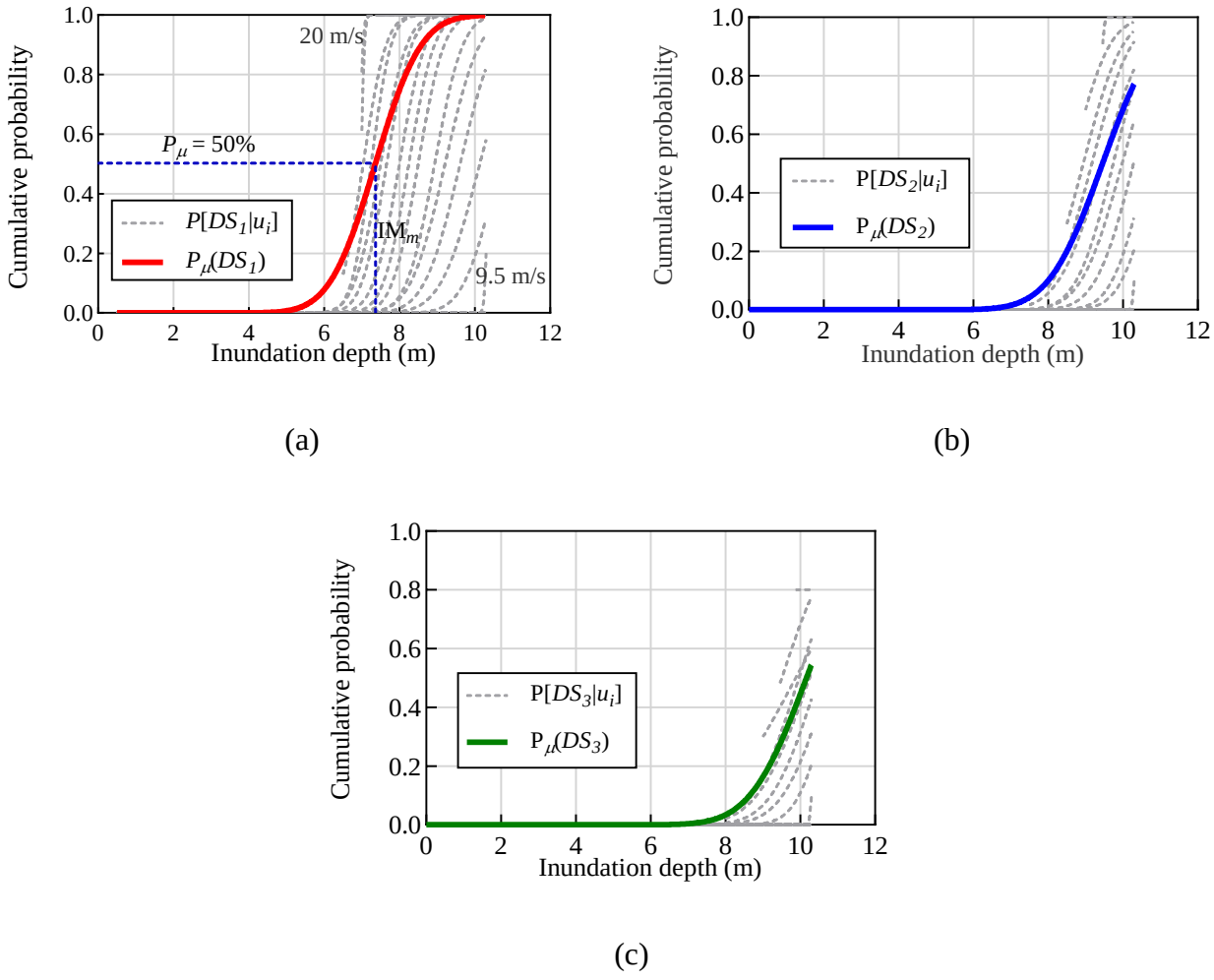


**Figure 6-8.** Fragility functions for inundation depth IM of the initial bridge: (a) *DS₁*; (b) *DS₂*; and (c) *DS₃*.

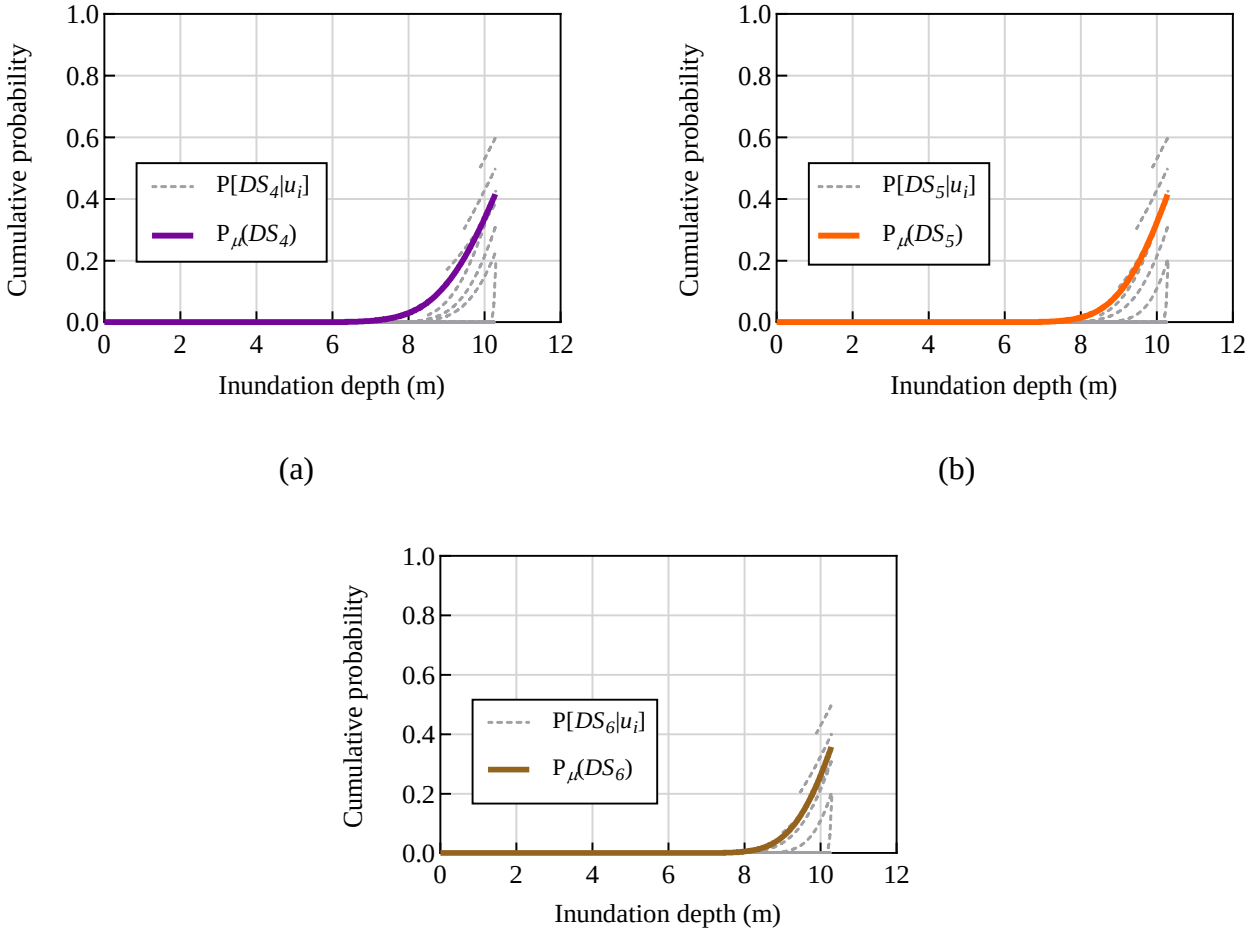


**Figure 6-9.** Fragility functions for inundation depth IM of the initial bridge: (a) *DS₄*; (b) *DS₅*; and (c) *DS₆*.

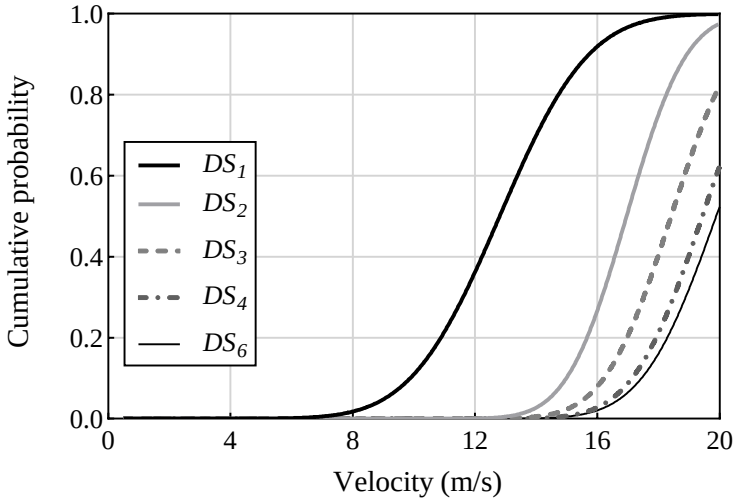


(a)

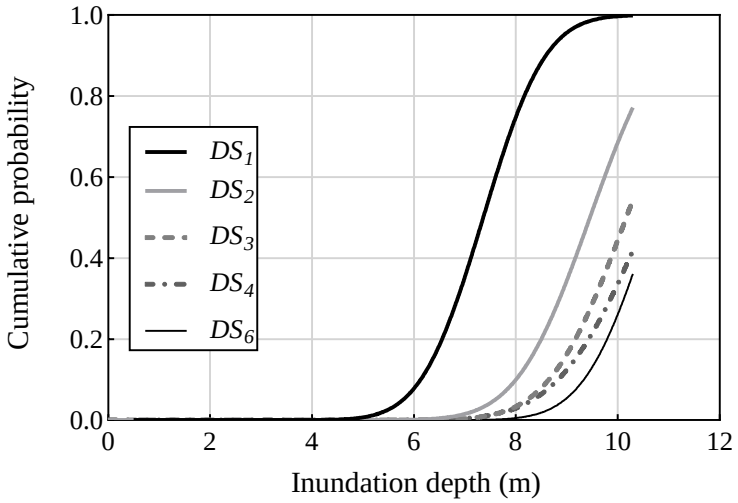


(b)

**Figure 6-10.** Mean fragility curves for initial bridge at $DS_1$, $DS_2$, $DS_3$, $DS_4$ and $DS_6$: (a) velocity IM; and (b) inundation depth IM.

## 6.4 Two-Parameter IM

### 6.4.1 Momentum Flux

A combination of the damage probability of velocity and inundation depth can be obtained using two-parameter IMs such as the momentum flux ($hu^2$). The ranges of momentum flux are generated by selecting small increments of both inundation depth and velocity, or the momentum flux itself is incremented with the velocity or inundation depth. This is because the magnitude of momentum flux is a function of both the inundation depth and velocity, and their increments have a significant influence on the bridge response. A momentum flux increment of 20.596 $m^3/s^2$ was used for 200 points until 4119.2 $m^3/s^2$, and the inundation depth was increased using the same increments adopted for the inundation and velocity IMs. The damage probability for one inundation depth (8.5 m) using momentum flux IM is shown in Figure 6-5(c). As the figure shows, an even distribution of the damage probability data (between 0 and 1) is obtained at all increments. Figures 6-11 and 6-12 show the overall fragility functions for momentum flux IM for the six damage states. The scatter in damage probability functions at each inundation depth for the momentum flux IM is less than the velocity and inundation IMs. To examine further the scatter in damage probability data of the different IMs used in this study, the standard deviations of the damage probability data points ($P_\sigma$) at the intensity measure ($IM_m$) that corresponds to a damage probability of 50% (see Figure 6-11(a)) are calculated and presented in Table 6-8. The standard deviations of the initial ($P_\sigma^{initial}$) and strengthened ($P_\sigma^{strengthened}$) bridge show that the use of momentum flux IM leads to a reduction in the discrepancy between the damage probability data compared to the singe-parameter IMs. In addition, the trend line of the mean damage probability data shows better correlation with the overall fragility functions representing each inundation

depth in comparison with the single-parameter IMs. However, the large standard deviations of momentum flux IMs indicate that the damage probability data still show some scatter, which is attributed to the cases corresponding to more than one possible value of hydrodynamic force. As in the velocity IM, at low inundation depths (6.5 m) the damage data are subjected to the $Fr_{limit}$ to exclude the unrealistic cases as shown in Figure 6-11(a).

**Table 6-8.** Summary of results for the damage assessment of the case study bridge.

| IM investigated | Performance level | Correlation with structural response | | Strengthening effect | | |
|---|---|---|---|---|---|---|
| | | $P_{\sigma}^{initial}$ | $P_{\sigma}^{strengthened}$ | $P_{\mu}^{initial}$ | $P_{\mu}^{strengthened}$ | % reduction in damage probability |
| Velocity | $DS_1$ | 0.46 | 0.43 | 0.50 | 0.24 | 52 |
| | $DS_2$ | 0.25 | 0.24 | 0.50 | 0.30 | 40 |
| | $DS_3$ | 0.13 | N/A[a] | 0.50 | 0.03 | 94 |
| | $DS_4$ | 0.07 | N/A[a] | 0.50 | 0.11 | 78 |
| | $DS_5$ | 0.07 | N/A[a] | 0.50 | 0.00 | 100 |
| | $DS_6$ | N/A[a] | N/A[b] | 0.50 | 0.00 | 100 |
| Inundation depth | $DS_1$ | 0.41 | 0.37 | 0.50 | 0.27 | 46 |
| | $DS_2$ | 0.34 | 0.35 | 0.50 | 0.43 | 14 |
| | $DS_3$ | 0.32 | 0.11 | 0.50 | 0.16 | 68 |
| | $DS_4$ | 0.23 | 0.11 | 0.50 | 0.20 | 60 |
| | $DS_5$ | 0.23 | 0.12 | 0.50 | 0.20 | 60 |
| | $DS_6$ | 0.20 | N/A[b] | 0.50 | 0.00 | 100 |
| Momentum flux | $DS_1$ | 0.37 | 0.31 | 0.50 | 0.10 | 80 |
| | $DS_2$ | 0.16 | 0.08 | 0.50 | 0.30 | 40 |
| | $DS_3$ | 0.00 | N/A[a] | 0.50 | 0.02 | 96 |
| | $DS_4$ | 0.00 | N/A[a] | 0.50 | 0.04 | 92 |
| | $DS_5$ | 0.00 | N/A[a] | 0.50 | 0.00 | 100 |
| | $DS_6$ | N/A[a] | N/A[b] | 0.50 | 0.00 | 100 |
| Moment of momentum flux | $DS_1$ | 0.00 | 0.00 | 0.50 | 0.05 | 90 |
| | $DS_2$ | 0.00 | 0.00 | 0.50 | 0.27 | 46 |
| | $DS_3$ | 0.00 | N/A[b] | 0.50 | 0.00 | 100 |
| | $DS_4$ | N/A[b] | N/A[b] | 0.50 | N/A[b] | N/A[b] |
| | $DS_5$ | N/A[b] | N/A[b] | 0.50 | N/A[b] | N/A[b] |
| | $DS_6$ | N/A[b] | N/A[b] | 0.50 | N/A[b] | N/A[b] |

Notes: $P_{\mu}^{initial}$ and $P_{\mu}^{strengthened}$ correspond to the $IM_m$ for initial bridge. The maximum value of $P_{\mu}$ is used in cases where it is below 50%.

[a] Not applicable as only one damage data is available.

[b] No damage data is available.

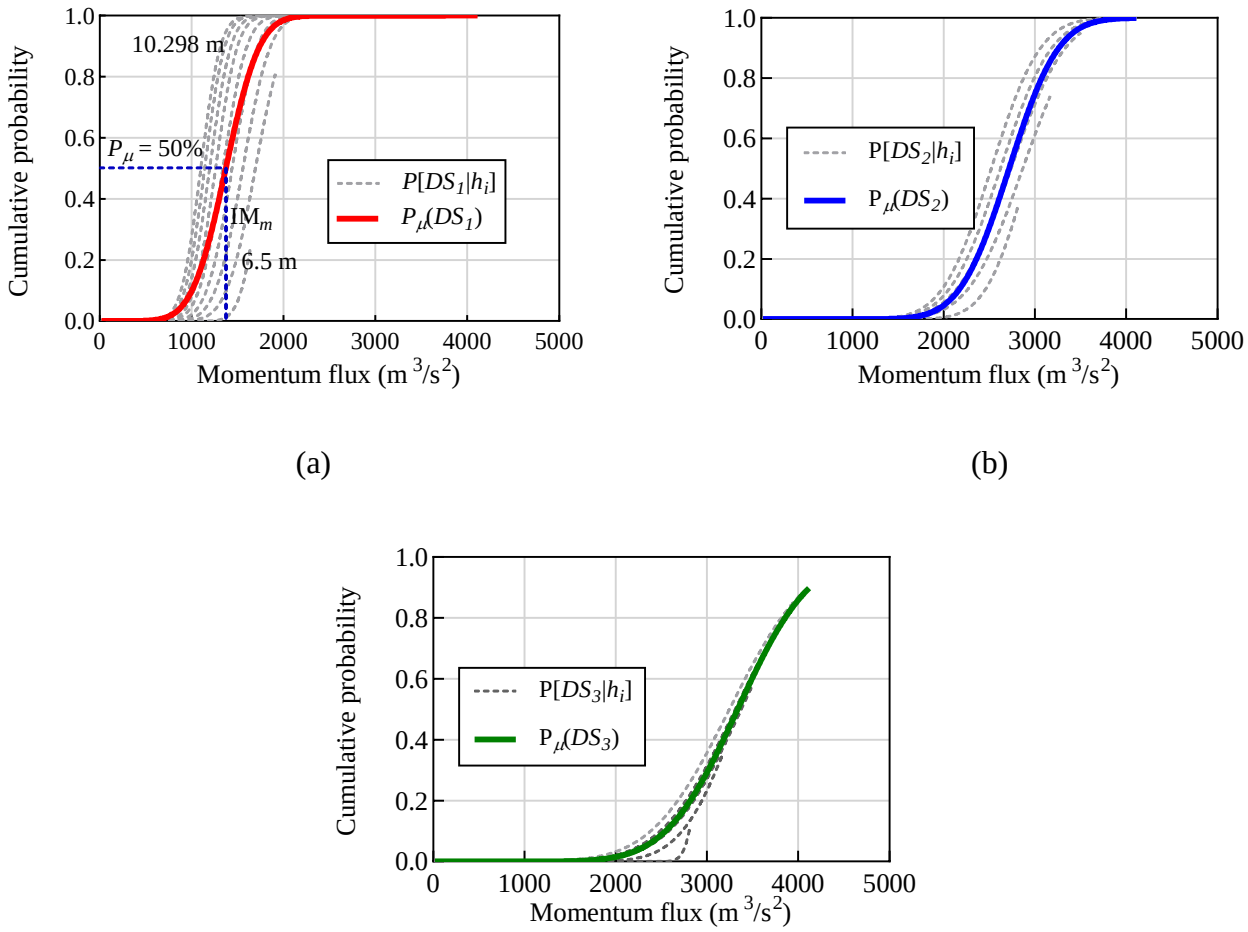


**Figure 6-11.** Fragility functions for momentum flux IM of the initial bridge: (a) $DS_1$; (b) $DS_2$; and (c) $DS_3$.

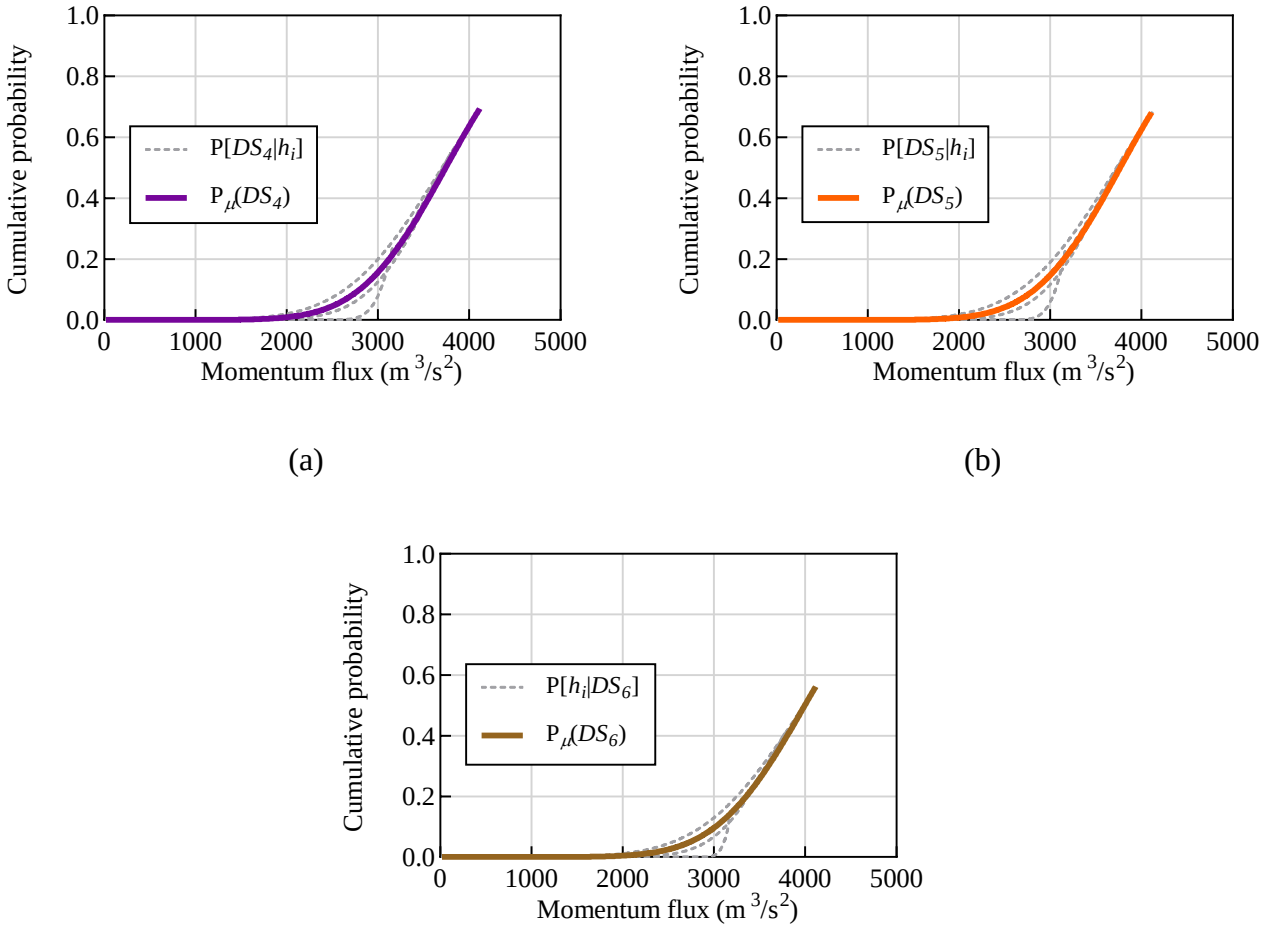


**Figure 6-12.** Fragility functions for momentum flux IM of the initial bridge: (a) *DS*$_4$; (b) *DS*$_5$; and (c) *DS*$_6$.

### 6.4.2 Moment of Momentum Flux

For the analyses that adopt the moment of momentum flux ($h^2u^2/2$) IM, an increment of 51.49 $m^4/s^2$ was used for 250 points until 12872.2 $m^4/s^2$. Figure 6-13 shows the fragility function of bridge using moment of momentum flux for the first three (pre-peak stage) damage states. The significant reduction in the scatter between the data at different inundation depths can be observed. In addition, there is no standard deviation at $IM_m$ as shown in **Table 6-8**. This means that the same damage probability values were obtained at $IM_m$, which indicates almost no discrepancy in the bridge response. In fact, the trend lines representing the different inundations show a typical fragility function. Hence, the use of moment of momentum flux is more efficient for representing the structural response than the other IMs, as each damage probability data point represents only one case of hydrodynamic force. Figures 6-14(a and b) show the fragility function mean trend lines at different damages states for the momentum flux and moment of momentum flux IMs. Overall, the fragility functions using the momentum flux show higher damage probability values compared to the inundation depth and velocity. The damage probability data for the moment of momentum flux at $DS_2$ and $DS_3$ are relatively smaller than the momentum flux (see Figures 6-14(a and b)). In this study, the velocity corresponding to the maximum moment of momentum flux was 15.6 m/s for an inundation depth of 10.298 m. The corresponding velocities increase with the decrease in inundation depth, but due to $Fr_{limit}$, the resulting forces were not included in the analysis. Hence, the resulting response in the structure did not represent the damage beyond $DS_3$ for the range of moment of momentum flux values considered in the analysis presented in this study. It should be mentioned that the increments and number of data points of the two-parameter IMs were selected to provide accurate estimation of the fragility function with acceptable computational time. Hence, the

increase in the maximum moment of momentum flux may result in differences (if larger increments are considered) of the estimated fragility functions or larger computational time (if more data points are considered). The overall analysis results show that the two-parameter IMs show an inverse relationship with the inundation, which is also observed in the velocity IM.

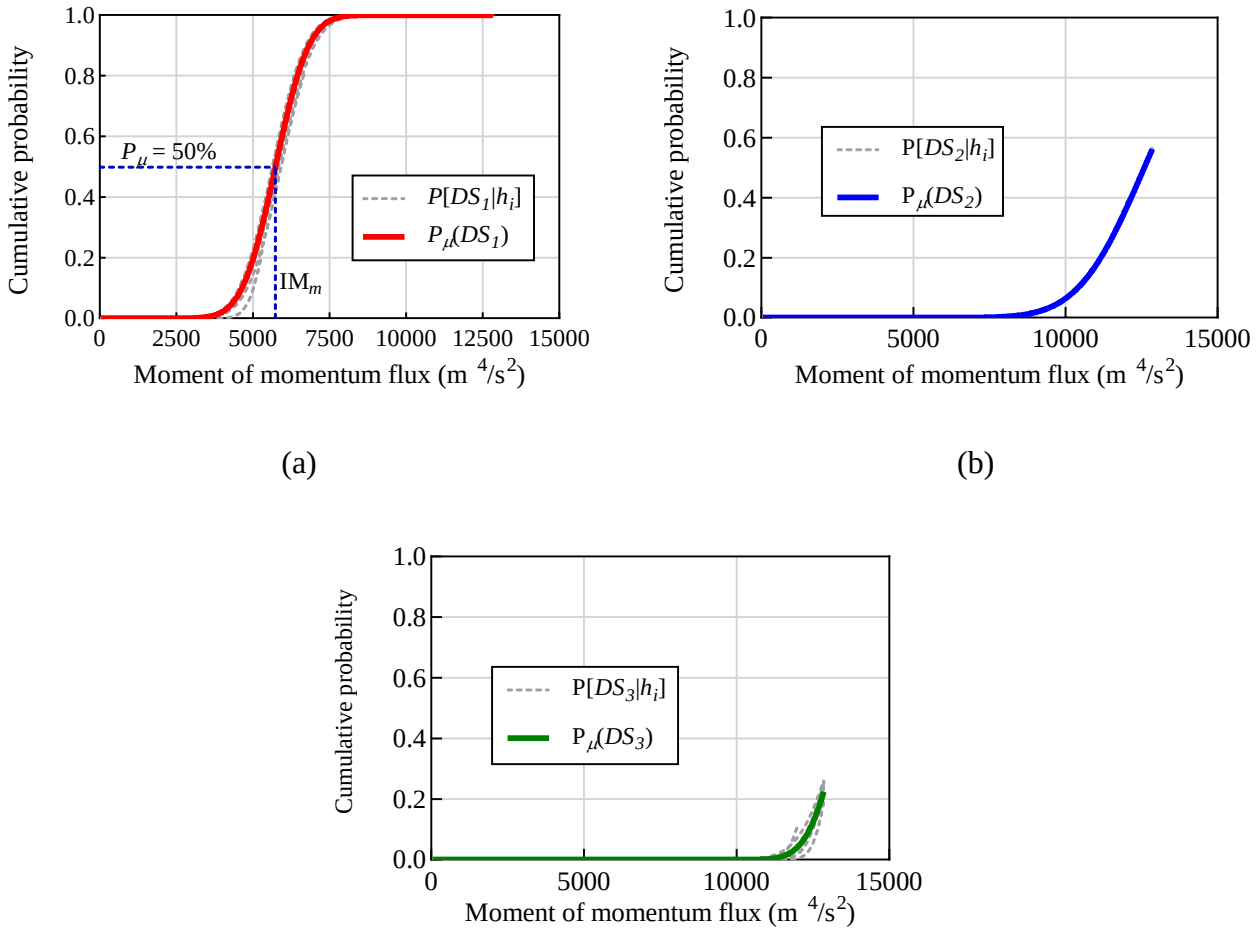


**Figure 6-13.** Fragility functions for moment of momentum flux IM of the initial bridge: (a) *DS1*; (b) *DS2*; and (c) *DS3*.

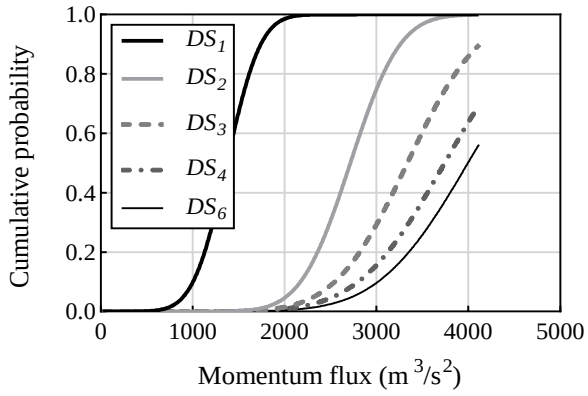


(d)

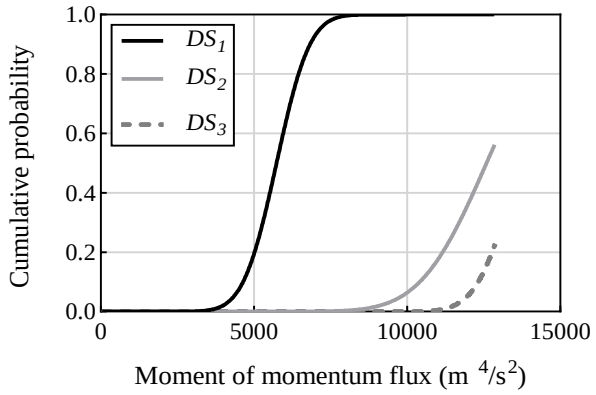


(b)

**Figure 6-14.** Mean fragility curves for initial bridge at *DS₁*, *DS₂*, *DS₃*, *DS₄* and *DS₆*: (a) momentum flux; and (b) moment of momentum flux.

### 6.5 Fragility Functions of Strengthened Bridge

The fragility of bridge with FRP-confined piers is investigated for all damage states and IMs. As in the initial bridge, the scatter in data for the different IMs at all damage states for the strengthened bridge are shown in Figures 6-15 to 6-21. Figure 6-22 shows the mean trend

lines of fragility functions for all IMs. These trend lines are used to examine the reduction in damage probability in the strengthened bridge. A comparison of the fragility analyses results between the initial and strengthened bridge is presented in Table 6-8. In addition, Figures 6-23 to 6-26 show a comparison of the fragility functions at $DS_1$, $DS_2$, $DS_3$ and $DS_6$ for all IMs. The mean damage probabilities data of initial ($P_{\mu}^{initial}$) and strengthened ($P_{\mu}^{strengthened}$) bridge at $IM_m$ are compared in Table 6-8, and their reduction percentages are summarized to examine the viability of FRP jackets for reducing the vulnerability of bridges under extreme wave forces. The results show that the strengthened bridge exhibited significant enhancement in capacity at all performance levels. In particular, the flexural ductility of strengthened bridge, which is defined by the reserve strength in the post-peak stage, was improved. This is shown by the significant reduction in damage probability at collapse stage (50% drop) $DS_6$, which was about 100% (except the moment of momentum flux). However, the fragility functions of strengthened bridge show some variation in the increase in capacity among the different IMs. For instance, the bridge showed a reduction in damage probability for inundation depth IM of about 52% for the cracking performance level ($DS_1$), while it was about 40% for the momentum flux. In addition, the damage probability for $DS_5$ was reduced by about 100% for velocity and momentum flux IMs, while it showed a drop of only 60% for the inundation depth. The reduction percentages in the two-parameter IMs are generally higher than the single-parameter IMs, which is attributed to the improvement in the accuracy of predicting the structural response. For example, the cracking ($DS_1$) probability of damage of strengthened bridge was about 24%, 27%, 10 and 5% for the velocity, inundation depth, momentum flux and moment of momentum flux IMs, respectively. In other words, the reduction in damage probability in the moment of momentum flux at $DS_1$ was about 90%, while it was almost about half of this percentage

(46%) in inundation depth IM. This significant difference indicates the advantage of using two-parameter IMs for providing more accurate representation of the enhancement of retrofit strategies for bridges under extreme wave hazards.

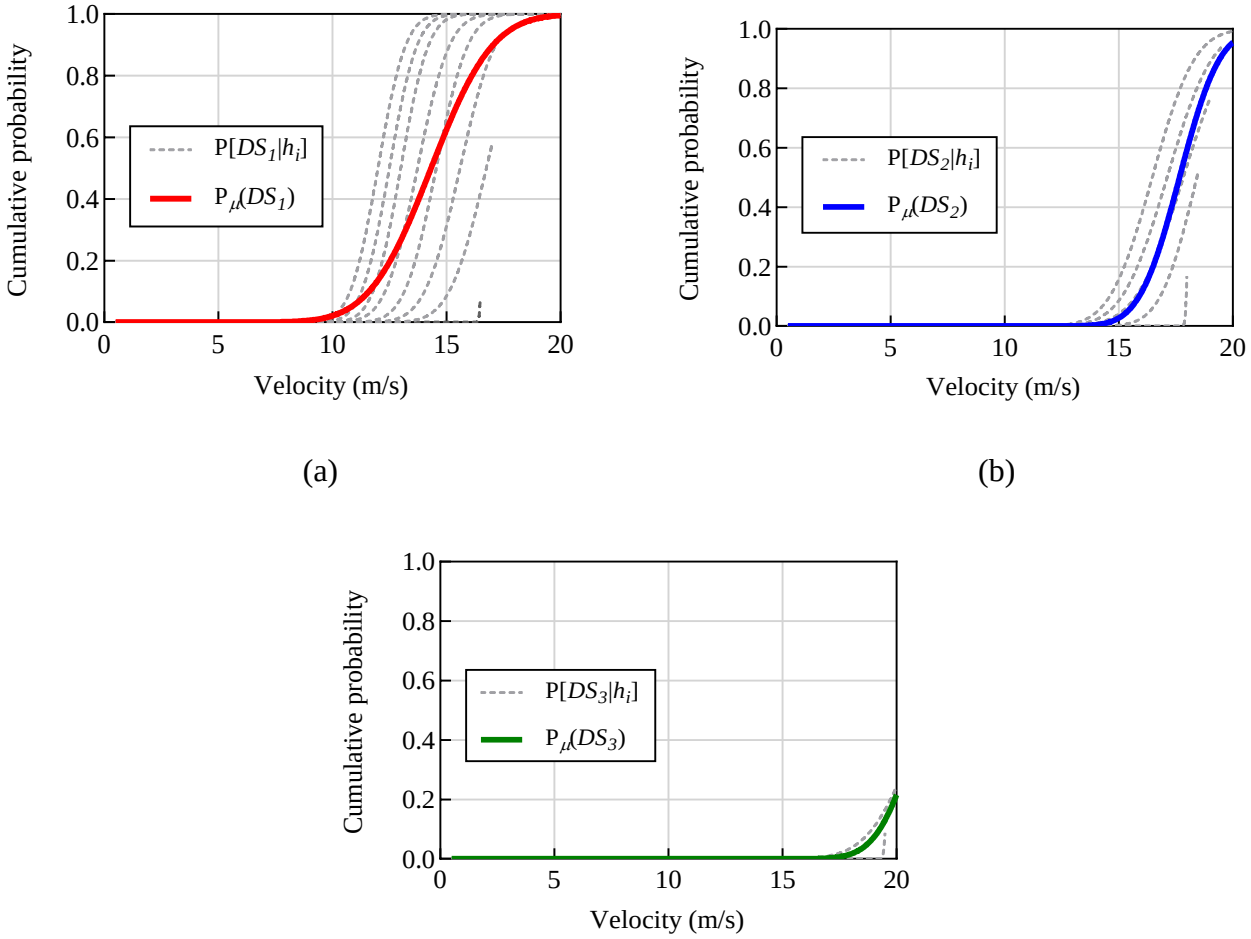


**Figure 6-15.** Fragility functions for velocity IM of the strengthened bridge: (a) *DS₁*; (b) *DS₂*; and (c) *DS₃*.

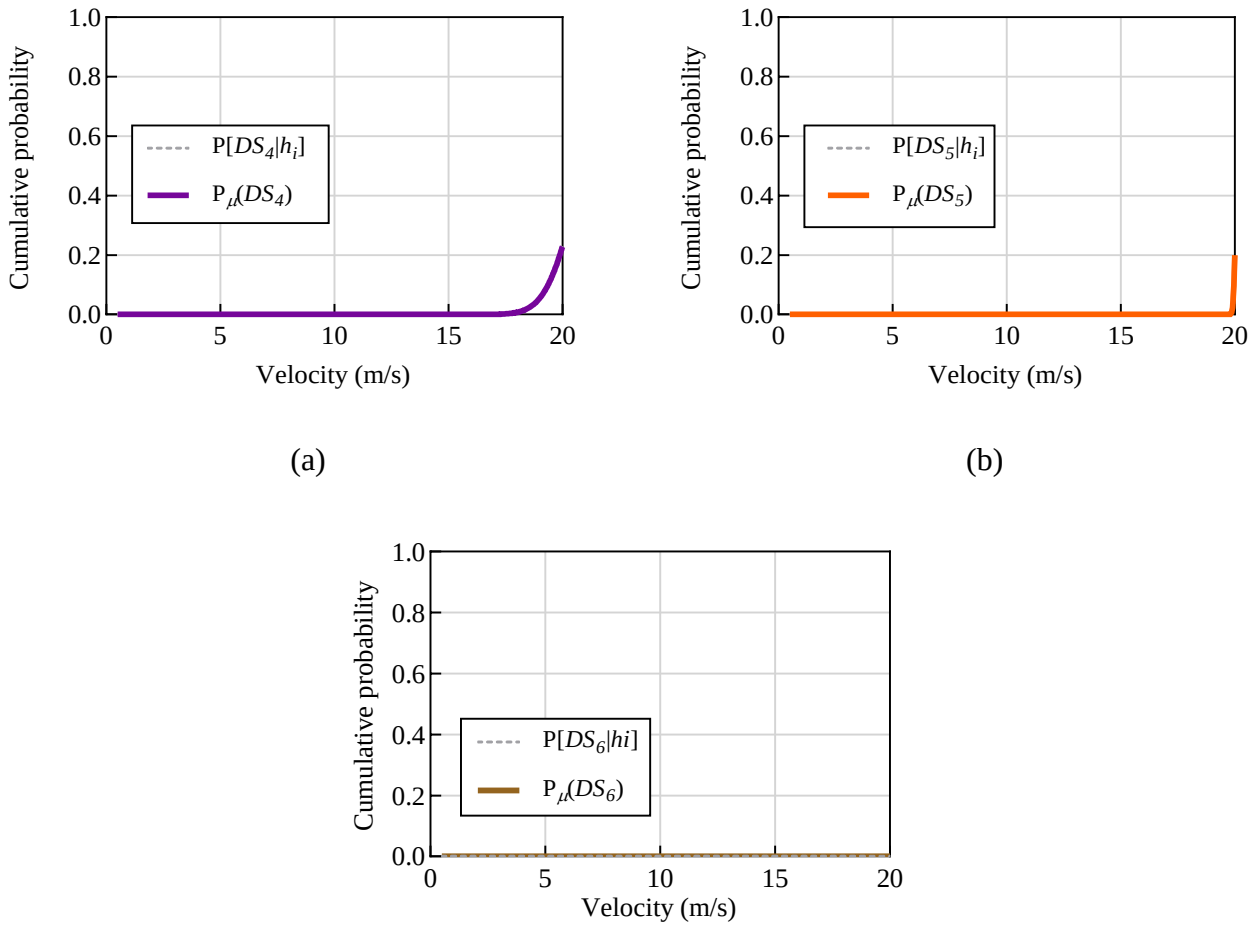


**Figure 6-16.** Fragility functions for velocity IM of the strengthened bridge: (a) *DS*$_4$; (b) *DS*$_5$; and (c) *DS*$_6$.

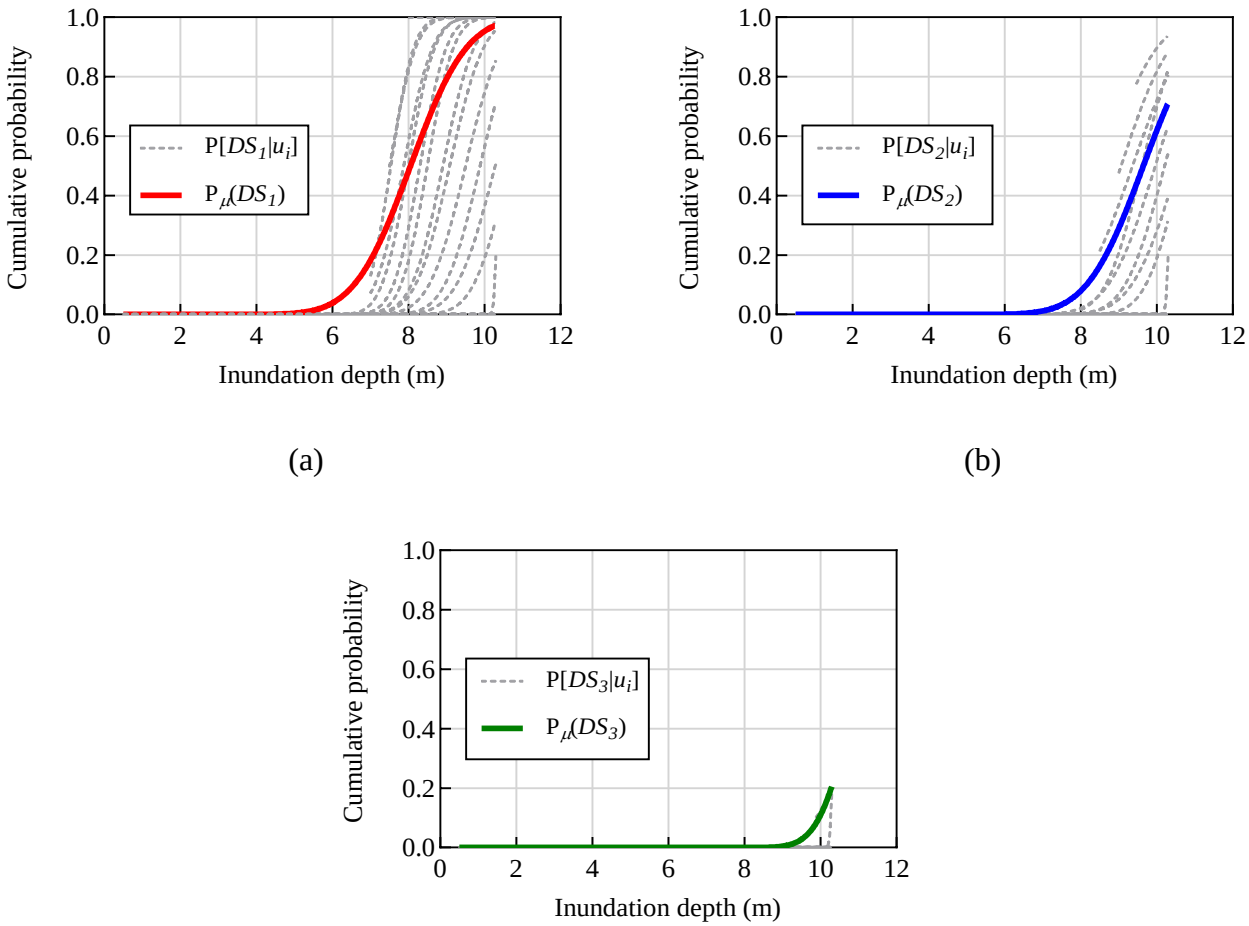


**Figure 6-17.** Fragility functions for inundation depth IM of the strengthened bridge: (a) *DS*$_1$; (b) *DS*$_2$; and (c) *DS*$_3$.

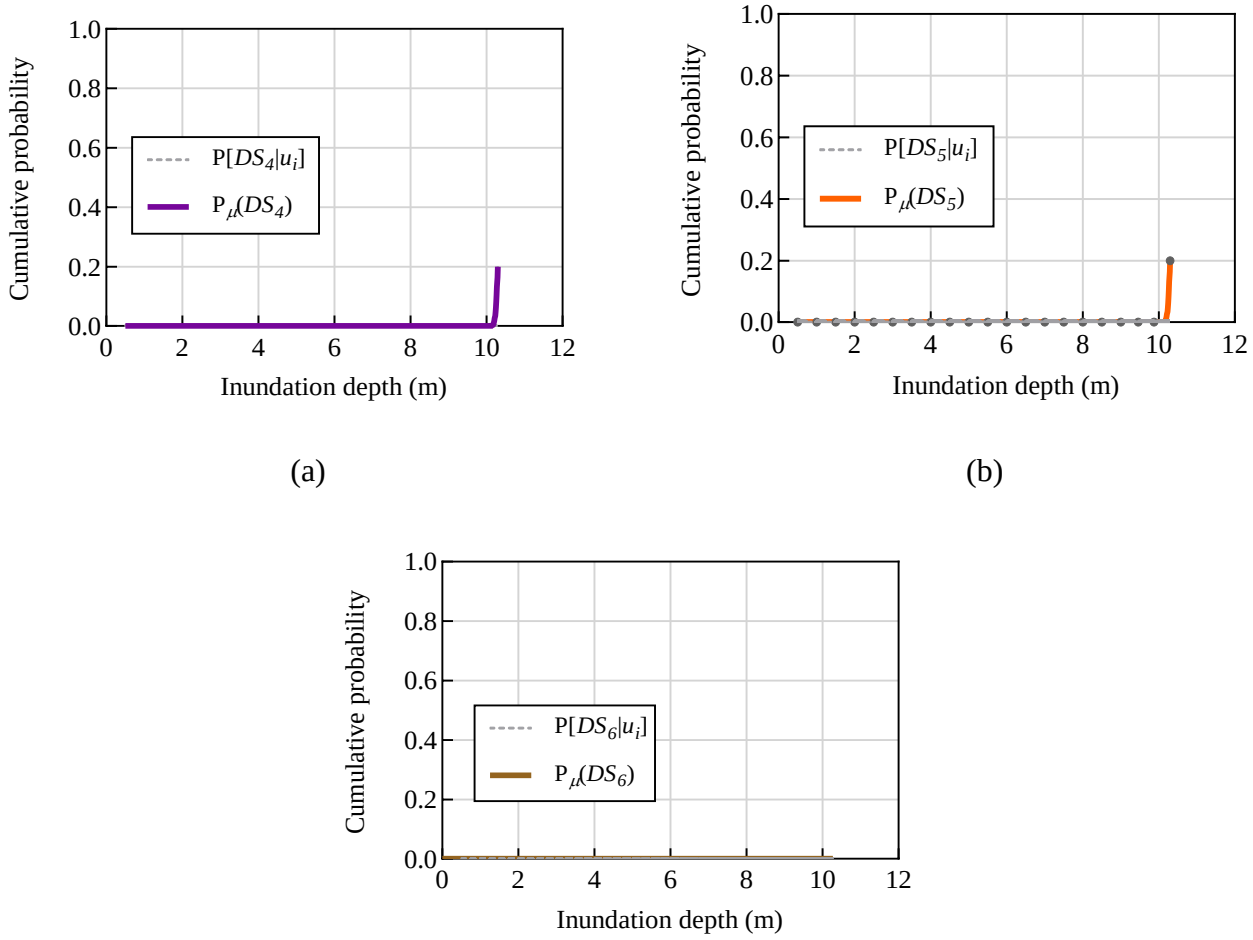


**Figure 6-18.** Fragility functions for inundation depth IM of the strengthened bridge: (a) *DS*$_4$; (b) *DS*$_5$; and (c) *DS*$_6$.

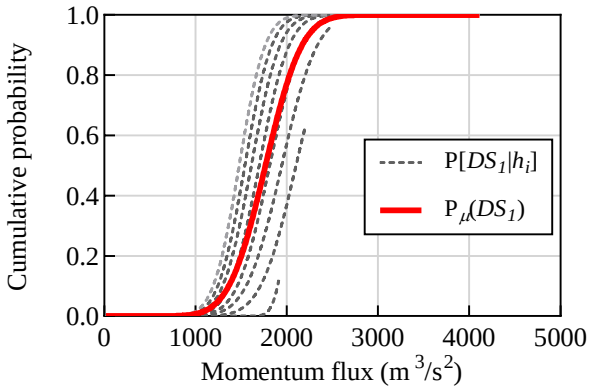


(a)

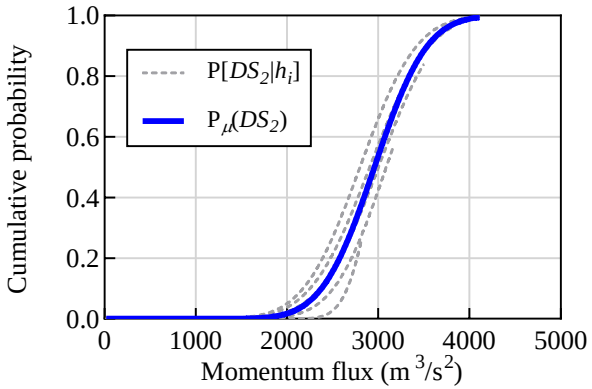


(b)

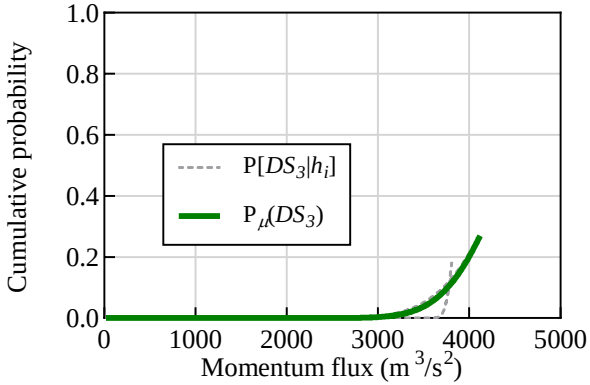


(c)

**Figure 6-19.** Fragility functions for momentum flux IM of the strengthened bridge: (a) *DS₁*; (b) *DS₂*; and (c) *DS₃*.

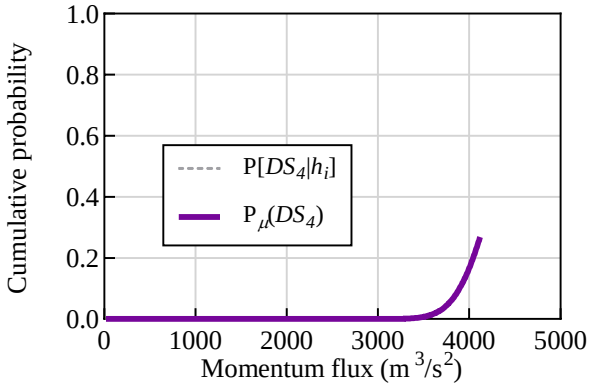


(a)

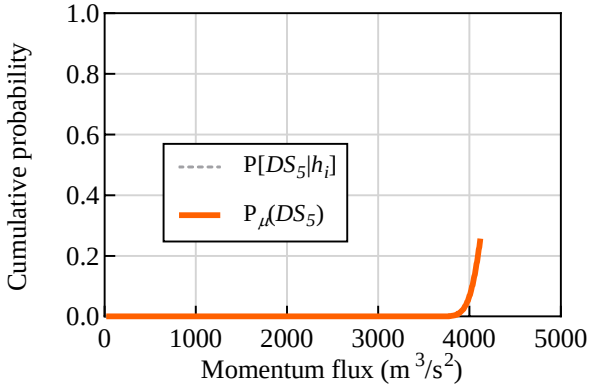


(b)

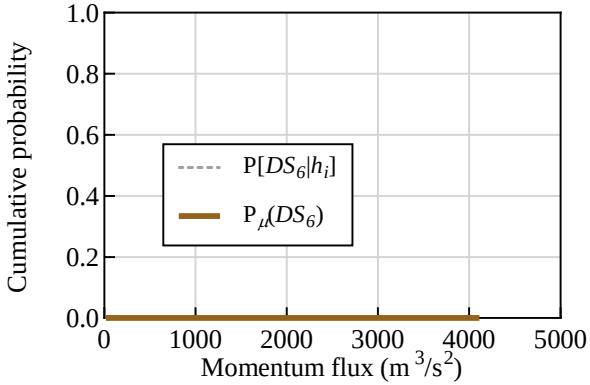


(c)

**Figure 6-20.** Fragility functions for momentum flux IM of the strengthened bridge: (a) *DS*$_4$; (b) *DS*$_5$; and (c) *DS*$_6$.

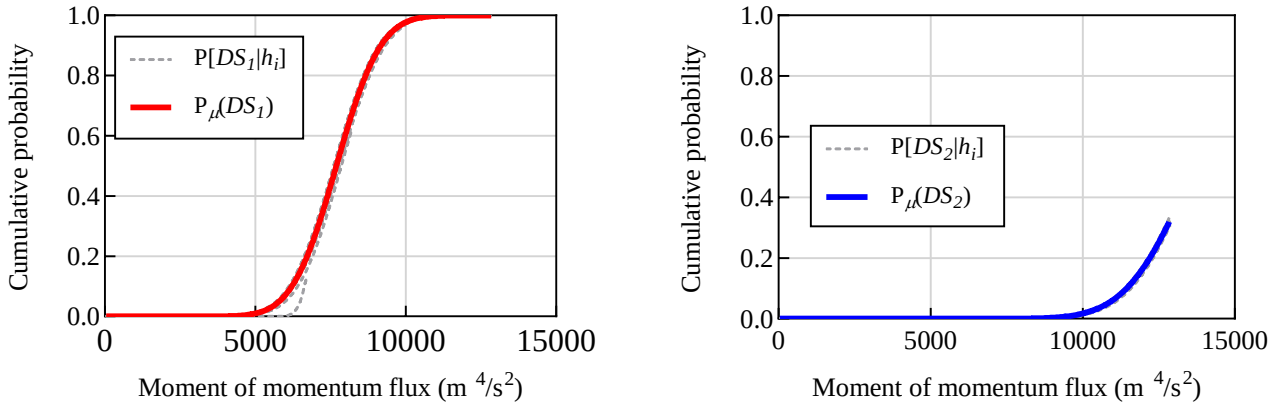


**Figure 6-21.** Fragility functions for moment of momentum flux IM of the strengthened bridge: (a) $DS_1$ and (b) $DS_2$.

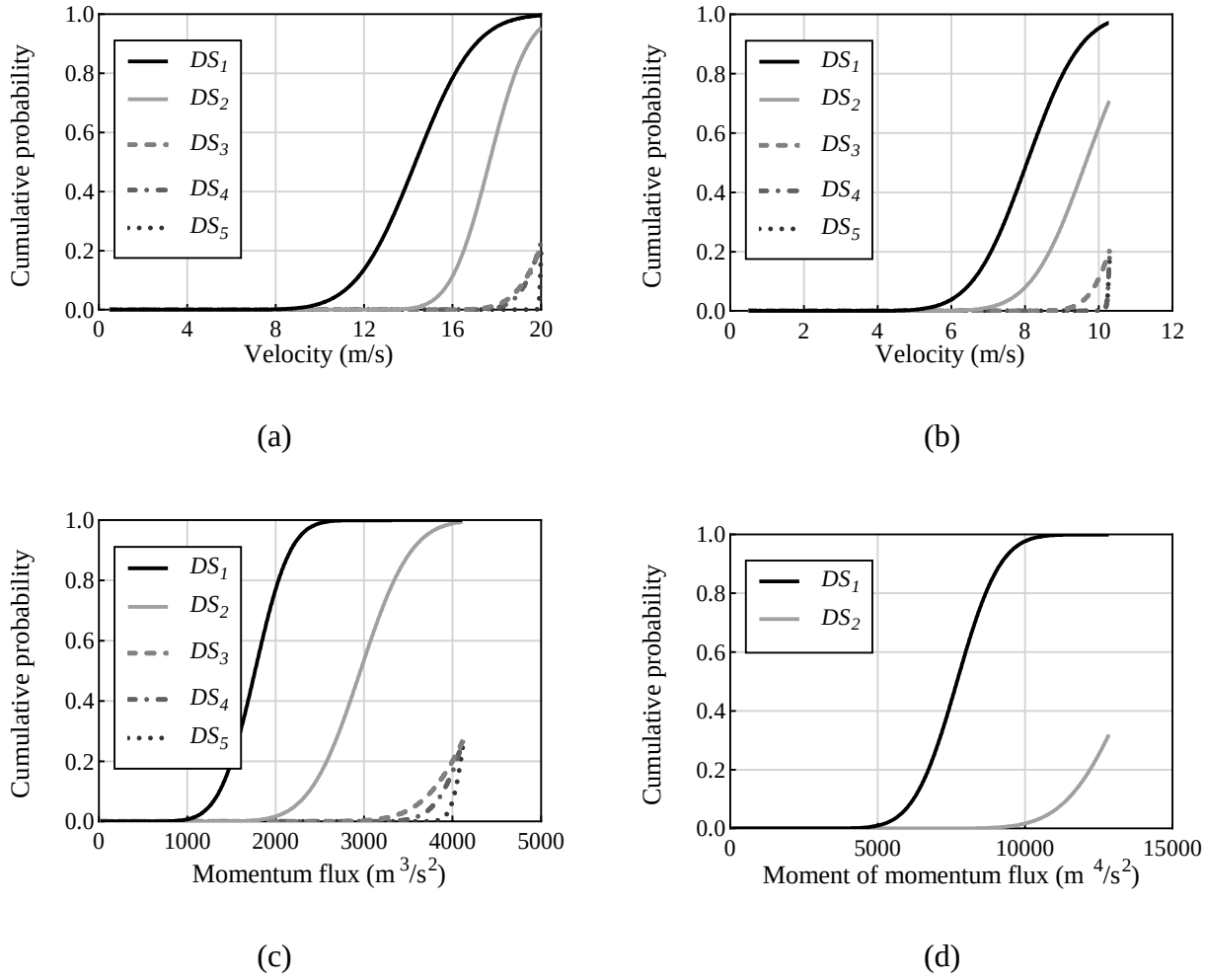


**Figure 6-22.** Mean fragility curves for strengthened bridge at $DS_1$, $DS_2$, $DS_3$, $DS_4$ and $DS_5$: (a) velocity; (b) inundation depth; (c) momentum flux; and (d) moment of momentum flux.

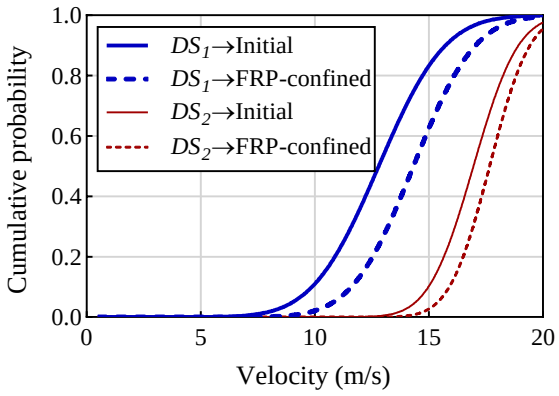


(a)

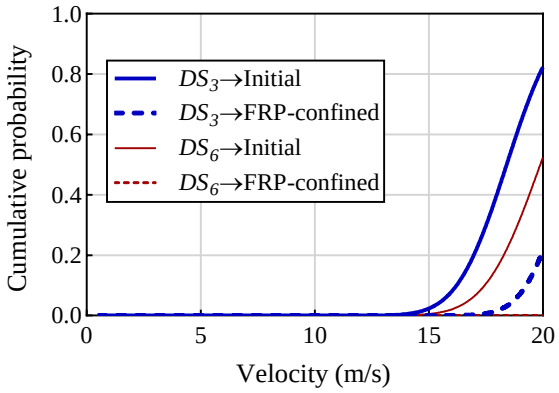


(b)

**Figure 6-23.** Fragility functions for the initial and FRP-confined bridge for velocity IMs: (a) first crack ($DS_1$) and yielding ($DS_2$); and (b) peak ($DS_3$) and complete collapse at 50% drop ($DS_6$).

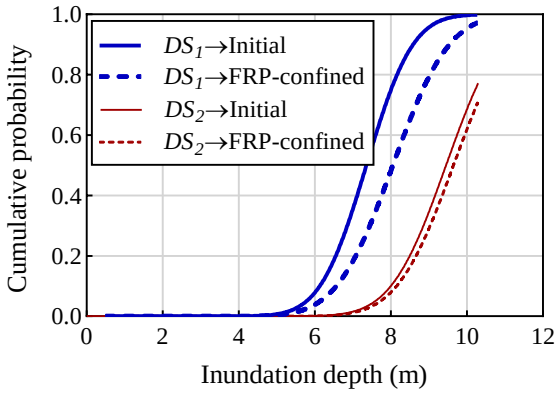


(a)

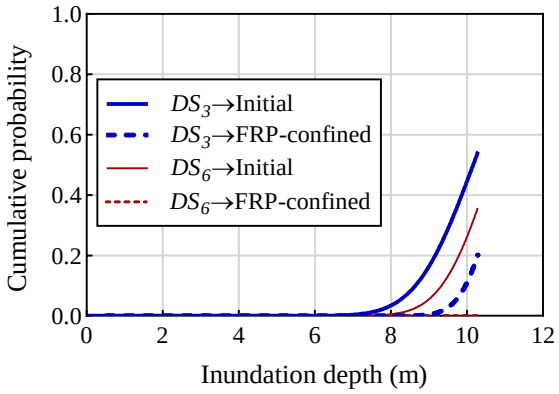


(b)

**Figure 6-24.** Fragility functions for the initial and FRP-confined bridge for inundation depth IMs: (a) first crack ($DS_1$) and yielding ($DS_2$); and (b) peak ($DS_3$) and complete collapse at 50% drop ($DS_6$).

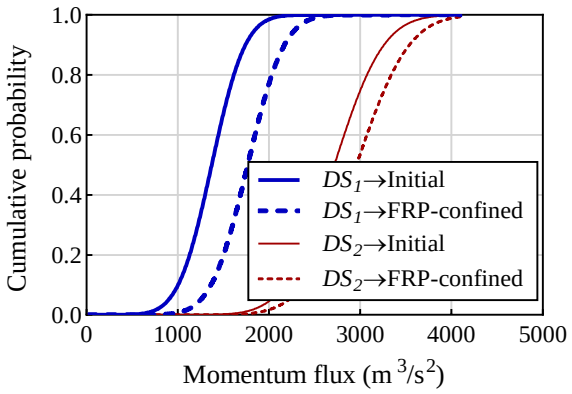


(a)

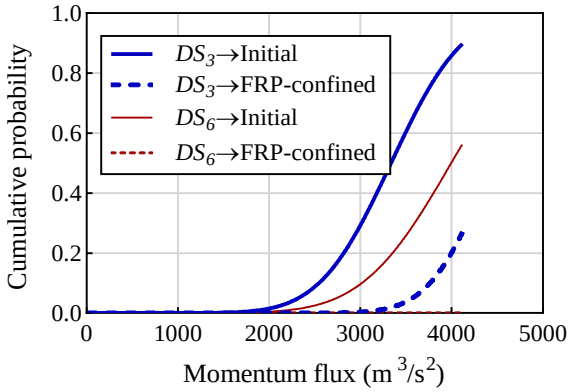


(b)

**Figure 6-25.** Fragility functions for the initial and FRP-confined bridge for momentum flux IMs: (a) first crack ($DS_1$) and yielding ($DS_2$); and (b) peak ($DS_3$) and complete collapse at 50% drop ($DS_6$).

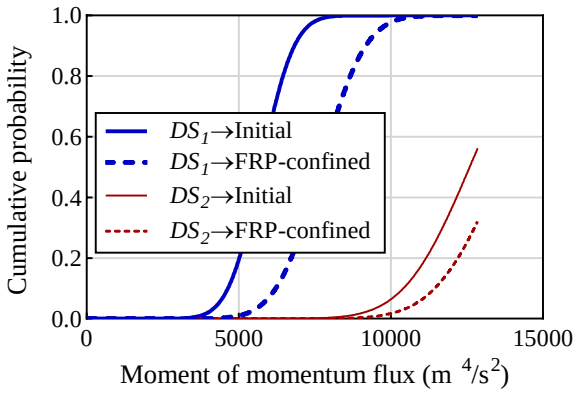


(a)

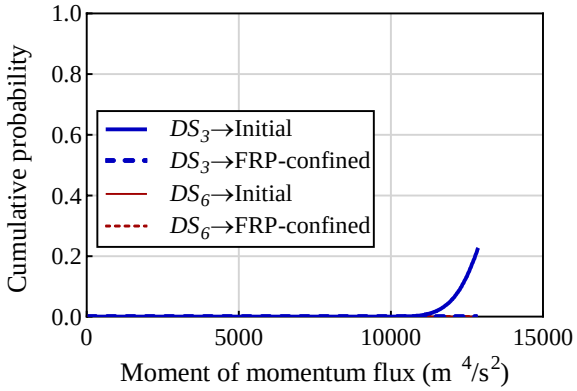


(b)

**Figure 6-26.** Fragility functions for the initial and FRP-confined bridge for moment of momentum flux IMs: (a) first crack ($DS_1$) and yielding ($DS_2$); and (b) peak ($DS_3$) and complete collapse at 50% drop ($DS_6$).

## 6.6 Application of Fragility Analysis Results for Resilience Quantification

The resilience restoration indices discussed in Chapter 3 can be applied to the damage probability results obtained from the fragility functions for the different IMs adopted in this study. Figure 6-27 illustrates the drop in performance in an example of fragility at IM = $x$, for a certain damage state. For the sake of illustration, it is assumed in this study that the damage index used for estimating the performance is inversely proportional to the damage probability obtained from the fragility analysis. For instance, at a damage probability of 40%, the performance index would be 60% (see Figure 6-27). Hence, a probability of damage of 100% would provide a performance index of 0% (complete collapse), while a probability of damage of 0% would provide a fully functional bridge ($Q$ = 100%). The resilience restoration for a bridge at the instant of extreme event can be estimated using the unified index $R_5$ that simultaneously takes into account the effect of time, resources and environmental impact of the different restoration strategies. The relationship in Figure 3-4 is adopted for the different performance levels. The variation in performance levels was estimated based on the assumption that the larger performance level requires less restoration time, resources and environmental impact. Therefore, the resilience quantification of the bridge for the different restoration strategies can be estimated at any IM. Tables 6-9 to 6-12 present the unified resilience indices for different IMs and performance levels. As can be seen, the effect of different recovery elements has a significant effect on the resilience index. In addition, the resilience quantification as a function of specific IMs is useful for the stakeholders to relate the level of hazards to the required resources, time and environmental impact for different recovery options. For example, at a velocity of 17.5 m/s the performance is expected to drop to 70% (see Table 6-9). If the time is specified as the priority, followed by the resources due to budget capping specified by the government, the resilience

importance factors can be taken as follows: $I_t$=0.67; $I_c$=0.33; and $I_e$=0. For such priorities, the available resilience indices can be 89.8, 86.1 and 83.6. The selection of any of these indices and their corresponding time, resources and environmental impact data would be based on the minimum quality aimed by the decision makers. For instance, if the minimum unified resilience index, $R_{min}$ is specified to be at 85% or greater to assure that the project is performed at the maximum possible quality, then a resilience index of 86.1% is selected the velocity value of 17.5 m/s. This would correspond to a time, cost and environmental impact values of 43 days, $\$136.7\times10^4$ and $0.37\times10^6$ kg, respectively. The same process for the different hazard intensities can be applied to all IMs.

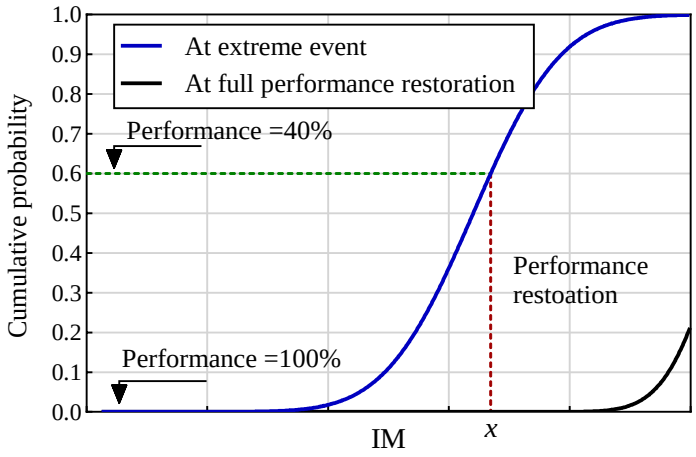


(a)

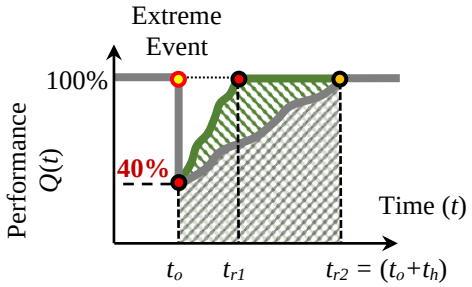


(b)

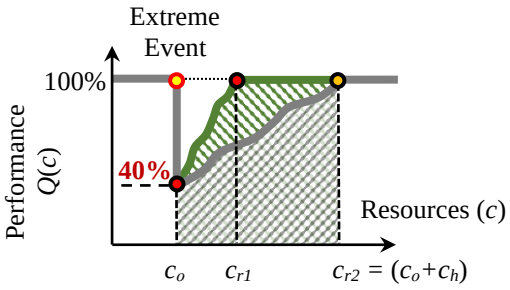


(c)

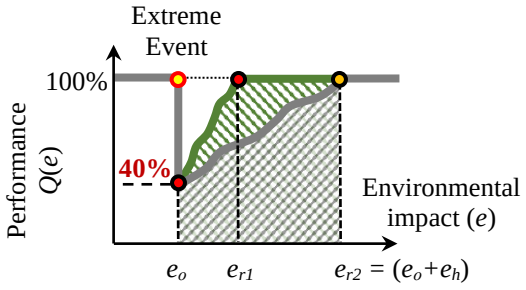


(d)

**Figure 6-27.** Application of fragility functions for resilience quantification: (a) example of fragility functions at extreme event for performance drop to 40%) and after restoration; (b) resilience triangle of time; (c) resilience triangle of resources; and (d) resilience triangle of environmental impact.

**Table 6-9.** Resilience assessment of bridge restoration based on the damage data from fragility analysis for velocity IM of initial bridge at $DS_3$.

| Velocity (m/s) | Performance at instant of extreme event (%) | Time at full performance restoration ($t_r$) (days) | | Resources at full performance restoration ($c_r$) ($\times 10^4$ \$) | | Environmental impact at full performance restoration ($e_r$) ($\times 10^6$ kg) | | Unified resilience factors $R_5$ (%) | | | | | | | |
|---|---|---|---|---|---|---|---|---|---|---|---|---|---|---|---|
| | | | | | | | | $I_t$=0; $I_c$=1; $I_e$=0 | $I_t$=1; $I_c$=0; $I_e$=0 | $I_t$=0; $I_c$=0; $I_e$=1 | $I_t$=0.67; $I_c$=0.33; $I_e$=0 | $I_t$=0; $I_c$=0.67; $I_e$=0.33 | $I_t$=0.67; $I_c$=0; $I_e$=0.33 | $I_t$=0.33; $I_c$=0.33; $I_e$=0.33 | $I_t$=0.33; $I_c$=0; $I_e$=0.67 |
| 17.5 | 70 | $t_{r1} = t_c$ | 27 | $c_{r1} = c_c$ | 148.7 | $e_{r1}$ | 0.6 | 82.6 | 93.3 | 84.3 | 89.8 | 83.1 | 90.3 | 85.9 | 87.3 |
| | | $t_{r2}$ | 43 | $c_{r2}$ | 136.7 | $e_{r2}$ | 0.37 | 84.2 | 87.0 | 93.3 | 86.1 | 87.2 | 89.1 | 87.3 | 91.2 |
| | | $t_{r3}=t_n$ | 53 | $c_{r5} = c_n$ | 133.3 | $e_{r3}$ | 0.3 | 84.7 | 83.1 | 96.1 | 83.6 | 88.4 | 87.4 | 87.1 | 91.8 |
| 18.4 | 50 | $t_{r1} = t_c$ | 44 | $c_{r1} = c_c$ | 247.8 | $e_{r1}$ | 1.0 | 69.1 | 86.6 | 68.6 | 80.9 | 69.0 | 80.7 | 74.0 | 74.5 |
| | | $t_{r2}$ | 71 | $c_{r2}$ | 227.8 | $e_{r2}$ | 0.62 | 71.8 | 76.0 | 83.5 | 74.7 | 75.7 | 78.5 | 76.4 | 81.0 |
| | | $t_{r3}=t_n$ | 89 | $c_{r5} = c_n$ | 222.2 | $e_{r3}$ | 0.5 | 72.6 | 69.0 | 88.2 | 70.2 | 77.8 | 75.3 | 75.8 | 81.9 |
| 19.8 | 20 | $t_{r1} = t_c$ | 71 | $c_{r1} = c_c$ | 396.4 | $e_{r1}$ | 1.6 | 49.0 | 76.0 | 45.0 | 67.1 | 47.7 | 65.8 | 56.1 | 55.2 |
| | | $t_{r2}$ | 114 | $c_{r2}$ | 364.4 | $e_{r2}$ | 1.0 | 53.3 | 59.1 | 68.6 | 57.2 | 58.4 | 62.3 | 59.7 | 65.5 |
| | | $t_{r3}=t_n$ | 142 | $c_{r5} = c_n$ | 355.6 | $e_{r3}$ | 0.8 | 54.5 | 48.1 | 76.4 | 50.3 | 61.8 | 57.5 | 59.1 | 67.1 |

**Table 6-10.** Resilience assessment of bridge restoration based on the damage data from fragility analysis for inundation depth IM of initial bridge at $DS_3$.

| Inundation depth (m) | Performance at instant of extreme event (%) | Time at full performance restoration ($t_r$) (days) | | Resources at full performance restoration ($c_r$) ($\times 10^4$ \$) | | Environmental impact at full performance restoration ($e_r$) ($\times 10^6$ kg) | | Unified resilience factors $R_5$ (%) | | | | | | | |
|---|---|---|---|---|---|---|---|---|---|---|---|---|---|---|---|
| | | | | | | | | $I_t$=0; $I_c$=1; $I_e$=0 | $I_t$=1; $I_c$=0; $I_e$=0 | $I_t$=0; $I_c$=0; $I_e$=1 | $I_t$=0.67; $I_c$=0.33; $I_e$=0 | $I_t$=0; $I_c$=0.67; $I_e$=0.33 | $I_t$=0.67; $I_c$=0; $I_e$=0.33 | $I_t$=0.33; $I_c$=0.33; $I_e$=0.33 | $I_t$=0.33; $I_c$=0; $I_e$=0.67 |
| 9.25 | 78 | $t_{r1} = t_c$ | 20 | $c_{r1} = c_c$ | 109.0 | $e_{r1}$ | 0.44 | 87.9 | 96.1 | 90.6 | 93.4 | 88.8 | 94.3 | 90.6 | 92.4 |
| | | $t_{r2}$ | 31 | $c_{r2}$ | 100.2 | $e_{r2}$ | 0.27 | 89.1 | 91.8 | 97.3 | 90.9 | 91.8 | 93.6 | 91.8 | 95.4 |
| | | $t_{r3}=t_n$ | 39 | $c_{r5} = c_n$ | 97.8 | $e_{r3}$ | 0.22 | 89.5 | 88.6 | 99.2 | 88.9 | 92.7 | 92.1 | 91.5 | 95.7 |
| 10.0 | 55 | $t_{r1} = t_c$ | 40 | $c_{r1} = c_c$ | 223.0 | $e_{r1}$ | 0.9 | 72.5 | 88.2 | 72.5 | 83.0 | 72.5 | 83.0 | 77.0 | 77.7 |
| | | $t_{r2}$ | 64 | $c_{r2}$ | 205.0 | $e_{r2}$ | 0.56 | 74.9 | 78.8 | 85.9 | 77.5 | 78.5 | 81.1 | 79.1 | 83.5 |
| | | $t_{r3}=t_n$ | 80 | $c_{r5} = c_n$ | 200.0 | $e_{r3}$ | 0.45 | 75.6 | 72.5 | 90.2 | 73.5 | 80.4 | 78.3 | 78.6 | 84.3 |
| 10.298 | 46 | $t_{r1} = t_c$ | 48 | $c_{r1} = c_c$ | 267.6 | $e_{r1}$ | 1.08 | 66.5 | 85.1 | 65.4 | 78.9 | 66.1 | 78.6 | 71.6 | 71.9 |
| | | $t_{r2}$ | 77 | $c_{r2}$ | 246.0 | $e_{r2}$ | 0.67 | 69.4 | 73.7 | 81.5 | 72.3 | 73.4 | 76.3 | 74.1 | 78.9 |
| | | $t_{r3}=t_n$ | 96 | $c_{r5} = c_n$ | 240.0 | $e_{r3}$ | 0.54 | 70.2 | 66.2 | 86.6 | 67.5 | 75.6 | 73.0 | 73.6 | 79.9 |

**Table 6-11.** Resilience assessment of bridge restoration based on the damage data from fragility analysis for momentum flux IM of initial bridge at $DS_3$.

| Momentum flux ($m^3/s^2$) | Performance at instant of extreme event (%) | Time at full performance restoration ($t_r$) (days) | | Resources at full performance restoration ($c_r$) ($\times 10^4$ \$) | | Environmental impact at full performance restoration ($e_r$) ($\times 10^6$ kg) | | Unified resilience factors $R_5$ (%) | | | | | | | |
|---|---|---|---|---|---|---|---|---|---|---|---|---|---|---|---|
| | | | | | | | | $I_t$=0; $I_c$=1; $I_e$=0 | $I_t$=1; $I_c$=0; $I_e$=0 | $I_t$=0; $I_c$=0; $I_e$=1 | $I_t$=0.67; $I_c$=0.33; $I_e$=0 | $I_t$=0; $I_c$=0.67; $I_e$=0.33 | $I_t$=0.67; $I_c$=0; $I_e$=0.33 | $I_t$=0.33; $I_c$=0.33; $I_e$=0.33 | $I_t$=0.33; $I_c$=0; $I_e$=0.67 |
| 2818.64 | 80 | $t_{r1} = t_c$ | 18 | $c_{r1} = c_c$ | 99.1 | $e_{r1}$ | 0.4 | 89.3 | 96.9 | 92.1 | 94.4 | 90.2 | 95.3 | 91.8 | 93.7 |
| | | $t_{r2}$ | 28 | $c_{r2}$ | 91.1 | $e_{r2}$ | 0.25 | 90.4 | 92.9 | 98.0 | 92.1 | 92.9 | 94.6 | 92.8 | 96.4 |
| | | $t_{r3}=t_n$ | 36 | $c_{r5} = c_n$ | 88.9 | $e_{r3}$ | 0.2 | 90.7 | 89.8 | 100.0 | 90.1 | 93.7 | 93.2 | 92.5 | 96.6 |
| 3241.22 | 56 | $t_{r1} = t_c$ | 39 | $c_{r1} = c_c$ | 218.0 | $e_{r1}$ | 0.88 | 73.2 | 88.6 | 73.3 | 83.5 | 73.2 | 83.6 | 77.6 | 78.3 |
| | | $t_{r2}$ | 63 | $c_{r2}$ | 200.4 | $e_{r2}$ | 0.55 | 75.6 | 79.2 | 86.3 | 78.0 | 79.1 | 81.5 | 79.5 | 83.9 |
| | | $t_{r3}=t_n$ | 78 | $c_{r5} = c_n$ | 195.6 | $e_{r3}$ | 0.44 | 76.2 | 73.3 | 90.6 | 74.3 | 81.0 | 79.0 | 79.2 | 84.9 |
| 3975.6 | 15 | $t_{r1} = t_c$ | 76 | $c_{r1} = c_c$ | 421.2 | $e_{r1}$ | 1.7 | 45.7 | 74.1 | 41.1 | 64.7 | 44.1 | 63.2 | 53.1 | 52.0 |
| | | $t_{r2}$ | 121 | $c_{r2}$ | 387.2 | $e_{r2}$ | 1.06 | 50.3 | 56.4 | 66.2 | 54.4 | 55.5 | 59.6 | 57.0 | 63.0 |
| | | $t_{r3}=t_n$ | 151 | $c_{r5} = c_n$ | 377.8 | $e_{r3}$ | 0.85 | 51.5 | 44.6 | 74.5 | 46.9 | 59.1 | 54.5 | 56.3 | 64.6 |

**Table 6-12.** Resilience assessment of bridge restoration based on the damage data from fragility analysis for moment of momentum flux IM of initial bridge at $DS_3$.

| Moment of momentum flux ($m^4/s^2$) | Performance at instant of extreme event (%) | Time at full performance restoration ($t_r$) (days) | | Resources at full performance restoration ($c_r$) ($\times 10^4$ \$) | | Environmental impact at full performance restoration ($e_r$) ($\times 10^6$ kg) | | Unified resilience factors $R_5$ (%) | | | | | | | |
|---|---|---|---|---|---|---|---|---|---|---|---|---|---|---|---|
| | | | | | | | | $I_t$=0; $I_c$=1; $I_e$=0 | $I_t$=1; $I_c$=0; $I_e$=0 | $I_t$=0; $I_c$=0; $I_e$=1 | $I_t$=0.67; $I_c$=0.33; $I_e$=0 | $I_t$=0; $I_c$=0.67; $I_e$=0.33 | $I_t$=0.67; $I_c$=0; $I_e$=0.33 | $I_t$=0.33; $I_c$=0.33; $I_e$=0.33 | $I_t$=0.33; $I_c$=0; $I_e$=0.67 |
| 12782.7 | 80 | $t_{r1} = t_c$ | 18 | $c_{r1} = c_c$ | 99.1 | $e_{r1}$ | 0.4 | 89.3 | 96.9 | 92.1 | 94.4 | 90.2 | 95.3 | 91.8 | 93.7 |
| | | $t_{r2}$ | 28 | $c_{r2}$ | 91.1 | $e_{r2}$ | 0.25 | 90.4 | 92.9 | 98.0 | 92.1 | 92.9 | 94.6 | 92.8 | 96.4 |
| | | $t_{r3}=t_n$ | 36 | $c_{r5} = c_n$ | 88.9 | $e_{r3}$ | 0.2 | 90.7 | 89.8 | 100.0 | 90.1 | 93.7 | 93.2 | 92.5 | 96.6 |
| 12821.2 | 79 | $t_{r1} = t_c$ | 19 | $c_{r1} = c_c$ | 104.1 | $e_{r1}$ | 0.42 | 88.6 | 96.5 | 91.4 | 93.9 | 89.5 | 94.8 | 91.2 | 93.0 |
| | | $t_{r2}$ | 30 | $c_{r2}$ | 95.7 | $e_{r2}$ | 0.26 | 89.7 | 92.1 | 97.6 | 91.4 | 92.4 | 94.0 | 92.2 | 95.8 |
| | | $t_{r3}=t_n$ | 37 | $c_{r5} = c_n$ | 93.3 | $e_{r3}$ | 0.21 | 90.1 | 89.4 | 99.6 | 89.6 | 93.2 | 92.8 | 92.1 | 96.2 |
| 12872.5 | 77 | $t_{r1} = t_c$ | 20 | $c_{r1} = c_c$ | 114.0 | $e_{r1}$ | 0.46 | 87.3 | 96.1 | 89.8 | 93.2 | 88.1 | 94.0 | 90.1 | 91.9 |
| | | $t_{r2}$ | 33 | $c_{r2}$ | 104.8 | $e_{r2}$ | 0.29 | 88.5 | 91.0 | 96.5 | 90.2 | 91.1 | 92.8 | 91.1 | 94.6 |
| | | $t_{r3}=t_n$ | 41 | $c_{r5} = c_n$ | 102.2 | $e_{r3}$ | 0.23 | 88.9 | 87.8 | 98.8 | 88.2 | 92.2 | 91.5 | 90.9 | 95.2 |

## 6.7 Summary

This chapter presented detailed fragility analyses of a case study bridge before and after strengthening at different IMs and performance levels. The damage probabilities were estimated using the time-history analyses considering all the uncertainties in structural and force parameters. The damage probability data were computed at each increment of inundation depth (for velocity, momentum flux and moment of momentum flux) and velocity (for inundation depth). This process was repeated for all increments of velocity and inundation depths to construct the overall fragility function of the bridge for each IM. The results showed the two-parameter IMs (momentum flux and moment of momentum flux) are more efficient in the prediction of structural response, which was shown by the significant reduction in the scatter (measured by the standard deviation) of damage probability data. The viability of FRP jackets for enhancing the ductility of bridge was also examined. The bridge with FRP-confined piers showed significant reduction in the damage probability compared to the initial bridge. In fact, no damage probability was obtained for the complete collapse damage state (50% drop) in the strengthened bridge for all IMs. Larger reduction percentage in the damage probability was observed in the two-parameter fragility functions, which shows that they provide better accuracy for estimating the capacity enhancement due to strengthening.

The outcome of the research reported here will be valuable in developing fragility functions for bridges under flood loading. Furthermore, the method proposed to quantify resilience can be applied to determine the required level of resilience and the corresponding investment. Finally, the research presented here demonstrated the ability of fragility analysis

to understand the required level of strengthening for a level of resilience needed by the managing authority.

# CHAPTER 7

# CONCLUSIONS AND RECOMMENDATIONS

## 7.1 Summary

Bridges are susceptible to significant damage during extreme wave hazards such as floods, hurricanes and tsunamis. The frequency and severity of these disasters are expected to increase as a result of climate change and global warming.

The development of fragility models for the quantification of the level of damage of bridges is an essential step towards establishing resilience assessment frameworks as well as selecting appropriate restoration strategies. Most of the available research efforts on fragility models under extreme wave hazards are devoted to simply supported bridges, and little attention has been given to bridges with strong deck connectivity. The resulting potential damage in piers due to the force transfer from deck to substructure impairs the functionality of bridge and increases the recovery cost.

In this research, a comprehensive framework for developing simulation-based (analytical) fragility functions for bridges subjected to significant hydrodynamic forces was presented. The work presented in this research addressed specifically the failure in bridges that are considered integral or built/retrofitted with strong connection between deck and substructure. The detailed fragility assessment framework paves the way for the development of different retrofit schemes for bridges subjected to extreme wave hazards. In addition, new definitions for quantifying the resilience restoration was presented. The definitions simultaneously account for the time, resources (cost) and environmental impacts of different recovery options with variable importance levels to different stakeholders.

## 7.2 Conclusions

The following are the main conclusions obtained from this research.

### 7.2.1 Literature Review (Resilience Assessment Phases)

- Existing empirical methods for estimating wave forces assist in practical design and risk assessment of bridges located in hazard-prone areas. The majority of these methods are limited to hurricane conditions that have different wave properties from other hazards such as tsunamis and flood loading. Hence, further improvements of wave force models are required to cover a wider range of wave and bridge characteristics.
- The various analysis approaches on the response of bridges assume limited connectivity with the substructure. More detailed models of bearings and connections are required to examine the force transfer and performance of piers for possible design and retrofitting schemes.
- Most of the current analytical fragility functions are provided for simply-supported bridges subjected to hurricane-generated waves, in which wave height and clearance are taken as the main intensity measures. Fragility assessment methodologies can be developed for bridges subjected to various force components (e.g. impact and hydrodynamic), and new intensity measures (e.g. momentum flux and flow rate) can be included to provide a better prediction of bridge responses.
- The existing models of resilience restorations can be expanded to include more hazard types (i.e. extreme waves) and recovery elements.

### 7.2.2 Resilience Quantification

- The unified resilience index shows the significant effect of resources on the resilience factor. The unified resilience measure obtained from the multiplication of time and resources indices is conservative, since for instance, in the case of equal indices of time and resources resilience the calculated unified index is always lower than both cases.
- The use of importance factors in the estimation of resilience is significant, as it provides an indication of the predominant recovery element determined by the decision makers.
- Using the proposed new concept, the resilience can be linked to sustainability assessment of bridges by considering the environmental impact resulting from energy consumption and gas emissions associated with the post-disaster recovery operations.

### 7.2.3 Fragility Functions Development Methodology

- A framework for the construction of fragility functions of bridges subjected to extreme wave forces can be developed, where the static and time-history analyses are adopted.
- The performance curves at each inundation depth of bridge can be obtained using static analysis. This is important for identifying the performance levels required for computing the damage probability.
- The use of momentum flux and kinematic moment of momentum flux IMs was adopted in the fragility analysis. The initial results of time-history analysis showed

that the difference in drifts obtained for the same value of moment of momentum flux at two different inundations is significantly lower than the difference in drifts obtained for the case of constant momentum flux.

### 7.2.4 Fragility Functions of a Case Study Bridge

- The comparison of the pier model pushover analysis and cyclic load strength envelope (push region) results showed that the bridge pier performance can be predicted with acceptable accuracy with appropriate geometrical and material models.
- The capacity curves of strengthened bridge showed significant enhancement in both strength and ductility. For instance, the drift at collapse (50% drop in strength) increased by about 111% over the initial drift at an inundation depth of 10.298 m.
- The time-history analysis results showed that the bridge can undergo significant drifts that are larger than the drift at complete collapse performance level (50% drop in strength) at relatively high inundation depths (e.g. 10.298 m) and flow velocities (e.g., 17.5 m/s).
- The use of FRP jackets for piers was effective for preventing the collapse of bridge at large hydrodynamic forces. This shows the advantage of using the FRP jackets for enhancing the ductility capacity of bridges under extreme wave hazards.

### 7.2.5 Fragility Analysis Results

- The use of two-parameter IMs results in significant reduction in the scatter of fragility data between different inundation depths. The use of moment of momentum flux provided almost no deviation in the fragility data at the intensity measure corresponding to a damage probability of 50%.
- The strengthened bridges showed significant reduction in their damage probability at the post-peak stage. There was no damage probability for the strengthened bridge at all IMs.
- The percentage reduction in the damage probability data in strengthened bridges was higher in the fragility functions with two-parameter IMs. This shows that the use of two-parameter IMs can provide better indication of the enhancement in strength due to the reduction in the discrepancies in the fragility data.

## 7.3 Recommendations for Future Research

- The existing empirical methods for the estimation of wave forces are important for the design and vulnerability assessment of bridges located in high-risk areas. Further research is needed to address the shortcomings associated with the applicability of these methods such as the limitation in their applicability over a large range of bridge classes and hazard types.
- Although the possible deck restraint methods such as high strength bars and restrainer cables, can prevent deck unseating failure, the damage in piers due to force transfer needs to be examined through numerical models of various bridge classes.

In addition, advanced testing techniques can be adopted to capture the complex behavior of piers.

- The fragility models developed in this research were mainly based on the global failure of bridge. However, the local failure in bridge elements can result in different collapse mechanisms. Therefore, fragility models that take into account the local member failures can be developed to provide more reliable vulnerability assessment methods of fragility of bridges under extreme wave hazards.
- The existing efforts for incorporating the resilience metric as a decision variable in the loss analysis stage of PEER PBEE methodology can be expanded to wave hazards by considering the variations in the analysis phases such as the changes in the characteristics of hazard.
- Future studies can focus on expanding the quantification of resilience using the resilience triangle concept by including the effect of redundancy (fourth element) on the recovery time, cost and robustness. This is because the existence of more functional bridges within a network can facilitate the recovery operations in the post-hazard stage, which results in a shorter recovery time. The use of such unified resilience index can provide a more efficient evaluation of the various restoration strategies.

## REFERENCES


AASHTO. (2008). *Guide specifications for bridges vulnerable to coastal storms*, American Association of State Highway and Transportation Officials (AASHTO), Washington, DC.

Aghl, P. P., Naito, C., and Riggs, H. (2014). "Full-scale experimental study of impact demands resulting from high mass, low velocity debris." *Journal of Structural Engineering*, 140(5), 04014006 (1-11).

Aghl, P. P., Naito, C., and Riggs, H. (2015). "Effect of nonstructural mass on debris impact demands: Experimental and simulation studies." *Engineering Structures*, 88, 163-175.

Agrawal, A., Ghosn, M., Alampalli, S., and Pan, Y. (2011). "Seismic fragility of retrofitted multispan continuous steel bridges in New York." *Journal of Bridge Engineering*, 17(4), 562-575.

Akiyama, M., Frangopol, D. M., Arai, M., and Koshimura, S. (2013). "Reliability of bridges under tsunami hazards: Emphasis on the 2011 Tohoku-oki earthquake." *Earthquake Spectra*, 29(s1), S295-S314.

Alam, M. S., Barbosa, A. R., Scott, M. H., Cox, D. T., and van de Lindt, J. W. (2017). "Development of physics-based tsunami fragility functions considering structural member failures." *Journal of Structural Engineering*, 144(3), 04017221 (1-17).

Apelt, C.J. (1986a). "Flood loads on submerged bridges." *Institution of Engineers Australia, Queensland Division Tchnical Papers, Queensland, Australia*, 27(19): 17-23.

Apelt, C. J. (1986b). "Flood forces on bridges." *Proceedings of the 13th ARRB-5th/REAAA Combined Conference*, Adelaide, Australian Road Research Board, Melbourne, Australia, 40-46.

ASCE. (2016). “Minimum design loads for buildings and other structures.” ASCE/SEI 7-16, Reston, VA.

Ataei, N. (2013). “Vulnerability assessment of coastal bridges subjected to hurricane events.” Ph.D. thesis, Rice University, Houston, TX.

Ataei Ataei, N., and Padgett, J. E. (2011). “Coastal bridge reliability during hurricane events: Comparison of fragility curves by static and dynamic simulation.” *Proceedings of the ASCE Structures Congress*. ASCE, Reston, VA.

Ataei, N., and Padgett, J. E. (2012). “Probabilistic modeling of bridge deck unseating during hurricane events.” *Journal of Bridge Engineering*, 18(4), 275-286.

Ataei, N., and Padgett, J. E. (2013a). “Fragility assessment of coastal bridges under hurricane events using enhanced probabilistic capacity models.” *Proceedings of the Advances in Hurricane Engineering: Learning from Our Past*, 691-702.

Ataei, N., and Padgett, J. E. (2013b). “Limit state capacities for global performance assessment of bridges exposed to hurricane surge and wave.” *Structural Safety*, 41, 73-81.

Ataei, N., and Padgett, J. E. (2015a). “Fragility surrogate models for coastal bridges in hurricane prone zones.” *Engineering Structures*, 103, 203-213.

Ataei, N., and Padgett, J. E. (2015b). “Influential fluid–structure interaction modelling parameters on the response of bridges vulnerable to coastal storms.” *Structure and Infrastructure Engineering*, 11(3), 321-333.

Ataei, N., Stearns, M., and Padgett, J. (2010). “Response sensitivity for probabilistic damage assessment of coastal bridges under surge and wave loading.” *Transportation Research Record: Journal of the Transportation Research Board*, 2202(1), 93-101.

Attary, N., Unnikrishnan, V. U., van de Lindt, J. W., Cox, D. T., and Barbosa, A. R. (2017). "Performance-based tsunami engineering methodology for risk assessment of structures." *Engineering Structures*, 141, 676-686.

Attary, N., van de Lindt, J. W., Unnikrishnan, V. U., Barbosa, A. R., and Cox, D. T. (2016). "Methodology for development of physics-based tsunami fragilities." *Journal of Structural Engineering*, 143(5), 04016223 (1-12).

Aviram, A., Mackie, K. R., and Stojadinovic, B. (2008). "Effect of abutment modeling on the seismic response of bridge structures." *Earthquake Engineering and Engineering Vibration*, 7(4), 395-402.

Ayyub, B. M., and Haldar, A. (1984). "Practical structural reliability techniques." *Journal of Structural Engineering*, 110(8), 1707-1724.

Ayyub, B. M., and Lai, K.-L. (1991). "Selective sampling in simulation-based reliability assessment." *International journal of pressure vessels and piping*, 46(2), 229-249.

Azadbakht, M., and Yim, S. C. (2014). "Simulation and estimation of tsunami loads on bridge superstructures." *Journal of Waterway, Port, Coastal, and Ocean Engineering*, 141(2), 04014031 (1-20).

Azadbakht, M., and Yim, S. C. (2016). "Effect of trapped air on wave forces on coastal bridge superstructures." *Journal of Ocean Engineering and Marine Energy*, 2(2), 139-158.

Baji, H., and Ronagh, H. R. (2014). "A probabilistic study on the ductility of reinforced concrete sections." *Advances in Structural Engineering*, 17(9), 1315-1327.

Bartlett, F. M., and MacGregor, J. G. (1996). "Statistical analysis of the compressive strength of concrete in structures." *ACI Materials Journal*, 93, 158-168.

Bitner-Gregersen, E. M., Ewans, K. C., and Johnson, M. C. (2014). “Some uncertainties associated with wind and wave description and their importance for engineering applications.” *Ocean Engineering*, 86, 11-25.

Bocchini, P., Decò, A., and Frangopol, D. (2012). “Probabilistic functionality recovery model for resilience analysis.” *Proceedings of the Bridge Maintenance, Safety, Management, Resilience and Sustainability.* UK: CRC Press, Taylor and Francis, 1920-1927.

Bocchini, P., and Frangopol, D. (2010). “On the applicability of random field theory to transportation network analysis.” *Proceedings of the Bridge maintenance, safety, management and life-cycle optimization.* UK: CRC Press, Taylor and Francis, 3025-3032.

Bocchini, P., and Frangopol, D. (2011). “Resilience-driven disaster management of civil infrastructure.” *Proceedings of the Computational methods in structural dynamics and earthquake engineering*, Keynote paper, Institute of Structural Analysis and Antiseismic Research, School of Civil Engineering, National Technical University of Athens (NTUA), 1-11.

Bocchini, P., and Frangopol, D. M. (2010). “Optimal resilience-and cost-based postdisaster intervention prioritization for bridges along a highway segment.” *Journal of Bridge Engineering*, 17(1), 117-129.

Bocchini, P., and Frangopol, D. M. (2011). “A stochastic computational framework for the joint transportation network fragility analysis and traffic flow distribution under extreme events.” *Probabilistic Engineering Mechanics*, 26(2), 182-193.

Bocchini, P., and Frangopol, D. M. (2012). “Restoration of bridge networks after an earthquake: Multicriteria intervention optimization.” *Earthquake Spectra*, 28(2), 426-455.

Bocchini, P., Frangopol, D. M., Ummenhofer, T., and Zinke, T. (2013). “Resilience and sustainability of civil infrastructure: Toward a unified approach.” *Journal of Infrastructure Systems*, 20(2), 04014004 (1-16).

Bradley, B. A. (2010). “Epistemic uncertainties in component fragility functions.” *Earthquake Spectra*, 26(1), 41-62.

Bradner, C. (2008). “Large-Scale Laboratory Observations of Wave Forces on a Highway Bridge Superstructure.” M.S. thesis, Oregon State University, Corvallis, OR.

Bradner, C., Schumacher, T., Cox, D., and Higgins, C. (2010). “Experimental setup for a large-scale bridge superstructure model subjected to waves.” *Journal of Waterway, Port, Coastal, and Ocean Engineering*, 137(1), 3-11.

Bradner, C., Schumacher, T., Cox, D., and Higgins, C. (2011). “Large–Scale Laboratory Observations of Wave Forces on a Highway Bridge Superstructure.” *OTREC RR-11-10. Portland*, OR: Transportation Research and Education Center (TREC).

Braga, F., Gigliotti, R., and Laterza, M. (2006). “Analytical stress–strain relationship for concrete confined by steel stirrups and/or FRP jackets.” *Journal of Structural Engineering*, 132(9), 1402-1416.

Bricker, J. D., and Nakayama, A. (2014). “Contribution of trapped air, deck superelevation, and nearby structures to bridge deck failure during a tsunami.” *Journal of Hydraulic Engineering*, 140(5), 05014002 (1-7).

Broccardo, M., Esposito, S., Galanis, P., and Stojadinovic, B. (2017). “Application of the PEER-PBEE Framework for Probabilistic Resilience Assessment of a Structural

System." *Proceedings of the International Symposium on Sustainability and Resiliency of Infrastructure.*

Broccardo, M., Galanis, P., Esposito, S., and Stojadinovic, B. (2015). "Resilience-based risk assessment of civil systems using the PEER framework for seismic hazard." *Proceedings of the 25th European Safety and Reliability Conference (ESREL*), Zurich, Switzerland, September 7-10.

Bruneau, M., Chang, S. E., Eguchi, R. T., Lee, G. C., O'Rourke, T. D., Reinhorn, A. M., Shinozuka, M., Tierney, K., Wallace, W. A., von Winterfeldt, D. (2003). "A framework to quantitatively assess and enhance the seismic resilience of communities." *Earthquake Spectra*, 19(4), 733-752.

Bruneau, M., and Reinhorn, A. (2007). "Exploring the concept of seismic resilience for acute care facilities." *Earthquake Spectra*, 23(1), 41-62.

Bueno, R. (2017). *Puerto Rico, climatic extremes, and the economics of resilience*. GDAE Climate Policy Brief No. 6.

Burbidge, D., Cummins, P. R., Mleczko, R., and Thio, H. K. (2008). "A probabilistic tsunami hazard assessment for Western Australia." *Pure and Applied Geophysics*, 165(11-12), 2059-2088.

BITRE (Bureau of Infrastructure, Transport and Regional Economics) (2018). *Key Australian infrastructure statistics*. Department of Infrastructure, Regional Development and Cities: Canberra, Australia.

Cai, Y., Agrawal, A., Qu, K., and Tang, H. (2017). "Numerical Investigation of Connection Forces of a Coastal Bridge Deck Impacted by Solitary Waves." *Journal of Bridge Engineering*, 23(1), 04017108 (1-21).

California Department of Transportation (CALTRANS) (2013). *Seismic design criteria: Version 1.7*, Sacramento, CA.

Caprani, C. (2018). *Are Australian bridges safe, and can we do better?*, The Conversation, retrieved on Januray 14, 2019, from https://theconversation.com/are-australian-bridges-safe-and-can-we-do-better-101825.

Cardone, D., and Flora, A. (2016). "An alternative approach for the seismic rehabilitation of existing RC buildings using seismic isolation." *Earthquake Engineering and Structural Dynamics*, 45(1), 91-111.

Chandrasekaran, S., and Banerjee, S. (2015). "Retrofit optimization for resilience enhancement of bridges under multihazard scenario." *Journal of Structural Engineering*, 142(8), C4015012 (1-12).

Charvet, I., Macabuag, J., and Rossetto, T. (2017). "Estimating tsunami-induced building damage through fragility functions: critical review and research needs." *Frontiers in Built Environment*, 3, 36.

Chen, C., Melville, B. W., Nandasena, N., and Farvizi, F. (2017). "An Experimental Investigation of Tsunami Bore Impacts on a Coastal Bridge Model with Different Contraction Ratios." *Journal of Coastal Research*, 34(2), 460-469.

Chinnarasri, C., Thanasisathit, N., Ruangrassamee, A., Weesakul, S., and Lukkunaprasit, P. (2013). "The impact of tsunami-induced bores on buildings." *Proceedings of the Institution of Civil Engineers-Maritime Engineering*, 166(1), 14-24.

Choe, D.-E., Gardoni, P., and Rosowsky, D. (2010). "Fragility increment functions for deteriorating reinforced concrete bridge columns." *Journal of engineering mechanics*, 136(8), 969-978.

Choe, D.-E., Gardoni, P., Rosowsky, D., and Haukaas, T. (2008). “Probabilistic capacity models and seismic fragility estimates for RC columns subject to corrosion.” *Reliability Engineering and System Safety*, 93(3), 383-393.

Choe, D.-E., Gardoni, P., Rosowsky, D., and Haukaas, T. (2009). “Seismic fragility estimates for reinforced concrete bridges subject to corrosion.” *Structural Safety*, 31(4), 275-283.

Cimellaro, G. P., Reinhorn, A. M., and Bruneau, M. (2010). “Framework for analytical quantification of disaster resilience.” *Engineering Structures*, 32(11), 3639-3649.

Comber, M. V., Poland, C., and Sinclair, M. (2012). “Environmental impact seismic assessment: Application of performance-based earthquake engineering methodologies to optimize environmental performance.” *Proceedings of the ASCE Structures Congress*. ASCE, Chicago, Illinois,910-921.

Cornell, C. A., Jalayer, F., Hamburger, R. O., and Foutch, D. A. (2002). “Probabilistic basis for 2000 SAC federal emergency management agency steel moment frame guidelines.” *Journal of Structural Engineering*, 128(4), 526-533.

Court, A., Simonen, K., Webster, M., Trusty, W., and Morris, P. (2012). “Linking next-generation performance-based seismic design criteria to environmental performance (ATC-86 and ATC-58).” *Proceedings of the ASCE Structures Congress*. ASCE, Chicago, Illinois, 922-928.

Cuomo, G., Shimosako, K.-i., and Takahashi, S. (2009). “Wave-in-deck loads on coastal bridges and the role of air.” *Coastal Engineering*, 56(8), 793-809.

D’Amato, M., Braga, F., Gigliotti, R., Kunnath, S., and Laterza, M. (2012). “A numerical general-purpose confinement model for non-linear analysis of R/C members.” *Computers and Structures*, 102, 64-75.

Dale, V. H., Joyce, L. A., McNulty, S., Neilson, R. P., Ayres, M. P., Flannigan, M. D., Hanson, P. J., Irland, L. C., Lugo, A. E., Peterson, C. J., Simberloff, D., Swanson, F. J., Stocks, B. J., Wotton, B. M. (2001). "Climate change and forest disturbances: climate change can affect forests by altering the frequency, intensity, duration, and timing of fire, drought, introduced species, insect and pathogen outbreaks, hurricanes, windstorms, ice storms, or landslides." *BioScience*, 51(9), 723-734.

De Risi, R., Goda, K., Mori, N., and Yasuda, T. (2017). "Bayesian tsunami fragility modeling considering input data uncertainty." *Stochastic environmental research and risk assessment*, 31(5), 1253-1269.

Decò, A., Bocchini, P., and Frangopol, D. M. (2013). "A probabilistic approach for the prediction of seismic resilience of bridges." *Earthquake Engineering and Structural Dynamics*, 42(10), 1469-1487.

Decò, A., and Frangopol, D. M. (2011). "Risk assessment of highway bridges under multiple hazards." *Journal of Risk Research*, 14(9), 1057-1089.

Deng, L., and Cai, C. (2009). "Bridge scour: Prediction, modeling, monitoring, and countermeasures." *Practice Periodical on Structural Design and Construction*, 15(2), 125-134.

Denson, K. H. (1978). *Wave forces on causeway-type coastal bridges.* Technical Report MS 39762, Water Resources Research Institute, Mississippi State University, Mississippi State, Miss.

Denson, K. H. (1980). *Wave forces on causeway-type coastal bridges: Effects of angle of wave incidence and cross-section shape.* Water Resources Research Institute, Mississippi State University, Mississippi State, Miss.

Denson, K. H. (1982). *Steady-state drag, lift and rolling-moment coefficients for inundated inland bridges*. Report No. MSHD-RD-82-077, Federal Highway Administration. Mississippi State, MS.

Devi, Y. S., and Barbhuiya, A. (2017). "Bridge pier scour in cohesive soil: a review." *Sādhanā*, 42(10), 1803-1819.

Dias, W., Yapa, H., and Peiris, L. (2009). "Tsunami vulnerability functions from field surveys and Monte Carlo simulation." *Civil Engineering and Environmental Systems*, 26(2), 181-194.

Douglass, S. L., Chen, Q., Olsen, J., Edge, B., and Brown, D. (2006). *Wave forces on bridge decks*. The U.S. Department of Transportation, Federal Highway Administration, Office of Bridge Technolog, Washington, D.C.

Douglass, S. L., Hughes, S., Rogers, S., and Chen, Q. (2004). *The impact of Hurricane Ivan on the coastal roads of Florida and Alabama: a preliminary report*. Coastal Transportation Engineering Research and Education Center, University of South Alabama, Mobile, Ala.

Dueñas-Osorio, L., and Padgett, J. E. (2011). "Seismic reliability assessment of bridges with user-defined system failure events." *Journal of engineering mechanics*, 137(10), 680-690.

Ellingwood, B. R. (2001). "Earthquake risk assessment of building structures." *Reliability Engineering and System Safety*, 74(3), 251-262.

Ettema, R., Yoon, B., Nakato, T., and Muste, M. (2004). "A review of scour conditions and scour-estimation difficulties for bridge abutments." *KSCE Journal of Civil Engineering*, 8(6), 643-650.

FEMA (Federal Emergency Management Agency). (2008). *Guidelines for design of structures for vertical evacuation from tsunamis*. FEMA P-646, Washington, DC.

FEMA. (2012). *Engineering Principles and Practices for Retrofitting Flood-Prone Residential Structures (Third Edition)* . FEMA P-259, Washington, DC.

FEMA (Federal Emergency Management Agency). (2013). *Tsunami methodology technical manual*. Washington, DC.

FEMA (Federal Emergency Management Agency) (2017). *Hazus Tsunami Model Technical Guidance*. Herndon, VA.

Filippou, F. C., Popov, E. P., and Bertero, V. V. (1983). *Effects of bond deterioration on hysteretic behavior of reinforced concrete joints*. Report to the National Science Foundation, NO. UCB/EERC-83/19, Earthquake Engineering Research Center, University of California, Berkeley, California.

Finnemore, E., and Franzini, J. (2002). *Fluid Mechanics with Engineering Applications* (Tenth Edition). McGraw-Hill, New York.

Foytong, P., Ruangrassamee, A., and Lukkunaprasit, P. (2013). "Correlation analysis of a reinforced-concrete building under tsunami load pattern and effect of masonry infill walls on tsunami load resistance." *The IES Journal Part A: Civil and Structural Engineering*, 6(3), 173-184.

Foytong, P., Ruangrassamee, A., Lukkunaprasit, P., and Thanasisathit, N. (2015). "Behaviours of reinforced-concrete building under tsunami loading." *The IES Journal Part A: Civil and Structural Engineering*, 8(2), 101-110.

Frangopol, D. M., and Bocchini, P. (2011). "Resilience as optimization criterion for the rehabilitation of bridges belonging to a transportation network subject to

earthquake." *Proceedings of the ASCE Structures Congress*. ASCE, Las Vegas, Nevad, 2044-2055.

Fukuyama, H., Kato, H., Ishihara, T., Tajiri, S., Tani, M., Okuda, Y., and Nakano, Y. (2011). "Structural design requirement on the tsunami evacuation buildings." UJNR, Tokyo.

Gardoni, P., and Rosowsky, D. (2011). "Seismic fragility increment functions for deteriorating reinforced concrete bridges." *Structure and Infrastructure Engineering*, 7(11), 869-879.

Geist, E. L., and Parsons, T. (2006). "Probabilistic analysis of tsunami hazards." *Natural Hazards*, 37(3), 277-314.

Ghobarah, A. (2001). "Performance-based design in earthquake engineering: state of development." *Engineering Structures*, 23(8), 878-884.

Ghobarah, A., Saatcioglu, M., and Nistor, I. (2006). "The impact of the 26 December 2004 earthquake and tsunami on structures and infrastructure." *Engineering Structures*, 28(2), 312-326.

Ghosh, J., and Padgett, J. E. (2010). "Aging considerations in the development of time-dependent seismic fragility curves." *Journal of Structural Engineering*, 136(12), 1497-1511.

Gidaris, I., Padgett, J. E., Barbosa, A. R., Chen, S., Cox, D., Webb, B., and Cerato, A. (2017). "Multiple-hazard fragility and restoration models of highway bridges for regional risk and resilience assessment in the united states: state-of-the-art review." *Journal of Structural Engineering*, 143(3), 04016188 (1-17).

Godart, B. (2017). "New and on-going Challenges for Structural Engineers regarding Existing Structures." *Structural Engineering International*, 27(4), 481-481.

Günay, S., and Mosalam, K. M. (2013). “PEER performance-based earthquake engineering methodology, revisited.” *Journal of Earthquake Engineering*, 17(6), 829-858.

Guo, A., Fang, Q., Bai, X., and Li, H. (2015). “Hydrodynamic experiment of the wave force acting on the superstructures of coastal bridges.” *Journal of Bridge Engineering*, 20(12), 04015012 (1-11).

Haehnel, R. B., and Daly, S. F. (2004). “Maximum impact force of woody debris on floodplain structures.” *Journal of Hydraulic Engineering*, 130(2), 112-120.

Harris, H. G., and Sabnis, G. M. (1999). *Structural modeling and experimental techniques* (Second Edition). CRC press, Boca Raton, Fla.

Hashemi, M., Tsang, H., Al-Ogaidi, Y., Wilson, J., and Al-Mahaidi, R. (2017). “Collapse Assessment of Reinforced Concrete Building Columns through Multi-Axis Hybrid Simulation.” *ACI Structural Journal*, 114(2), 437-450.

Hashemi, M. J., Al-Attraqchi, A. Y., Kalfat, R., and Al-Mahaidi, R. (2019). “Linking seismic resilience into sustainability assessment of limited-ductility RC buildings.” *Engineering Structures*, 188, 121-136.

Hashemi, M. J., Al-Mahaidi, R., Kalfat, R., and Burnett, G. (2015). “Development and validation of multi-axis substructure testing system for full-scale experiments.” *Australian Journal of Structural Engineering*, 16(4), 302-315.

Hashemi, M. J., and Mosqueda, G. (2014). “Innovative substructuring technique for hybrid simulation of multistory buildings through collapse.” *Earthquake Engineering and Structural Dynamics*, 43(14), 2059-2074.

Hayatdavoodi, M., and Ertekin, R. C. (2016). “Review of Wave Loads on Coastal Bridge Decks.” *Applied Mechanics Reviews*, 68(3), 030802 (1-16).

Hayatdavoodi, M., Seiffert, B., and Ertekin, R. C. (2014). "Experiments and computations of solitary-wave forces on a coastal-bridge deck. Part II: Deck with girders." *Coastal Engineering*, 88, 210-228.

Hayes, M. B. (2008). "Assessing the vulnerability of Delaware's coastal bridges to hurricane forces." M.S. thesis, University of Delaware, Newark, DE.

Huang, W., and Xiao, H. (2009). "Numerical modeling of dynamic wave force acting on Escambia bay bridge deck during Hurricane Ivan." *Journal of Waterway, Port, Coastal, and Ocean Engineering*, 135(4), 164-175.

Ibarra, L. F., and Krawinkler, H. (2005). *Global collapse of frame structures under seismic excitations*. Report No. 152, Final Report on PEER Project 3192002, Engineering Assessment Methodology, John A. Blume Earthquake Engineering Research Center, Stanford University.

Iemura, H., Iemura, H., Pradono, M. H., and Takahashi, Y. (2005). "Report on the tsunami damage on the bridges in Banda Aceh and some possible countermeasures." Proceedings of the 28th JSCE Earthquake Engineering Symposium, Japan Society of Civil Engineers, Tokyo, 1-10.

Imbsen, R. A. (2011). *AASHTO guide specifications for LRFD seismic bridge design (Second Edition)*. American Association of State Highway and Transport Officials (AASHTO), Washington, DC.

ICF International. (2007). *The Potential Impacts of Global Sea Level Rise on Transportation Infrastructure, Phase 1 - Final Report: the District of Columbia, Maryland, North Carolina and Virginia*. The U.S. Department of Transportation (DOT), Center for Climate Change and Environmental Forecasting, Washington, D.C.

Janoyan, K. D., Wallace, J. W., and Stewart, J. P. (2006). "Full-scale cyclic lateral load test of reinforced concrete pier-column." *ACI materials Journal*, 103(2), 178-187.

Jempson, M. (2000). "Flood and debris loads on bridges." Ph.D. thesis, The University of Queensland, Brisbane, St Lucia, QLD, Australia.

Jempson, M., Apelt, C., Fenske, T., and Parola, A. (1997). "Debris loadings on bridge superstructures and piers." *Proceedings of the Austroads Bridge Conference*, Sydney, New South Wales, Australia.

Jeong, S.-H., and Elnashai, A. S. (2007). "Probabilistic fragility analysis parameterized by fundamental response quantities." *Engineering Structures*, 29(6), 1238-1251.

Jin, J., and Meng, B. (2011). "Computation of wave loads on the superstructures of coastal highway bridges." *Ocean Engineering*, 38(17), 2185-2200.

Kameshwar, S., and Padgett, J. E. (2014). "Multi-hazard risk assessment of highway bridges subjected to earthquake and hurricane hazards." *Engineering Structures*, 78, 154-166.

Kaplan, P. (1992). "Wave impact forces on offshore structures: re-examination and new interpretations." *Proceedings of the Offshore technology conference*, Houston (TX), 79-86.

Kaplan, P., Murray, J., and Yu, W. (1995). "Theoretical analysis of wave impact forces on platform deck structures." *Proceedings of the 14th international conference on offshore mechanics and arctic engineering (OMAE)*, Copenhagen, Denmark, June 18-22, Volume 1 part A, ASME, 189-198.

Kashani, M. M., Lowes, L. N., Crewe, A. J., and Alexander, N. A. (2016). "Nonlinear fibre element modelling of RC bridge piers considering inelastic buckling of reinforcement." *Engineering Structures*, 116, 163-177.

Kaufman, S. M., Qing, C., Levenson, N., and Hanson, M. (2012). *Transportation during and after Hurricane Sandy*. Rudin Center for Transportation, New York University, Wagner Graduate School of Public Service, New York.

Kaviani, P., Zareian, F., and Taciroglu, E. (2012). "Seismic behavior of reinforced concrete bridges with skew-angled seat-type abutments." *Engineering Structures*, 45, 137-150.

Kawashima, K., and Buckle, I. (2013). "Structural performance of bridges in the Tohoku-oki earthquake." *Earthquake Spectra*, 29(S1), S315-S338.

Kerenyi, K., Sofu, T., and Guo, J. (2009). *Hydrodynamic forces on inundated bridge decks, Report No. FHWA-HRT-09-028*. Federal Highway Administration. Washington, DC.

Knutson, T. R., McBride, J. L., Chan, J., Emanuel, K., Holland, G., Landsea, C., Held, I., Kossin, J. P., Srivastava, A. K., Sugi, M. (2010). "Tropical cyclones and climate change." *Nature Geoscience*, 3, 157-163.

Ko, H.-S., Cox, D., Riggs, H., and Naito, C. (2014). "Hydraulic experiments on impact forces from tsunami-driven debris." *Journal of Waterway, Port, Coastal, and Ocean Engineering*, 141(3), 04014043 (1-11).

Kosa, K. (2011). "Damage analysis of bridges affected by tsunami due to Great East Japan earthquake." *Proceedings of the International Symposium on Engineering Lessons Learned from the 2011 Great East Japan Earthquake*, Tokyo.

Koshimura, S., Namegaya, Y., and Yanagisawa, H. (2009). "Tsunami fragility-a new measure to identify tsunami damage." *Journal of Disaster Research*, 479-488.

Koshimura, S., Oie, T., Yanagisawa, H., and Imamura, F. (2009). "Developing fragility functions for tsunami damage estimation using numerical model and post-tsunami data from Banda Aceh, Indonesia." *Coastal Engineering Journal*, 51(03), 243-273.

Krawinkler, H. (1996). “Pushover analysis: why, how, when and when not to use it.” *Proceedings of the 1996 convention of the structural engineering association of California*, Maui, Hawaii,17-36

Lau, T. L., Lukkunaprasit, P., Ruangrassamee, A., and Ohmachi, T. (2010). “Performance of bridges with solid and perforated parapets in resisting tsunami attacks.” *Journal of Earthquake and Tsunami*, 4(02), 95-104.

Lehrman, J. (2010). “Laboratory performance of highway bridge girder anchorages under hurricane induced wave loading.” M.S. thesis, Oregon State University, Corvallis, OR.

Lehrman, J. B., Higgins, C., and Cox, D. (2011). “Performance of highway bridge girder anchorages under simulated hurricane wave induced loads.” *Journal of Bridge Engineering*, 17(2), 259-271.

Livermore, S. N. (2014). “Evaluation of tsunami design codes and recommendations for bridges susceptible to tsunami inundation.” Ph.D. thesis, University of Washington, Seattle, WA.

Longuet-Higgins, M. S. (1983). “On the joint distribution of wave periods and amplitudes in a random wave field.” *Proceedings of the Royal Society of London. A, Mathematical and Physical Sciences*, 389(1797), 241-258.

Lu, Y., and Panagiotou, M. (2013). “Three-dimensional cyclic beam-truss model for nonplanar reinforced concrete walls.” *Journal of Structural Engineering*, 140(3), 04013071 (1-11).

Lupoi, G., Franchin, P., Lupoi, A., and Pinto, P. E. (2006). “Seismic fragility analysis of structural systems.” *Journal of Engineering Mechanics*, 132(4), 385-395.

Macabuag, J., and Rossetto, T. (2014). “Towards the development of a method for generating analytical tsunami fragility functions.” *Proceedings of the Second European conference on earthquake engineering and seismology*, Istanbul, August 25-29.

Macabuag, J., Rossetto, T., and Lloyd, T. (2014). “Structural analysis for the generation of analytical tsunami fragility functions.” *Proceedings of the 10th International Conference on Urban Earthquake Engineering*, Earthquake Engineering Research Institute, Anchorage, AK.

Mackie, K. R., and Stojadinović, B. (2005). *Fragility basis for California highway overpass bridge seismic decision making*. Report No. 2003/16, Pacific Earthquake Engineering Research Center, University of California, Berkeley, CA.

Mangalathu, S., Jeon, J. S., and DesRoches, R. (2018). “Critical uncertainty parameters influencing seismic performance of bridges using Lasso regression.” *Earthquake Engineering and Structural Dynamics*, 47(3), 784-801.

Mangalathu, S., Soleimani, F., and Jeon, J.-S. (2017). “Bridge classes for regional seismic risk assessment: Improving HAZUS models.” *Engineering Structures*, 148, 755-766.

Marin, J., and Sheppard, D. M. (2009). “Storm surge and wave loading on bridge superstructures.” *Proceedings of the Structures Congress: Don't Mess with Structural Engineers: Expanding Our Role*, Austin, TX, 557-566.

Maruyama, K., Tanaka, Y., and Hosoda, A. (2012). “Damage of bridges structures by huge tsunami and evaluation of tsunami force on bridges.” *Proceedings of the 8th International Symposium on Social Management Systems, SSMS2012- Disaster Prevention and Reconstruction Management*, United Nations Office for Disaster Risk Reduction, New York, 1-8.

Mas, E., Bricker, J., Kure, S., Adriano, B., Yi, C., Suppasri, A., and Koshimura, S. (2014). "Field survey report and satellite image interpretation of the 2013 Super Typhoon Haiyan in the Philippines." *Natural Hazards and Earth System Sciences Discussions*, 2, 3741-3767.

Matsutomi, H., and Okamoto, K. (2010). "Inundation flow velocity of tsunami on land." *Island Arc*, 19(3), 443-457.

Mazinani, I., Binti Ismail, Z., and Hashim, A. M. (2015). "An overview of tsunami wave force on coastal bridge and open challenges." *Journal of Earthquake and Tsunami*, 9(02), 1550006 (1-25).

McAllister, T. (2014). *The performance of essential facilities in Superstorm Sandy. Proceedings of the Structures Congress*, Boston, Massachusetts, 2269- 2281.

McConnell, K., Allsop, W., and Cruickshank, I. (2004). *Piers, jetties and related structures exposed to waves: guidelines for hydraulic loadings*. London: Thomas Telford.

McDonald, S. (2017). *Hurricane Harvey: Bridge Collapses Over Greens Bayou*. Patch Media, retrieved on May 04, 2018, from: https://patch.com/texas/midtownhouston/breaking-bridge-over-greens-bayou-collapses.

McKenna, F., Fenves, G., and Scott, M. (2013). *Computer program OpenSees: Open system for earthquake engineering simulation*, Pacific Earthquake Engineering Center, University of California, Berkeley, CA.

McPherson, R. L. (2008). "Hurricane induced wave and surge forces on bridge decks." M.S. thesis, Texas AandM University, TX.

Melchers, R. E. (1999). *Structural reliability analysis and prediction* (Second Edition): John Wiley and Sons.

Menegotto, M., and Pinto, P. E. (1973). "Method of analysis for cyclically loaded reinforced concrete plane frames including changes in geometry and non-elastic behavior of elements under combined normal force and bending." *Proceedings of the IABSE Symposium (Lisboa): Resistance and Ultimate Deformability of Structures Acted on by Well-Defined Repeated Loads*, Vol. 13, International Association for Bridge and Structural Engineering (IABSE), Zurich, Switzerland, 15-22

Meng, B., and Jin, J. (2007). "Uplift wave load on the superstructure of coastal bridges." *Proceedings of the Structures Congress: New Horizons and Better Practices*. Long Beach, California.

Minasny, B., and McBratney, A. B. (2006). "A conditioned Latin hypercube method for sampling in the presence of ancillary information." *Computers and geosciences*, 32(9), 1378-1388.

Mirza, S. A., and MacGregor, J. G. (1979). "Variability of mechanical properties of reinforcing bars." *Journal of the Structural Division*, 105(5), 921-937.

Moehle, J., and Deierlein, G. G. (2004). "A framework methodology for performance-based earthquake engineering." *Proceedings of the 13th World Conference on Earthquake Engineering (CD-ROM)*, Canadian Association for Earthquake Engineering, Vancouver, Canada.

Moon, E. (2018). *The damage from Hurricane Florence is still growing*. Pacific Standard, The Social Justice Foundation, retrieved on October 05, 2018, from: https://psmag.com/news/the-damage-from-hurricane-florence-is-still-growing.

Morison, J., Johnson, J., and Schaaf, S. (1950). "The force exerted by surface waves on piles." *Journal of Petroleum Technology*, 2(05), 149-154.

Mosqueda, G., Porter, K. A., O'Connor, J., and McAnany, P. (2007). "Damage to engineered buildings and bridges in the wake of Hurricane Katrina." *Proceedings of the Forensic Engineering Symposium at Structures Congress*, California.

Nanayakkara, K., and Dias, W. (2016). "Fragility curves for structures under tsunami loading." *Natural Hazards*, 80(1), 471-486.

Nasim, M., Setunge, S., Zhou, S., and Mohseni, H. (2019). "An investigation of water-flow pressure distribution on bridge piers under flood loading." *Structure and Infrastructure Engineering*, 15(2), 219-229.

Nawy, E. (2000). *Reinforced concrete: A fundamental approach* (Fifth Edition). Pearson Prentice Hall.

Neuenhofer, A., and Filippou, F. C. (1997). "Evaluation of nonlinear frame finite-element models." *Journal of Structural Engineering*, 123(7), 958-966.

Nezamian, A., and Setunge, S. (2007). "Case study of application of FRP composites in strengthening the reinforced concrete headstock of a bridge structure." *Journal of composites for construction*, 11(5), 531-544.

Nielson, B. G. (2005). "Analytical fragility curves for highway bridges in moderate seismic zones." Ph.D. thesis, Georgia Institute of Technology, Atlanta, GA.

Nielson, B. G., and DesRoches, R. (2007). "Seismic fragility methodology for highway bridges using a component level approach." *Earthquake Engineering and Structural Dynamics*, 36(6), 823-839.

Nouri, Y., Nistor, I., Palermo, D., and Cornett, A. (2010). "Experimental investigation of tsunami impact on free standing structures." *Coastal Engineering Journal*, 52(01), 43-70.

Nowak, A. S., and Collins, K. R. (2013). *Reliability of structures* (Second Edition ed.): CRC Press.

Onai, A., and Tanaka, N. (2015). "Numerical analysis considering the effect of trapping the floatage by coastal forests and fragility curve of houses." *Journal of Japan Society of Civil Engineers, Ser. B1 (Hydraulic Engineering)*, 71(4), 727-732.

Padgett, J. E. (2007). "Seismic vulnerability assessment of retrofitted bridges using probabilistic methods." Ph.D. thesis, Georgia Institute of Technology: Atlanta, GA.

Padgett, J. E., and DesRoches, R. (2007). "Bridge functionality relationships for improved seismic risk assessment of transportation networks." *Earthquake Spectra*, 23(1), 115-130.

Padgett, J. E., and DesRoches, R. (2007). "Sensitivity of seismic response and fragility to parameter uncertainty." *Journal of Structural Engineering*, 133(12), 1710-1718.

Padgett, J. E., and DesRoches, R. (2008). "Methodology for the development of analytical fragility curves for retrofitted bridges." *Earthquake Engineering and Structural Dynamics*, 37(8), 1157-1174.

Palermo, D., Nistor, I., Al-Faesly, T., and Cornett, A. (2012). "Impact of tsunami forces on structures: The University of Ottawa experience." *Proceedings of the Fifth International Tsunami Symposium (ISPRA-2012)*, Tsunami Society International, 3-5 September, Joint Research Centre, Ispra, Italy.

Park, H., Cox, D. T., Lynett, P. J., Wiebe, D. M., and Shin, S. (2013). "Tsunami inundation modeling in constructed environments: A physical and numerical comparison of free-surface elevation, velocity, and momentum flux." *Coastal Engineering*, 79, 9-21.

Park, H., Wiebe, D. M., Cox, D. T., and Cox, K. (2014). “Tsunami inundation modeling: Sensitivity of velocity and momentum flux to bottom friction with application to building damage at Seaside, Oregon.” *Coastal Engineering Proceedings*, 1(34), 1.

Park, J., Towashiraporn, P., Craig, J. I., and Goodno, B. J. (2009). “Seismic fragility analysis of low-rise unreinforced masonry structures.” *Engineering Structures*, 31(1), 125-137.

Park, S., van de Lindt, J. W., Cox, D., Gupta, R., and Aguiniga, F. (2012). “Successive earthquake-tsunami analysis to develop collapse fragilities.” *Journal of Earthquake Engineering*, 16(6), 851-863.

Petrone, C., Rossetto, T., and Goda, K. (2017). “Fragility assessment of a RC structure under tsunami actions via nonlinear static and dynamic analyses.” *Engineering Structures*, 136, 36-53.

Porter, K. A. (2003). “An overview of PEER’s performance-based engineering methodology.” *Proceedings of the 9th international conference on applications of statistics and probability in civil engineering ICASP9*, San Francisco, CA, USA, Rotterdam: Millpress, 973-980.

Priestley, M. N., Seible, F., and Calvi, G. M. (1996). *Seismic design and retrofit of bridges*, John Wiley and Sons.

Pritchard, R. (2013). “2011 to 2012 Queensland floods and cyclone events: Lessons learnt for bridge transport infrastructure.” *Australian Journal of Structural Engineering*, 14(2), 167-176.

QDMR (Queensland Department of Main Roads). (2003). *Bridge Inspection Report, Tenthill Creek Bridge*. Queensland, Australia.

Queensland Government. (2013). *Flood costs to top $2.5 billion*. The Honourable Tim Nicholls, Treasurer and Minister for Trade, Department of the Premier and Cabinet, Queensland, Australia, retrieved on Janurary 14, 2019 from: http://statements.qld.gov.au/Statement/2013/4/17/flood-costs-to-top-25-billion.

Qu, K., Tang, H., Agrawal, A., and Cai, Y. (2017). "Hydrodynamic Effects of Solitary Waves Impinging on a Bridge Deck with Air Vents." *Journal of Bridge Engineering*, 22(7), 04017024 (1-14).

Rajeev, P., and Tesfamariam, S. (2012). "Seismic fragilities for reinforced concrete buildings with consideration of irregularities." *Structural Safety*, 39, 1-13.

Riggs, H., Cox, D., Naito, C., Kobayashi, M., Aghl, P. P., Ko, H.-S., and Khowitar, E. (2014). "Experimental and analytical study of water-driven debris impact forces on structures." *Journal of Offshore Mechanics and Arctic Engineering*, 136(4), 041603 (1-8).

Robertson, I., Yim, S., Riggs, H., and Young, Y. (2007). "Coastal bridge performance during hurricane Katrina." *Proceedings of the 3rd International conference on structural engineering, mechanics and computation*, Cape Town, South Africa.

Robertson, I. N., Riggs, H. R., Yim, S. C., and Young, Y. L. (2007). "Lessons from Hurricane Katrina storm surge on bridges and buildings." *Journal of Waterway, Port, Coastal, and Ocean Engineering*, 133(6), 463-483.

Rodriguez-Nikl, T. (2015). "Linking disaster resilience and sustainability." *Civil Engineering and Environmental Systems*, 32(1-2), 157-169.

Rosowsky, D. V., and Ellingwood, B. R. (2002). "Performance-based engineering of wood frame housing: Fragility analysis methodology." *Journal of Structural Engineering*, 128(1), 32-38.

Saadatmanesh, H., Ehsani, M. R., and Jin, L. (1997). “Repair of earthquake-damaged RC columns with FRP wraps.” *ACI Structural Journal*, 94, 206-215.

Sadeghian, P., and Fam, A. (2014). “Strengthening slender reinforced concrete columns using high-modulus bonded longitudinal reinforcement for buckling control.” *Journal of Structural Engineering*, 141(4), 04014127 (1-12).

Salem, H., and Helmy, H. (2014). “Numerical investigation of collapse of the Minnesota I-35W bridge.” *Engineering Structures*, 59, 635-645.

Salem, H., Mohssen, S., Kosa, K., and Hosoda, A. (2014). “Collapse analysis of Utatsu Ohashi Bridge damaged by Tohuku Tsunami using applied element method.” *Journal of Advanced Concrete Technology*, 12(10), 388-402.

Salem, H., Mohssen, S., Nishikiori, Y., and Hosoda, A. (2016). “Numerical Collapse Analysis of Tsuyagawa Bridge Damaged by Tohoku Tsunami.” *Journal of Performance of Constructed Facilities*, 30(6), 04016065 (1-12).

Schumacher, T., Higgins, C., Bradner, C., Cox, D., and Yim, S. C. (2008). “Large-scale wave flume experiments on highway bridge superstructures exposed to hurricane wave forces.” *Proceedings of the 6th National Seismic Conference on Bridges and Highways*, Charleston, South Carolina.

Scott, B. D., Park, R., and Priestley, M. J. (1982). “Stress strain behaviour of concrete confined by overlapping hoops at low and high strain rates.” *ACI Journal*, 79(2):13-27.

Scott, M. H., and Fenves, G. L. (2006). “Plastic hinge integration methods for force-based beam–column elements.” *Journal of Structural Engineering*, 132(2), 244-252.

Scott, M. H., Franchin, P., Fenves, G. L., and Filippou, F. C. (2004). “Response sensitivity for nonlinear beam–column elements.” *Journal of Structural Engineering*, 130(9), 1281-1288.

Scott, M. H., Kidarsa, A., and Higgins, C. (2008). “Development of bridge rating applications using OpenSees and Tcl.” *Journal of Computing in Civil Engineering*, 22(4), 264-271.

Sedgh, R., Dhakal, R., and Carr, A. (2015). “State of the Art: Challenges in analytical modelling of multi-storey shear wall buildings.” *Proceedings of the New Zealand Society for Earthquake Engineering Annual Conference (NZSEE2015)*, Rotorua, New Zealand, Paper Number: O-15.

Seiffert, B., Ertekin, R. C., and Robertson, I. N. (2014). “Experimental investigation on the role of entrapped air on solitary wave forces on a coastal bridge deck.” *Proceedings of the 33rd international conference on ocean, offshore and arctic engineering, ASME,* San Francisco, Paper No. OMAE2014-24571, pp. V04BT02A039 (1-8).

Seiffert, B., Hayatdavoodi, M., and Ertekin, R. C. (2014). “Experiments and computations of solitary-wave forces on a coastal-bridge deck. Part I: Flat plate.” *Coastal Engineering*, 88, 194-209.

Seiffert, B. R., Ertekin, R. C., and Robertson, I. N. (2015). “Wave loads on a coastal bridge deck and the role of entrapped air.” *Applied Ocean Research,* 53, 91-106.

Setunge, S., Kumar, A., Nezamian, A., De Silva, S., Carse, A., Spathonis, J., Chandler , L., Gilbert, D., Johnson, B., Jeary, A., Pham, L. (2002). *Case Study: Comparison of current QDMR practices and applicability of FRP technology*. Report 2002-005-C-02, Decision Support Tools for Concrete Infrastructure Rehabilitation, CRC for Construction Innovation, Australia.

Setunge, S., Lokuge, W., Mohseni, H., and Karunasena, W. (2014). "Vulnerability of road bridge infrastructure under extreme flood events." *Proceedings of the AFAC and Bushfire and Natural Hazards CRC Conference (AFAC 2014)*, University of Southern Queensland, QLD, Australia.

Shafiei, S., Melville, B. W., and Shamseldin, A. Y. (2016). "Experimental investigation of tsunami bore impact force and pressure on a square prism." *Coastal Engineering*, 110, 1-16.

Shafiei, S., Melville, B. W., Shamseldin, A. Y., Beskhyroun, S., and Adams, K. N. (2016). "Measurements of tsunami-borne debris impact on structures using an embedded accelerometer." *Journal of Hydraulic Research*, 54(4), 435-449.

Sheikholeslami, R., and Razavi, S. (2017). "Progressive Latin Hypercube Sampling: An efficient approach for robust sampling-based analysis of environmental models." *Environmental modelling and software*, 93, 109-126.

Sheppard, D. M., and Marin, J. (2009). *Wave loading on bridge decks*. Technical Report No. FDOT BD545-58, UF00056675, Florida Department of Transportation, Tallahassee, FL.

Shinozuka, M., Feng, M. Q., Lee, J., and Naganuma, T. (2000). "Statistical analysis of fragility curves." *Journal of engineering mechanics*, 126(12), 1224-1231.

Shinozuka, M., Murachi, Y., Dong, X., Zhou, Y., and Orlikowski, M. J. (2003). "Effect of seismic retrofit of bridges on transportation networks." *Earthquake Engineering and Engineering Vibration*, 2(2), 169-179.

Shoji, G., and Moriyama, T. (2007). "Evaluation of the structural fragility of a bridge structure subjected to a tsunami wave load." *Journal of Natural Disaster Science*, 29(2), 73-81.

Shr, J.-F., and Chen, W. T. (2004). "Setting maximum incentive for incentive/disincentive contracts for highway projects." *Journal of Construction Engineering and management*, 130(1), 84-93.

Shuka, A. R. (2017). "An Exploration of the Relationship between Construction Cost and Duration in Highway Projects." M.S. thesis, University of Colorado, Boulder, CO.

Siqueira, G. H., Sanda, A. S., Paultre, P., and Padgett, J. E. (2014). "Fragility curves for isolated bridges in eastern Canada using experimental results." *Engineering Structures*, 74, 311-324.

Spacone, E., Ciampi, V., and Filippou, F. (1996). "Mixed formulation of nonlinear beam finite element." *Computers and Structures*, 58(1), 71-83.

Spacone, E., Ciampi, V., and Filippou, F. C. (1992). *A beam element for seismic damage analysis*. Rep. No. UCB/EERC-92/07, University of California, Berkeley, CA.

Stearns, M., and Padgett, J. E. (2011). "Impact of 2008 Hurricane Ike on bridge infrastructure in the Houston/Galveston region." *Journal of Performance of Constructed Facilities*, 26(4), 441-452.

Suppasri, A., Koshimura, S., and Imamura, F. (2011). "Developing tsunami fragility curves based on the satellite remote sensing and the numerical modeling of the 2004 Indian Ocean tsunami in Thailand." *Natural Hazards and Earth System Sciences*, 11(1), 173.

Tainsh, J. (1965). *Investigation of forces on submerged bridge beams*. Report No.108. Department of Public Works, New South Wales University. Sydney, Australia, 1-25.

Tapia, C., Ghosh, J., and Padgett, J. E. (2011). "Life cycle performance metrics for aging and seismically vulnerable bridges." *Proceedings of the Structures Congress*, Las Vegas, Nevada, 1937-1948.

Taucer, F., Spacone, E., and Filippou, F. C. (1991). *A fiber beamcolumn element for seismic response analysis of reinforced concrete structures*. Report 91/17. EERC, Earthquake Engineering Research Center (EERC), University of California, Berkeley, California.

Tavares, D. H., Padgett, J. E., and Paultre, P. (2012). "Fragility curves of typical as-built highway bridges in eastern Canada." *Engineering Structures*, 40, 107-118.

Tekie, P. B., and Ellingwood, B. R. (2003). "Seismic fragility assessment of concrete gravity dams." *Earthquake Engineering and Structural Dynamics*, 32(14), 2221-2240.

Thio, H., Somerville, P., and Polet, J. (2010). *Probabilistic tsunami hazard in California*. PEER Report 2010/108, Pacific Earthquake Engineering Research. Center, University of California, Berkeley.

Unjoh, S. (2006). "Damage investigation of bridges affected by tsunami during 2004 North Sumatra Earthquake, Indonesia." *Proceedings of the Fourth International Workshop on Seismic Design and Retrofit of Transportation Facilities*. San Francisco.

Wahalathantri, B. L., Lokuge, W., Karunasena, W., and Setunge, S. (2015). "Vulnerability of floodways under extreme flood events." *Natural Hazards Review*, 17(1), 04015012 (1-12).

Wei, H.-H., Skibniewski, M. J., Shohet, I. M., and Yao, X. (2015). "Lifecycle environmental performance of natural-hazard mitigation for buildings." *Journal of Performance of Constructed Facilities*, 30(3), 04015042 (1-13).

Wiggins, J. (2018). *Bridge infrastructure at risk from corrosion as trucks get heavier, engineers say*. The Australian Financial Review, retrieved on January 14, 2019, from https://www.afr.com/business/bridge-infrastructure-at-risk-from-corrosion-as-trucks-get-heavier-engineers-say-20180904-h14x76.

Xiang, B., Yang, Z., Zhu, B., and Yin, R. (2018). “Numerical Investigation of Extreme Wave-Induced Loading on Box Girder in Marine Environment.” *Journal of Marine Science and Engineering*, 6(1), 16.

Xu, G., and Cai, C. (2014). “Wave forces on Biloxi Bay Bridge decks with inclinations under solitary waves.” *Journal of Performance of Constructed Facilities*, 29(6), 04014150 (1-13).

Xu, G., and Cai, C. (2015). “Numerical simulations of lateral restraining stiffness effect on bridge deck–wave interaction under solitary waves.” *Engineering Structures*, 101, 337-351.

Xu, G., and Cai, C. (2017). “Numerical investigation of the lateral restraining stiffness effect on the bridge deck-wave interaction under Stokes waves.” *Engineering Structures*, 130, 112-123.

Xu, G., Cai, C., and Chen, Q. (2016). “Countermeasure of Air Venting Holes in the Bridge Deck–Wave Interaction under Solitary Waves.” *Journal of Performance of Constructed Facilities*, 31(1) 04016071 (1-16).

Xu, G., Cai, C., and Deng, L. (2017). “Numerical prediction of solitary wave forces on a typical coastal bridge deck with girders.” *Structure and Infrastructure Engineering*, 13(2), 254-272.

Xu, G., Cai, C., and Han, Y. (2015). “Investigating the characteristics of the solitary wave-induced forces on coastal twin bridge decks.” *Journal of Performance of Constructed Facilities*, 30(4), 04015076 (1-17).

Zevenbergen, L., Arneson, L., Hunt, J., and Miller, A. C. (2012). *Hydraulic design of safe bridges*. Technical Report FHWA-HIF-12-018, Federal Highway Administration, Washington, DC.

Zhang, J., and Huo, Y. (2009). “Evaluating effectiveness and optimum design of isolation devices for highway bridges using the fragility function method.” *Engineering Structures*, 31(8), 1648-1660.

Zhang, J., Huo, Y., Brandenberg, S. J., and Kashighandi, P. (2008). “Effects of structural characterizations on fragility functions of bridges subject to seismic shaking and lateral spreading.” *Earthquake Engineering and Engineering Vibration*, 7(4), 369-382.

Zhong, J., Gardoni, P., and Rosowsky, D. (2012). “Seismic fragility estimates for corroding reinforced concrete bridges.” *Structure and Infrastructure Engineering*, 8(1), 55-69.

# APPENDIX

## DAMAGE STATES DATA

The following tables present the damage states data used in developing fragility functions.

**Table A-1.** Damage states for inundation depth = 10.298 m.

| Damage state | | Initial | | Strengthened with FRP jackets | |
|---|---|---|---|---|---|
| 1st crack | $DS_1$ | Drift | 0.000874 | Drift | 0.0013595 |
| | | Load | 1666840 N | Load | 2278350 N |
| Yield | $DS_2$ | Drift | 0.0032 | Drift | 0.00386 |
| | | Load | 3893680 N | Load | 4264570 N |
| Peak | $DS_3$ | Drift | 0.00575 | Drift | 0.0284 |
| | | Load | 4671300 N | Load | 5896040 N |
| 10% drop | $DS_4$ | Drift | 0.0152 | Drift | 0.0407118 |
| | | Load | 4201120 N | Load | 5314900 N |
| 20% drop | $DS_5$ | Drift | 0.0177 | Drift | 0.0562488 |
| | | Load | 3748870 N | Load | 4721770 N |
| 50% drop | $DS_6$ | Drift | 0.0533 | Drift | 0.112643 |
| | | Load | 2338340 N | Load | 2953090 N |

**Table A-2.** Damage states for inundation depth = 9.879 m.

| Damage state | | Initial | | Strengthened with FRP jackets | |
|---|---|---|---|---|---|
| 1st crack | $DS_1$ | Drift | 0.00085 | Drift | 0.001262 |
| | | Load | 1697560 N | Load | 2253200 N |
| Yield | $DS_2$ | Drift | 0.00311 | Drift | 0.003739 |
| | | Load | 3969730 N | Load | 4347670 N |
| Peak | $DS_3$ | Drift | 0.00561 | Drift | 0.028816 |
| | | Load | 4781910 N | Load | 6083080 N |
| 10% drop | $DS_4$ | Drift | 0.0158 | Drift | 0.038163 |
| | | Load | 4326100 N | Load | 5469200 N |
| 20% drop | $DS_5$ | Drift | 0.0185 | Drift | 0.051418 |
| | | Load | 3829180 N | Load | 4868850 N |
| 50% drop | $DS_6$ | Drift | 0.0537 | Drift | 0.109779 |
| | | Load | 2392700 N | Load | 3041980 N |

**Table A-3.** Damage states for inundation depth = 9.46 m.

| Damage state | | Initial | | Strengthened with FRP jackets | |
|---|---|---|---|---|---|
| 1st crack | $DS_1$ | Drift | 0.000825 | Drift | 0.001214 |
| | | Load | 1735270 N | Load | 2290880 N |
| Yield | $DS_2$ | Drift | 0.00296 | Drift | 0.003544 |
| | | Load | 4026970 N | Load | 4409060 N |
| Peak | $DS_3$ | Drift | 0.00549 | Drift | 0.027044 |
| | | Load | 4908540 N | Load | 6338090 N |
| 10% drop | $DS_4$ | Drift | 0.0168 | Drift | 0.036658 |
| | | Load | 4419780 N | Load | 5720040 N |
| 20% drop | $DS_5$ | Drift | 0.0196 | Drift | 0.049743 |
| | | Load | 3926990 N | Load | 5071620 N |
| 50% drop | $DS_6$ | Drift | 0.0541 | Drift | 0.112012 |
| | | Load | 2445950 N | Load | 3172980 N |

**Table A-4.** Damage states for inundation depth = 9.0 m.

| Damage state | | Initial | | Strengthened with FRP jackets | |
|---|---|---|---|---|---|
| 1st crack | $DS_1$ | Drift | 0.000801 | Drift | 0.00119 |
| | | Load | 1790000 N | Load | 2382250 N |
| Yield | $DS_2$ | Drift | 0.00289 | Drift | 0.003253 |
| | | Load | 4180000 N | Load | 4443730 N |
| Peak | $DS_3$ | Drift | 0.00537 | Drift | 0.026437 |
| | | Load | 5070000 N | Load | 6651840 N |
| 10% drop | $DS_4$ | Drift | 0.0182 | Drift | 0.036002 |
| | | Load | 4560000 N | Load | 5992190 N |
| 20% drop | $DS_5$ | Drift | 0.021 | Drift | 0.048917 |
| | | Load | 4060000 N | Load | 5320380 N |
| 50% drop | $DS_6$ | Drift | 0.0528 | Drift | 0.115411 |
| | | Load | 2550000 N | Load | 3331420 N |

**Table A-5.** Damage states for inundation depth = 8.5 m.

| Damage state | | Initial | | Strengthened with FRP jackets | |
|---|---|---|---|---|---|
| 1st crack | $DS_1$ | Drift | 0.000753 | Drift | 0.001117 |
| | | Load | 1818700 N | Load | 2430760 N |
| Yield | $DS_2$ | Drift | 0.00274 | Drift | 0.003132 |
| | | Load | 4315020 N | Load | 4623090 N |
| Peak | $DS_3$ | Drift | 0.0052 | Drift | 0.026437 |
| | | Load | 5270590 N | Load | 7017420 N |
| 10% drop | $DS_4$ | Drift | 0.0196 | Drift | 0.035274 |
| | | Load | 4740700 N | Load | 6320070 N |
| 20% drop | $DS_5$ | Drift | 0.0226 | Drift | 0.048505 |
| | | Load | 4222540 N | Load | 5614870 N |
| 50% drop | $DS_6$ | Drift | 0.0537 | Drift | 0.118057 |
| | | Load | 2641960 N | Load | 3517050 N |

**Table A-6.** Damage states for inundation depth = 8.0 m.

| Damage state | | Initial | | Strengthened with FRP jackets | |
|---|---|---|---|---|---|
| 1st crack | $DS_1$ | Drift | 0.000728 | Drift | 0.001092 |
| | | Load | 1904790 N | Load | 2569840 N |
| Yield | $DS_2$ | Drift | 0.00269 | Drift | 0.003035 |
| | | Load | 4573150 N | Load | 4857390 N |
| Peak | $DS_3$ | Drift | 0.0051 | Drift | 0.024811 |
| | | Load | 5508090 N | Load | 7471470 N |
| 10% drop | $DS_4$ | Drift | 0.0208 | Drift | 0.034303 |
| | | Load | 4961500 N | Load | 6729000 N |
| 20% drop | $DS_5$ | Drift | 0.0241 | Drift | 0.047291 |
| | | Load | 4405390 N | Load | 5975460 N |
| 50% drop | $DS_6$ | Drift | 0.055 | Drift | 0.120193 |
| | | Load | 2749320 N | Load | 3744570 N |

**Table A-7.** Damage states for inundation depth = 7.5 m.

| Damage state | | Initial | | Strengthened with FRP jackets | |
|---|---|---|---|---|---|
| 1st crack | $DS_1$ | Drift | 0.000692 | Drift | 0.001068 |
| | | Load | 1955670 N | Load | 2736070 N |
| Yield | $DS_2$ | Drift | 0.00259 | Drift | 0.00301 |
| | | Load | 4833900 N | Load | 5190420 N |
| Peak | $DS_3$ | Drift | 0.004965 | Drift | 0.024544 |
| | | Load | 5783990 N | Load | 7963180 N |
| 10% drop | $DS_4$ | Drift | 0.0221 | Drift | 0.033307 |
| | | Load | 5129660 N | Load | 7172760 N |
| 20% drop | $DS_5$ | Drift | 0.02565 | Drift | 0.047218 |
| | | Load | 4609730 N | Load | 6370520 N |
| 50% drop | $DS_6$ | Drift | 0.0561 | Drift | 0.121941 |
| | | Load | 0.056055 N | Load | 3980960 N |

**Table A-8.** Damage states for inundation depth = 7.0 m.

| Damage state | | Initial | | Strengthened with FRP jackets | |
|---|---|---|---|---|---|
| 1st crack | $DS_1$ | Drift | 0.000655 | Drift | 0.001044 |
| | | Load | 2077640 N | Load | 2935550 N |
| Yield | $DS_2$ | Drift | 0.00249 | Drift | 0.002986 |
| | | Load | 5120820 N | Load | 5581000 N |
| Peak | $DS_3$ | Drift | 0.014566 | Drift | 0.022699 |
| | | Load | 6167190 N | Load | 8572270 N |
| 10% drop | $DS_4$ | Drift | 0.022626 | Drift | 0.032045 |
| | | Load | 5548970 N | Load | 7723960 N |
| 20% drop | $DS_5$ | Drift | 0.026292 | Drift | 0.046101 |
| | | Load | 4927630 N | Load | 6858980 N |
| 50% drop | $DS_6$ | Drift | 0.057147 | Drift | 0.123325 |
| | | Load | 3079450 N | Load | 4286990 N |

**Table A-9.** Damage states for inundation depth = 6.5 m.

| Damage state | | Initial | | Strengthened with FRP jackets | |
|---|---|---|---|---|---|
| 1st crack | $DS_1$ | Drift | 0.000619 | Drift | 0.000995 |
| | | Load | 2161070 N | Load | 3122170 N |
| Yield | $DS_2$ | Drift | 0.00239 | Drift | 0.00284 |
| | | Load | 5406870 N | Load | 5948190 N |
| Peak | $DS_3$ | Drift | 0.017285 | Drift | 0.022432 |
| | | Load | 6629960 N | Load | 9233190 N |
| 10% drop | $DS_4$ | Drift | 0.023257 | Drift | 0.031657 |
| | | Load | 5965290 N | Load | 8305680 M |
| 20% drop | $DS_5$ | Drift | 0.026923 | Drift | 0.045446 |
| | | Load | 5299470 N | Load | 7390770 N |
| 50% drop | $DS_6$ | Drift | 0.060012 | Drift | 0.124757 |
| | | Load | 3135040 N | Load | 4616640 N |

**Table A-10.** Damage states for inundation depth = 6.0 m.

| Damage state | | Initial | | Strengthened with FRP jackets | |
|---|---|---|---|---|---|
| 1st crack | $DS_1$ | Drift | 0.000582 | Drift | 0.000971 |
| | | Load | 2337330 N | Load | 3410250 N |
| Yield | $DS_2$ | Drift | 0.00229 | Drift | 0.002598 |
| | | Load | 5909260 N | Load | 6301250 N |
| Peak | $DS_3$ | Drift | 0.018402 | Drift | 0.021461 |
| | | Load | 7189030 N | Load | 10048300 N |
| 10% drop | $DS_4$ | Drift | 0.023767 | Drift | 0.030564 |
| | | Load | 6469900 N | Load | 9043210 N |
| 20% drop | $DS_5$ | Drift | 0.027433 | Drift | 0.044742 |
| | | Load | 5745590 N | Load | 8035600 N |
| 50% drop | $DS_6$ | Drift | 0.059041 | Drift | 0.126262 |
| | | Load | 3589840 N | Load | 5017590 N |

**Table A-11.** Damage states for inundation depth = 5.5 m.

| Damage state | | Initial | | Strengthened with FRP jackets | |
|---|---|---|---|---|---|
| 1st crack | $DS_1$ | Drift | 0.000546 | Drift | 0.00085 |
| | | Load | 2472880 N | Load | 3481980 N |
| Yield | $DS_2$ | Drift | 0.00219 | Drift | 0.002136 |
| | | Load | 6482270 N | Load | 6432060 N |
| Peak | $DS_3$ | Drift | 0.019348 | Drift | 0.020052 |
| | | Load | 7861550 N | Load | 11039900 N |
| 10% drop | $DS_4$ | Drift | 0.02418 | Drift | 0.02935 |
| | | Load | 7081520 N | Load | 9941520 N |
| 20% drop | $DS_5$ | Drift | 0.027821 | Drift | 0.043698 |
| | | Load | 6287990 N | Load | 8827620 N |
| 50% drop | $DS_6$ | Drift | 0.068411 | Drift | 0.127646 |
| | | Load | 3388420 N | Load | 5516630 N |

**Table A-12.** Damage states for inundation depth = 5.0 m.

| Damage state | | Initial | | Strengthened with FRP jackets | |
|---|---|---|---|---|---|
| 1st crack | $DS_1$ | Drift | 0.000509 | Drift | 0.000777 |
| | | Load | 2739220 N | Load | 3726300 N |
| Yield | $DS_2$ | Drift | 0.00209 | Drift | 0.001991 |
| | | Load | 7112020 N | Load | 7016140 N |
| Peak | $DS_3$ | Drift | 0.019883 | Drift | 0.019057 |
| | | Load | 8684630 N | Load | 12186500 N |
| 10% drop | $DS_4$ | Drift | 0.024277 | Drift | 0.028015 |
| | | Load | 7824430 N | Load | 11038400 N |
| 20% drop | $DS_5$ | Drift | 0.028161 | Drift | 0.043504 |
| | | Load | 6946950 N | Load | 9746770 N |
| 50% drop | $DS_6$ | Drift | 0.061201 | Drift | 0.129467 |
| | | Load | 4345260 N | Load | 6088020 N |